MECHANICAL BEHAVIOUR OF DAMAGED REINFORCED CONCRETE PIPES REPAIRED WITH LAYERED SANDWICH FIBER COMPOSITES

by

Thomas James Goill

Submitted in partial fulfilment of the requirements

for the degree of Master of Applied Sciences

at

Dalhousie University

Halifax, Nova Scotia

March 2021

Table of Contents:

List of Tables:

List of Figures:

ABSTRACT:

Trenchless pipe repair can offer time and cost savings over traditional excavation and replacement of damaged pipes. Conventional repair methods using prefabricated steel liners are not effective due to significant loss of discharge capacity, especially for non-circular cross-sections. The objective of this thesis is to introduce a novel layered sandwich system composed of fiber-reinforced polymer (FRP) composites. Concrete pipes with a length of 500 mm and inner diameter of 380 mm are stressed to simulate damage; cracks at the crown, invert and springline are produced by loading via the three-edge-bearing (TEB) test setup (ASTM C497). The damaged pipes are repaired with multiple layers of FRPs sandwiching thin layers of a syntactic foam core. The sandwich system will save FRP materials and provide the required stiffness based on the mechanics of sandwich composites. The sandwich system is applied with epoxy resin to the entire length of the inner diameter of the pipes. The repaired specimens are then loaded to failure via the three-edge-bearing test. The highest load was achieved by a hybrid sandwich liner composed of Glass Fibre Reinforced Polymer (GFRP), syntactic foam, and Carbon Fibre Reinforced Polymer (CFRP). Finite Element Analysis (FEA) was performed in ABAQUS and results were compared to experimental results. The load versus strain plots of FEA and experimental results were in agreement and had an average test/model ratio of 1.00 and COV of 47.88%. A parametric study was performed in ABAQUS of a pipe model had an inner diameter of 762mm, a wall thickness of 152.4mm, and a length of 1000mm with varying layers of GFRP, Syntactic foam, and CFRP. Results from the parametric study showed that the most effective way to increase stiffness is to increase the number of GFRP and CFRP plies as the syntactic foam plies offer a marginal increase in stiffness.

List of Abbreviations and Symbols

ASTM – American Society for Testing and Materials

CCTV – Closed-Circuit Television

CDP – Concrete Damage Plasticity

CFRP – Carbon Fibre Reinforced Polymer

CIPP – Cured In Place Pipe

COV – Coefficient of Variation

E – Modulus of Elasticity

E_0 – Linear Elastic Modulus of concrete

EF fitting – Eelectrofusion Fitting

EPA – Environmental Protection Agency

f'_c – Compressive Strength of Concrete

f_r – Tensile Strength of Concrete

FEA – Finite Element Analysis

FRP – Fibre Reinforced Polymer

GFRP – Glass Fibre Reinforced Polymer

GRP – Glass Reinforced Plastic

HDPE – High Density Polyethylene

M – Moment

LE – Elastic Strain in ABAQUS

NATS – Northwest Arm Trunk Sewer

NDT – Non-Destructive Testing

P – Applied Load at Crown

PE – Plastic Strain in ABAQUS

PE – Polyethylene

PVC – Polyvinyl Chloride

PU – Polyurethane

R – Mean Radius

RCP – Reinforced Concrete Pipe

SYN-FRCP – Polypropylene Fiber-Reinforced Concrete Pipes

TEB – Three-Edge Bearing

UV – Ultraviolet

Chapter 1. Introduction

1.1 Motivation

Ensuring that infrastructure meets design requirements is necessary for public safety. Failure to inspect and meet design requirements can result in premature failure leading to social disruption, financial costs, and casualties. Once an asset is deemed to be deficient, the next course of action is to determine the economic feasibility of replacing the asset or repairing the asset. In the case of buried pipes, the decision can be broadly grouped into either replacement with the open-cut method or repair with trenchless technology. Cost and social impact of construction projects are important factors to consider in project management. The open-cut method is the traditional method of rehabilitation or replacement of damaged buried pipes (Das et al., 2016). In urban areas, open-cut replacement projects can cause significant social disruption by impeding traffic and access to business store fronts for days to weeks (Lueke & Ariaratnam, 2001a). Trenchless methods of rehabilitation offer increased efficiencies when they are suitable for the project and cause minimal social disruption to the surrounding environment compared to open cut projects (Lueke & Ariaratnam, 2001a). The objective of trenchless rehabilitation is to restore the strength of a buried pipe to its original value or greater. Rehabilitation of a non-damaged pipe may be performed to increase the strength of the pipe to accommodate new loads at the surface beyond the original design. Flow rate is not necessarily compromised when reducing the pipe cross section in trenchless rehabilitation because both friction and water infiltration in plastic pipes are reduced compared to concrete (Plastic Pipe Institute, 2008).

Maintenance and repair are essential steps of any asset's life cycle. Infrastructure such as culverts, sewer systems or other sub-grade piping used to channel fluids must be monitored and inspected to verify the integrity of the pipe. In most cases, access to the culvert or piping is limited

as they are buried or submerged (Meegoda & Zou, 2015). Sewer systems and other pipes with restricted access often rely on visual inspection performed by an inspector via remote controlled closed circuit television (CCTV) cameras (Dirksen et al., 2013; Plastic Pipe Institute, 2008; Sorrell, 1995). Upon determining the condition of the asset, an economic decision can be made based on the severity of the damage and deterioration rate of the asset (Meegoda & Zou, 2015). A full culvert replacement is often cost prohibitive unless absolutely necessary as a single culvert replacement costs more than multiple rehabilitation procedures which can restore the culvert to near perfect condition (Meegoda & Zou, 2015). Excavation and replacement can be preferred if the pipe is less than 6 feet below ground, there are few obstructions above and below ground such as utility lines or buildings, or the diameter of the pipe needs to be increased significantly (Sorrell, 1995). Trenchless rehabilitation offers repair options for inaccessible pipes buried as deep as 50 feet below grade, pipes surrounded by utilities which make excavation difficult or unsafe, or pipe repairs that must be completed in a relatively short timeframe (Sorrell, 1995). Trenchless rehabilitation methods typically reduce the diameter of the pipe apart from pipe bursting. Pipe bursting is the only trenchless technology method capable of fully replacing a buried pipe (Ariaratnam et al., 2014). Trenchless rehabilitation methods such as slip-lining and Cured in Place Pipe (CIPP) have been proven to be cost and performance effective (Meegoda & Zou, 2015). The use of a fibre reinforced polymer (FRP) fabric sandwich technology will be explored as a design to optimise material properties in FRP liner design relevant to CIPP and wet FRP layup. Currently, there are no standards or codes that address the structural analysis of FRP materials for the rehabilitation of concrete pipes. There is currently a research gap in the failure mechanics of Reinforced Concrete Pipe (RCP) rehabilitated with FRP materials.

1.2 Objectives

This thesis aims to:

- Explore the loading behaviour and failure modes of damaged RCP repaired with FRP liners.
- Provide a foundation for future research on larger scales for the development of accurate design procedures and code recommendations.

1.3 Scope

The objectives will be achieved by:

- Simulating damage to RCP in the three-edge bearing (TEB) test
- Repairing the damaged RCP with FRP materials
- Testing the repaired RCP in the TEB test
- Comparing FEA results to experimental data
- Performing a parametric study using with FEA software

Wet FRP layup would not be feasible for an in-service RCP with 380mm inner diameter due to inaccessibility. The scope of this project narrows to exploring the loading behaviour of RCP repaired with FRP liners and providing suggestions for future research.

1.4 Thesis Layout

The thesis is composed of 5 chapters: Introduction, Literature Review, Experimental Program, Numerical Study, and Conclusions and Recommendations. The Introduction, Chapter 1, begins with the motivations and significance of this research to the industry of trenchless technologies. Chapter 1 ends with the objectives, scope, and thesis layout to provide a detailed outline and description of the project to come. The Literature Review, Chapter 2, reviews the

current methods of pipe rehabilitation and replacement, as well as mechanics of pipe loading and failure modes of FRP materials bonded to concrete. The Experimental Program, Chapter 3, describes the materials, fabrication procedures, test set up and instrumentation. Chapter 3 ends with the results, observations, and discussion of the results. The Numerical Study, Chapter 4, describes the procedure and parameters used in the FEA software ABAQUS and compares FEA results to the experimental results of Chapter 3. A parametric study performed in ABAQUS at the end of Chapter 4. The Conclusions and Recommendations, Chapter 5, summarises the findings of the research and provides guidance for future studies.

Chapter 2. Literature Review

This chapter consists of an industry review of trenchless technologies, theory behind the repair of RCP with FRP materials and concludes with identifying research gaps. The industry review covers the open cut method, pipe bursting, sliplining, CIPP, and FRP layup. The theory includes FRP sandwich technology, FRP rehabilitation of RC beams, and failure modes of FRP materials adhered to concrete.

2.1 Industry review

2.1.1 Open Cut Method

Traditionally, inaccessible sections of sub-grade infrastructure were accessed via the open cut method. The open cut method is the default method to fall back on when trenchless technology is not applicable (Das et al., 2016). Any section of pipe that needs rehabilitation must be taken out of service and the flow which normally follows path of the section in need must be rerouted or backed up for the period of the rehabilitation project (Stein & Stein, 2004b). Special consideration should be made to account for seasonal or otherwise heavy rainfalls (Stein & Stein, 2004b). The open-cut method requires that the area above the pipe section in need to be blocked off as excavation begins. After the repair, rehabilitation or replacement, the trench is filled and pavement is replaced if it was removed (Stein & Stein, 2004c). In urban areas as seen in Figure 2-1, Open-cut method projects often have a high social impact on local traffic due to detours, a risk of damage to properties and utilities, and a risk of premature damage to road structures during excavation (Stein & Stein, 2004c).

Costs of an open-cut project in a dense urban area can be twice the cost of a similar open-cut project in un-built areas due to costs of road and pedestrian traffic detours, removal of material from site, road reconstruction and ensuring municipal services are maintained in adjacent

properties (Stein & Stein, 2004c). Time-cost relationships of open-cut projects and cure-in-place lining projects developed by Sousa & Meireles (2018) revealed that trenchless cure-in-place linings performed better on small projects while open cut methods saw faster completion times for large projects with less variability in time performance (Sousa & Meireles, 2018).

Figure 2-1: Social Disruption of Open Cut Method (Stein & Stein, 2004c)

2.1.2 Pipe Bursting

Pipe bursting is a trenchless method of pipe replacement which employs a bursting head that expand or hammer the existing pipe outwards radially to accommodate the incoming replacement pipe. The general layout of a pipe bursting operation requires access at start and end of the section of pipe to be replaced; the pit at which the bursting head in fed is the insertion pit and the pit at the end of the pipe that houses the hydraulic tensioner or winch is the machine pit shown in Figure 2-2 (Lueke & Ariaratnam, 2001a; Stein & Stein, 2004a). Therefore, some excavation may be required depending on the specifics of the project.

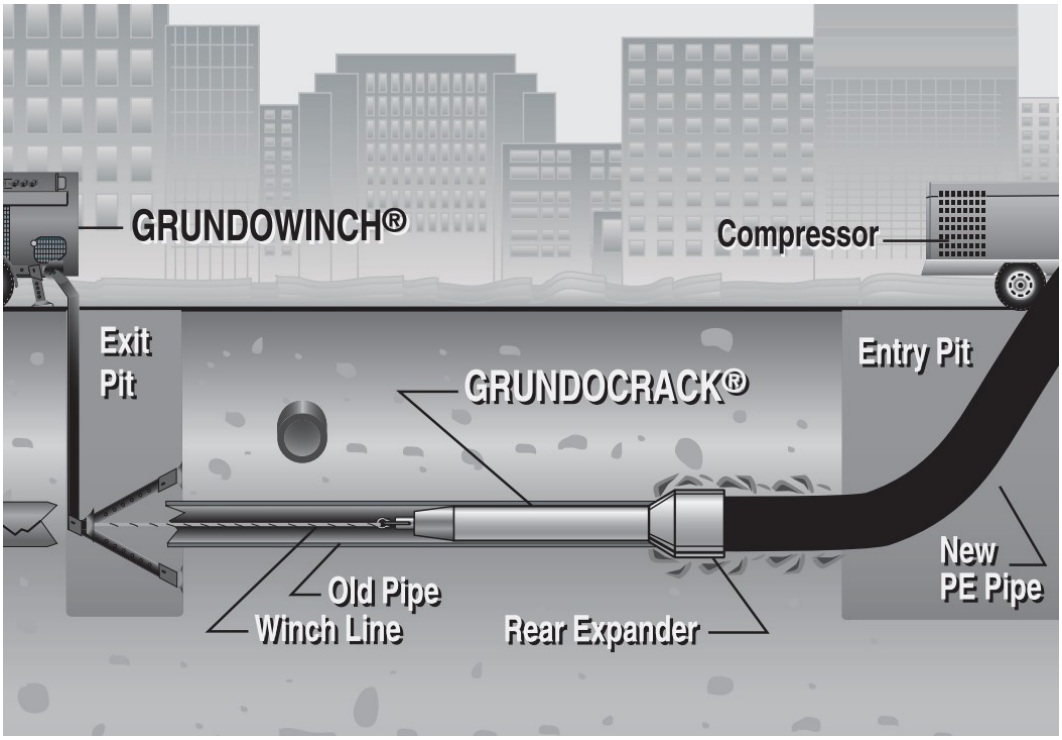

Figure 2-2: Diagram of Pneumatic Pipe Bursting (TT Technologies, 2006a)

Three methods of pipe bursting exist, and each utilises a specialised bursting head. Static, pneumatic, and hydraulic bursting heads can be used depending on the nature of the pipe bursting. Static pipe bursting only uses static forces to break apart the existing pipe which are applied through forces driven by a hydraulic system, or a winch which can push or pull rods, chains, or cables to drive the bursting head forward (Lueke & Ariaratnam, 2001a). As seen in Figure 2-3, static bursting methods typically use a cone shaped bursting head to impart a radial force against the walls of the existing pipe; the radial forces from the pulling of the cone shaped static bursting head cause the walls to fail in tension (Lueke & Ariaratnam, 2001a). Depending on the size of the new pipe, a rear expander may be necessary to disperse the fractured pieces into the surrounding soil to enlarge the diameter of the tunnel to make room for the new pipe (TT Technologies, 2017).

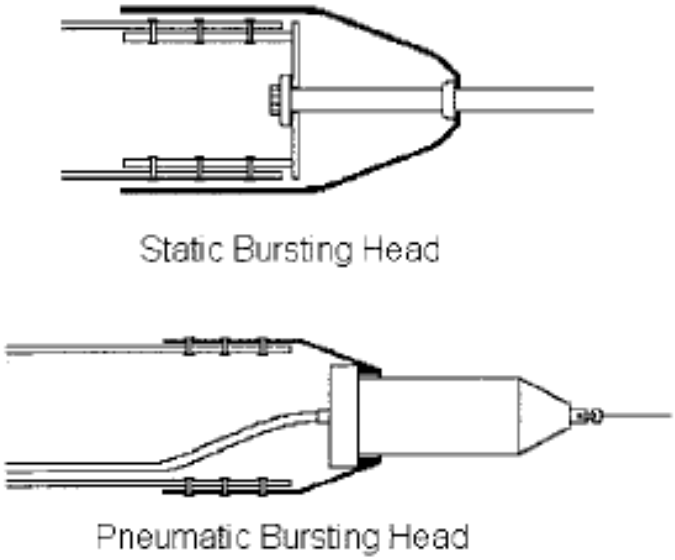

Figure 2-3: Static Bursting Head and Pneumatic Bursting Head (Lueke & Ariaratnam, 2001b)

Pneumatic bursting uses a percussive hammering force produced by compressed air to drive the bursting head into the old pipe depicted in Figure 2-2 (Lueke & Ariaratnam, 2001a). The hammering forces develop both radial and transverse forces which cause the old pipe to fail in tension and shear respectively (Lueke & Ariaratnam, 2001a). In addition to a tension cable system to guide the bursting head through the old pipe, an air compressor must be present at the insertion pit with air lines running to the bursting head through the new pipe (Lueke & Ariaratnam, 2001a).

Hydraulic expansion method of pipe bursting uses a hydraulic bursting head that is fitted with hydraulic cylinders which expand radially to push the walls of the old pipe into the surrounding soil (Lueke & Ariaratnam, 2001a). Hydraulic expansion bursting heads are seldom used in favor of simpler designs with less moving parts such as static bursting (Stein & Stein, 2004a). Ariaratnam et al. (2014) published a survey of 886 projects completed by 19 North American contractors which revealed that 51.8% of contractors owned static pipe bursting systems and 48.2% owned pneumatic bursting systems.

The equipment required for a project will depend on the depth, size and material of the host pipe, the length and terrain that must be traversed and the new pipe size and material (TT Technologies, 2006b). A survey of sewer, sanitary water, and service lateral projects, found that cast iron, ductile iron, polyvinyl chloride (PVC), vitrified clay, concrete, brick host pipes were candidates for pipe bursting and that 98.8% of new the pipe installed for these rehabilitation projects was high density polyethylene (HDPE) (Ariaratnam et al., 2014).

In comparison to conventual open-cut methods, pipe bursting will be a more suitable choice for pipe replacement for urban and deeply buried pipes. As the depth of the operation increases, the cost of open-cut projects increases, while the cost of pipe bursting projects is not significantly affected (Lueke & Ariaratnam, 2001a; Stein & Stein, 2004c). In terms of time, pipe bursting projects operating within hours and days while open-cut projects operate in days and weeks. the lack of surface disturbance gives pipe bursting an advantage in scheduling (Lueke & Ariaratnam, 2001a).

The design and procedure of a pipe bursting project must be carefully considered as there are limitations to what kind of systems can be candidates for pipe bursting. Straight pipes are the most suitable candidate as the stiffness of the new pipe may resist cornering bends (Ariaratnam et al., 2014). Increasing the diameter of the new pipe poses more challenges than replacement with a pipe of equal diameter. Surface heave can occur if the increase in pipe diameter is more than 50% which may result in damage to buildings and roadways (Ariaratnam et al., 2014; Isett, 2000). Pipe bursting is the only trenchless pipe rehabilitation method which allows for the increase of pipe diameter to accommodate a higher flowrate (Ariaratnam et al., 2014). Pipe bursting technology is relatively new and there is a limited amount of an available skilled workforce in comparison to traditional open-cut methods (Lueke & Ariaratnam, 2001a).

2.1.3 Sliplining

Sliplining is a method of pipe rehabilitation in which a new pipe of a smaller diameter is slipped into the host pipe without disturbance. Key elements to the design of a sliplining procedure include determining the pipe liner diameter, liner wall thickness, flow capacity and design of the access points (Plastic Pipe Institute, 2008). The selection of the pipe diameter is typically governed by the inner diameter of the existing pipe and any obstructions that may block the progress of the pipe (Plastic Pipe Institute, 2008). As a general guideline, the outer diameter of the liner should be 10% less than the inner diameter of the host pipe; host pipes with diameters over 24 inches commonly use liners that are 5% smaller in diameter (Plastic Pipe Institute, 2008).

Non pressurized pipes determine the required liner thickness by comparing the critical bucking pressure of the liner to the expected hydrostatic load due to the rising of the water table and determining if their respective ratio satisfies the design safety factor; a safety factor of 2 or greater is sufficient for evaluating long term loading (Plastic Pipe Institute, 2008). However, the external structure of the grout and existing pipe will provide the bulk of the structural support for the pipeline (Simpson et al., 2017). The gap between the liner and existing pipe is pumped with grout; this layer of grout is referred to as the grout annulus (Rohrsanierung & Bau GmbH, n.d.; Simpson et al., 2017). For sliplining where the host pipe is concrete, Simpson et al., (2017) found that the grout annulus strongly bonds with the external concrete pipe and does not bond well to HDPE sliplining. The increased structural strength of sliplining comes from the pumping of the grout annulus which is theorised to fill cracks in the host pipe (Simpson et al., 2017). The HDPE sliplining is essentially inactive under service loads and only experienced a diameter change of 0.01% (Simpson et al., 2017). The design of pressurized pipes includes the consideration of

internal stresses in addition to the external forces that may be considered for a non-pressurized pipe (Plastic Pipe Institute, 2008).

The flowrate will depend on the slope of the pipe, inner dimensions of the liner and frictional forces between the water and liner walls (Plastic Pipe Institute, 2008). An HDPE liner will exert less frictional forces on flowing water than other non-plastic piping materials (Plastic Pipe Institute, 2008). In theory, a non-plastic pipe of equal size should have a lower volumetric flow rate due to higher frictional forces. However, the decrease in frictional forces due to the HDPE liner do not offset the loss of flow rate due to decreased cross sectional area in all cases. Barber et al., (2005) found that 152.4mm (6 inch) pressurized steel pipes experienced a 10.8% to 21.4% loss of flow when lined with HDPE depending on the quality of the installation of the liner. The study only compared new pipes with clean interiors to their lined counterparts (Barber et al., 2005). A case study in Poland found that flow velocity and volumetric flow rate in their sewer increased after cleaning the accumulated hard sludge from the bottom of a 65 year old sewer and rehabilitating the sewer with Glass Reinforced Plastic (GRP) sections (Tomczak & Zielińska, 2017). Flow velocity in the sewer increased from 0.47 m/s to 1.27 m/s therefore protecting the sewer from further clogging build up as the rehabilitated velocity was over the 0.7 m/s threshold for sediment build up (Tomczak & Zielińska, 2017). Tullis & Anderson (2010) found that tapering the inlet of the culvert led to a geometry that was favorable to the discharge flow and increased the flow efficiency of the culvert.

The access points of a sliplined system refer to the interface between the lined pipe and the existing system. In the case of sewer systems, the access points will be termination points of the pipe such as manholes or headwalls (Plastic Pipe Institute, 2008). The gap between the host pipe and liner is referred to as the annulus space and must be filled and sealed for structural integrity

and to prevent infiltration of fluids (Plastic Pipe Institute, 2008; Simpson et al., 2017). Access points of non-pressurized systems are sealed by inserting an Okum ring into the grout filled annulus space, sealing the Okum ring in place with more grout and capping the annulus space entrance with a chemical resistance concrete (Plastic Pipe Institute, 2008). Pressurized piping will require fused connections to the liner capable of maintaining the pressure within the system (Plastic Pipe Institute, 2008).

The operational procedure for sliplining a host pipe with a polyethylene (PE) liner begins with inspection and cleaning of the host pipe. Closed-circuit television (CCTV) is used to survey the condition of the pipe and determine the location of potential obstructions such as bends between offset pipe segments (Plastic Pipe Institute, 2008). Cleaning of the host pipes is necessary to remove debris and dirt which can obstruct the progress of the liner; cleaning is often completed with a cleaning bucket machine, kites, plugs or the pulling of a test section of liner (Plastic Pipe Institute, 2008).

Depending on the geometry of the project, a method of joining pipe sections will be selected. For a continuous solid wall pipe, butt fusion can be used to join the individual section of the PE pipe (Plastic Pipe Institute, 2008). Butt fusion is a process in which two ends of HDPE pipe are heated on opposite ends of a heating plate and then are permanently joined by pressing the molten pipe ends together under pressure; the resulting joint can be as strong or stronger than the continuous pipe material (Plastic Pipe Institute, 2008; Zhao et al., 2002). Dust contamination negatively affect the quality of HDPE butt joints (Zhao et al., 2002). Zhao et al. (2002) recommend cleaning the welding surface of the pipe and the heater face before the joining of each section and the use of wind/dust shelters to minimize dust contamination.

Profile wall pipe sections can be used to line non-circular shapes such as ovals or egg shaped sewers and pipes can be joined by bell and spigot connections and have gaskets to maintain a water tight seal between segments (Plastic Pipe Institute, 2008; Rohrsanierung & Bau GmbH, 2013). Alternatively, butt fusion or electrofusion can be used to join profile wall sections. In the electrofusion process, an EF fitting (electrofusion fitting), which has spirals of exposed copper wires at the interface between the fitting and pipe, fits over the ends of two PE pipes to be joined (Shi et al., 2011). The EF fitting is connected to a welding machine and Joule's effect causes the copper wires to heat and expand the surrounding PE (Shi et al., 2011). Shi et al. (2011) recommend inspecting alignment in insertion of the pipes into the fitting as well as inspecting the fusion surface for dust, debris or moisture contamination and oxidation on the copper else a poor bond could be formed between the fitting and pipe resulting in premature failure. Cold welding and over welding should be avoided by operating at optimum welding power and time for optimal electrofusion joints (Shi et al., 2011).

After selecting a method of pipe joining most suited to the project, the excavation and execution phases can begin. The size and dimensions of the access pit will depend on several factors based on the geometry of the operation (Plastic Pipe Institute, 2008). The depth of the host pipe, diameter of the host and liner pipes and stiffness of the liner pipe will influence the amount of space necessary to insert the liner into the host pipe (Plastic Pipe Institute, 2008). In general, shallower pipelines with smaller pipe diameters require smaller access pits than deeper pipelines with larger diameters (Plastic Pipe Institute, 2008).

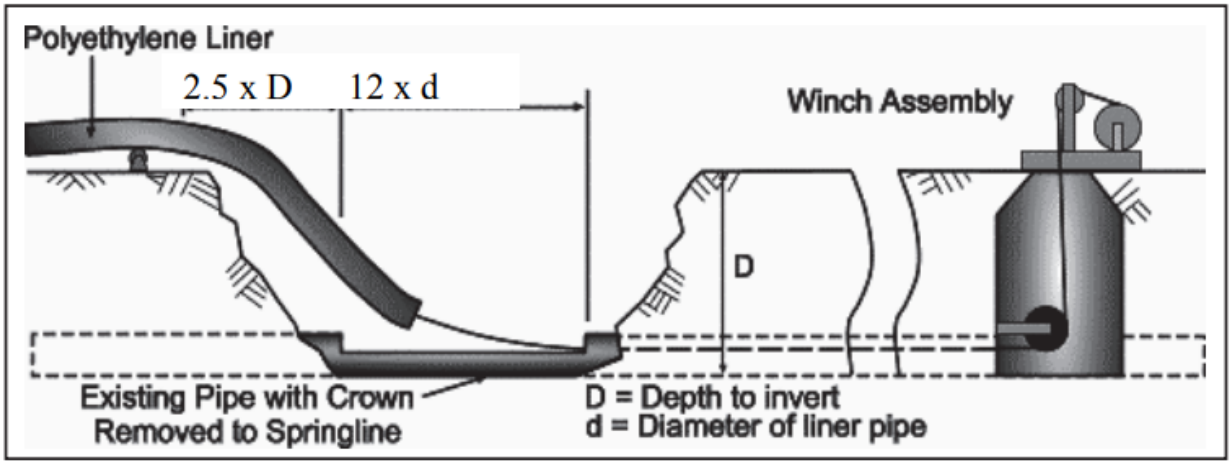

Figure 2-4: Pull Method of Sliplining (Plastic Pipe Institute, 2008)

The insertion of the liner is completed by either the push or pull method depending on how the sections of liner were joined. Solid wall pipe joined by butt fusion can be installed with the push or pull method or a combination of the two (Plastic Pipe Institute, 2008). However, profile wall pipe which has been joined by gasketed bell and spigot must use the push method to maintain a watertight gasket connection between segments (Plastic Pipe Institute, 2008). The pull technique employs a pulling head attached to the starting end of the liner and pulls the head through the host pipe with a winch and cable system depicted in Figure 2-4 (Plastic Pipe Institute, 2008). As shown in Figure 2-5, the push method uses heavy machinery, which might have otherwise been used to excavate the access pit, to push a choker strap wrapped around the liner down and into the host pipe (Plastic Pipe Institute, 2008). The choker must be loosened and reattached manually after each pull (Plastic Pipe Institute, 2008). Light flow can be maintained during the sliplining operation of non-pressurized pipes as the flowing fluid can lubricate the movement of the liner (Plastic Pipe Institute, 2008). Non-pressurized flows below 50% of the host pipe capacity can be accommodated during installation; excess flow can be controlled by blocking or bypassing the host pipe (Plastic Pipe Institute, 2008). Once the liner is installed, the annual gap can be grouted

and sealed as described earlier and the service and terminal connections can be connected completing the pipe network (Plastic Pipe Institute, 2008).

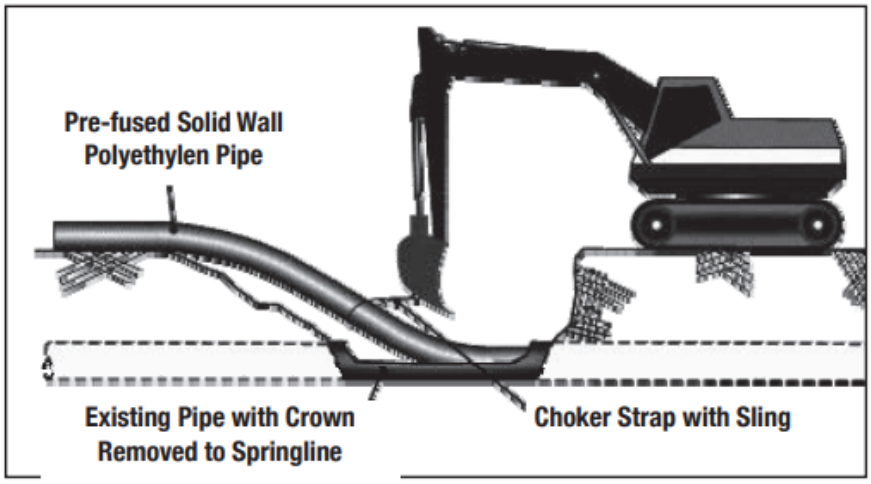

Figure 2-5: Push Method of Sliplining (Plastic Pipe Institute, 2008)

In a case study performed by Kuliczkowska & Gierczak (2013), a concrete sewer main was experiencing excess flow due to groundwater infiltration. The sewer main was rehabilitated with an HDPE slipliner which stopped the infiltration of groundwater. The project was expected to see a net cost benefit after 3 years of operation due to the decreased volume of sewage to be processed (Kuliczkowska & Gierczak, 2013). However, after 12 months, the HDPE liner failed because the annulus gap was not filled with grout due to insufficient access by a contractor despite them knowing the critical structural role of the grout (Kuliczkowska & Gierczak, 2013). Without the grout in the annulus gap, groundwater infiltration was allowed to accumulate and the resulting pressure buckled the liner as modulus of elasticity of the HDPE liner decreases over time (Kuliczkowska & Gierczak, 2013). A stiffer HDPE pipe was engineered to not require an annulus grout filling and replaced the buckled liner (Kuliczkowska & Gierczak, 2013). Quality of the liner must be monitored as imperfections in the liner surface can weaken the critical buckling pressure leading to premature failure. A study performed by Bakeer et al. (1999) found that HDPE pipe with deformed oval cross sections and pipes with partially confined liners will buckle under

pressures as much as 50% lower than circular counterparts under uniform loading, which may occur in instances of groundwater infiltration of the host pipe (Bakeer et al., 1999). Bakeer et al. (1999) recommend that should a flexible pipe be installed in an oval or broken pipe, the liner should be accordingly designed with a lower buckling resistance. The findings of Bakeer et al. (1999) agree with the case study of Kuliczkowska & Gierczak (2013) as an unconfined HDPE liner buckled in a damaged pipe that experience groundwater infiltration.

2.1.4 Cure in Place Pipe (CIPP)

CIPP lining is a rehabilitation method which employs the use of FRP technology to form an FRP pipe within the deteriorating host pipe. The core components of an CIPP lining are the fabric tube liner and resin. To comply with American Society for Testing and Materials Standards (ASTM F2019, ASTM F1743), the fabric should be composed of a minimum of two distinct tube layers of glass fibers. The glass fibers should be corrosion resistant, strong enough to manage the pulling forces experienced during installation, and resistant to abrasion and chemicals at the inner surface layer of fabric (ASTM International, 2011). The fabric should provide a close fit with the host pipe. The fabric should fit within the host pipe and have the ability to expand past the host pipe's nominal diameter to reduce the risk of ground water infiltration between the liner and host pipe (ASTM International, 2011). The use of a smaller diameter that expands into the host pipe is essential to ensuring wrinkling does not occur (ASTM International, 2011). Ultimate strength and strength of first cracking of a liner are decreased at wrinkled locations of CIPP liners (Das et al., 2016). CIPP liners often fail near wrinkle defects (Das et al., 2016).

The type of resin that is used to impregnate the fabric depends on the selected curing method. Resins are typically polyester, vinylester or epoxy-based resins (ASTM International, 2011). CIPP liners can be cured with heat, ultraviolet (UV) light or CIPP liners can be left to cure

ambiently (United Kingdom Society of Trenchless Technology, 2014). Ambient curing methods are simple as they do not require additional equipment but have significantly longer curing times (Das et al., 2016). Curing times for ambiently cured CIPP liners range between 2 to 12 hours while a similar curing time for a CIPP liner cured with steam can be as low as 30 minutes (Das et al., 2016). Steam or hot water can be used to heat a heat-activated curing resin. The heat cured resins usually consists of a vinylester thermoset and heat catalyst system (ASTM International, 2011). UV cured resins have similar components with the difference being in the catalyst system. A photo-initiator system which responds to the UV light emitted by the UV curing lights must be added to the resin mixture (ASTM International, 2011).

Other material components of the CIPP fabric tube include the external foils, and calibration hose. The external foils are typically layers of polyurethane (PU), polyethylene (PE) or polyvinyl chloride (PVC) which are impermeable to moisture and the resins used in production, and act as a protective layer during installation and handling (ASTM International, 2011; United Kingdom Society of Trenchless Technology, 2014). The calibration hose is often a removable PVC tube on the inner diameter of the fabric tube that facilitates the inflation of the CIPP liner by pressing the liner firmly against the walls of the host pipe (ASTM International, 2011; United Kingdom Society of Trenchless Technology, 2014).

The design of FRP composites for CIPP liner application must meet minimum design requirements for flexural strength and flexural modulus specified by ASTM F1216 (ASTM International, 2016). For application in pressurized pipes, FRP composites must also meet a minimum requirement for tensile strength (ASTM International, 2016). Flexural properties can be obtained by performing the three-point-bending test and similarly tensile testing for tensile strength. Ji et al. (2018) found that glass fibers performed better than carbon fiber reinforced

materials in flexural tests and was more suited for application in CIPP liners. In addition to its flexural properties, glass fibers allow for the penetration of UV light for application with UV liners (Ji et al., 2018).

Prior to installation, the host pipe must be inspected and cleaned. Inspection should be performed by CCTV camera inspection, else manned entry when possible (ASTM International, 2011). Debris and obstructions caused by disintegrating pipes or other factors, such as water infiltration and pipe deformation, which can affect the fit of the liner during installation should be addressed before CIPP lining commences (ASTM International, 2011; United Kingdom Society of Trenchless Technology, 2014). Some sections of pipe must be replaced in the cases of obstacles that cannot be removed by cleaning such as tuberculation due to corrosion and service fittings (Das et al., 2016). CIPP lining is challenging for small diameter pipes, sharp bends, changes in elevation and transitions between pipe diameters (Das et al., 2016).

Unlike sliplining, the flow in the line to be lined with CIPP must be plugged or bypassed and the affected public should be notified (ASTM International, 2011). Flow during the lining process can cause wrinkles and failure of the liner to adhere to the walls. Therefore, the line must have no obstructions or flowing fluid within the pipe.

The CIPP liner can be impregnated with the appropriate resin for the selected curing process at the manufacturing facility or in a mobile facility on site (ASTM International, 2011). Once the impregnation (wet-out) process is complete and the fabric lining is saturated with resin, the CIPP liner can be stored and transported to site when required (ASTM International, 2011). Jaganathan et al. (2007) found that the longitudinal folds creased into the liner for ease of transportation and installation can cause stress concentrations where the fold meets gaps or irregularities in the host pipe. Longitudinal folds tend to cause surface irregulars when the liner is

oversized to reduce gaps between host pipe and liner (Jaganathan et al., 2007). Oversizing the liner is a common practice to ensure external pressure cannot build in the annulus gap; an oversizing limit is proposed by Jaganathan et al. (2007) that limits the oversize of the liner based on properties of the pipe.

CIPP installation does not typically require access pits and can often be completed with access provided by manholes when working on sewer systems. Since CIPP liners cannot accommodate valves, valve boxes must be replaced with open-cut methods and the open pit can be used to access the remaining pipe for CIPP (Das et al., 2016). ASTM F2019 recommends the use of rollers and winch cables to pull the liner in place as shown in Figure 2-6 (ASTM International, 2011). However, CIPP liners can be installed by inversion which employs a liner gun which inverts the liner into the host pipe with air or water pressure (United Kingdom Society of Trenchless Technology, 2014). The rate of speed at which the liner is installed should be limited to avoid winkles or stretching of the liner and elongation of the liner should be verified once the operation is complete (ASTM International, 2011; United Kingdom Society of Trenchless Technology, 2014).

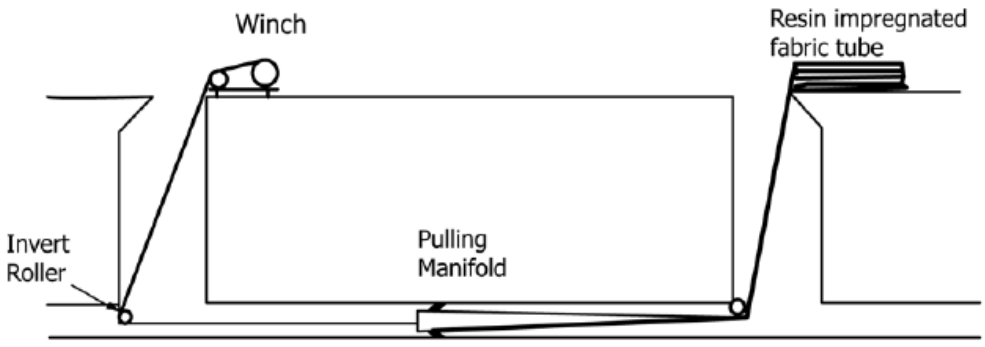

Figure 2-6: CIPP Liner Installation with Winch (ASTM International, 2011)

The installed CIPP liner is then inflated with air, steam or water, depending on the curing method (ASTM International, 2011; United Kingdom Society of Trenchless Technology, 2014). For UV cured resins, a "multi-lamp ultraviolet curing assembly" or "light train" is pulled though the liner at a speed controlled by computers while air pressure is maintained in the line (ASTM International, 2011; United Kingdom Society of Trenchless Technology, 2014). The steam and air curing process shown in Figure 2-7 ensures that the temperature of water and steam is monitored and controlled for the duration of the curing time (United Kingdom Society of Trenchless Technology, 2014). UV-curing resins cure the fastest and can achieve thinner thicknesses than other resins (United Kingdom Society of Trenchless Technology, 2014). Steam cured resins are the next quickest to cure then water and ambient curing resins (United Kingdom Society of Trenchless Technology, 2014).

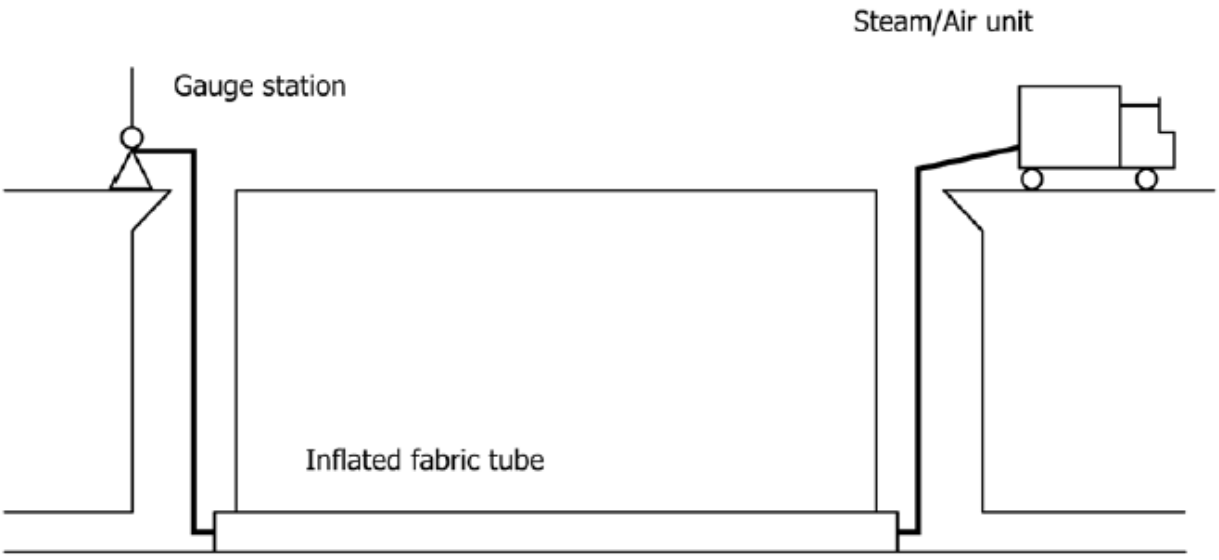

Figure 2-7: Inflation of CIPP Liner with Steam/Air (ASTM International, 2011)

Upon the completion of curing, the length of pipe should be inspected for defects and if any areas do not meet standards then the affected section of pipe may need to have the CIPP lining removed and replaced (ASTM International, 2011). Several factors can lead to failure of a liner.

Excess resin, inadequate curing times and temperatures can lead to wrinkles and fold in the liner which are damaging defects (Das et al., 2016). The pressure applied to keep the liner to the host pipe walls influences the thickness of the walls; thinner, denser walls are produced with high pressure and thicker, less dense weaker walls were produced with lower pressures (Das et al., 2016). A combination of high temperature and high humidity can lead to increase pull times and result in the liner sticking to the inside of the host pipe, hardening in place and blocking the host pipe (Das et al., 2016). Liner thickness can vary due to errors in manufacturing and resin impregnation; liner compatibility with the host pipe must be checked before installation (Das et al., 2016). Once the CIPP liner has proved to be satisfactory, the line can return to normal operation (ASTM International, 2011).

Research on the environmental impact that CIPP liners have on the environment is in its early stages but strongly suggest that procedures and materials need to be altered. In a study of four CIPP installation sites, Li et al. (2019) has found that UV cured CIPP liners release chemical compounds into the local environment during installation and curing of the liner; 19 chemicals were confirmed with analytical methods to have been released. Aqueous styrene, dibutyl phthalate and phenol were found in concentrations above water quality standards; Aqueous styrene was found in concentrations above 48 h aquatic toxicity threshold (Li et al., 2019). A study of seven CIPP installations performed with steam cured styrene-bared resins, found that styrene was present at 5 of the 7 sites in concentrations above the Environmental Protection Agency's (EPA) maximum limit for drinking water and remained above this limit for 5 to 71 days after installation (Donaldson, 2009). The maximum length of time styrene was detected in any amount was 88 days after installation (Donaldson, 2009). Styrene is of a concern as it can be toxic to aquatic wildlife and is classified as a mutagen and potential carcinogen by the EPA (Donaldson, 2009). Resin spills

can be harmful to local aquatic wildlife due to their styrene content (Donaldson, 2009). A 11 to 15 Litres (3 to 4 gallon) spill of uncured resin caused the death of over 5500 fish in the creek downstream from the installation site (Donaldson, 2009). Li et al. (2019) suggest more environmentally conscious practices during CIPP installation to mitigate the amount of chemicals released into the local environment; such practices include the use of barriers and mats to keep the CIPP liner off the ground and to collect particles from cutting the liner, rising the installed liner before service and collecting and disposing the rinse water, and testing the water quality of the CIPP liner before it is allowed to become operational (Li et al., 2019).

The Northwest Arm Trunk Sewer (NATS) located in Halifax, N.S. was found to be leaking waste into the Halifax harbour after inspection (Kezdi, 2018). A pilot project on one of the arms of the NATS confirmed that CIPP liner could be used on the large non-circular sewer (Kezdi, 2018). The non-circular cross section of the sewer meant that the ASTM F1216 design process was not applicable and the design of the liner had to be specifically engineered for the NATS project (Kezdi, 2018). The project saw 13 installations of CIPP ranging from 75m to the longest single run of CIPP liner in Canada which measured 682m (Kezdi, 2018). Weight restrictions of bridges forced design constraints such as multiple smaller vacuum cleaning units and in-situ resin impregnation (wet-out) (Kezdi, 2018). One location, shot no. 9, could not accommodate in-situ wet-out and a rare technique referred to as an “in-field wet-splice” was used for the first time in Canada (Kezdi, 2018). the section was completed with two CIPP liners which had been wet-out in the manufacturing facility and were stitched during the installation of the liner (Kezdi, 2018). The contract was awarded in May 2017 and the project was completed by December 5th 2017 (Halifax, 2018; Kezdi, 2018).

2.1.5 FRP Layup

Where manned entry is possible and there is sufficient space to work, hand layup of FRP is possible for sewer and culvert repair. For structural repair, a tested and proven combination of fibers, resins and application methods are applied by code for each case (Bank, 2006). The most common combinations are glass or carbon fibre and epoxy resins; epoxy resins are chosen over other resins due to its stronger adhesive properties and lower shrinkage after curing than other industrial resins (Bank, 2006). As mentioned in the CIPP section, ASTM F2019 (2011) suggests the use of polyester, vinylester, or epoxy resins for CIPP liners.

The installation of FRP strengthening system can be completed in a few simple steps. In the case of reinforced concrete, any damage on the surface must be repaired and the surface must be sandblasted smooth and cleaned; a clean smooth surface is essential for FRP installation (Bank, 2006). The concrete is sealed with an application of primer once the surface is dry (Bank, 2006). Any apparent holes or gaps can be filled with putty and then the FRP layers can be applied to the smooth surface (Bank, 2006). A protective layer of epoxy is applied over the installed FRP as the finishing coat (Bank, 2006).

FRP wet-layup has proven to be an effective method of repairing prestressed concrete pipes back to or above their original pipe classes strength requirements. Park et al. (2015) have tested the performance of FRP repair by pre-cracking a concrete pipe with a diameter of 610mm, repairing the pipe with FRP and re-testing the rehabilitated concrete pipe. The Three-Edge Bearing (TEB) test procedure is outlined in ASTM C497. Load is applied through a wood beam lined with a rubber strip at the crown of the concrete pipe. Normalized load (D-load) describes the applied load to the concrete pipe relative to the pipe dimensions; D-load represents newtons per linear meter of pipe per millimeter of inside diameter (N/m/mm=kN/m/m) (Park et al., 2015). Following

the TEB test procedure, load was applied to undamaged pipes to simulate damage. Applying load at the crown will cause the formation of vertical cracks on the inner diameter at the crown and invert, and then horizontal cracks along the exterior spring-line as load increases (Park et al., 2015). Park et al. (2015) removed load before the appearance of spring-line cracks to ensure the pipe was not overstressed to failure. Environmental saltwater damage was simulated by bathing pipes repaired with Carbon Fibre Reinforced Polymer (CFRP) in a 3% saline solution for 3000 hours (Park et al., 2015). Results from testing showed that steel wire RCP and polypropylene fiber-reinforced concrete pipes (SYN-FRCP) could be repaired with multiple CFRP layers. Park et al. (2015) compared test results to the ultimate D-Load pipe class requirements described by ASTM C76M in Table 2-1. For pipes under 1500mm in diameter, meeting or exceeding the D-Load requirement to produce a 0.3mm crack is sufficient to be accepted into a pipe class if all other requirements are met (ASTM International, 2020). The RCPs required 2 layers of CFRP to have a repaired strength meeting requirements for Class III pipes and 1 layer to meet strength requirements of Class II pipes (Park et al., 2015). SYN-FRCP repaired with single and double layers of CFRP met Class I and Class II pipe strength requirements but failed to reach Class III (Park et al., 2015). Repaired concrete pipes bathed in the 3% saline solution for 3000 hours showed no significant degradation of strength (Park et al., 2015). Lee & Karbhari (2005) have also confirmed that wet layup of FRP can be engineered to withstand internal and external pressures experienced by large diameter concrete pipes. While wet layup of FRP was an acceptable method, adhesion of FRP strips was found to be equally acceptable with the added benefit of minimizing field work and future inspection processes (Lee & Karbhari, 2005).

Table 2-1: D-Load Value Requirements for Pipe Classes to produce a 0.3mm crack and Ultimate Load (ASTM International, 2020)

Pipe Class	I	II	III	IV	V
D-Load - 0.3mm Crack (N m^{-1} mm^{-1})	40	50	65	100	140
D-Load - Ultimate (N m^{-1} mm^{-1})	60	75	100	150	175

2.2 Theory of FRP Rehabilitation

2.2.1 FRP sandwich technology

Wet layup of FRP allows for the creation of sandwich structures. The use of FRP sandwich structures in pipe rehabilitation could allow for increased strength above the strength of the original pipe design without sacrificing volumetric flow due to loss of cross-sectional area. Industrial CIPP liners already utilise layered composite technology. As stated in ASTM F2019, additional intermediate fiberglass tubes can be added to satisfy static needs (ASTM International, 2011). The use of FRP sandwich structures may reduce the number of layers required in situations where extra liner strength is required while minimizing the cross-sectional area lost. The interstitial core of the FRP structure must be a flexible core that cannot ripple or wave as the lining conforms to walls of the pipe. The use of flexible non-woven microballoon/microsphere cores can achieve this goal. Non-woven microballoon core materials find application as a cost-effective core material in sandwich structures in the aerospace, automotive and construction industries (FRP Services & Company, 2016). Microballoon cores have been found to increase stiffness while maintaining a thin profile, reduce weight compare to conventional alternatives, and reduce resin absorption (Murphy, 1998). The use of microballoon core in CIPP and wet-layup rehabilitation projects has the potential of decreasing material costs, installation time (in the case of wet-layup), and wall thickness thereby increasing flowrate.

The geometry of FRP sandwich structures with a microballoon core material is analogous to a steel I-beam. The objective of the core material is to increase the moment of inertia while minimizing cost and strategically optimising the material properties of each sandwich layer. The layer in contact with the concrete may have a comparable modulus of elasticity to promote a more compatible bond between materials. The core material may be low cost and reduce resin consumption. The extreme fibre may be a stiffer material with high tensile strength as it will experience the highest tensile strains furthest away from the neutral axis as exhibited in . Wrapped in a U shape along the tension side of reinforced concrete beam, a hybrid Glass Fibre Reinforced Polymer (GFRP) and CFRP specimen with one ply of each achieved an ultimate load approximately 10% higher than either a CFRP specimen of 2 plies or GFRP specimen of 3 plies (Attari et al., 2012). The use of a hybrid FRP laminate composed of glass and carbon fibre composites have found to be effective at strengthening a reinforced concrete beam with less than 20% reduction in ductility compared to a control beam (Attari et al., 2012).

2.2.2 FRP Rehabilitation of RC beams

Sha & Davidson (2020) have analysed the bond-slip relationship between FRP laminates and a reinforced concrete beam; closed form solutions were developed for interfacial stresses between a concrete beam and externally bonded FRP under uniformly distributed load via composite beam theory. The interfacial stresses can be predicted with closed form solutions in good agreement with FEA and analytical results (Sha & Davidson, 2020).

Teng et al. (2003) identifies 6 failure modes of FRP bonded to the tension side of a reinforced concrete beam. These modes include FRP rupture, concrete crushing at compression face, shear failure, concrete cover separation, shear failure of concrete, plate end interface debonding and intermediate crack-induced interfacial debonding (Teng et al., 2003). Intermediate

crack-induced debonding is a mode of failure for concrete with FRP bonded to the tension face. As a crack in the concrete widens, delamination is initiated at the interface of the crack and bonded FRP (Teng et al., 2003). Of the failure modes of FRP adhered to RC identified by Teng et al. (2003), intermediate crack-induced debonding is a potential mode of failure for an RCP specimen repaired with FRP because cracks at the crown and invert on the tension face of the pipe are in contact with the FRP liner. The crown and invert are critical zones for failure and will experience higher moments than elsewhere on the pipe as shown in .

Concrete specimens with multiple spaced grooves of 1mm and 3mm groove width were covered by externally bonded CFRP and tested in single shear pull-out and three-point bending by Wan et al. (2018). The 1mm grooves were achieved by plugging a 3mm grove with 1mm of Teflon sheets and allowing epoxy to fill the remaining gap, the Teflon sheets were removed after curing to reveal the gap. Epoxy infiltration was inhibited by a silicone sealant for the 3mm grooves. The 1mm grooved specimens were found to have a bond strength comparable to control specimens and higher than the 3mm grooved specimens due to a more even stress distribution across the loaded specimen (Wan et al., 2018). The bond between RCP and FRP at the crown and invert is not expected to be compromised by the initial cracks but only as the cracks begin to widen under loading.

When tested in 4-point bending, increasing layers of CFRP adhered to a concrete beam changed the failure mode from FRP rupture to delamination (Toutanji et al., 2006). Observations showed that flexural cracks initiated delamination of concrete with greater layers of CFRP and the delamination propagated towards the shear span (Toutanji et al., 2006). For concrete with fewer layers of CFRP, the controlling factor for failure was the tensile strength of the CFRP resulting in

FRP rupture (Toutanji et al., 2006). Delamination is a preferable mode of failure as the delaminated FRP liner may still act as an intact pipe.

2.2.3 Castigliano Method Moment Calculation

The Castigliano method may be used to determine deflection and define moments via virtual work (Watkins, 2000). The Castigliano method assumes that the specimen acts as a thin-walled ring with symmetrical two plate loading with constant stiffness throughout the walls of the specimen (Watkins, 2000). Heger (1962) calculated the moment within the concrete pipe walls in TEB loading at radial locations using the Castigliano method for initial cracking at the crown and invert and the column analogy method for stage two cracking which additionally includes cracks at the springline of the pipe as seen in Figure 2-8. The Castigliano method yield moments defined at the crown and springline such that (Watkins, 2000):

$$M_{Crown/Invert} = \frac{PR}{\pi}$$

$$M_{Springline} = PR\left(\frac{1}{\pi} - \frac{\sin 45}{2}\right)$$

Where P is applied load at the crown and R is mean radius (Becerril García & Moore, 2016). Becerril García & Moore (2016) found that the closed form solutions of the Castigliano method moment calculations were accurate within 25% for determining the average flexural properties of RCP in TEB loading. The RCP specimens were 300mm in length with internal and external diameter of 610mm and 800mm respectively (Becerril García & Moore, 2016). Becerril García & Moore (2016) also determined that increasing the spacing between the lower bearing strips cradling the invert of the TEB test negatively affected both the magnitude of the moments developed in the ring wall as well as the horizontal and vertical diameter change during loading. An experimentally determined modulus of elasticity (E) can effectively predict flexural RCP behaviour in TEB loading (Becerril García & Moore, 2016).

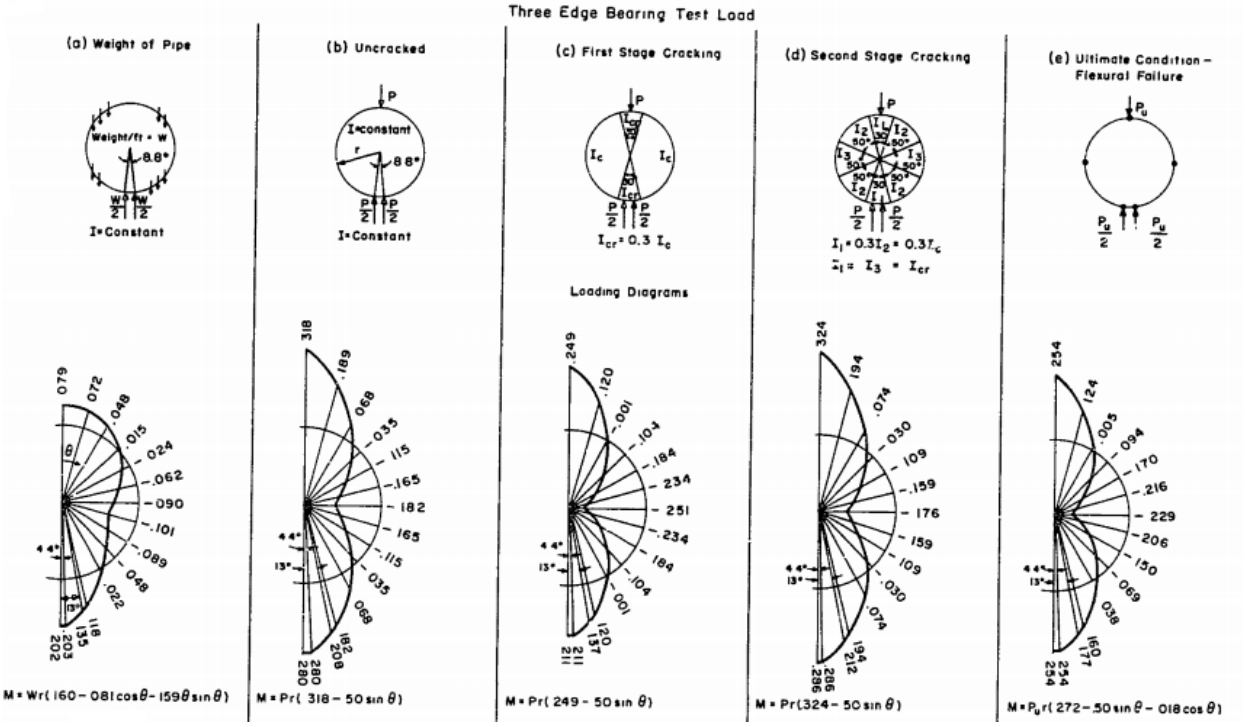

Figure 2-8: Theoretical Three-Edge Bearing (TEB) Moment Distributions (Heger, 1962)

In reinforced concrete beams with FRP composites applied to the tension side, the evolution of flexural behaviour was defined as having three distinct linear regions as seen in Figure 2-9. The slopes of the regions relate to the stage of loading; the first slope corresponds to the FRP beam with uncracked concrete behaviour, the second slope beings as the concrete in the beam becomes cracked, and the third slope represents the plastic behaviour of concrete beyond yielding until failure (Attari et al., 2012). Such evolution of moments in a concrete pipe was calculated by Heger (1962) in Figure 2-8.

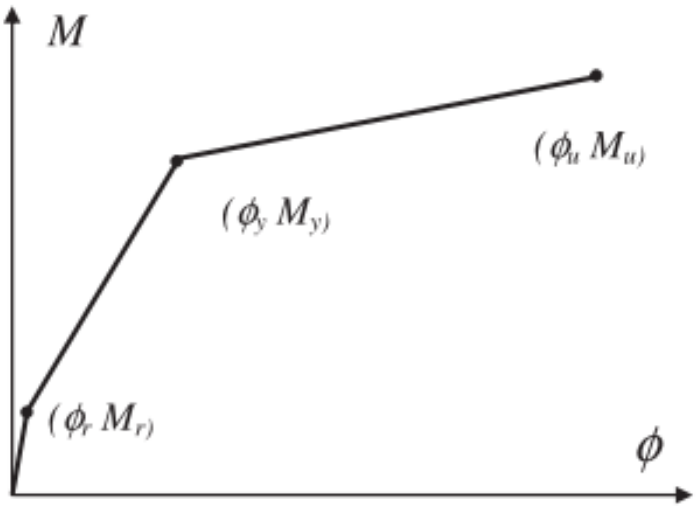

Figure 2-9: Segmented Moment vs. Curvature in Reinforced Concrete Beam Strengthened with FRP composites (Attari et al., 2012)

2.3 Research Gaps

There is potential for future research on the subject of RCP repaired with FRP liners. The closed form moment calculations from the Castigliano method have not yet been tested on cracked RCP specimens or cracked RCP specimens repaired with FRP materials in TEB loading. The loading behaviour of RCP repaired with FRP materials has yet to be modelled. Performance of RCP repaired with sandwich FRP composites in TEB loading has yet to be tested. There are currently no guidelines or standards relevant to structural analysis of FRP rehabilitation. FEA has not yet been used to model the behaviour of RCP repaired with FRP liners. Cyclical and in service conditions have not been evaluated for FRP liner repairs of RCP.

Chapter 3. Experimental Program

A series of TEB tests were carried out on RCP specimens which were damaged and repaired with FRP materials. The objective of the repair is to meet or exceed uncracked loading behaviour. The structure of the FRP liner was varied between tests. The liners tested include GFRP or CFRP only liners and sandwich liners with GFRP, CFRP, or a hybrid of CFRP and GFRP skins with a syntactic foam core. The hybrid sandwich liner can be seen in Figure 3-1 applied to the inner diameter of the RCP specimen. Vertical displacement, horizontal displacement, and strain at the crown and springline were collected as data during the TEB tests. The ultimate limit states are considered as there currently no reference standards for serviceability states. This chapter describes the test matrix, materials, instrumentation, test setup, results, and observations of the experiments.

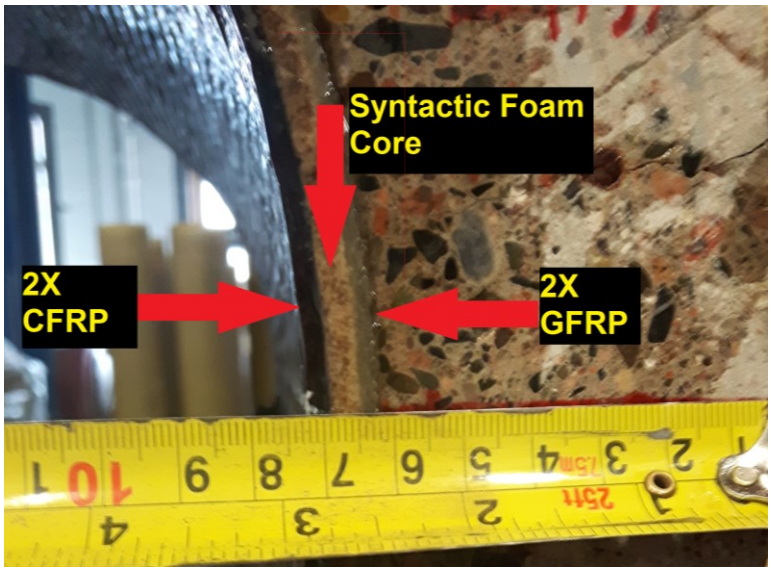

Figure 3-1: Hybrid Sandwich Structure of CFRP, Syntactic Foam and GFRP

3.1 Materials

3.1.1 FRP Materials

The sandwich liner is composed of CFRP or GFRP skins, and a syntactic foam of non-woven polyester fibre with 40%vol microballoons. The composite was impregnated with an epoxy

resin. The syntactic foam used was Bulkermat+BSP, T-4000 with a longitudinal tensile strength and modulus of 6.4MPa and 1190MPa respectively, and transverse tensile strength and modulus of 5.0MPa and 1000MPa respectively as described by the manufacturer after curing with epoxy resin. The CFRP, GFRP and epoxy resin were commercial productions designed for structural applications. Material properties were taken from the provided material properties data sheets from the manufacturer. The CFRP used was QuakeWrap™ VU18C Carbon Fabric with a tensile strength of 3.8GPa and tensile modulus of 231GPa. The GFRP used was QuakeWrap™ VU27G Glass Fabric with a tensile strength of 3.24GPa and tensile modulus of 72.4GPa. The epoxy used was QuakeBond™ J300SR Saturating Resin with a pot life of 3 to 4 hours, tensile strength of 49.3MPa and tensile modulus of 1995MPa.

The laminated material properties of the FRP materials can be see in Table 3-1. The nominal thickness of the laminated CFRP, GFRP, and syntactic foam core material are 1.3mm, 1.01mm, and 4.1mm, respectively. The laminated CFRP had a tensile strength of 708MPa and tensile modulus of 68,600MPa. The laminated GFRP had a tensile strength of 587MPa and tensile modulus of 27,400MPa. Experimental results find that the resin impregnated syntactic foam core has an elastic modulus of 353.6MPa after curing (MacDonnell & Sadeghian, 2020). Tensile strength of the syntactic foam after lamination was taken to be 6.4MPa in the longitudinal direction as per the manufacturer.

Table 3-1: Laminated FRP Material Properties in the Longitudinal Direction

	GFRP	CFRP	Syntactic Foam
Tensile Strength (MPa)	587	708	6.4
Tensile Modulus (MPa)	27,400	69,600	353.6
Nominal Thickness (mm)	1.01	1.3	4.1

3.1.2 RCP Materials

The RCP materials are concrete and steel rebar. As seen in "Appendix I: Experimental Compressive Strength of Concrete," the average ultimate compression strength of the concrete pipes was experimentally determined to be 54.73MPa. The steel rebar present in the reinforced concrete consisted of a spiral stirrup at a pitch of 69.85mm and 9 longitudinal rebar spaced evenly at every 40° across the circumference. The spiral stirrups and longitudinal steel rebar are 5mm in diameter and have a minimum yield strength of 450MPa according to the manufacturer (Strescon, Bedford, NS, Canada).

3.2 Three-Edge Bearing (TEB) Test

As described in ASTM C497M, the TEB test is a standardized method for testing the strength of concrete pipes (ASTM International, 2018). The TEB test setup was used to test the ultimate loads and subsequent D-load (normalised load) of the RCP specimens. The setup was constructed of commercially available softwood, and a steel I beam, with tolerances within the acceptable limits described in C497M. As shown in Figure 3-2a, the 0.5m RCP section was loaded onto the lower bearing strips of the setup and the upper bearing beam was lowered onto the crown of the specimen. Load is applied to the specimen via hydraulic press at a uniform loading rate not exceeding 43.8kN per linear meter of pipe per minute and halted as cracks being to appear at the crown and invert. The hydraulic pump valve was opened to the same position for each test. The damaged specimen is repaired with the prescribed repair method and tested again beyond peak load at the same uniform loading rate. The D-load is calculated by dividing the load (N) by the length of the pipe specimen (m) and inner diameter of the pipe (mm) (ASTM International, 2018).

The vertical displacement was measured with a string potentiometer affixed to the upper and lower bearing strips. The horizontal displacement was measured with a linear potentiometer

affixed to the frame of the hydraulic press and contacting CFRP strips, seen in Figure 3-2a, which had been leveled and glued to the outer springline of the specimen to provide a flat measurement surface as the specimen depresses with load. Strain at the inner crown and inner springline at the extreme fibre of the FRP was measured with the use of strain gauges. During the damage simulation phase, only vertical displacement was measured. Strain at the crown and springline, and horizontal and vertical displacement were measured for the specimens which had been repaired with FRP.

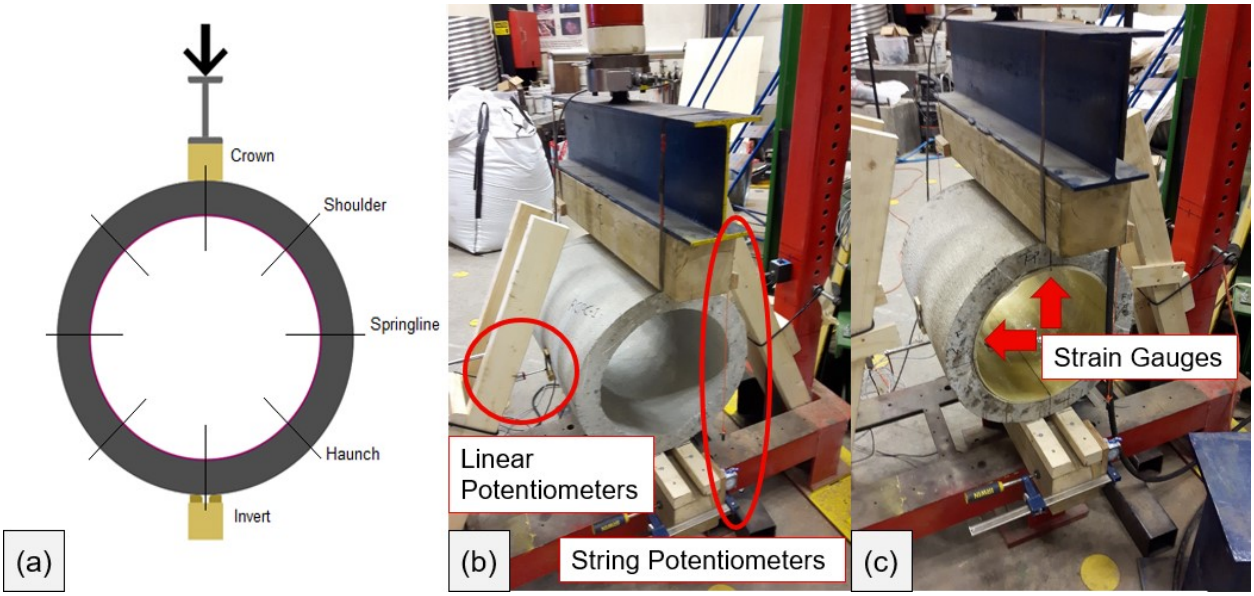

Figure 3-2: Instrumentation and Three-Edge Bearing (TEB) Test Setup (a) Diagram of TEB test; (b) String Potentiometer and Linear Potentiometer Location; (c) Strain Gauge Location

3.3 Specimen Preparation

3.3.1 RCP specimens

Five RCPs with a nominal pipe diameter of 375mm, inner diameter of 381mm, and length of 2.4m were donated from a local pipe manufacturer's seconds pile which may have been rejected or returned for any reason and cut into four 0.5m specimens seen in Figure 2-1. A 381mm inner diameter was chosen to facilitate storage and maneuverability of the specimens within the labs. Control tests were performed to determine pipes of similar concrete strength. Pipes 4, 5 and 1 were

found to have comparable compressive concrete strength. Average f'_c values of each pipe were calculated from 3 samples tested in compression. Pipe 4 was found to have an average f'_c value of 54.77MPa with Coefficient of Variation (COV) of 14.87%, Pipe 5 was found to have an average f'_c value of 53.85MPa with COV of 9.07%, and Pipe 1 was found to have an average f'_c value of 56.42MPa with COV of 14.32%.

Figure 3-3:Cutting of Full-length RCP into 500mm Specimens

3.3.2 Damage Simulation

Damage was simulated by applying load to the specimens via TEB. The distinct audible crack as the crown and invert cracked simultaneously was used as a standard reference of damage between specimens. Cracking at the crown and invert is evidence that an RCP in the field may be compromised as the inner diameter of the pipe is the most accessible for inspection and the greater moments at the crown an invert will cause cracking on the inner diameter of the pipe. Shown in

Figure 3-5a, the load is applied to a metal I beam acting as a load spreader which presses the wooden top beam onto the crown of the pipe. Two smaller wooden bearing strips cradle the invert of the pipe. A load cell screwed to the hydraulic press and I beam measures the applied load. As seen in Figure 3-5b, string potentiometers attached to the upper and lower wood beams on opposite ends of setup measured vertical displacement. A difference between the experimental tests and in-situ application is that the cracks in concrete at the crown and invert are allowed to close once load is removed from the cracked RCP specimen. It would be expected that wider cracks would make delamination more likely at lower loads as seen in Wan et al. (2018).

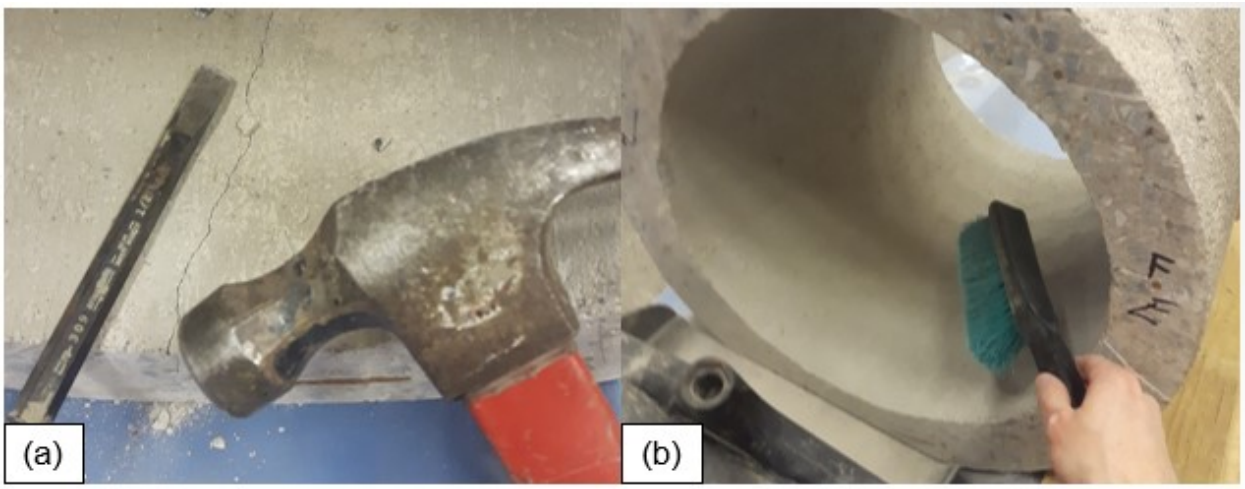

Figure 3-4: (a) Removal of Protrusions (b) Dust Removal with Brush and Compressed Air

3.3.3 Wet FRP layup

After the RCP specimens had been damaged, the inner concrete surface was prepared for wet FRP layup. Seen in Figure 3-4, Protrusions were removed with a hammer and chisel and dust was removed with a brush and blasts of air from an air compressor. Once smooth and free of dust and debris, an epoxy coat was layered onto the inner concrete surface ready to accept wetted FRP material as seen in Figure 3-5. In the longitudinal direction, carbon and glass fabrics were cut to double the inner circumference plus an additional 10cm for overlap allowing a continuous double layer of FRP skins. The syntactic foam was cut to the length of 1 circumference including the

thickness of the FRP skin. The syntactic foam layer is butt joined when the ends of the layer meet with any gap larger than 2mm filled with a strip of syntactic foam. Epoxy resin was mixed and let sit for 20 to 30 minutes to allow the resin to become more viscous for better adhesion to the crown. Resin was applied to one circumference length of fabric at a time. A 30-minute pause was taken before and after the application of the syntactic foam layer to allow the resin to become tacky between layer applications. Overlapping sections and butt joints were alternated between the haunches of the pipe to avoid the addition of an extra ply to measurement locations. After curing, excess fabric which extended past the concrete was trimmed with a angle grinder and flap disk. A light brush of epoxy was applied to the cut edges.

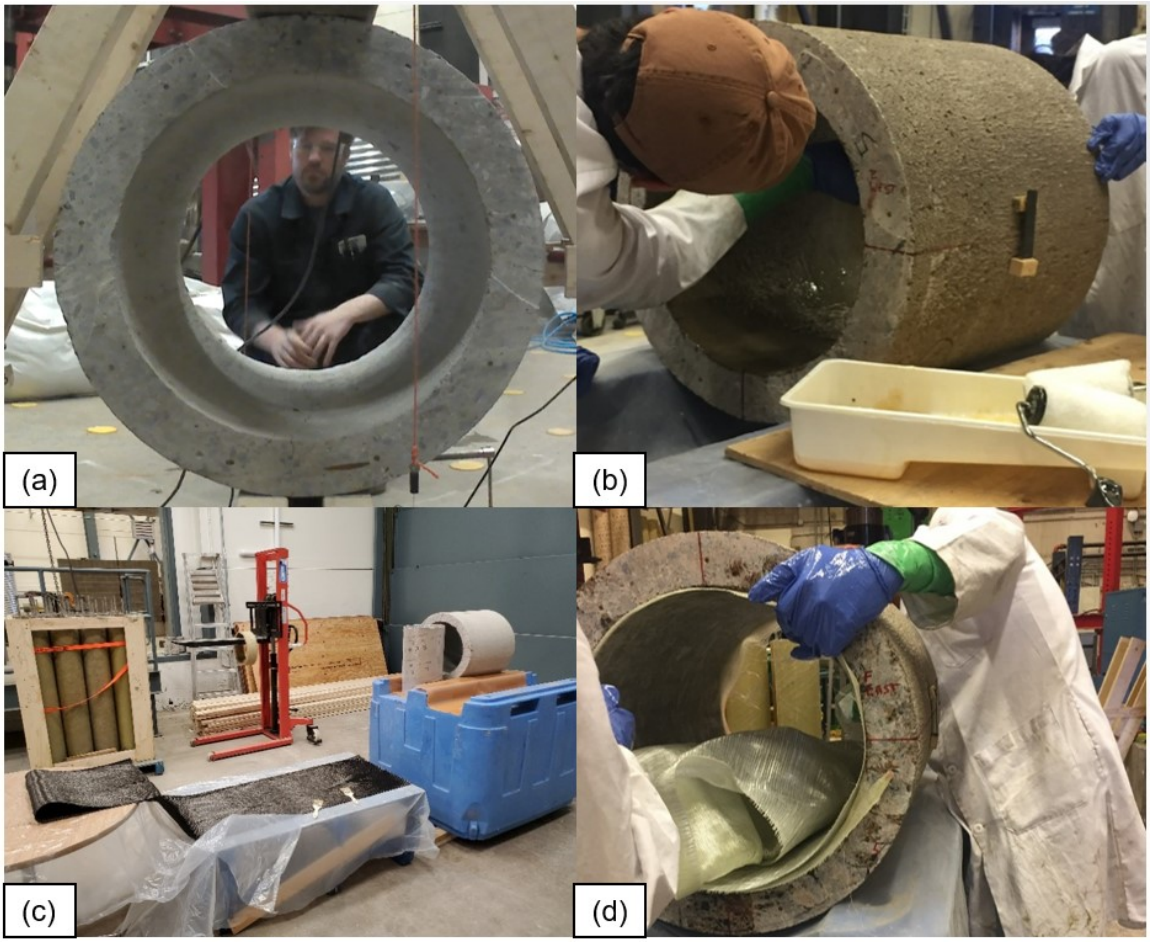

Figure 3-5: Installation of FRP Liners (a) Damage Simulation in TEB; (b) Wetting of Inner Concrete Surface with Epoxy; (c) Wetting of Outer FRP Circumference Before Application; (d) Unravelling of FRP Within the Specimen During Application

3.4 Test Matrix

The test matrix in Table 3-2 describes the repair system applied to each specimen using a wet-layup method. Where a layer of fiber is described by a single letter where G = GFRP, C = CFRP, B = syntactic foam core. The order of the letters describes the order of the layers starting with the fabric in contact with the RCP (e.g., GGBCC starts with two layers of GFRP in contact with the RCP, a syntactic foam core and two layers of CFRP acting as the exposed surface of the liner). The liners to be tested will be referred to as GFRP liner (GGGG), GFRP sandwich liner (GGBGG), and hybrid sandwich liner (GGBCC). In total, 3 control tests were performed and 7 tests with FRP liner repairs were preformed: 1 GFRP only liner, 2 GFRP sandwich liners, 2 hybrid sandwich liners, 1 CFRP only liner. Figure 3-6 displays the tested RCP specimens.

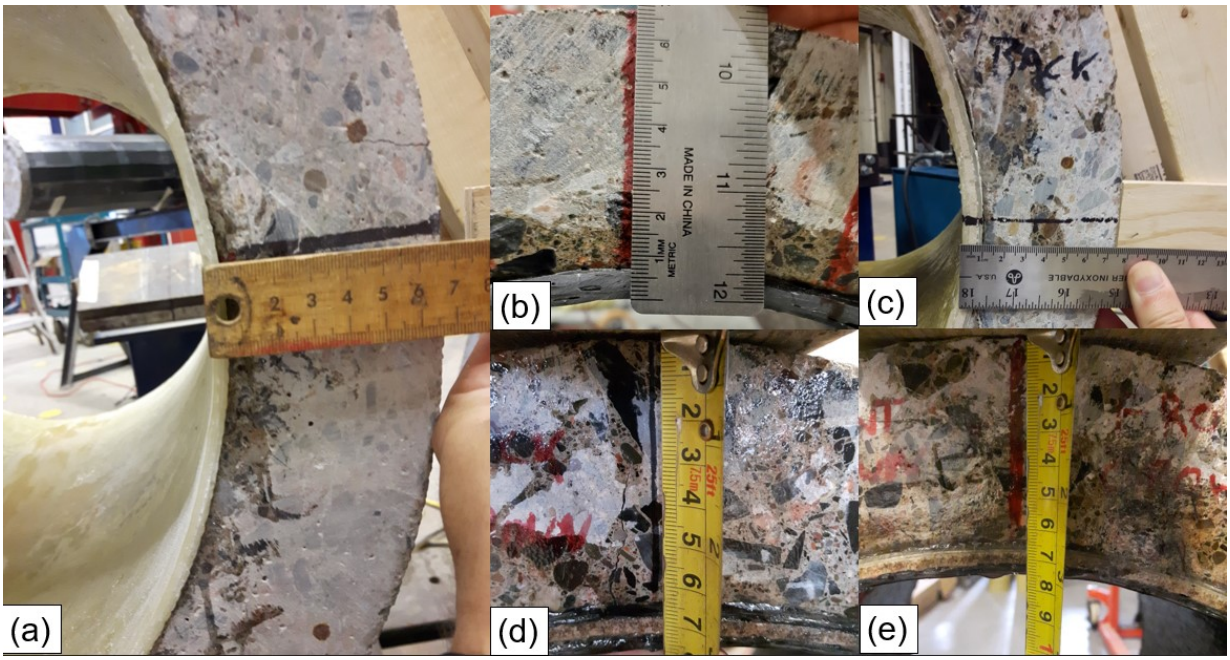

Figure 3-6: Repaired RCP with FRP Liners (a) GGGG (b) CCCC (c) GGBGG (d) CCBCC (e) GGBCC

Table 3-2: Text Matrix of Liner Repair Systems

Specimen	Control	GGGG	GGBGG	GGBCC	CCBCC	CCCC
RCP 1	X					X
RCP 4	X	X	X	X		
RCP 5	X		X	X	X	

3.5 Results and Discussion

3.5.1 D-Load, Vertical Displacement, and Strain

All FRP repaired specimens outperformed the control tests in terms of maximum D-load achieved as seen in Table 3-3 and Table 3-4. The highest D-Load was achieved by GGBCC - RCP 5 at 803N m^{-1} mm^{-1} with a crown strain of 1119με and vertical displacement of 6.95mm. The highest crown strain was achieved by GGBGG - RCP 5 at 1804με with a D-Load of 629N m^{-1} mm^{-1} and vertical displacement of 5.26mm. The highest D-Load was achieved by Control - RCP 5 which reached 265N m^{-1} mm^{-1} at a vertical displacement of 11.63mm as seen on Table 3-4 and Figure 3-7. The gap in data after the initial peak of the control plots on Figure 3-7 is due to the vertical displacement of the specimens changing faster than the time interval between data collection points. Data points were collected every tenth of a second. D-Load vs Strain at the crown and springline for all specimens was plotted on Figure 3-8. Plots comparing the maximum D-Load of repaired RCP specimens with the D-Load required to produce the initial damaging cracks are plotted in Figure 3-9. Data below 25kN (Approximately 130kN D-Load) was truncated and replaced with a linear projection to account for seating of the specimen. In Figure 3-9, the crack series represents the D-load vs vertical displacement data collected in the damage phase up until the crown and invert cracked on the RCP specimen. All repaired specimens achieved higher D-Loads and vertical displacements than the initial crack of the bare RCP specimens.

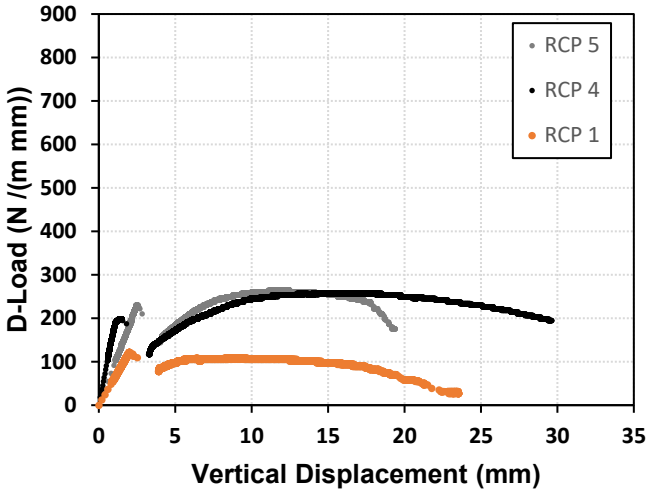

Figure 3-7: D-Load vs. Vertical Displacement of RCP 4, RCP 5, and RCP 1 Control Tests

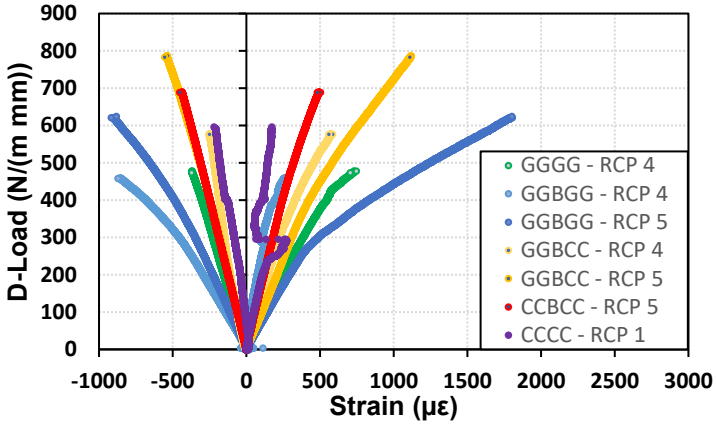

Figure 3-8: D-Load vs. Strain of All Specimens at Crown (Positive Strain) and Springline (Negative Strain)

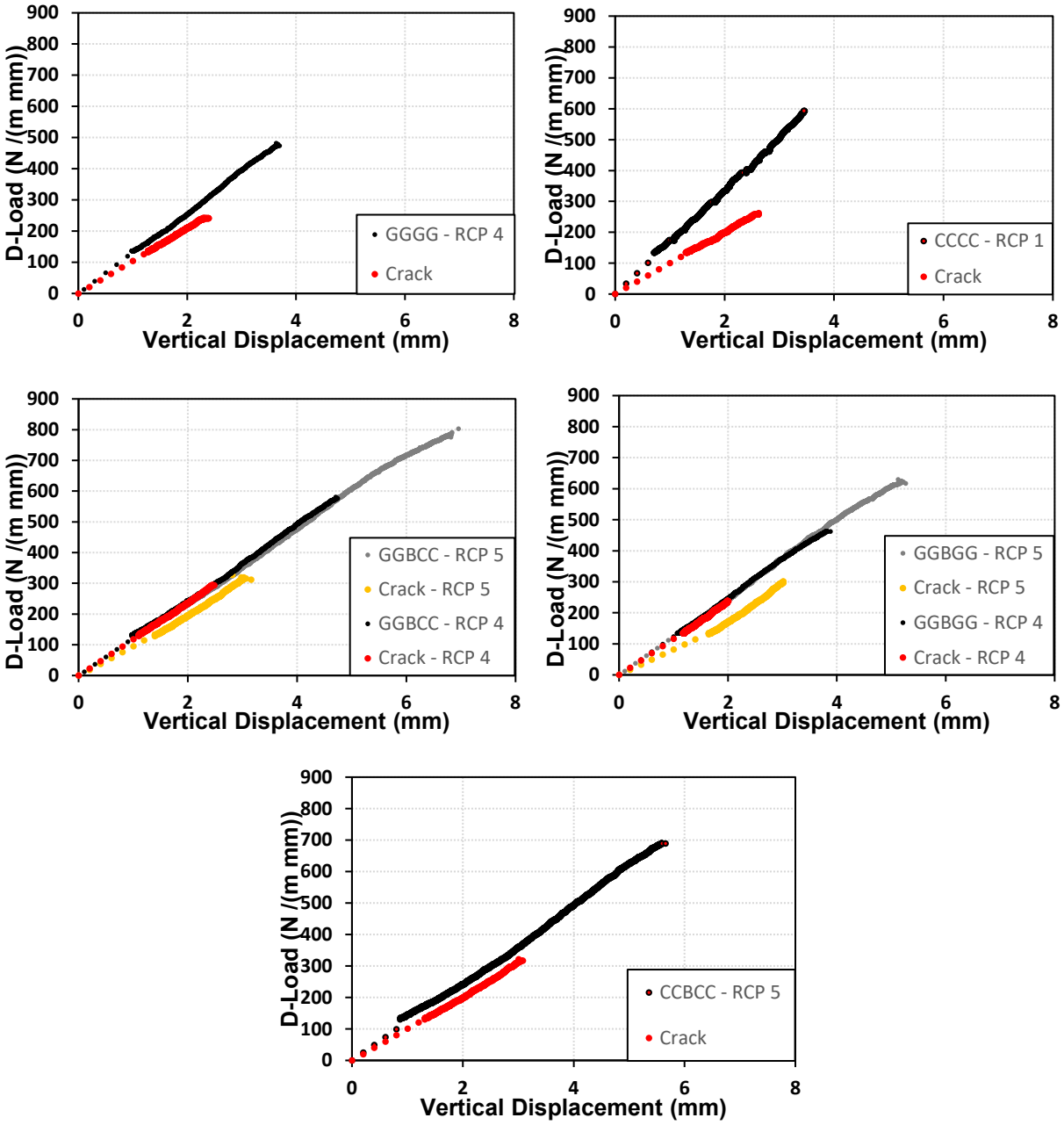

Figure 3-9: D-Load vs Vertical Displacement of RCP Specimens Repaired with FRP Liners

Table 3-3: Maximum Values of D-Load, Vertical Displacement, Horizontal Displacement, Crown Strain, and Springline Strain for RCP Specimens Before and After Repair with FRP

	Initial Crack MAXIMUM VALUES			Repair MAXIMUM VALUES					
Specimen	Load (kN)	D-Load (N m^{-1} mm^{-1})	Vertical (mm)	Load (kN)	D-Load (N m^{-1} mm^{-1})	Vertical (mm)	Horizontal (mm)	Crown Stain (με)	Springline Strain (με)
GGGG RCP 4	45	241	2.39	89	482	3.69	-1.19	746	-374
CCCC RCP 1	49	262	2.62	111	594	3.46	-1.64	273	-221
GGBGG RCP 4	45	237	2.01	87	462	3.88	-1.38	278	-873
GGBGG RCP 5	56	301	3.01	118	629	5.26	-2.76	1804	-918
GGBCC RCP 4	56	294	2.48	110	581	4.74	-1.52	584	-253
GGBCC RCP 5	62	327	3.16	153	803	6.95	-2.72	1119	-554
CCBCC RCP 5	60	321	3.08	129	690	5.66	-2.78	504	-453

Table 3-4: Vertical Displacement at Maximum D-Load for Control RCP Specimens

	Load (kN)	D-Load (N m^{-1} mm^{-1})	Vertical (mm)
Control - RCP 4	49	258	13.46
Control - RCP 5	51	265	11.63
Control - RCP 1	23	121	2.04

3.5.2 Observations and Discussion

The accuracy of the D-Load vs vertical displacement plots will be further discussed in the numerical section when compared to FEA results. Fixing the string potentiometer to the upper and lower wood bearing strips may have included the measurement of the compression of wood in the displacement measurement. Since the measurement location and test setup was consistent across all tests, the measured values may be compared to each other. All repaired specimens achieved

higher D-Loads than the initial crack of the bare RCP specimens and control specimens. CCCC - RCP 1 which experienced a minor delamination, as exhibited by the strain profile in Figure 3-8, before reaching peak load was able to outperform control specimen and the initial cracking D-load. Therefore, the repair of damaged RCP with FRP materials may be considered successful.

Seen in Figure 3-10, still frames at the moment of failure were taken from video recordings of each test. Visual analysis between the frame before and after failure reveals the location and mode of failure. The initial cracks at the inner crown and invert, and at the outer springline open simultaneously and the liner delamination propagates from the location at which the cracks at the crown and invert meet the liner. Such that the mode of failure can be categorised as crack induced debonding. It was observed that GGBCC - RCP 5 failed at the highest D-load among all tests as a new crack formed at the crown. All other specimens failed as the original cracks from the damaging phase opened. The GGBCC - RCP 5 test occurred later in the testing timeline and may have benefited from prior application experience which led to better adhesion of the liner and subsequently the development of a new crack failure in the concrete of the crown. Between GGBCC RCP 4 and RCP 5 the maximum D-load increased from 294N m^{-1} mm^{-1} to 327 N m^{-1} mm^{-1} an increase of 11%. Between GGBGG RCP 4 and RCP 5 the maximum D-load increased from 237N m^{-1} mm^{-1} to 301 N m^{-1} mm^{-1} an increase of 27%. The experience of the FRP appliers may be factor in the delamination of FRP liners under load.

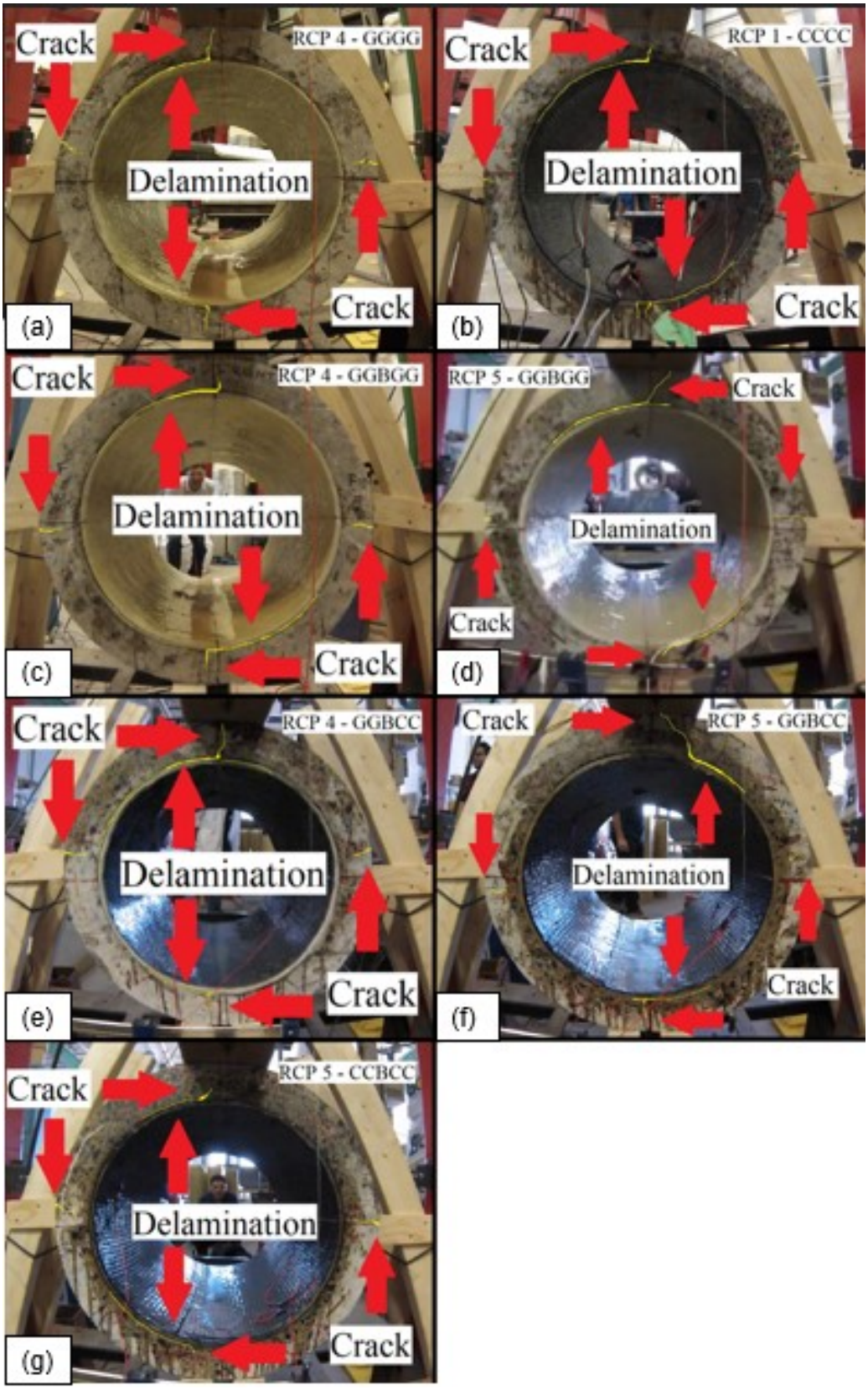

Figure 3-10: Stills at the Moment of Failure for Repaired RCP Specimens with Failures Highlighted in Yellow

Chapter 4. Simplified Finite Element Analysis

A numerical study was conducted to model the elastic behaviour of damaged RCP repaired with FRP materials in a TEB loading setup. Cross sectional analysis using the moment evolution equations described in subchapter 2.2 resulted in high order polynomials that require iterative solutions. The assumptions made to describe the cracked sections of RCP in the moment calculation by Heger (1962) for first and second stage cracking did not yield calculated strains that agreed with experimental results and subsequent adjustments to the width of the cracked sections did not improve results. FEA in ABAQUS was chosen to model the behaviour of the RCP specimens repaired with FRP liners before delamination. In this chapter, the model is described, and the results are compared with empirical data presented in Chapter 3. A parametric study was performed with a pipe model of inner diameter of 762mm, wall thickness of 152.4mm, and length of 1000mm. A hybrid sandwich of GFRP, Syntactic foam, and CFRP layers were applied in the parametric model. The number of layers were varied to achieve different thicknesses of FRP layers. Results of the parametric study are discussed.

4.1 Model Description

FEA was performed to gain a better understanding of the distribution and development of strain within the specimens. The student edition of ABAQUS was used to perform FEA analysis on the loading of a concrete pipe lined with FRP materials. It is assumed that the model is in plane stress due to upper and lower bearing strips of the TEB setup with no force applied in the Z direction. A circular cross section in the XY plane was modelled to match the dimensions of the experimental specimens of varying liner composition. As seen in Figure 4-1, a mesh with a reduced integration, linear element type of CPS4R was used to define the models with a limit of 1000 nodes as allowed by the student edition of ABAQUS. Nominal material properties and thicknesses were

used to define the FRP materials and average dimensions of the RCP were used to model the specimens with an average inner diameter of 380mm, average wall thickness of 63.5mm and length set to 500mm.

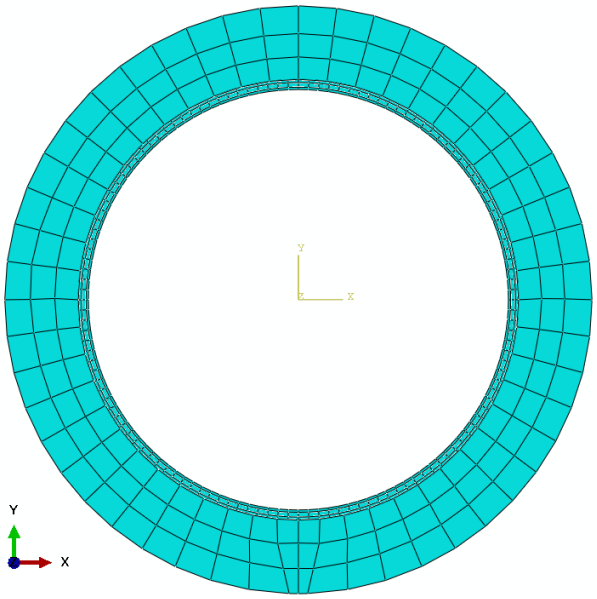

Figure 4-1: Mesh and Orientation of FRP Sandwich Liner on Concrete Pipe in ABAQUS

4.2 Materials

The material properties of the FRP materials were taken from manufacturer data sheets and experimental results. Laminated with epoxy, the CFRP had a tensile strength of 708MPa and tensile modulus of 68,600MPa. Laminated with epoxy, the GFRP had a tensile strength of 587MPa and tensile modulus of 27,400MPa. Experimental results find that the resin impregnated syntactic foam core has an elastic modulus of 353.6MPa after curing (MacDonnell & Sadeghian, 2020). Tensile strength of the syntactic foam after lamination was taken to be 6.4MPa in the longitudinal direction as per the manufacturer. Figure 4-2 and Figure 4-3 display the idealised stress strain curves used to describe the FRP materials laminated with epoxy in ABAQUS. The bond between the FRP liner and concrete was assumed to be perfect for these models as the objective of this study to explore the behaviour of RCP repaired with FRP liners before delamination.

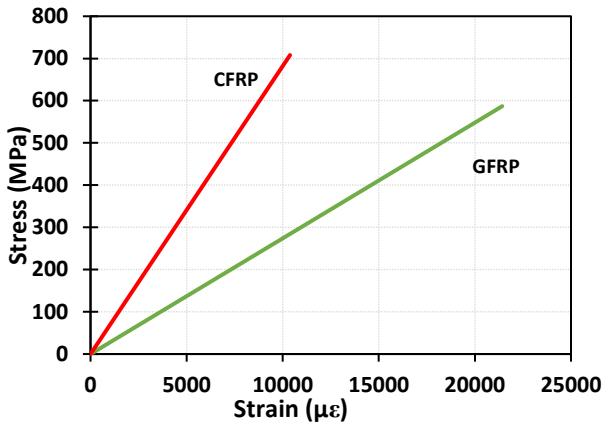

Figure 4-2: Idealised Stress Strain Curve for CFRP and GFRP Fabric Laminated with Epoxy Resin

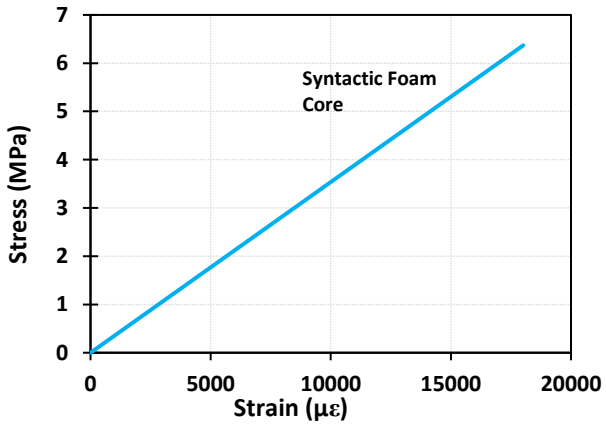

Figure 4-3: Idealised Stress Strain Curve for Bulkermat Syntactic Foam Core Laminated with Epoxy Resin

Table 4-1: ABAQUS Input Parameters for Laminated FRP Material Properties

	GFRP	CFRP	Syntactic Foam
Tensile Strength (MPa)	587	708	6.4
Tensile Modulus (MPa)	27,400	69,600	353.6
Nominal Thickness (mm)	1.01	1.3	4.1

The FEA was simplified to have a solid concrete wall to accommodate the limited number of nodes available in the student version of ABAQUS. The concrete damage plasticity (CDP) model in ABAQUS was selected to model the inelastic behaviour of concrete. Mohamed & Nehdi (2016) implemented the CDP model to describe concrete behaviour of RC pipes in TEB test loading. The expected failure modes of concrete are concrete cracking at the inner crown and invert, and outer springline and concrete crushing at the outer crown and invert, and inner springline. The linear elastic region of concrete is shown in Figure 4-4. The plastic behaviour of concrete was modeled by the CDP model in ABAQUS. As seen in "Appendix I: Experimental Compressive Strength of Concrete," the average ultimate compression strength of the concrete pipes was experimentally determined to be 54.73MPa. Default values for the concrete damage plasticity model in ABAQUS were selected (*ABAQUS/CAE Defining a Concrete Damaged Plasticity Model*, n.d.). The value of dilation angle in the CDP model was selected to be 31° which was used in the development in of the simplified CDP model available in ABAQUS; the dilation angle normally ranges from 20° to 40° (Hafezolghorani et al., 2017). The poisson ratio was assumed to be 0.2 (Chansawat et al., 2009). The elastic modulus of concrete (E_0) and tensile strength of concrete (f_r) were calculated respectively (Chansawat et al., 2009):

$$E_0 = 4733\sqrt{f'_c}$$
$$f_r = 0.623\sqrt{f'_c}$$

Table 4-2: ABAQUS Input Parameters for Concrete Material Properties

	f'_c (MPa)	E (MPa)	f_r (MPa)	Poisson Ration	dilation angle (°)	ϵ	σ_{b0}/σ_{c0}	K_c	μ
Concrete	54.72	35014	4.60	0.2	31	0.1	1.16	0.666667	0

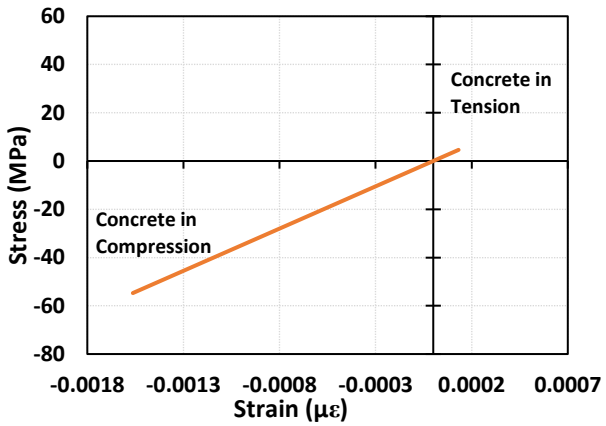

Figure 4-4: Idealised Elastic Stress Strain Curve for Concrete in Compression and Tension

4.3 Analysis Procedure

FEA was performed in the student version of ABAQUS. The 2D model was drafted with dimensions provided from the manufacturer for FRP materials and average dimensions measured from the RCP specimens. A negative load was applied to the crown of the specimen to simulate the contact of the upper bearing strip. Two pinned boundary conditions simulated the contact of the lower bearing strips with a gap of 31.75mm to match the gap between the rounded bearing strips used in testing. The gap between pined boundary conditions in the parametric study was increased to 57.45mm to ensure the model would comply with spacing requirements of ASTM C497M. The applied load was increased until ABAQUS would return a convergence error. Contour plots would be collected for elastic (LE) and plastic (PE) strain, while the load and strain data was exported and plotted in excel. Series with duplicate data points at the same time interval had the second data point truncated. ABAQUS separates elastic and plastic strain such that total strain would be the sum of both LE and PE.

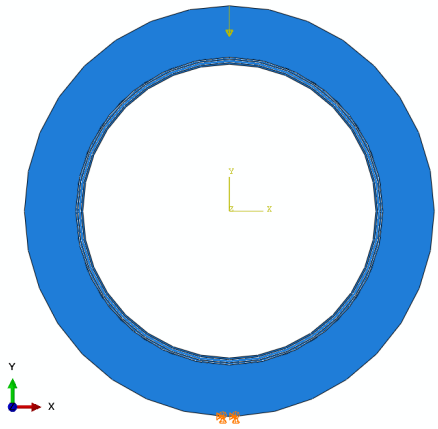

Figure 4-5: Load (Crown) and Two Boundary Condition (Invert) Locations on FEA in ABAQUS

4.4 Mesh Sensitivity and Model Limitations

The model which has been used in FEA has been simplified to accommodate limitation of the student edition of ABAQUS. Steel rebar was not considered in FEA and instead the walls of the RCP were made to be solid concrete. Concrete damage was not simulated in the model, it was assumed that the applied FRP liner returned the concrete to pre-cracked strength. The bond between FRP materials and concrete was assumed to be perfect as predicting delamination failure was beyond the scope of the project. The simplified concrete stress strain curve does not capture cracking before reaching the ultimate strength of concrete. The plastic behaviour beyond the ultimate strength of concrete is described by the CDP model in ABAQUS.

A mesh sensitivity analysis was performed with an alternative mesh with a three-node linear plain stress element type CPS3 seen in Figure 4-6 (*ABAQUS/CAE Two-Dimensional Solid Element Library*, n.d.). The mesh used in the FEA trials was 4-node bilinear, reduced integration with hourglass control element type CPS4R shown in Figure 4-1 (*ABAQUS/CAE Two-Dimensional Solid Element Library*, n.d.). Seen in Figure 4-7, the agreement between FEA and experimental results within the range of experimental data but begins diverging beyond the maximum of the experimental results.

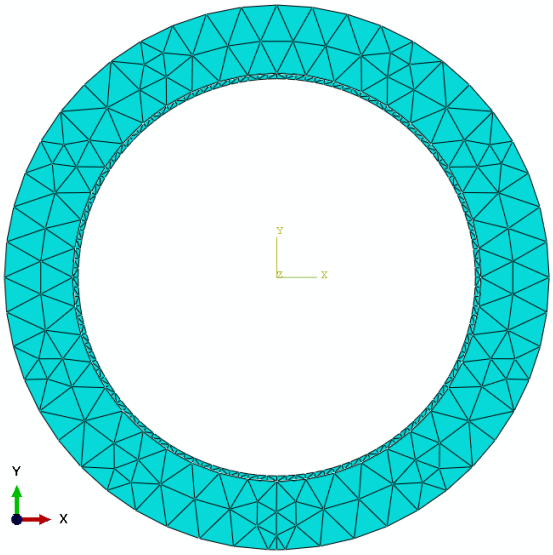

Figure 4-6: Alternative mesh with element type CPS3 for the GGGG specimen

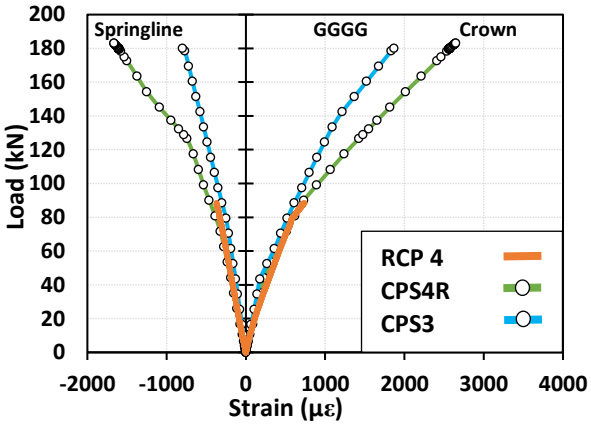

Figure 4-7: Experimental Results of RCP 4 GGGG specimen plotted against FEA results with element types CPS4R and CPS3

Reduced integration element types in ABAQUS, such as CPS4R, can experience a problem described as hourglassing seen in Figure 4-8. Coarser meshes with reduced integration element types in ABAQUS experience a problem in bending. In some cases, the paths through the single integration point at the centroid, represented by the dotted lines in Figure 4-8, remain unchanged after distortion resulting in a zero-energy mode (*ABAQUS/CAE Reduced Integration*, n.d.). The propagation of this error can lead to low accuracy results and is responsible for increased flexibility in FEA. ABAQUS compensates for this problem with an added hourglass stiffness factor and

recommends to use a mesh with at least 4 elements across the thickness of a model which will carry bending loads (*ABAQUS/CAE Reduced Integration*, n.d.).

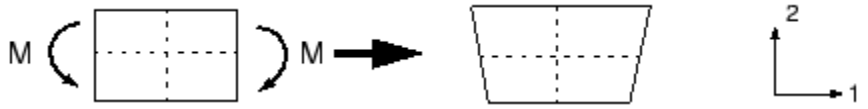

Figure 4-8: Hourglassing Problem with Reduced Integration Element Types (ABAQUS/CAE Reduced Integration, n.d.)

4.5 Model Verification

The plots in ABAQUS share the same three sloped curve as described by Attari et al. (2012). As seen in Figure 4-10, plastic strain begins to develop at 53kN at the crown and 81kN at the springline signaling that cracking has commenced. On the respective elastic strain plot seen on Figure 4-9, the elastic load vs strain profiles exhibit an inflection point corresponding to the development of plastic strain. Contour plots of the plastic strain on Figure 4-11 illustrate the plastic strain first developing at the inner crown and subsequently at the outer springline. The second inflection point on the plastic strain plot which signals the maximum strength of concrete has been reached occurs at 89kN at the crown and 126kN at the springline. The three sloped curve is most prominent on the springline plots of load vs. plastic strain. A full catalogue of load vs. strain profiles is available in Appendix II; all other FEA results exhibited similar behaviour. The efficacy of the FRP liners demonstrated in Figure 4-12 which compares a bare concrete pipe to a concrete pipe with a GFRP liner (GGGG); the bare concrete pipe has developed a significant amount of plastic strain at the crown and invert while the GFRP liner specimen has yet to experience plastic strain. Figure 4-13 displays load vs. strain plots comparing experimental results for strain at the crown to the full results from ABAQUS for the strain at the crown. The full load vs strain plots show that most specimens experience delamination before or shortly after the slope begins deflection. The inflection points corresponding to concrete cracking and ultimate concrete strain

may be reference points for determining safe operating limits. FEA results were extended beyond experimental results to gain understanding of the specimen's expected behaviour if delamination has been postponed.

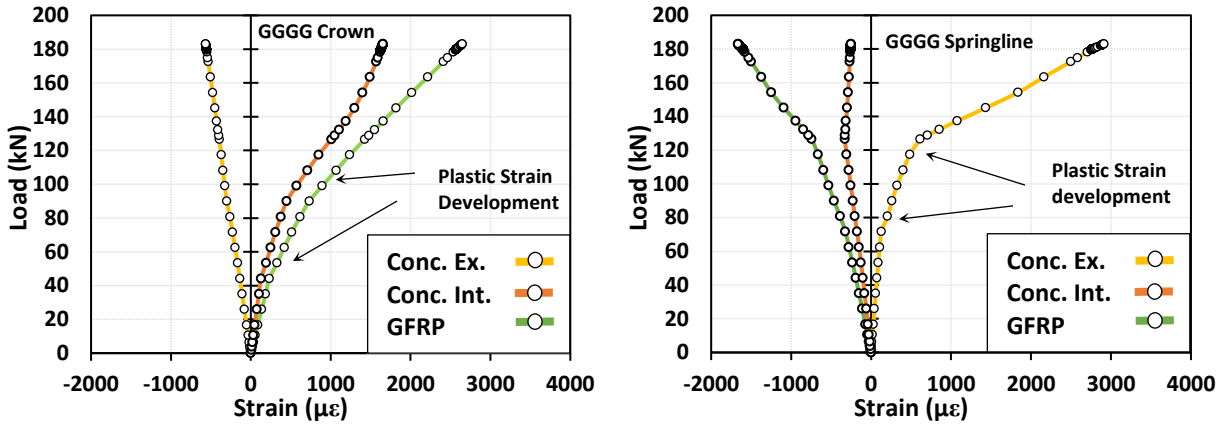

Figure 4-9: Load vs. Strain Plot of Hybrid Sandwich Liner at Each Layer of the Crown (Left) Springline (Right)

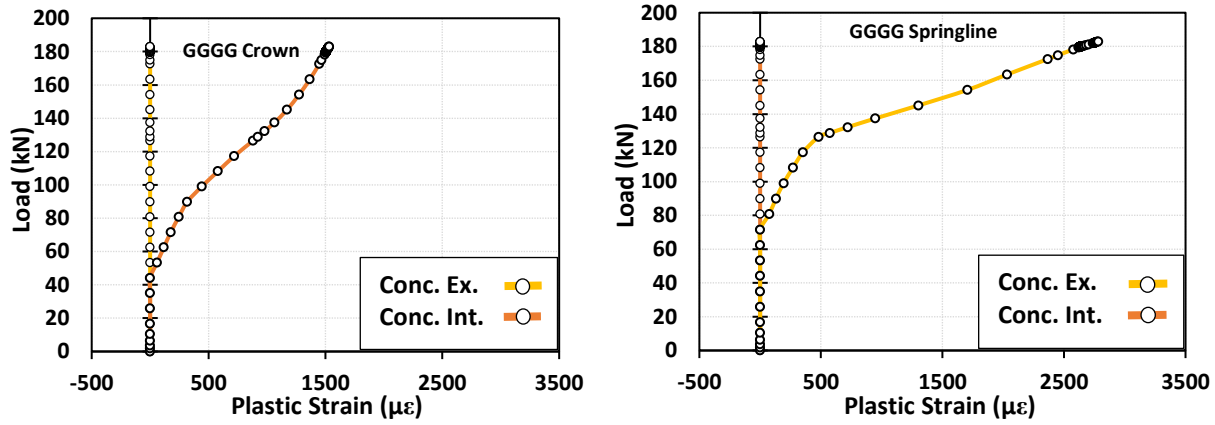

Figure 4-10: Load vs. Plastic Strain in Concrete at Exterior face and Interface layers of the Crown (Left) and Springline (Right)

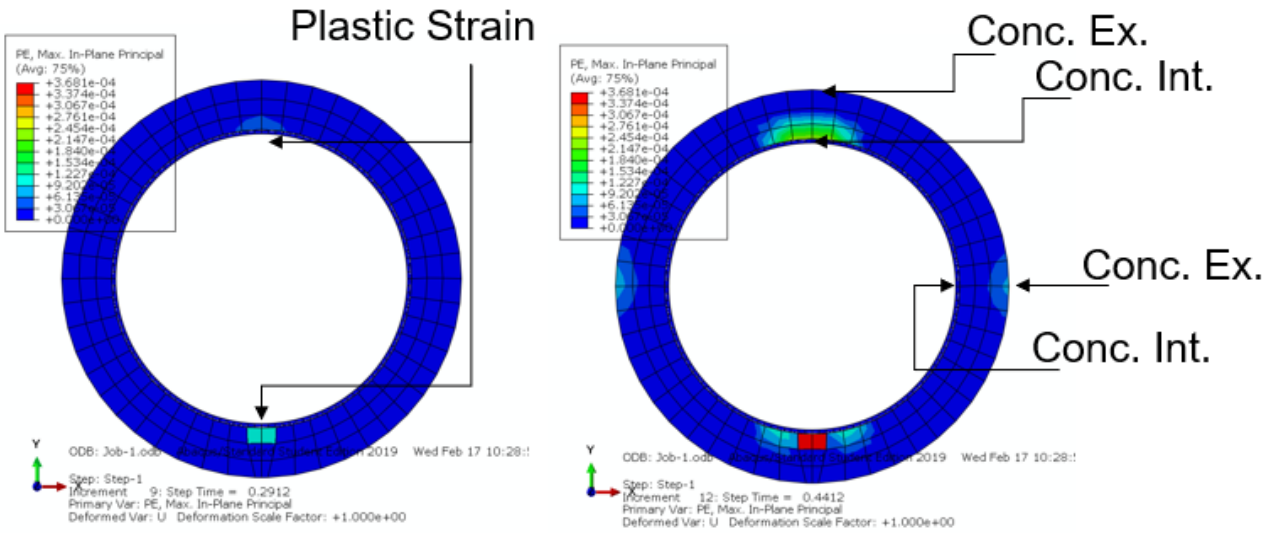

Figure 4-11: Plastic Strain Contour Plot of GFRP Only Specimen at 53kN (Left) 81kN (Right)

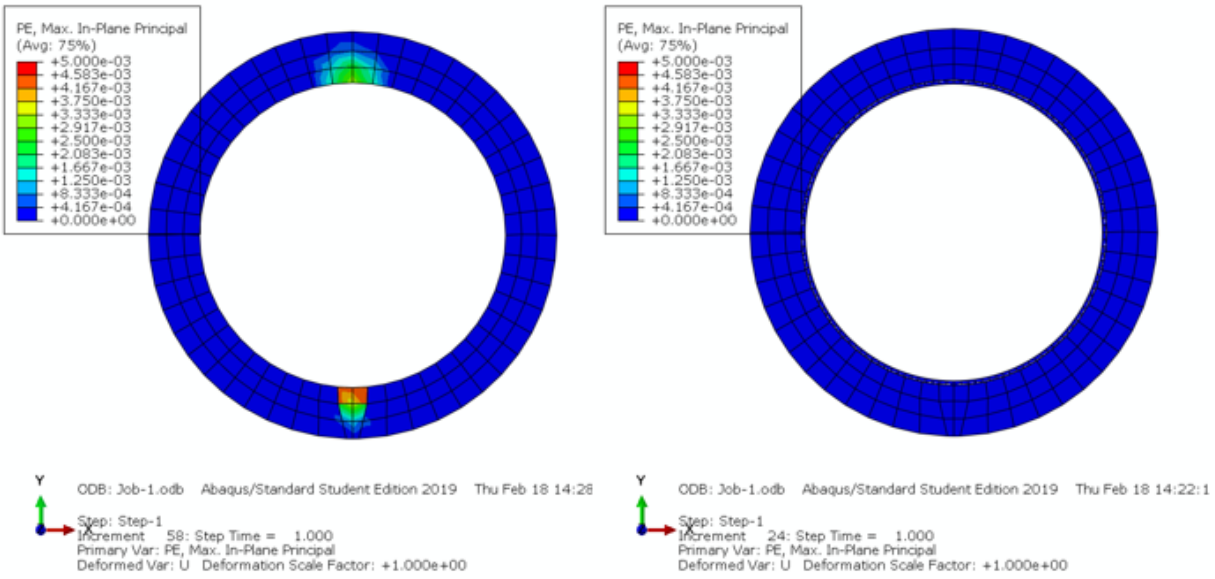

Figure 4-12: Plastic Strain Contour Plot of Bare Concrete (Left), GFRP Only Specimen (Right) at 65kN

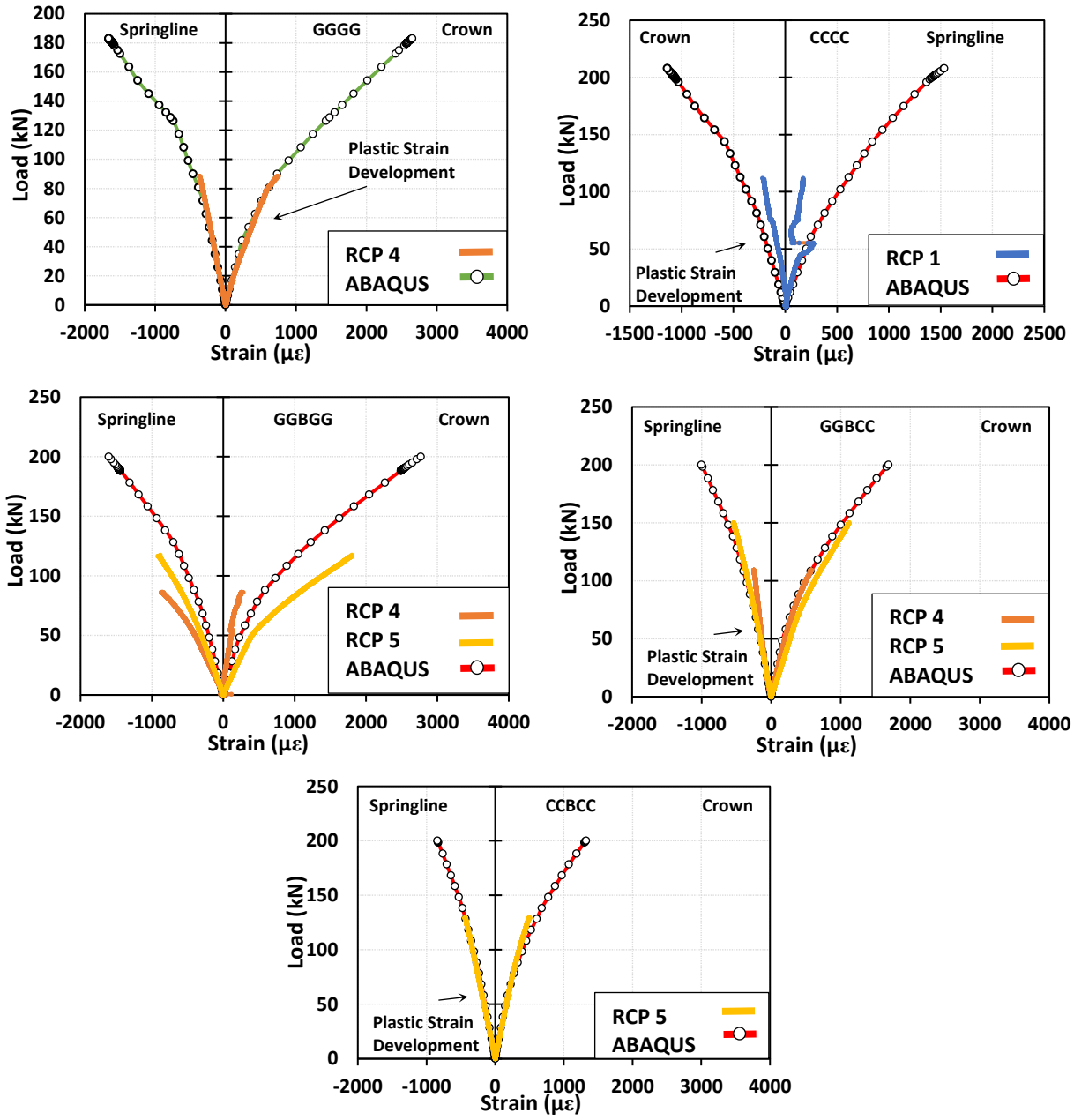

Figure 4-13: Load vs. Strain Plot of Empirical and Full FEA Results

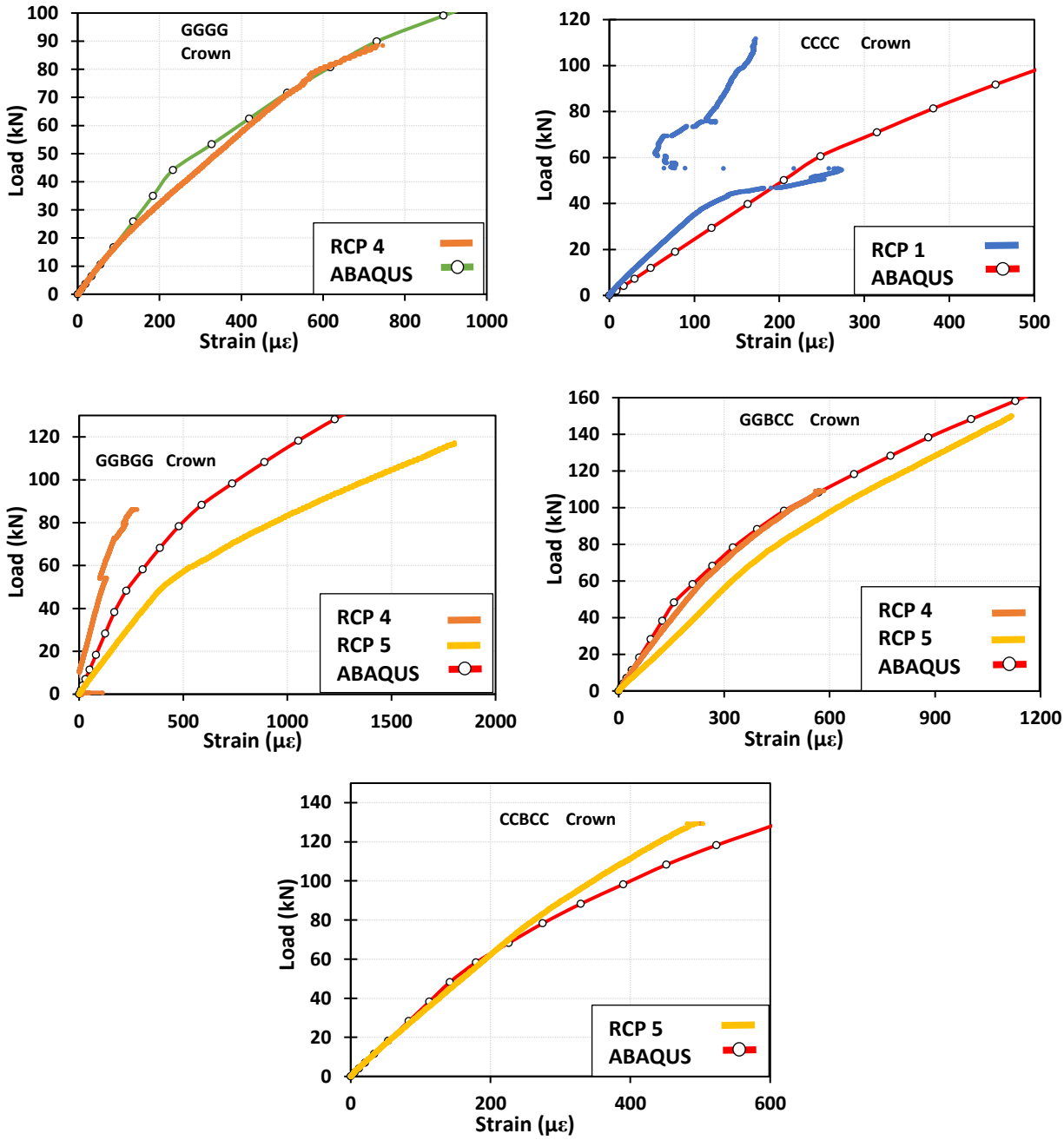

Figure 4-14: Load Vs. Strain Plots Comparing Experimental and FEA results in ABAQUS

Figure 4-14 displays experimental strain data collected at the crown of each specimen plotted against crown strain data from FEA in ABAQUS. Apart from the CCCC and GGBGG specimens, the experimental and ABAQUS plots appear to share similar curve shapes corroborated with the COV values in Table 4-3. The CCCC specimen appears to have had a minor premature failure which caused a jog in the data. The GGBGG data generated by ABAQUS plots between

the two experimental runs. As the curing time between layers was lengthened for RCP 5-GGBGG, the bonding between FRP layers and concrete may have been improved leading to higher a failure load. The shape of the curves is similar and exhibit pseudo-linear behaviour. Seen in Table 4-3, The Coefficient of Variation (COV) for each specimen was below 20% across all tests apart from the CCCC specimen which exhibited a premature failure and had a higher COV of 51.93%. A COV of 20% or lower is considered to indicate that the variation between series is low.

There is a discrepancy between the FEA results and experimental results of horizontal and vertical diameter change seen in Figure 4-15. A potential source of error is the test setup for measuring displacement. Vertical displacement was measured with a string potentiometer strung from the upper wood bearing strip to the lower wood bearing strip. At these locations, the compression of the wood bearing strips may have interfered with vertical displacement results. The rigid CFRP strips glued to wood and subsequently glued to the outer springline of the specimen, may not have accurately reacted to the compression of the specimen with the same resolution that can be achieved with FEA.

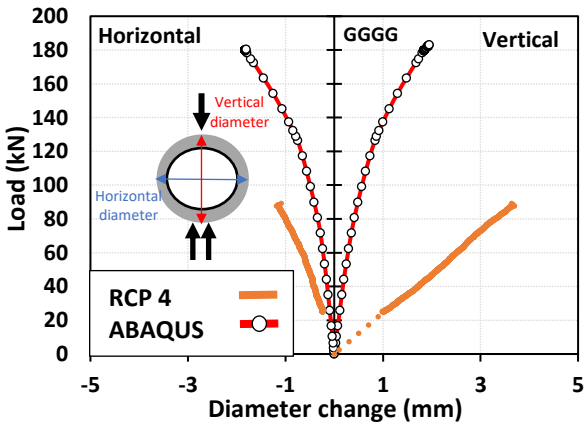

Figure 4-15: Comparison of Load vs. Vertical Diameter change for a GFRP Only Liner in ABAQUS and Experimental Results

Table 4-3: Test/Model Ratios for Crown Strain with COV (%)

Specimen		ABAQUS		TEST		Test/Model		
		Load (kN)	Strain (με)	Load (kN)	Strain (με)	Ratio	Avg Ratio	COV (%)
GGGG	RCP 4	25.85	136	25.27	144	1.06	1.04	5.05
		53.30	328	52.78	360	1.10		
		80.75	618	81.03	603	0.98		
		89.90	731	88.46	746	1.02		
CCCC	RCP 1	29.38	120	29.336	81	0.67	0.38	51.93
		70.98	315	71.056	80	0.25		
		91.78	454	91.768	141	0.31		
		112.58	612	111.863	172	0.28		
GGBGG	RCP 4	28.25	125	28.25	49	0.39	0.42	9.11
		48.25	227	48.32	105	0.46		
		68.25	388	68.39	150	0.39		
		78.25	479	78.05	211	0.44		
	RCP 5	28.25	125	28.25	213	1.70	1.73	3.19
		48.25	227	48.32	380	1.68		
		68.25	388	68.39	692	1.78		
		108.25	891	107.79	1586	1.78		
GGBCC	RCP 4	28.25	92	28.25	104	1.13	1.08	7.71
		48.25	158	48.32	185	1.17		
		88.25	394	88.46	407	1.03		
		108.25	569	107.79	566	0.99		
	RCP 5	28.25	92	28.25	152	1.66	1.42	19.15
		48.25	158	48.32	258	1.63		
		88.25	394	88.46	518	1.31		
		148.25	1003	147.93	1094	1.09		
CCBCC	RCP 5	28.25	83	28.25	86	1.03	0.94	12.10
		58.25	179	57.98	186	1.04		
		88.25	329	88.46	294	0.89		
		128.25	603	127.86	484	0.80		
						TOTAL	1.00	47.88

4.6 Parametric Study

A parametric study was conducted to explore results of larger diameter concrete pipes. The wet layup method of trenchless rehabilitation is more practically applied to larger diameter pipes rather than small diameter pipes due to ease of manned access. The parametric pipe model had an inner diameter of 762mm, a wall thickness of 152.4mm, and a length of 1000mm. The hybrid liner

structure consisting of double layers of GFRP and CFRP was selected due to it achieving the highest peak D-load in testing. The number of GFRP and CFRP sheets was varied between 2 and 6 in intervals of two and syntactic foam core layers were varied from 0 to 3. The nomenclature of specimens begins with the layer in contact with concrete and subsequent layers follow the hyphen. The number indicates the number of plies in the layer and the letter the fabric type; G for GFRP, C for CFRP, B for Syntactic Foam. The resultant specimen labels can be seen in Table 4-4.

Table 4-4: Test Matrix of Parametric Study

Hybrid Layers		Syntactic Foam Layers			
		0	1	2	3
	2	2G-2C	2G-B-2C	2G-2B-2C	2G-3B-2C
	4	4G-4C	4G-B-4C	4G-2B-4C	4G-3B-4C
	6	6G-6C	6G-B-6C	6G-2B-6C	6G-3B-6C

The strain at the extreme fibre of the FRP liner was compared between all the specimens as seen in Figure 4-16. Each additional layer shifts the load versus strain curve upwards yielding higher loads at similar strains. Increasing the number of GFRP and CFRP plies in the sandwich increases the load bared at a given strain to a greater extent. Since the FEA does not account for delamination failure, data points closest to 2000με were compared in Table 4-5. The increase in load due to additional layers of syntactic foam, which accounted for a maximum increase of 78kN between 6G6C and 6G 3B 6C, is lower than the increase of load for additional GFRP and CFRP plies. The increase of load between 2G 2C and 4G 4C was 172kN and 158kN between 4G 4C and 6G 6C. This data suggests that increasing the number of GFRP and CFRP plies is a more effective method of increasing the load bearing of the FRP liner at a given strain as seen in Figure 4-17.

The loading behaviour exhibits distinct slopes beginning with the first three described in the model verification section and an additional fourth slope. Figure 4-18 and Figure 4-19 display

the load vs. elastic strain and load vs. plastic strain plots, respectively. The springline best exhibits the distinct slope sections with the first three sections corresponding to elastic loading with no plastic strain, concrete cracking and achieving maximum concrete strength. The fourth slope can be explained by the additional development of plastic strain at the interior of the concrete springline at 931kN. The implication being that the entire cross section of springline is experiencing plastic strain. Additional research is required to determine the behaviour of large concrete pipes lined with FRP materials.

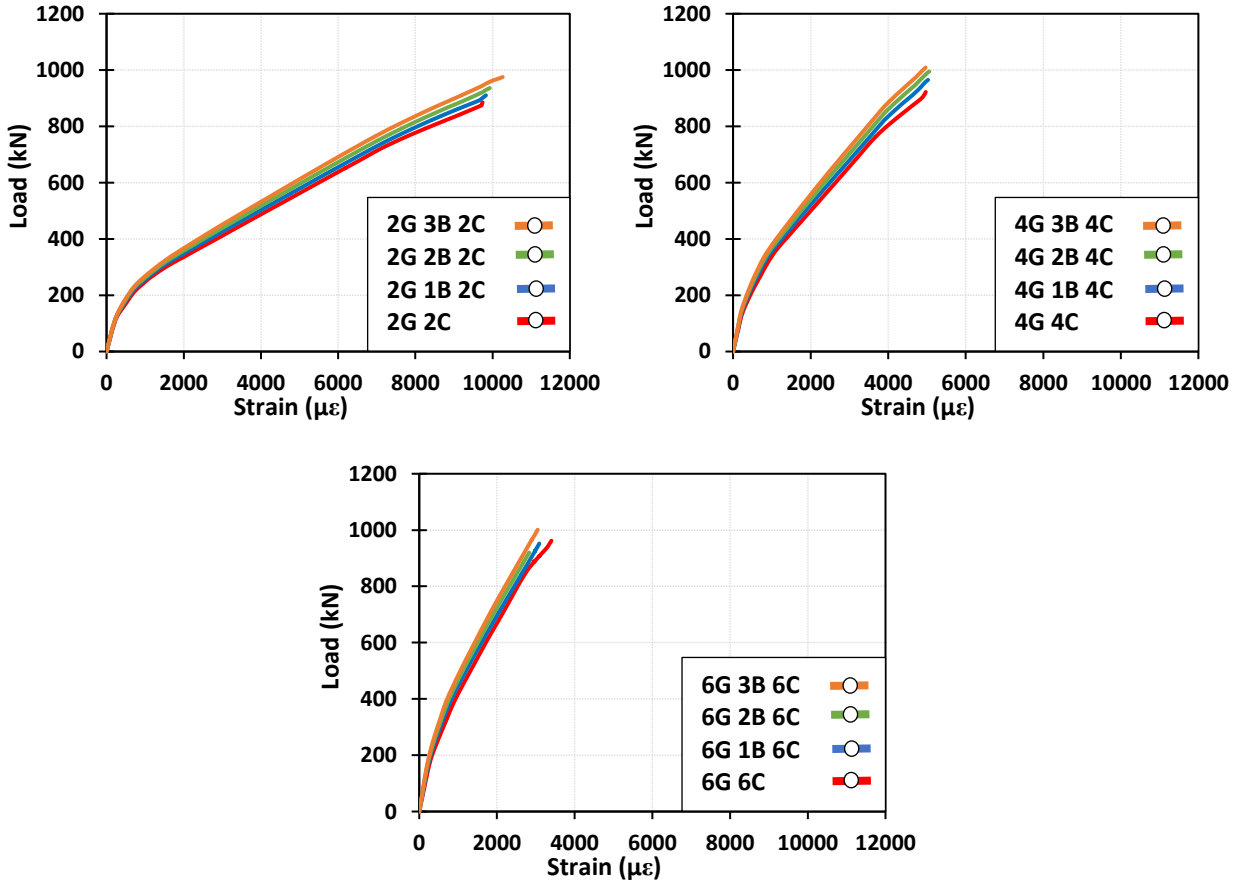

Figure 4-16: Comparison of Extreme Fibre Strain of FRP Liner with Varying Layers of Syntactic Foam (data has been fitted with lines for visualisation)

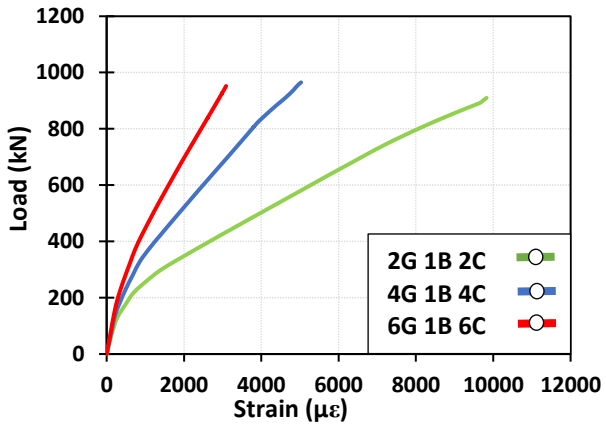

Figure 4-17: Comparison of Extreme Fibre Strain of FRP Liner with Varying Skin Layers

Table 4-5: Loads of Parametric Specimens at Closest Data Point to 2000με

	Load (kN)	strain (με)
2G2C	335	1990
2G1B2C	345	1957
2G2B2C	366	2100
2G3B2C	369	2026
4G4C	507	2047
4G 1B 4C	522	2006
4G 2B 4C	553	2076
4G 3B 4C	559	2012
6G6C	665	1982
6G 1B 6C	706	2039
6G 2B 6C	728	2015
6G 3B 6C	743	1976

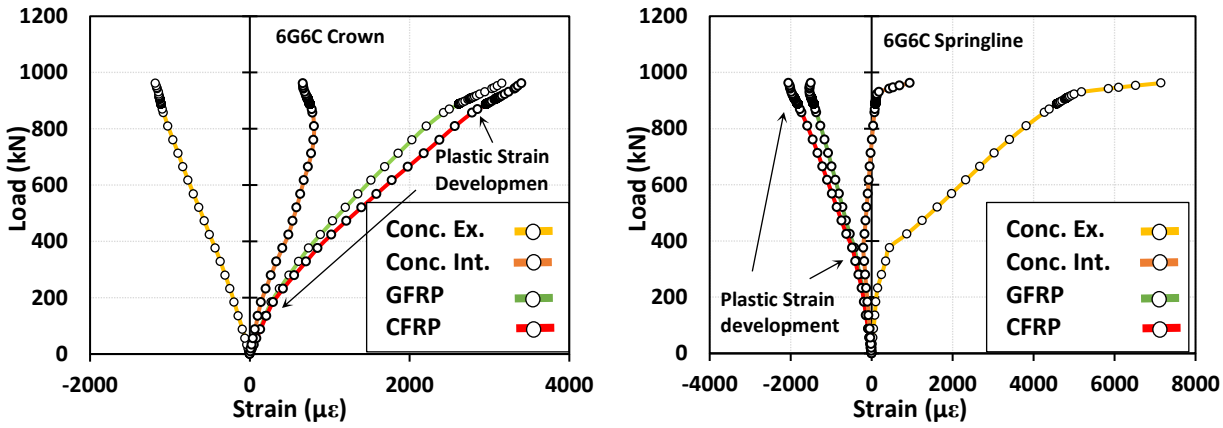

Figure 4-18: Load vs. Strain for 6G6C at Crown (Left) and Springline (Right)

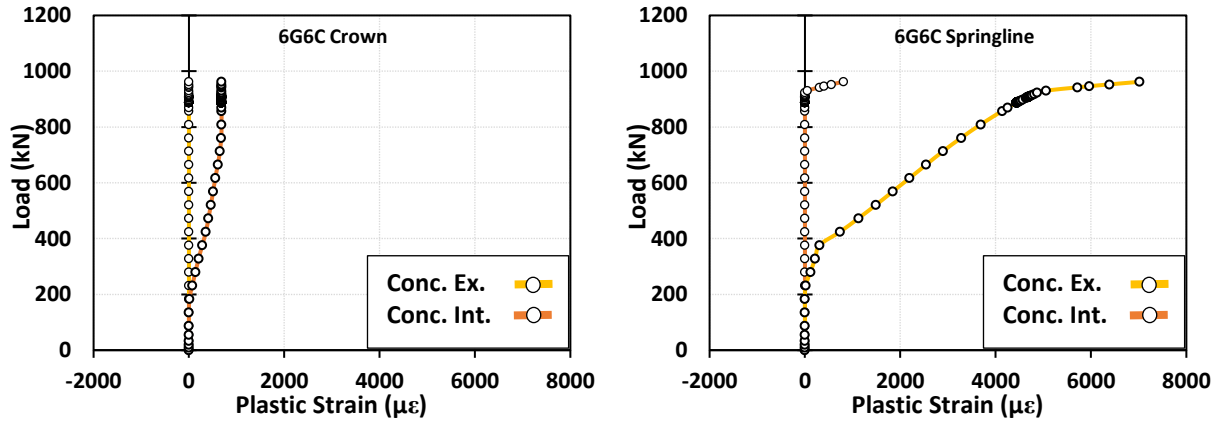

Figure 4-19: Load vs. Plastic Strain for 6G6C at Crown (Left) and Springline (Right)

Chapter 5. Conclusions and Recommendations

The objective of this thesis was to explore the behaviour and failure modes of RCP repaired with FRP liners and subsequently provide a foundation for future works and design recommendations. To achieve this objective, RCP specimens were damaged and then repaired with FRP materials to be tested in TEB loading. Experimental results were compared to FEA results from ABAQUS. A parametric FEA study was performed to explore the behaviour of larger diameter RCPs repaired with varying layers of FRP materials.

Load vs. strain plots of both FEA and experimental results displayed 3 sloped behaviour associated with the elastic, cracking and plastic strains of concrete. Inflection points corresponded with a development of plastic strain in the concrete at the inner crown and outer springline in FEA results. The plots of FEA and test results were visually in agreement and had an overall test/model ratio of 1.00 and COV of 47.88%. The specimen with a CFRP only liner was an outlier due to a minor premature delamination which had a test/model ratio of 0.38 and COV of 51.93%; the COV of all other test/model ratios were below 20%.

Results from the parametric study showed that the most effective way to increase stiffness is to increase the number of GFRP and CFRP plies as the syntactic foam plies offer a marginal increase in stiffness. Load versus strain curves exhibited 4 slopes with inflection points corresponding with the development of plastic strain in concrete at the crown and springline: the final slope corresponding to development of plastic strain at the interior springline. Delamination behaviour at on larger scale pipes has not been investigated. The development of plastic strains in concrete may offer a reference point for assessing the risk of delamination.

Vertical and Horizontal displacement measurements did not agree with FEA results. A potential source of error is the instrumentation setup. String potentiometers were connected to the upper and lower wood bearings strips to measure vertical displacement. Horizontal displacement was measured with linear potentiometers fixed to the frame and contacting the specimen on strips of CFRP glued to wood block that held the CFRP strip vertically to the specimen. Instrumentation should measure directly on the RCP specimen as the compression of wood and movement of fixtures may have affected results. A digital measurement method such as Digital Image Correlation (DIC) may otherwise be employed if available.

Additional research on material properties and mechanics of delamination failure of FRP liners should be conducted to better predict the performance of FRP liners used in repair of RCP structures. The load or strain at which delamination occurs was not predicted in these experiments. However, future studies may examine the use of the inflection points as reference points to assess delamination risk from crack induced debonding. The mode of failure observed for all specimens was crack induced debonding. Additional material property testing and FEA design with greater detail and node count may be performed to determine the significance of helical rebar in damaged RCP repaired with FRP liner. Rebar was omitted in the FEA due to the node limit of the student version of ABAQUS. Non-Destructive Testing (NDT) may be performed before testing in the future to verify the quality of the FRP to concrete bond. Cyclic loading tests should also be considered for long term use of the liners.

Bibliography

ABAQUS/CAE Defining a concrete damaged plasticity model. (n.d.). Dassault Systèmes. Retrieved 19 November 2020, from https://abaqus-docs.mit.edu/2017/English/SIMACAECAERefMap/simacae-t-prpmechanicalplasticconcretedamagedmodel.htm

ABAQUS/CAE Reduced integration. (n.d.). Dassault Systèmes. Retrieved 5 April 2021, from https://abaqus-docs.mit.edu/2017/English/SIMACAEGSARefMap/simagsa-c-ctmreduced.htm

ABAQUS/CAE Two-dimensional solid element library. (n.d.). Dassault Systèmes. Retrieved 5 April 2021, from https://abaqus-docs.mit.edu/2017/English/SIMACAEELMRefMap/simaelm-r-2delem.htm

Ariaratnam, S. T., Lueke, J. S., & Michael, J. K. (2014). Current trends in pipe bursting for renewal of underground infrastructure systems in North America. *Underground Infrastructure Research 2012*, *39*, 41–49. https://doi.org/10.1016/j.tust.2012.04.003

ASTM International. (2011). *ASTM F2019-11 Standard Practice for Rehabilitation of Existing Pipelines and Conduits by the Pulled in Place Installation of Glass Reinforced Plastic (GRP) Cured-in-Place Thermosetting Resin Pipe (CIPP)*. https://doi.org/10.1520/F2019-11

ASTM International. (2016). *ASTM F1216-16 Standard Practice for Rehabilitation of Existing Pipelines and Conduits by the Inversion and Curing of a Resin-Impregnated Tube*. https://doi.org/10.1520/F1216-16

ASTM International. (2018). *ASTM F2994-18 Standard Practice for Utilization of Mobile, Automated Cured-In-Place Pipe (CIPP) Impregnation Systems*. https://doi.org/10.1520/F2994-18

ASTM International. (2020). *ASTM C76M-20, Standard Specification for Reinforced Concrete Culvert, Storm Drain, and Sewer Pipe (Metric)*. http://www.astm.org/cgi-bin/resolver.cgi?C76M-20

Attari, N., Amziane, S., & Chemrouk, M. (2012). Flexural strengthening of concrete beams using CFRP, GFRP and hybrid FRP sheets. *Non Destructive Techniques for Assessment of Concrete*, *37*, 746–757. https://doi.org/10.1016/j.conbuildmat.2012.07.052

Bakeer, R. M., Barber, M. E., Pechon, S. E., Taylor, J. E., & Chunduru, S. (1999). Buckling of HDPE Liners under External Uniform Pressure. *Journal of Materials in Civil Engineering*, *11*(4), 353–361. https://doi.org/10.1061/(ASCE)0899-1561(1999)11:4(353)

Bank, L. C. (2006). *Composites for construction: Structural design with FRP materials*. Hoboken, N.J. : John Wiley & Sons.

Barber, M. E., Bakeer, R. M., Sever, V. F., & Boyd, G. R. (2005). Effect of close-fit sliplining on the hydraulic capacity of a pressurized pipeline. *Tunnelling and Underground Space Technology*, *20*(1), 23–31. https://doi.org/10.1016/j.tust.2004.05.001

Becerril García, D., & Moore, I. D. (2016). Evaluation and application of the flexural rigidity of a reinforced concrete pipe. *Journal of Pipeline Systems Engineering and Practice*, *7*(1). https://doi.org/10.1061/(ASCE)PS.1949-1204.0000216

Chansawat, K., Potisuk, T., Miller, T. H., Yim, S. C., & Kachlakev, D. I. (2009). FE Models of GFRP and CFRP Strengthening of Reinforced Concrete Beams. *Advances in Civil Engineering*, *2009*, 152196. https://doi.org/10.1155/2009/152196

Das, S., Bayat, A., Gay, L., Salimi, M., & Matthews, J. (2016). A comprehensive review on the challenges of cured-in-place pipe (CIPP) installations. *Journal of Water Supply : Research and Technology - AQUA*, *65*(8), 583–596. Agricultural & Environmental Science Database; Earth, Atmospheric & Aquatic Science Database. https://doi.org/10.2166/aqua.2016.119

Del Viso, J. R., Carmona, J. R., & Ruiz, G. (2008). Shape and size effects on the compressive strength of high-strength concrete. *Cement and Concrete Research*, *38*(3), 386–395. https://doi.org/10.1016/j.cemconres.2007.09.020

Dirksen, J., Clemens, F. H. L. R., Korving, H., Cherqui, F., Le Gauffre, P., Ertl, T., Plihal, H., Müller, K., & Snaterse, C. T. M. (2013). The consistency of visual sewer inspection data. *Structure and Infrastructure Engineering*, *9*(3), 214–228. https://doi.org/10.1080/15732479.2010.541265

Donaldson, B. M. (2009). Environmental Implications of Cured-in-Place Pipe Rehabilitation Technology. *Transportation Research Record*, *2123*(1), 172–179. https://doi.org/10.3141/2123-19

FRP Services & Company. (2016). *Composites: Core Material*. FRP Services & Company. http://www.frpservices.com/us/composite/core-material.html

Hafezolghorani, M., Hejazi, F., Vaghei, R., Jaafar, M. S. B., & Karimzade, K. (2017). Simplified Damage Plasticity Model for Concrete. *Structural Engineering International*, *27*(1), 68–78. https://doi.org/10.2749/101686616X1081

Halifax. (2018, January 2). *Underground Overhaul*. Halifax. https://www.halifax.ca/home-property/halifax-water/about-your-water/capital-projects/underground-overhaul

Heger, F. J. (1962). *A Theory for the Structural Behavior of Reinforced Concrete Pipe* [Thesis (Ph. D.), Massachusetts Institute of Technology, Dept. of Civil and Sanitary Engineering]. https://dspace.mit.edu/handle/1721.1/15601

Isett, B. (2000). Repairing collection system pipes. *Water Environment & Technology*, *12*(8), 102. Agricultural & Environmental Science Database; Biological Science Database; Earth, Atmospheric & Aquatic Science Database; Research Library.

Jaganathan, A., Allouche, E., & Baumert, M. (2007). Experimental and numerical evaluation of the impact of folds on the pressure rating of CIPP liners. *Trenchless Technology*, *22*(5), 666–678. https://doi.org/10.1016/j.tust.2006.11.007

Ji, H., Yoo, S., Kim, J., & Koo, D. (2018). The Mechanical Properties of High Strength Reinforced Cured-in-Place Pipe (CIPP) Liner Composites for Urban Water Infrastructure Rehabilitation. *Water*, *10*(8), 983. https://doi.org/10.3390/w10080983

Kezdi, M. (2018, February 19). Preserving the Northwest Arm: Trenchless Shines on Daunting Underground Overhaul Project in Halifax. *Trenchless Technology*. https://trenchlesstechnology.com/northwest-arm-trenchless-cipp-halifax/

Kuliczkowska, E., & Gierczak, M. (2013). Buckling failure numerical analysis of HDPE pipes used for the trenchless rehabilitation of a reinforced concrete sewer. *Engineering Failure Analysis*, *32*, 106–112. https://doi.org/10.1016/j.engfailanal.2013.03.007

Lee, D. C., & Karbhari, V. M. (2005). Rehabilitation of Large Diameter Prestressed Cylinder Concrete Pipe (PCCP) with FRP Composites—Experimental Investigation. *Advances in Structural Engineering*, *8*(1), 31–44. https://doi.org/10.1260/1369433053749634

Li, X., Ra, K., Nuruddin, M., Teimouri Sendesi, S. M., Howarter, J. A., Youngblood, J. P., Zyaykina, N., Jafvert, C. T., & Whelton, A. J. (2019). Outdoor manufacture of UV-Cured

plastic linings for storm water culvert repair: Chemical emissions and residual. *Environmental Pollution*, *245*, 1031–1040. https://doi.org/10.1016/j.envpol.2018.10.080

Lueke, J. S., & Ariaratnam, S. T. (2001a). Rehabilitation of Underground Infrastructure Utilizing Trenchless Pipe Replacement. *Practice Periodical on Structural Design and Construction*, *6*(1), 25–34. https://doi.org/10.1061/(ASCE)1084-0680(2001)6:1(25)

Lueke, J. S., & Ariaratnam, S. T. (2001b). Rehabilitation of Underground Infrastructure Utilizing Trenchless Pipe Replacement. *Practice Periodical on Structural Design and Construction*, *6*(1), 25–34. https://doi.org/10.1061/(ASCE)1084-0680(2001)6:1(25)

MacDonnell, L., & Sadeghian, P. (2020). Experimental and analytical behaviour of sandwich composites with glass fiber-reinforced polymer facings and layered fiber mat cores. *Journal of Composite Materials*, *54*(30), 4875–4887. https://doi.org/10.1177/0021998320939625

Meegoda, J. N., & Zou, Z. (2015). Long-Term Maintenance of Culvert Networks. *Journal of Pipeline Systems Engineering and Practice*, *6*(4), 04015003. https://doi.org/10.1061/(ASCE)PS.1949-1204.0000194

Mohamed, N., & Nehdi, M. L. (2016). Rational finite element assisted design of precast steel fibre reinforced concrete pipes. *Engineering Structures*, *124*, 196–206. https://doi.org/10.1016/j.engstruct.2016.06.014

Murphy, J. S. (1998). Microballoons Cores. In *The reinforced plastics handbook* (2nd ed., pp. 113–118). Oxford.

Park, Y., Abolimaali, A., & Beakley, J. (2015, December 14). *Three Edge-Bearing Performances of RCP and SYN-FRCP Repaired with Externally Bonded CFRP*. 12th International Symposium on Fiber Reinforced Polymers for Reinforced Concrete Structures (FRPRCS-

12) & The 5th Asia-Pacific Conference on Fiber Reinforced Polymers in Structures (APFIS-2015) Joint Conference, Nanjing, China.

Plastic Pipe Institute. (2008). Chapter 11—Pipeline Rehabilitation by Sliplining with PE Pipe. In *Handbook of Polyethylene pipe second edition* (Second Edition). Plastics Pipe Institute. https://plasticpipe.org/publications/pe-handbook.html

Rohrsanierung & Bau GmbH. (n.d.). *Sliplinging Advantages*. Sliplining Advantages. http://www.rohrsanierungsgmbh.at/en/your_advantages/sliplining/

Rohrsanierung & Bau GmbH. (2013). *SLIPLINING for all man-entry pipelines*. Rohrsanierung & Bau GmbH. http://www.rohrsanierungsgmbh.at/fileadmin/user_upload/inhaltsbilder/Download/2013_sliplining_m.pdf

Sha, X., & Davidson, J. S. (2020). Analysis of interfacial stresses in concrete beams strengthened by externally bonded FRP laminates using composite beam theory. *Composite Structures*, *243*, 112235. https://doi.org/10.1016/j.compstruct.2020.112235

Shi, J., Zheng, J., Guo, W., & Qin, Y. (2011). Defects classification and failure modes of electrofusion joint for connecting polyethylene pipes. *Journal of Applied Polymer Science*, *124*(5), 4070–4080. https://doi.org/10.1002/app.35013

Simpson, B., Hoult, N. A., & Moore, I. D. (2017). Rehabilitated reinforced concrete culvert performance under surface loading. *Tunnelling and Underground Space Technology*, *69*, 52–63. https://doi.org/10.1016/j.tust.2017.06.007

Sorrell, P. (1995). Rehabilitatating underground pipes. *Plant Engineering*, *49*(7), 66.

Sousa, V., & Meireles, I. (2018). The Influence of the Construction Technology in Time-Cost Relationships of Sewerage Projects. *Water Resources Management*, *32*(8), 2753–2766. https://doi.org/10.1007/s11269-018-1956-y

Stein, D., & Stein, R. (2004a). *Rehabilitation and Maintenance of Drains and Sewers: Hydraulic and Static Pipe Bursting*. UNITRACC.Com. https://www.unitracc.com/know-how/fachbuecher/rehabilitation-and-maintenance-of-drains-and-sewers/rehabilitation/replacement-en/replacement-by-the-trenchless-method-en/unmanned-techniques-en/pipe-bursting-en/hydraulic-and-static-pipe-bursting-en

Stein, D., & Stein, R. (2004b). *Rehabilitation and Maintenance of Drains and Sewers: Maintaining the Drainage Capability*. UNITRACC.Com. https://www.unitracc.com/know-how/fachbuecher/rehabilitation-and-maintenance-of-drains-and-sewers/rehabilitation/maintaining-the-drainage-capability-en#6adf0cab4f148ca57276bd643e52565e

Stein, D., & Stein, R. (2004c). *Rehabilitation and Maintenance of Drains and Sewers: Replacement by the Open Cut Method*. UNITRACC.Com. https://www.unitracc.com/know-how/fachbuecher/rehabilitation-and-maintenance-of-drains-and-sewers/rehabilitation/replacement-en/replacement-by-the-open-cut-method-en

Teng, J., Chen, J., Smith, S., Lam, L., & Jessop, T. (2003). Behaviour and strength of FRP-strengthened RC structures: A state-of-the-art review. *Proc. Inst. Civil Eng.-Struct. Build.*, *156*(3), 334–335. https://doi.org/10.1680/stbu.156.3.334.37862

Tomczak, E., & Zielińska, A. (2017). Example of sewerage system rehabilitation using trenchless technology. *Ecological Chemistry and Engineering*, *24*(3), 405–416. Agricultural &

Environmental Science Database; Biological Science Database; Earth, Atmospheric & Aquatic Science Database. https://doi.org/10.1515/eces-2017-0027

Toutanji, H., Zhao, L., & Zhang, Y. (2006). Flexural behavior of reinforced concrete beams externally strengthened with CFRP sheets bonded with an inorganic matrix. *Engineering Structures*, *28*(4), 557–566. https://doi.org/10.1016/j.engstruct.2005.09.011

TT Technologies. (2006a). *A Guide to Pneumatic Pipe Bursting with the GRUNDOCRACK SYSTEM*. TT Technologies, Inc. http://www.tttechnologies.com/download/literature/grundocrack-pneumatic-guide-pipe-bursting.pdf

TT Technologies. (2006b). *A Guide to Pneumatic Pipe Bursting with the GRUNDOCRACK SYSTEM*. TT Technologies, Inc. http://www.tttechnologies.com/download/literature/grundocrack-pneumatic-guide-pipe-bursting.pdf

TT Technologies. (2017). *Grundoburst Static Pipe Bursting System*. TT Technologies, Inc. http://www.tttechnologies.com/download/literature/grundoburst-lit.pdf

Tullis, B. P., & Anderson, D. S. (2010). Slip-Lined Culvert Inlet End Treatment Hydraulics. *Journal of Irrigation and Drainage Engineering*, *136*(1), 31–36. https://doi.org/10.1061/(ASCE)IR.1943-4774.0000113

United Kingdom Society of Trenchless Technology. (2014). *Cured in Place Pipe Lining*. United Kingdom Society of Trenchless Technology. http://www.ukstt.org.uk/trenchless-technology/lining-techniques/cured-in-place-pipe-lining-cipp

Wan, B., Jiang, C., & Wu, Y.-F. (2018). Effect of defects in externally bonded FRP reinforced concrete. *Construction and Building Materials*, *172*, 63–76. https://doi.org/10.1016/j.conbuildmat.2018.03.217

Watkins, R. K. (2000). *Structural mechanics of buried pipes*. Boca Raton, FL : CRC Press.

Zhao, J. Q., Daigle, L., & Beaulieu, D. (2002). Effect of joint contamination on the quality of butt-fused high-density polyethylene (HDPE) pipe joints. *Canadian Journal of Civil Engineering*, *29*(5), 787–798. Agricultural & Environmental Science Database; Canadian Business & Current Affairs Database; Earth, Atmospheric & Aquatic Science Database.

Appendix I: Experimental Compressive Strength of Concrete

The compressive strength of concrete (f'c) was determined by completing compression tests on rectangular samples of concrete taken from the specimens after the TEB tests had been completed. Larger sections of concrete pipe were broken off from the damaged specimen with a sledgehammer and angle grinder; the shoulder and haunch were more easily separated due to the cracks and exposed rebar at the crown, invert and springline. Using a stationary concrete saw, the concrete sections were cut into 3 cubic specimens of approximately 63.5mm for each tested section of pipe. Two opposing cut faces were chosen to be the loading face of each specimen. The area of two loading faces was determined by tracing the faces onto graphing paper and recording the number of squares within the outlines. The chosen faces were capped with capping compound and positioned to be in contact with the loading plates, the lower of which was a hinge support. Load was applied until concrete cracking occurred, the highest load was recorded. Size effect was taken into consideration using the following empirical formula described by (Del Viso et al., 2008):

$$f_c = \sigma_{cub}\sqrt{\frac{L}{L + L_0}}$$

Where f_c is the compressive strength of concrete, σ_{cub} is the concrete strength of the cubic concrete specimen, L is the length of the sides of the cubic specimen, and L_0 is an empirical constant which was taken to be 20mm as in Del Viso et al., 2008 since the dimensions of the specimens tested were within the range used develop the constant. Results are tabulated in the following table:

Experimental results of compression tests on rectangular concrete samples taken from specimens

	Peak Load (kN)	Area 1 (mm^2)	Area 2 (mm^2)	Avg Area (mm^2)	f'c $_{cube}$ (MPa)	avg f'c $_{cube}$ (MPa)	COV (%)	f'c $_{cylinder}$ (MPa)
5 Control	193	3911	3992	3952	48.97	56.38	14.37	49.17
	225	4113	4032	4073	55.16			
	249	3831	3831	3831	65.03			
5 GGBGG	260	3871	3921	3896	66.79	61.70	7.53	53.81
	229	4022	3921	3972	57.68			
	229	3735	3821	3778	60.64			
5 GGBCC	251	4355	3841	4098	61.33	59.41	19.42	51.81
	267	3831	3810	3821	69.86			
	180	3831	3831	3831	47.03			
5 CCBCC	276	3831	3831	3831	72.00	69.49	11.79	60.60
	227	3790	3730	3760	60.33			
	294	3881	3831	3856	76.14			
4 Control	165	3085	3448	3266	50.39	51.17	21.20	44.62
	182	3044	2802	2923	62.39			
	120	2964	2933	2949	40.73			
4 GGGG	187	4012	3750	3881	48.14	62.79	21.06	54.75
	258	3841	3931	3886	66.39			
	282	3831	3821	3826	73.83			
4 GGBGG	202	3831	3871	3851	52.56	63.23	16.18	55.14
	234	3639	3639	3639	64.17			
	274	3690	3810	3750	72.95			
4 GGBCC	291	3831	3831	3831	76.06	74.04	2.93	64.57
	285	3831	3831	3831	74.32			
	276	3898	3790	3844	71.74			
1 Control	225	3831	3831	3831	58.64	55.59	5.02	48.48
	209	4032	3831	3931	53.18			
	216	4022	3831	3926	54.95			
1 CCCC	269	3831	3659	3745	71.86	73.80	7.75	64.35
	260	3800	3710	3755	69.30			
	311	3831	3931	3881	80.23			
					TOTAL:	62.76	12.27	54.73

Appendix II: Results of FE Model of Experimental Specimens from ABAQUS

GGGG Stress Contour Plot for 26kN, 53kN, 81kN, 90kN

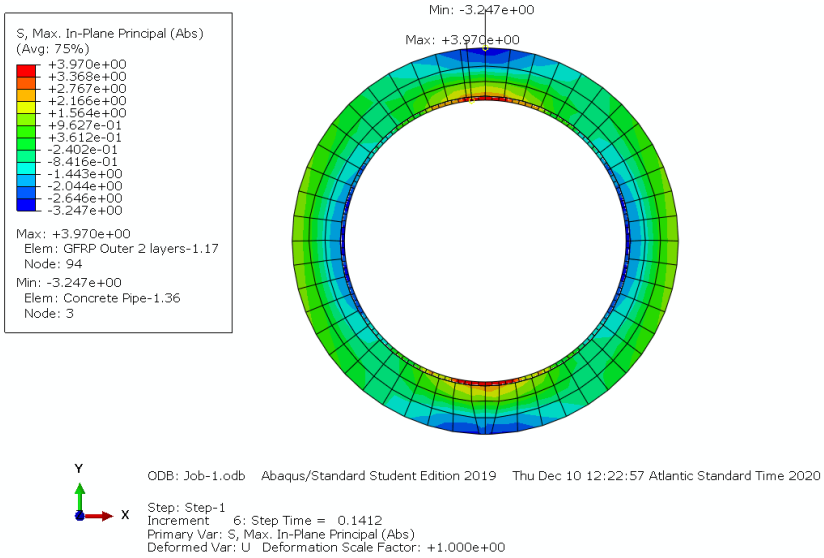

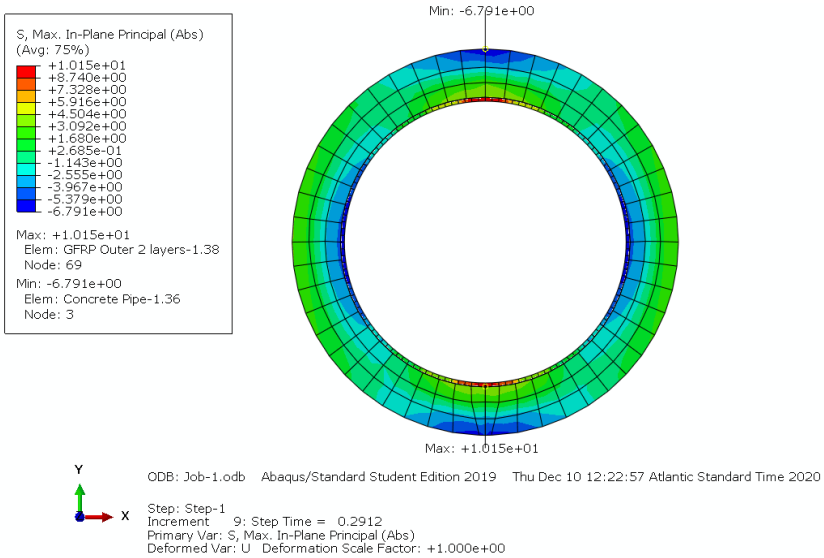

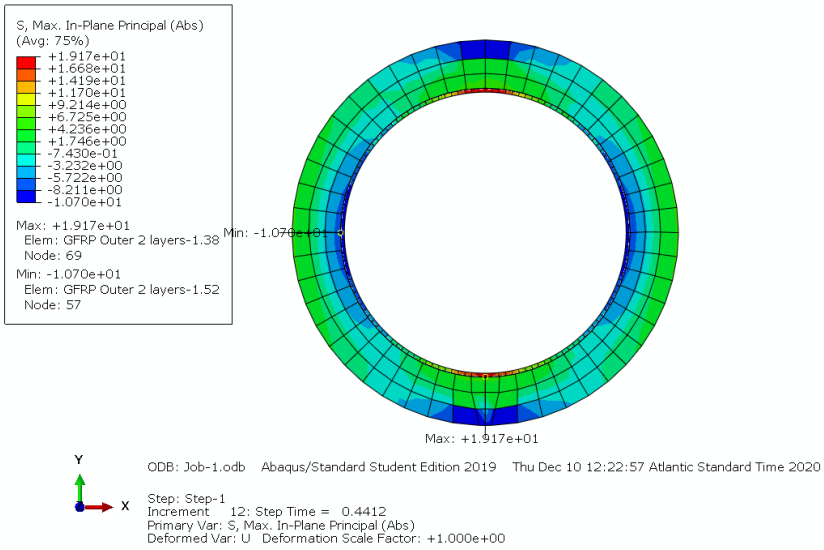
S, Max. In-Plane Principal (Abs)
(Avg: 75%)
+1.917e+01
+1.668e+01
+1.419e+01
+1.170e+01
+9.214e+00
+6.725e+00
+4.236e+00
+1.746e+00
-7.430e-01
-3.232e+00
-5.722e+00
-8.211e+00
-1.070e+01
Max: +1.917e+01
Elem: GFRP Outer 2 layers-1.38
Node: 69
Min: -1.070e+01
Elem: GFRP Outer 2 layers-1.52
Node: 57
Min: -1.070e+01
Max: +1.917e+01
Y
X
ODB: Job-1.odb Abaqus/Standard Student Edition 2019 Thu Dec 10 12:22:57 Atlantic Standard Time 2020
Step: Step-1
Increment 12: Step Time = 0.4412
Primary Var: S, Max. In-Plane Principal (Abs)
Deformed Var: U Deformation Scale Factor: +1.000e+00

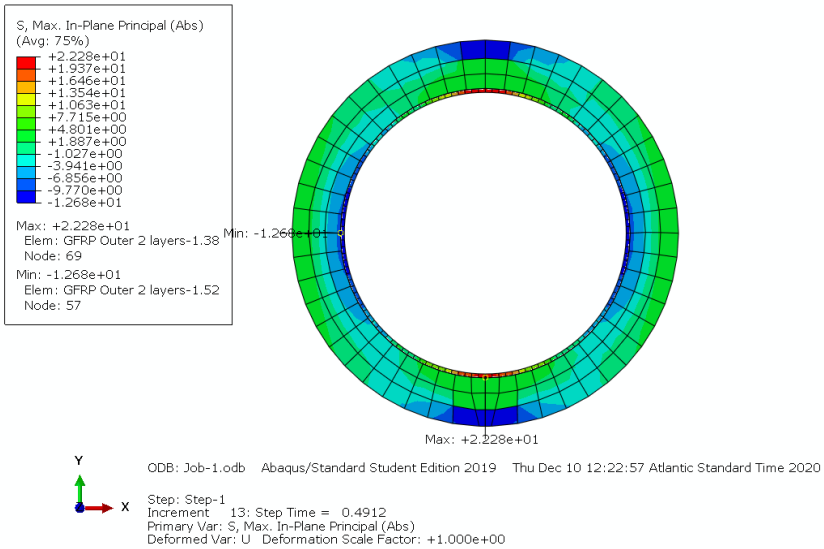
S, Max. In-Plane Principal (Abs)
(Avg: 75%)
+2.228e+01
+1.937e+01
+1.646e+01
+1.354e+01
+1.063e+01
+7.715e+00
+4.801e+00
+1.887e+00
-1.027e+00
-3.941e+00
-6.856e+00
-9.770e+00
-1.268e+01
Max: +2.228e+01
Elem: GFRP Outer 2 layers-1.38
Node: 69
Min: -1.268e+01
Elem: GFRP Outer 2 layers-1.52
Node: 57
Min: -1.268e+01
Max: +2.228e+01
Y
X
ODB: Job-1.odb Abaqus/Standard Student Edition 2019 Thu Dec 10 12:22:57 Atlantic Standard Time 2020
Step: Step-1
Increment 13: Step Time = 0.4912
Primary Var: S, Max. In-Plane Principal (Abs)
Deformed Var: U Deformation Scale Factor: +1.000e+00

GGGG Strain Contour Plot for 26kN, 53kN, 81kN, 90kN

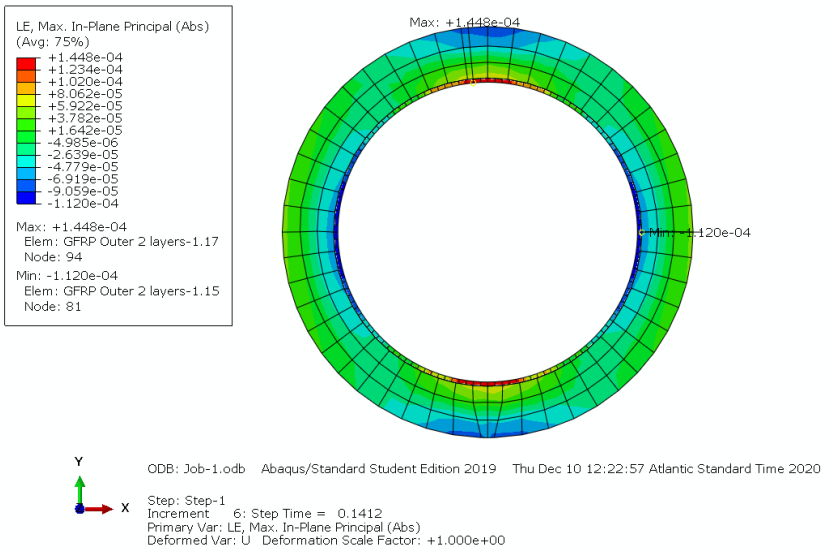

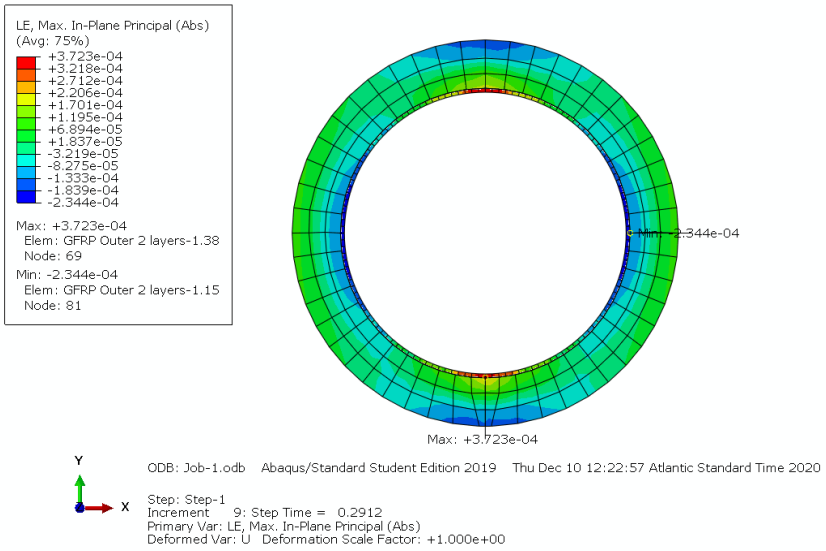

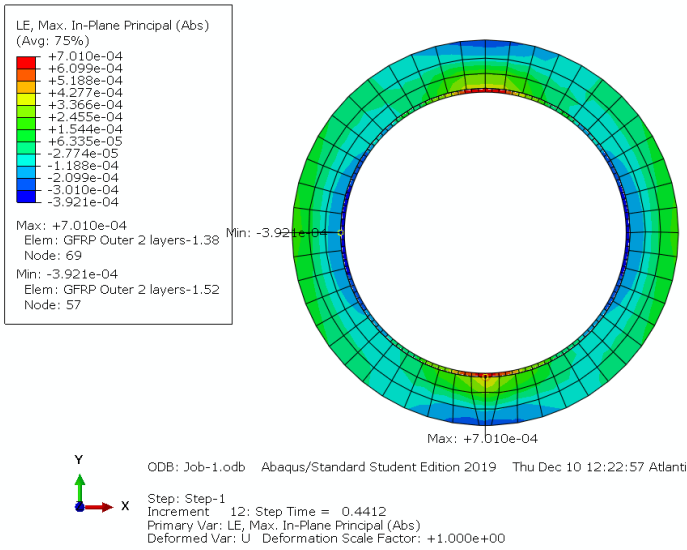
LE, Max. In-Plane Principal (Abs)
(Avg: 75%)
+7.010e-04
+6.099e-04
+5.188e-04
+4.277e-04
+3.366e-04
+2.455e-04
+1.544e-04
+6.335e-05
-2.774e-05
-1.188e-04
-2.099e-04
-3.010e-04
-3.921e-04
Max: +7.010e-04
Elem: GFRP Outer 2 layers-1.38
Node: 69
Min: -3.921e-04
Elem: GFRP Outer 2 layers-1.52
Node: 57
Min: -3.921e-04
Max: +7.010e-04
Y
X
ODB: Job-1.odb Abaqus/Standard Student Edition 2019 Thu Dec 10 12:22:57 Atlantic Standard Time 2020
Step: Step-1
Increment 12: Step Time = 0.4412
Primary Var: LE, Max. In-Plane Principal (Abs)
Deformed Var: U Deformation Scale Factor: +1.000e+00

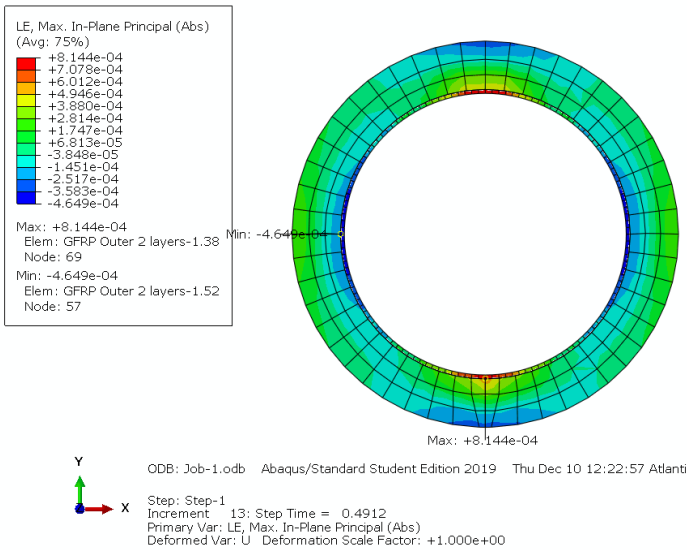
LE, Max. In-Plane Principal (Abs)
(Avg: 75%)
+8.144e-04
+7.078e-04
+6.012e-04
+4.946e-04
+3.880e-04
+2.814e-04
+1.747e-04
+6.813e-05
-3.848e-05
-1.451e-04
-2.517e-04
-3.583e-04
-4.649e-04
Max: +8.144e-04
Elem: GFRP Outer 2 layers-1.38
Node: 69
Min: -4.649e-04
Elem: GFRP Outer 2 layers-1.52
Node: 57
Min: -4.649e-04
Max: +8.144e-04
Y
X
ODB: Job-1.odb Abaqus/Standard Student Edition 2019 Thu Dec 10 12:22:57 Atlantic Standard Time 2020
Step: Step-1
Increment 13: Step Time = 0.4912
Primary Var: LE, Max. In-Plane Principal (Abs)
Deformed Var: U Deformation Scale Factor: +1.000e+00

GGGG Plastic Strain Contour Plot for 26kN, 53kN, 81kN, 90kN

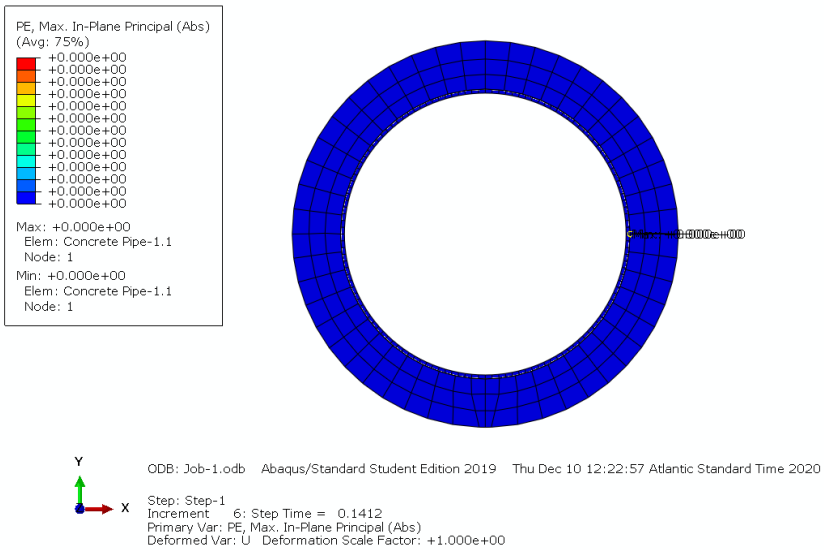

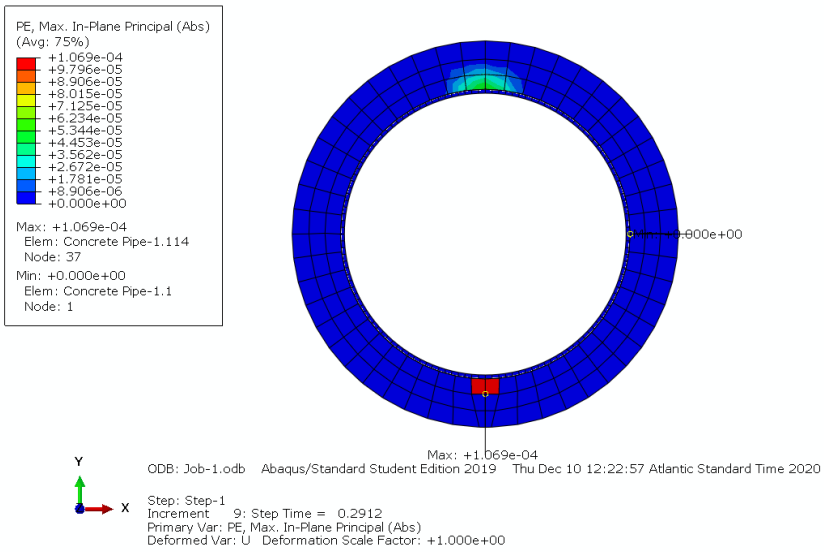

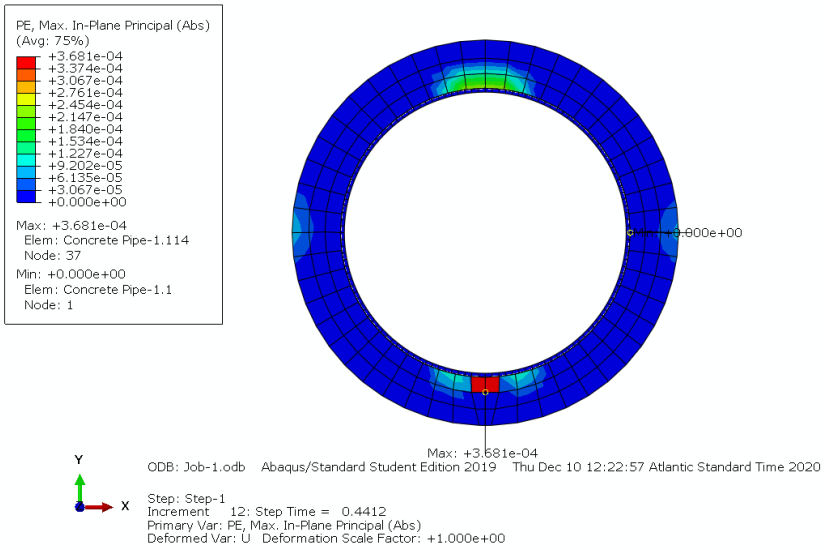
PE, Max. In-Plane Principal (Abs)
(Avg: 75%)
+3.681e-04
+3.374e-04
+3.067e-04
+2.761e-04
+2.454e-04
+2.147e-04
+1.840e-04
+1.534e-04
+1.227e-04
+9.202e-05
+6.135e-05
+3.067e-05
+0.000e+00
Max: +3.681e-04
Elem: Concrete Pipe-1.114
Node: 37
Min: +0.000e+00
Elem: Concrete Pipe-1.1
Node: 1
Max: +3.681e-04
Y
X
ODB: Job-1.odb Abaqus/Standard Student Edition 2019 Thu Dec 10 12:22:57 Atlantic Standard Time 2020
Step: Step-1
Increment 12: Step Time = 0.4412
Primary Var: PE, Max. In-Plane Principal (Abs)
Deformed Var: U Deformation Scale Factor: +1.000e+00

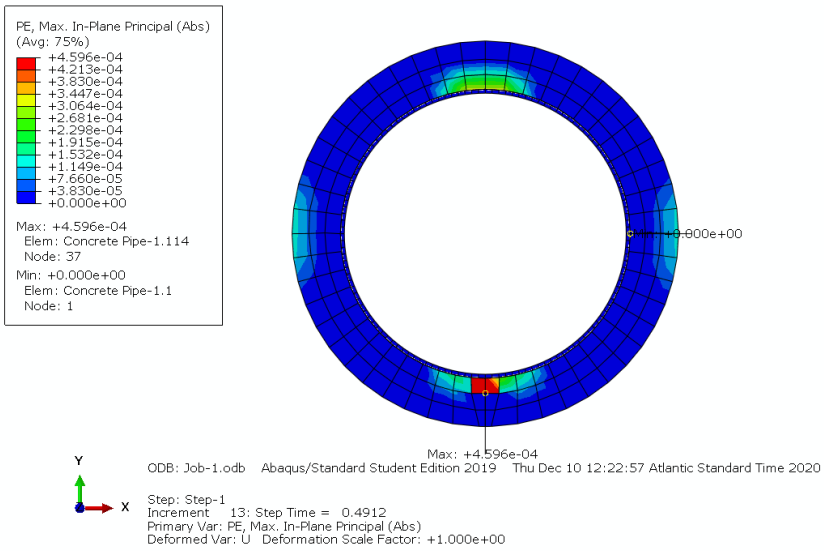
PE, Max. In-Plane Principal (Abs)
(Avg: 75%)
+4.596e-04
+4.213e-04
+3.830e-04
+3.447e-04
+3.064e-04
+2.681e-04
+2.298e-04
+1.915e-04
+1.532e-04
+1.149e-04
+7.660e-05
+3.830e-05
+0.000e+00
Max: +4.596e-04
Elem: Concrete Pipe-1.114
Node: 37
Min: +0.000e+00
Elem: Concrete Pipe-1.1
Node: 1
Max: +4.596e-04
Y
X
ODB: Job-1.odb Abaqus/Standard Student Edition 2019 Thu Dec 10 12:22:57 Atlantic Standard Time 2020
Step: Step-1
Increment 13: Step Time = 0.4912
Primary Var: PE, Max. In-Plane Principal (Abs)
Deformed Var: U Deformation Scale Factor: +1.000e+00

GGGG Load vs. Strain Plots from ABAQUS

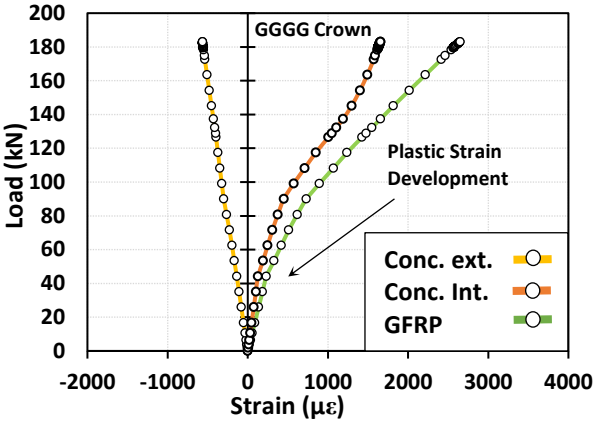

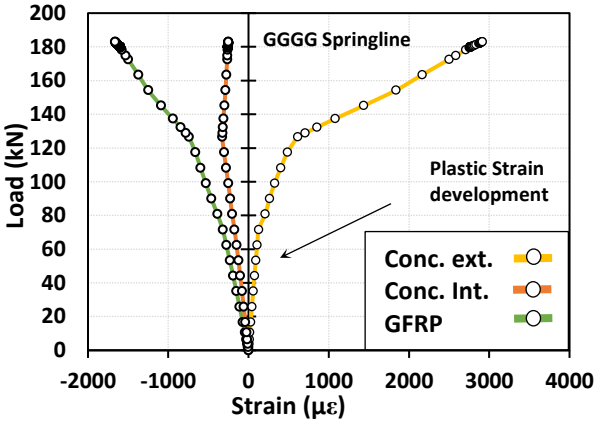

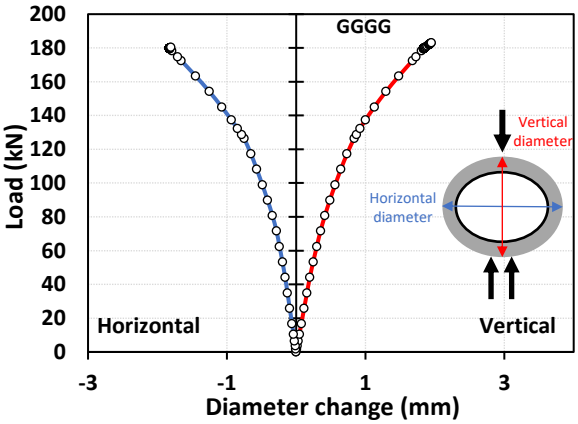

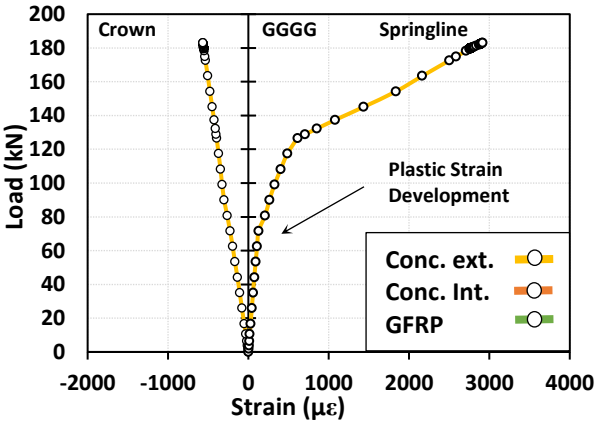

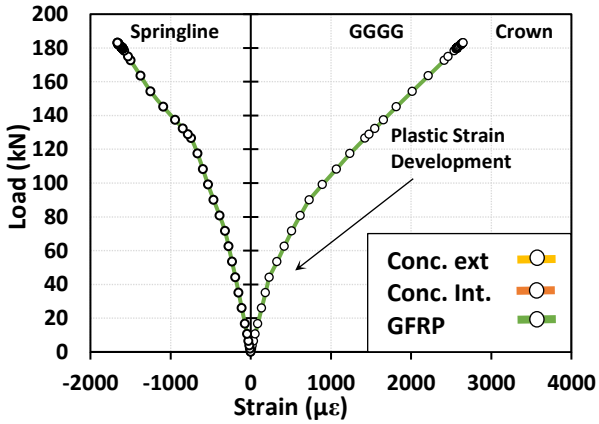

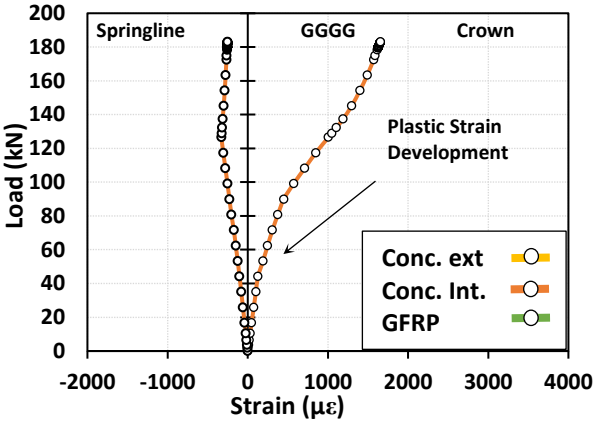
Springline
GGGG
Crown
Plastic Strain
Development
Conc. ext
Conc. Int.
GFRP
Load (kN)
Strain (με)

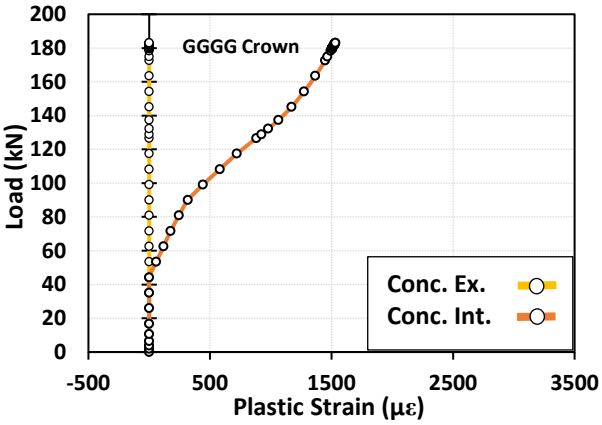
GGGG Crown
Conc. Ex.
Conc. Int.
Load (kN)
Plastic Strain (με)

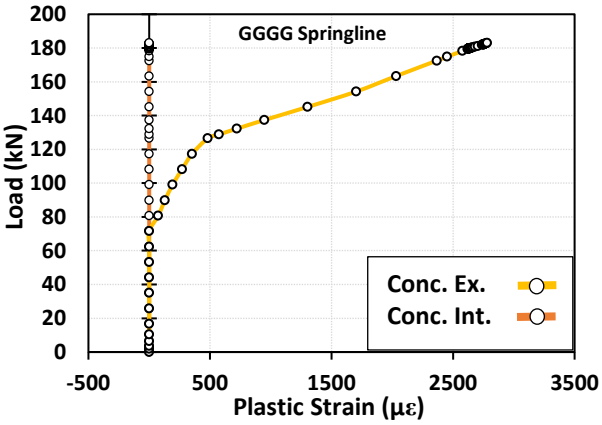
GGGG Springline
Conc. Ex.
Conc. Int.
Load (kN)
Plastic Strain (με)

CCCC Stress Contour Plot for 29kN, 71kN, 92kN, 113kN

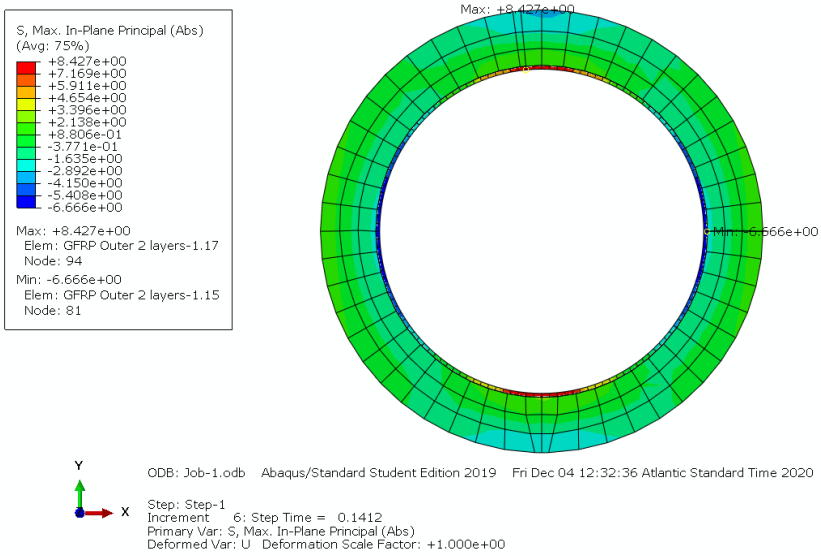

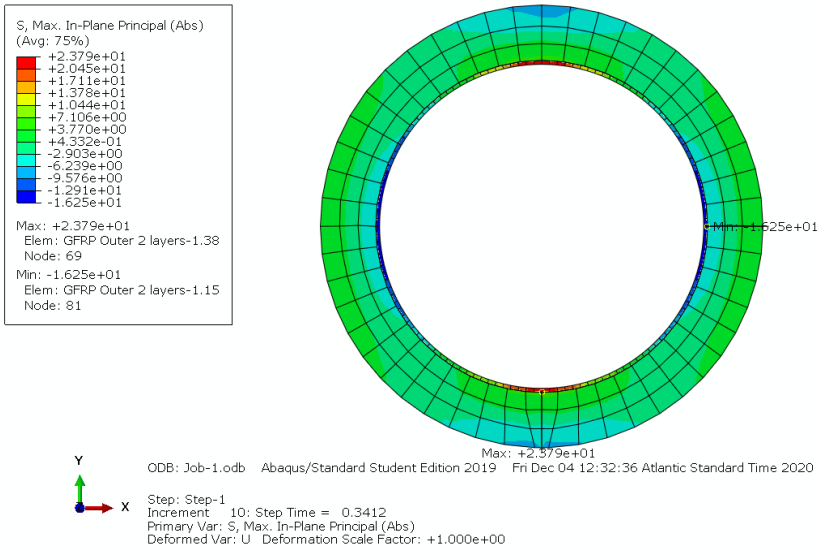

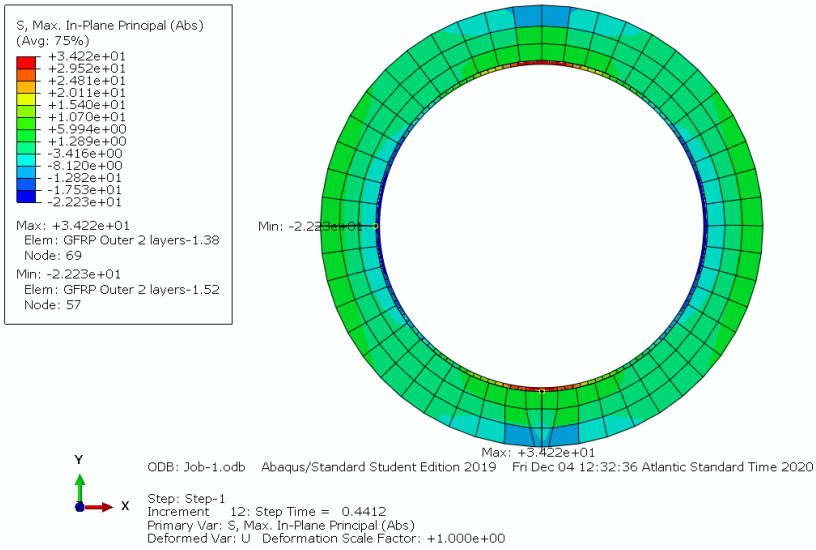
S, Max. In-Plane Principal (Abs)
(Avg: 75%)
+3.422e+01
+2.952e+01
+2.481e+01
+2.011e+01
+1.540e+01
+1.070e+01
+5.994e+00
+1.289e+00
-3.416e+00
-8.120e+00
-1.282e+01
-1.753e+01
-2.223e+01
Max: +3.422e+01
Elem: GFRP Outer 2 layers-1.38
Node: 69
Min: -2.223e+01
Elem: GFRP Outer 2 layers-1.52
Node: 57
Min: -2.223e+01
Max: +3.422e+01
Y
X
ODB: Job-1.odb Abaqus/Standard Student Edition 2019 Fri Dec 04 12:32:36 Atlantic Standard Time 2020
Step: Step-1
Increment 12: Step Time = 0.4412
Primary Var: S, Max. In-Plane Principal (Abs)
Deformed Var: U Deformation Scale Factor: +1.000e+00

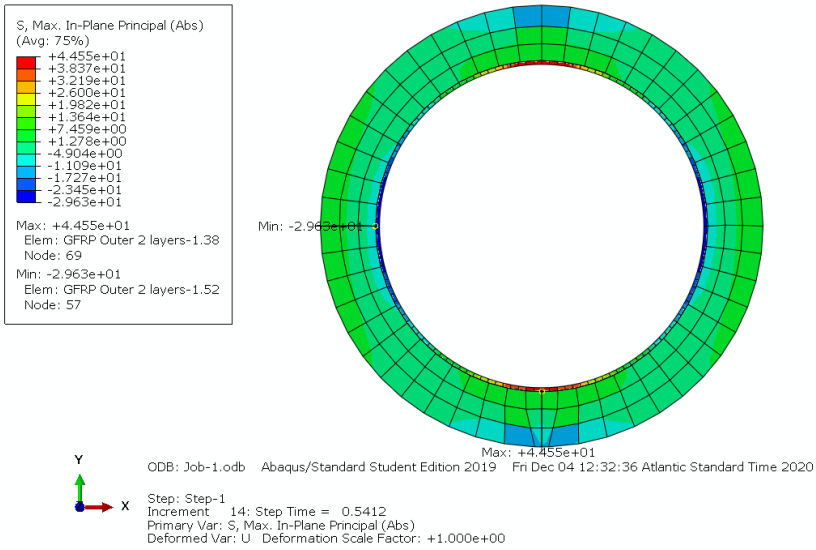
S, Max. In-Plane Principal (Abs)
(Avg: 75%)
+4.455e+01
+3.837e+01
+3.219e+01
+2.600e+01
+1.982e+01
+1.364e+01
+7.459e+00
+1.278e+00
-4.904e+00
-1.109e+01
-1.727e+01
-2.345e+01
-2.963e+01
Max: +4.455e+01
Elem: GFRP Outer 2 layers-1.38
Node: 69
Min: -2.963e+01
Elem: GFRP Outer 2 layers-1.52
Node: 57
Min: -2.963e+01
Max: +4.455e+01
Y
X
ODB: Job-1.odb Abaqus/Standard Student Edition 2019 Fri Dec 04 12:32:36 Atlantic Standard Time 2020
Step: Step-1
Increment 14: Step Time = 0.5412
Primary Var: S, Max. In-Plane Principal (Abs)
Deformed Var: U Deformation Scale Factor: +1.000e+00

CCCC Strain Contour Plot for 29kN, 71kN, 92kN, 113kN

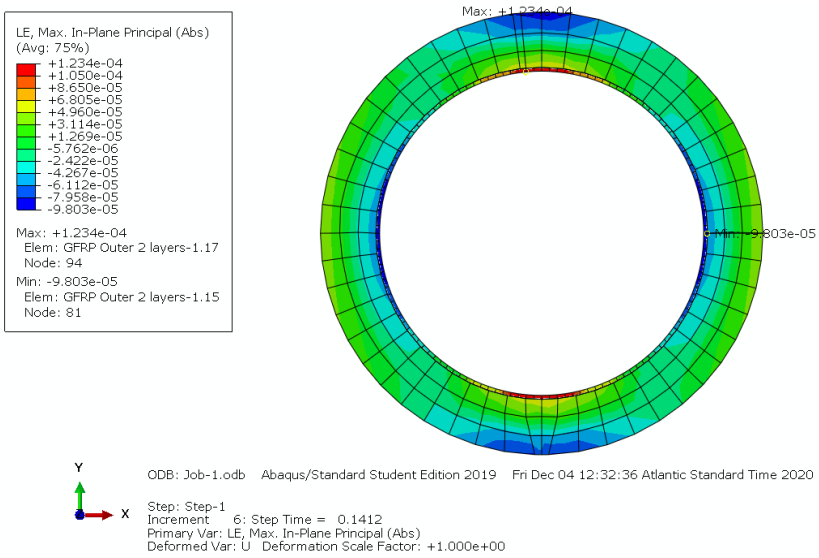

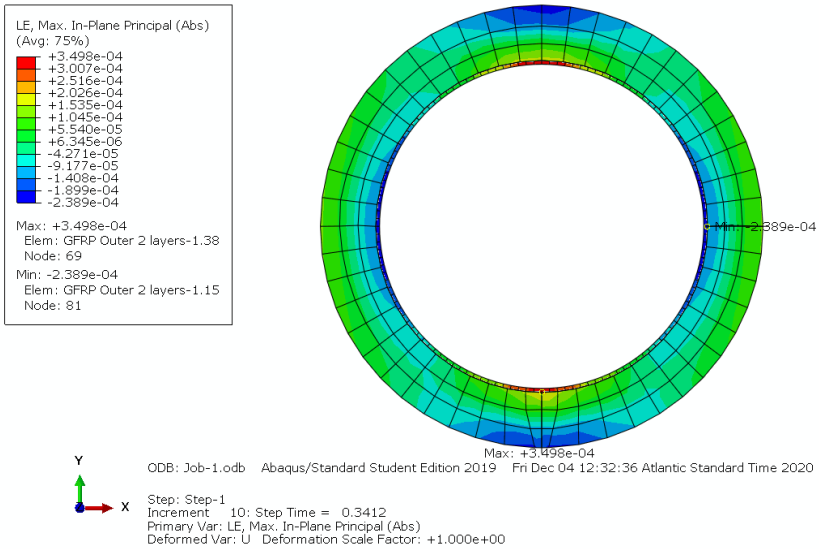

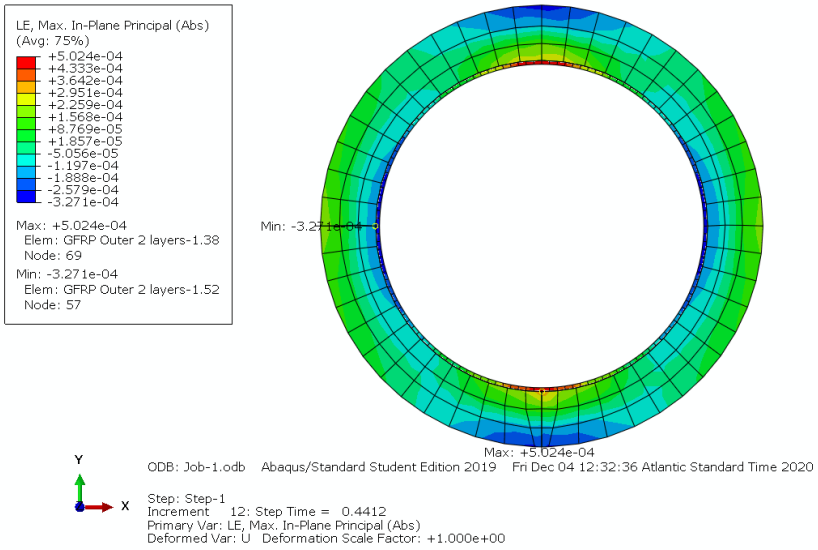
LE, Max. In-Plane Principal (Abs)
(Avg: 75%)
+5.024e-04
+4.333e-04
+3.642e-04
+2.951e-04
+2.259e-04
+1.568e-04
+8.769e-05
+1.857e-05
-5.056e-05
-1.197e-04
-1.888e-04
-2.579e-04
-3.271e-04
Max: +5.024e-04
Elem: GFRP Outer 2 layers-1.38
Node: 69
Min: -3.271e-04
Elem: GFRP Outer 2 layers-1.52
Node: 57
Min: -3.271e-04
Max: +5.024e-04
Y
X
ODB: Job-1.odb Abaqus/Standard Student Edition 2019 Fri Dec 04 12:32:36 Atlantic Standard Time 2020
Step: Step-1
Increment 12: Step Time = 0.4412
Primary Var: LE, Max. In-Plane Principal (Abs)
Deformed Var: U Deformation Scale Factor: +1.000e+00

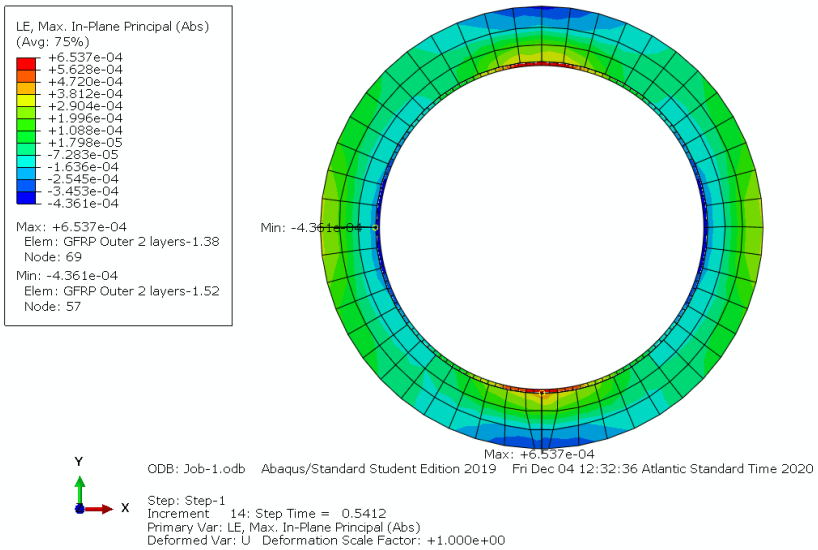
LE, Max. In-Plane Principal (Abs)
(Avg: 75%)
+6.537e-04
+5.628e-04
+4.720e-04
+3.812e-04
+2.904e-04
+1.996e-04
+1.088e-04
+1.798e-05
-7.283e-05
-1.636e-04
-2.545e-04
-3.453e-04
-4.361e-04
Max: +6.537e-04
Elem: GFRP Outer 2 layers-1.38
Node: 69
Min: -4.361e-04
Elem: GFRP Outer 2 layers-1.52
Node: 57
Min: -4.361e-04
Max: +6.537e-04
Y
X
ODB: Job-1.odb Abaqus/Standard Student Edition 2019 Fri Dec 04 12:32:36 Atlantic Standard Time 2020
Step: Step-1
Increment 14: Step Time = 0.5412
Primary Var: LE, Max. In-Plane Principal (Abs)
Deformed Var: U Deformation Scale Factor: +1.000e+00

CCCC Plastic Strain Contour Plot for 29kN, 71kN, 92kN, 113kN

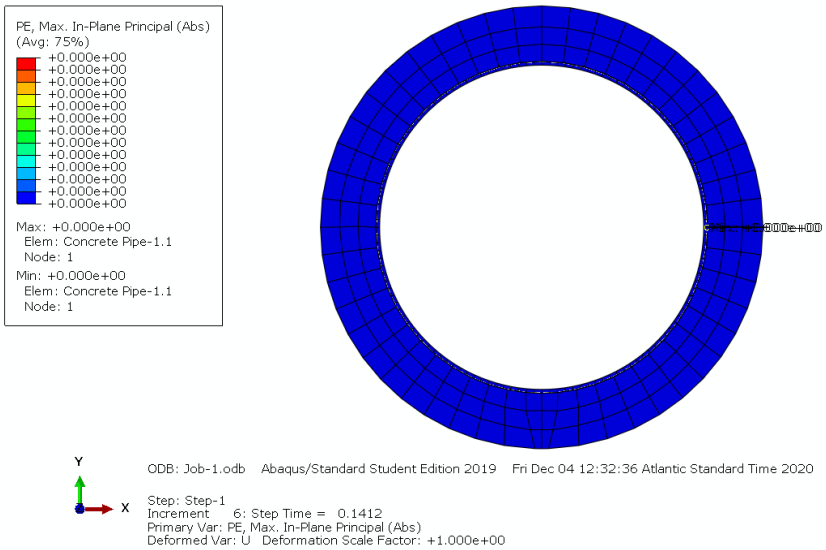

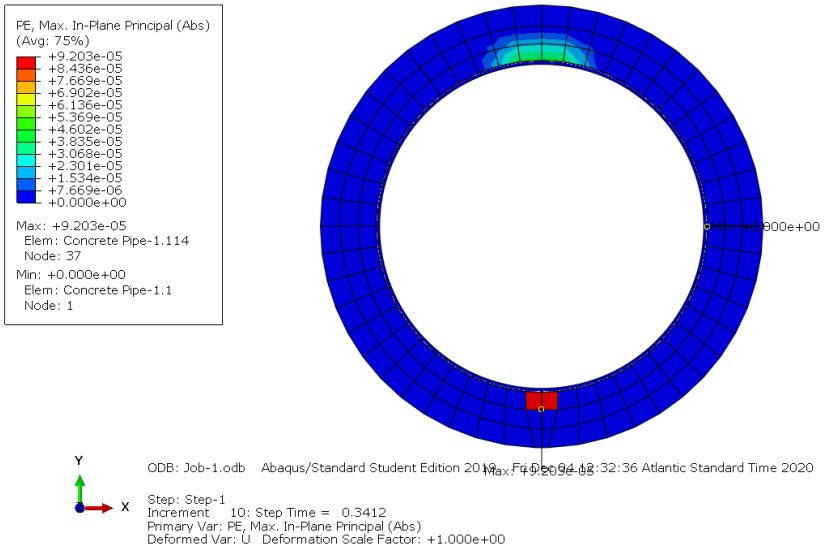

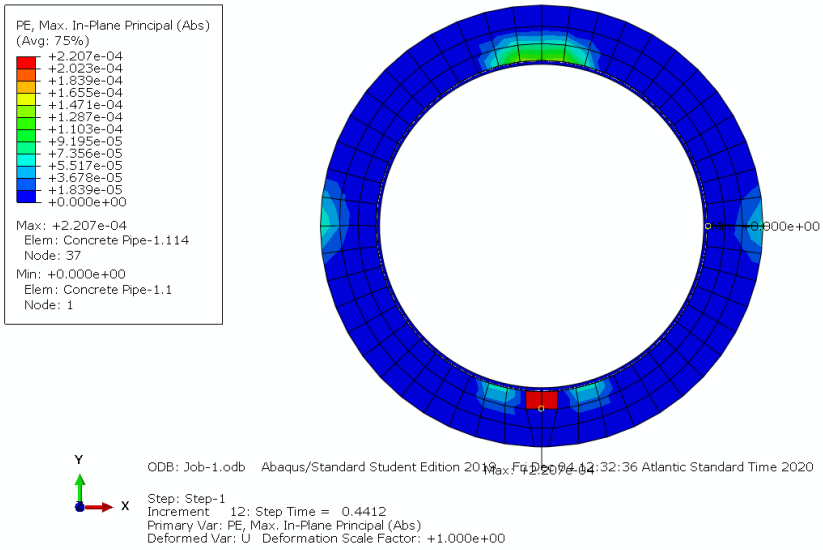
PE, Max. In-Plane Principal (Abs)
(Avg: 75%)
+2.207e-04
+2.023e-04
+1.839e-04
+1.655e-04
+1.471e-04
+1.287e-04
+1.103e-04
+9.195e-05
+7.356e-05
+5.517e-05
+3.678e-05
+1.839e-05
+0.000e+00
Max: +2.207e-04
Elem: Concrete Pipe-1.114
Node: 37
Min: +0.000e+00
Elem: Concrete Pipe-1.1
Node: 1
Y
X
ODB: Job-1.odb Abaqus/Standard Student Edition 2019 Fri Dec 04 12:32:36 Atlantic Standard Time 2020
Step: Step-1
Increment 12: Step Time = 0.4412
Primary Var: PE, Max. In-Plane Principal (Abs)
Deformed Var: U Deformation Scale Factor: +1.000e+00

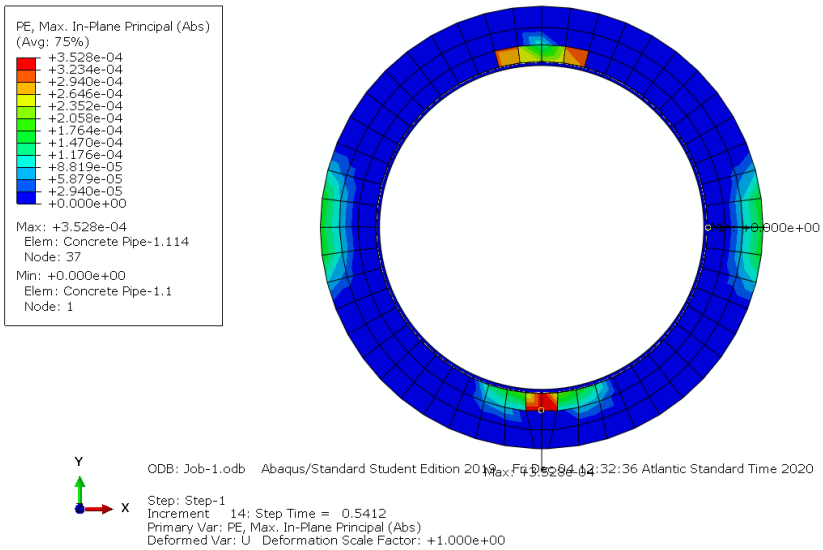
PE, Max. In-Plane Principal (Abs)
(Avg: 75%)
+3.528e-04
+3.234e-04
+2.940e-04
+2.646e-04
+2.352e-04
+2.058e-04
+1.764e-04
+1.470e-04
+1.176e-04
+8.819e-05
+5.879e-05
+2.940e-05
+0.000e+00
Max: +3.528e-04
Elem: Concrete Pipe-1.114
Node: 37
Min: +0.000e+00
Elem: Concrete Pipe-1.1
Node: 1
Y
X
ODB: Job-1.odb Abaqus/Standard Student Edition 2019 Fri Dec 04 12:32:36 Atlantic Standard Time 2020
Step: Step-1
Increment 14: Step Time = 0.5412
Primary Var: PE, Max. In-Plane Principal (Abs)
Deformed Var: U Deformation Scale Factor: +1.000e+00

CCCC Load vs. Strain Plots from ABAQUS

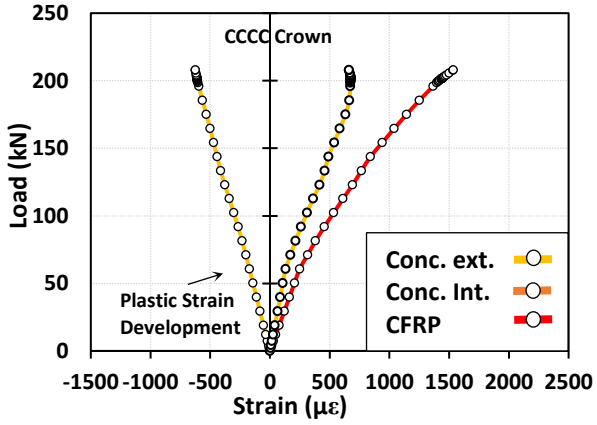

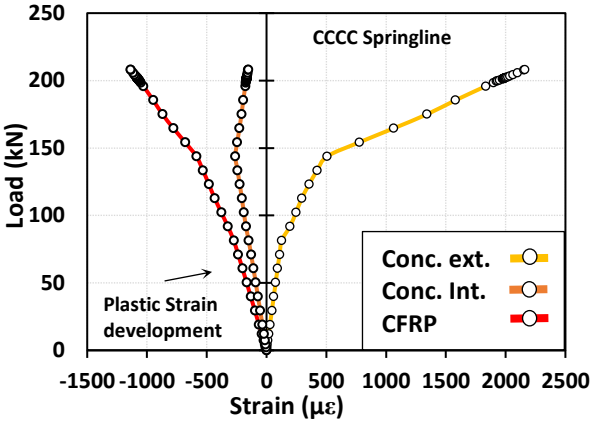

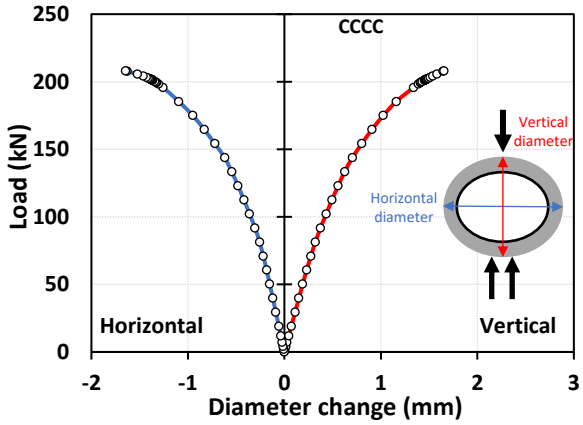

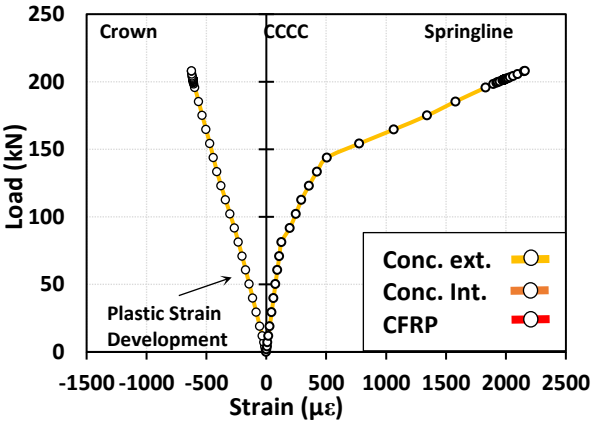

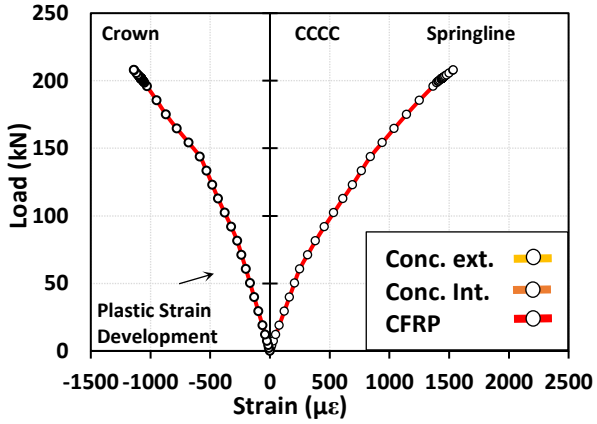

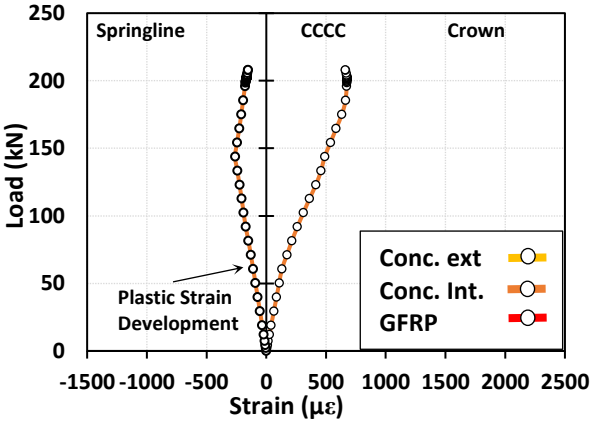

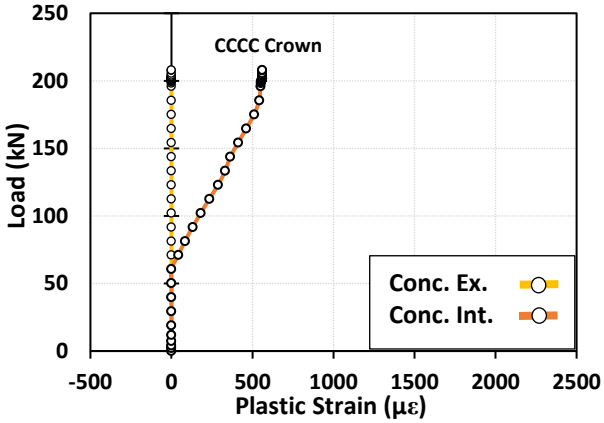
CCCC Crown
Load (kN)
250
200
150
100
50
0
-500
0
500
1000
1500
2000
2500
Plastic Strain (με)
Conc. Ex.
Conc. Int.

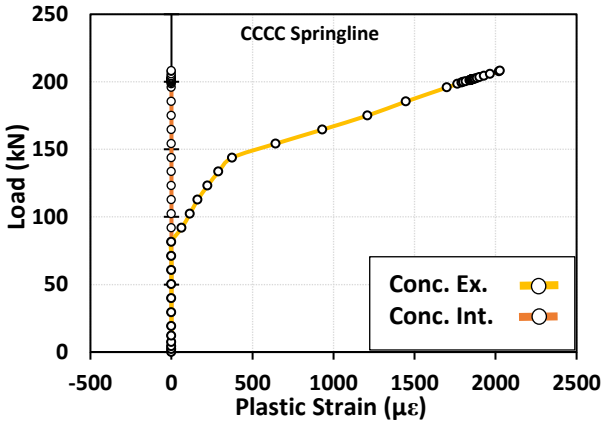
CCCC Springline
Load (kN)
250
200
150
100
50
0
-500
0
500
1000
1500
2000
2500
Plastic Strain (με)
Conc. Ex.
Conc. Int.

CCBCC Stress Contour Plot for 28kN, 58kN, 88kN, 128kN

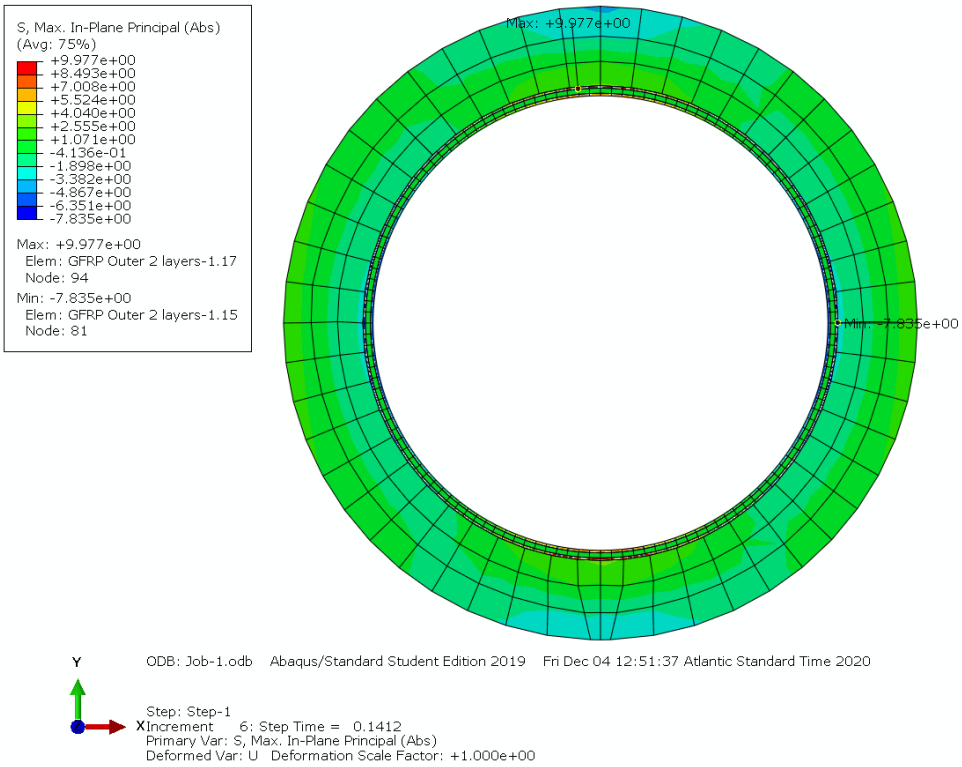

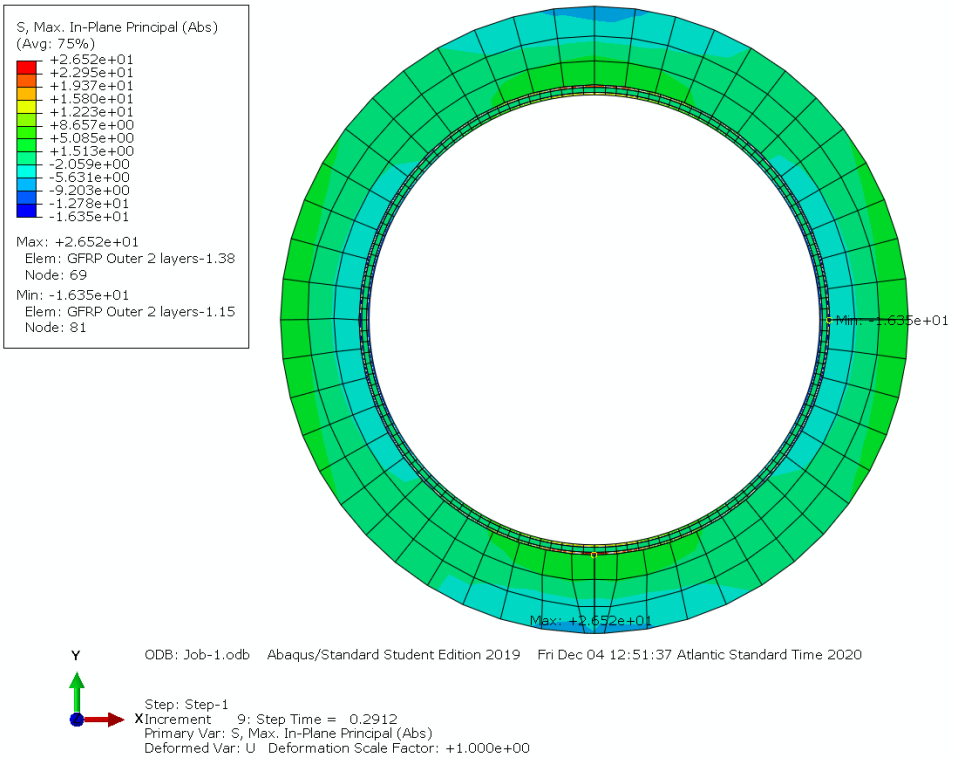

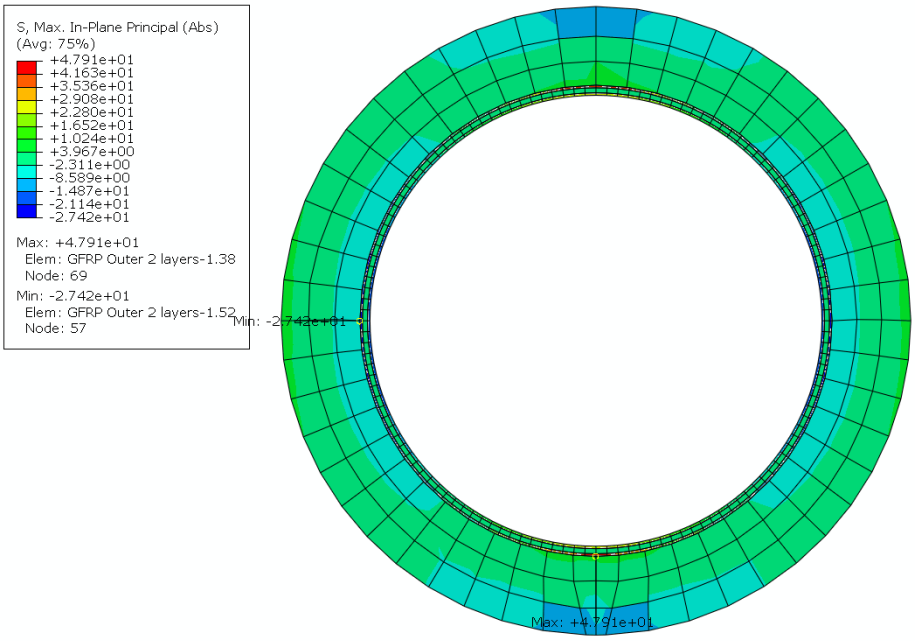
S, Max. In-Plane Principal (Abs)
(Avg: 75%)
+4.791e+01
+4.163e+01
+3.536e+01
+2.908e+01
+2.280e+01
+1.652e+01
+1.024e+01
+3.967e+00
-2.311e+00
-8.589e+00
-1.487e+01
-2.114e+01
-2.742e+01
Max: +4.791e+01
Elem: GFRP Outer 2 layers-1.38
Node: 69
Min: -2.742e+01
Elem: GFRP Outer 2 layers-1.52
Node: 57
Min: -2.742e+01
Max: +4.791e+01
Y
X
ODB: Job-1.odb Abaqus/Standard Student Edition 2019 Fri Dec 04 12:51:37 Atlantic Standard Time 2020
Step: Step-1
Increment 12: Step Time = 0.4412
Primary Var: S, Max. In-Plane Principal (Abs)
Deformed Var: U Deformation Scale Factor: +1.000e+00

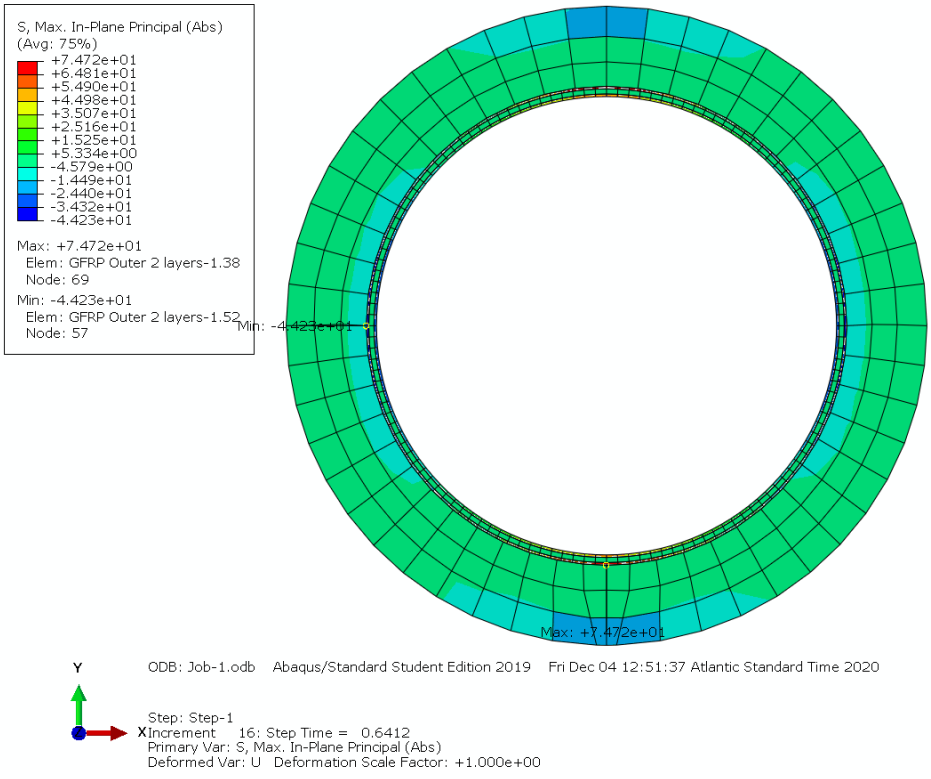
S, Max. In-Plane Principal (Abs)
(Avg: 75%)
+7.472e+01
+6.481e+01
+5.490e+01
+4.498e+01
+3.507e+01
+2.516e+01
+1.525e+01
+5.334e+00
-4.579e+00
-1.449e+01
-2.440e+01
-3.432e+01
-4.423e+01
Max: +7.472e+01
Elem: GFRP Outer 2 layers-1.38
Node: 69
Min: -4.423e+01
Elem: GFRP Outer 2 layers-1.52
Node: 57
Min: -4.423e+01
Max: +7.472e+01
Y
X
ODB: Job-1.odb Abaqus/Standard Student Edition 2019 Fri Dec 04 12:51:37 Atlantic Standard Time 2020
Step: Step-1
Increment 16: Step Time = 0.6412
Primary Var: S, Max. In-Plane Principal (Abs)
Deformed Var: U Deformation Scale Factor: +1.000e+00

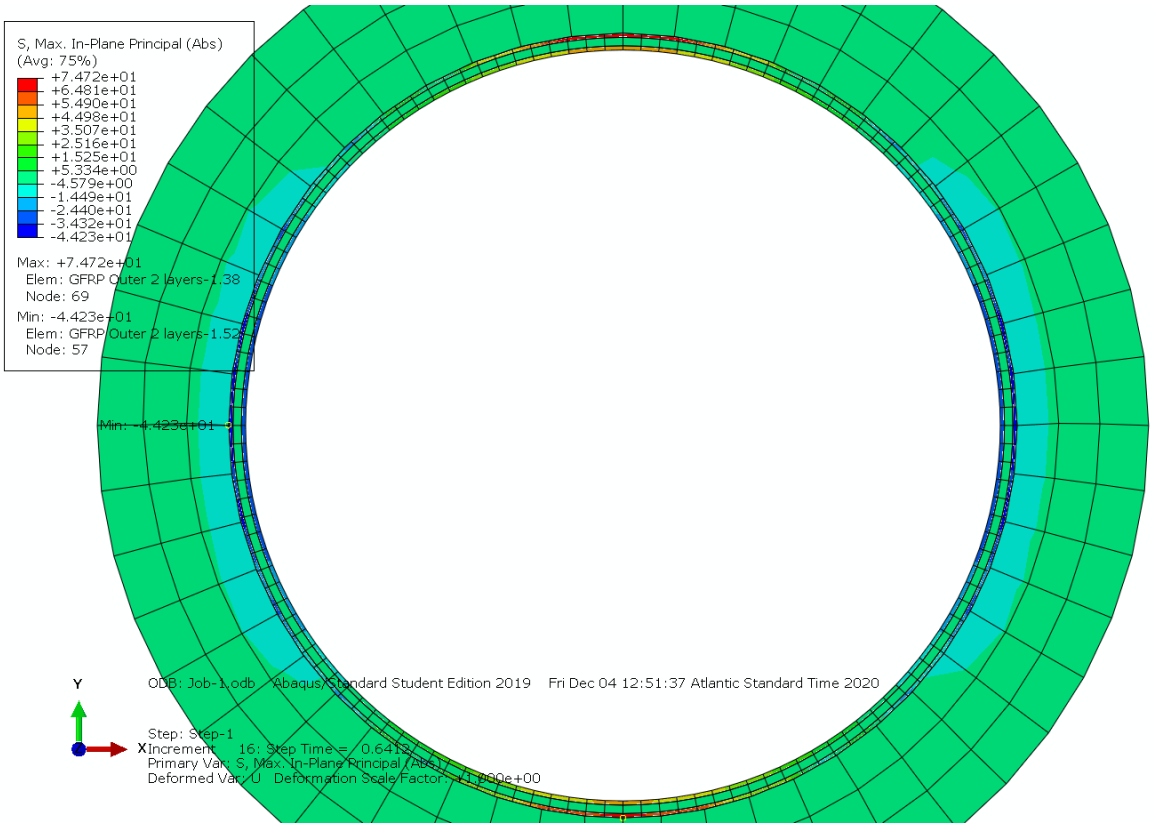
S, Max. In-Plane Principal (Abs)
(Avg: 75%)
+7.472e+01
+6.481e+01
+5.490e+01
+4.498e+01
+3.507e+01
+2.516e+01
+1.525e+01
+5.334e+00
-4.579e+00
-1.449e+01
-2.440e+01
-3.432e+01
-4.423e+01
Max: +7.472e+01
Elem: GFRP Outer 2 layers-1.38
Node: 69
Min: -4.423e+01
Elem: GFRP Outer 2 layers-1.52
Node: 57
Min: -4.423e+01
Y
X
ODB: Job-1.odb Abaqus/Standard Student Edition 2019 Fri Dec 04 12:51:37 Atlantic Standard Time 2020
Step: Step-1
Increment 16: Step Time = 0.6412
Primary Var: S, Max. In-Plane Principal (Abs)
Deformed Var: U Deformation Scale Factor: +1.000e+00

CCBCC Strain Contour Plot for 28kN, 58kN, 88kN, 128kN

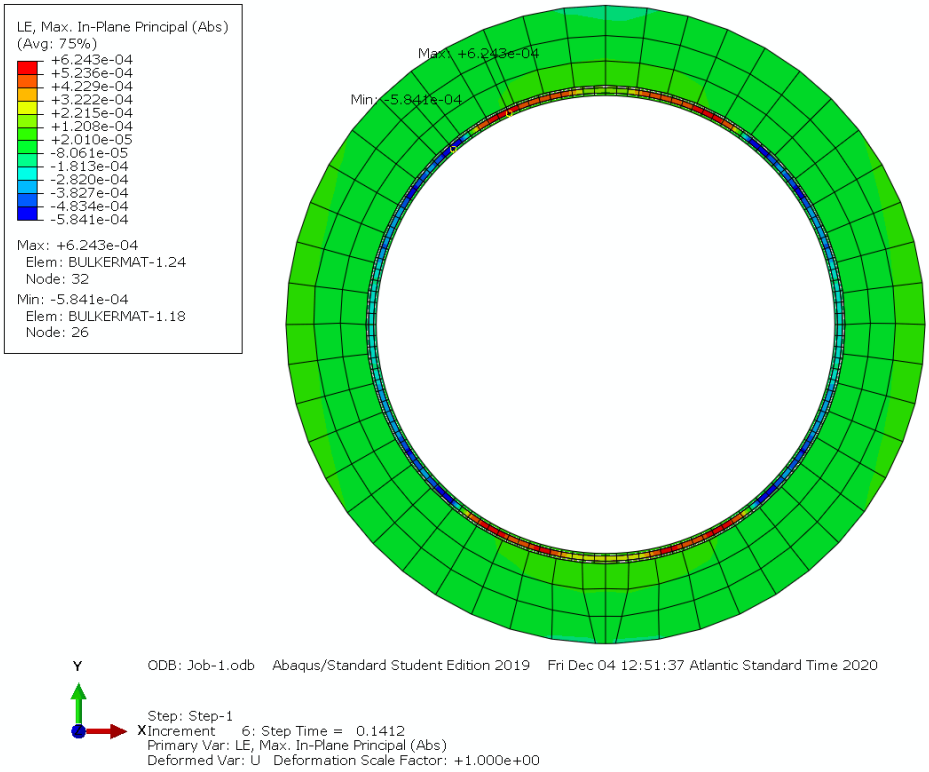

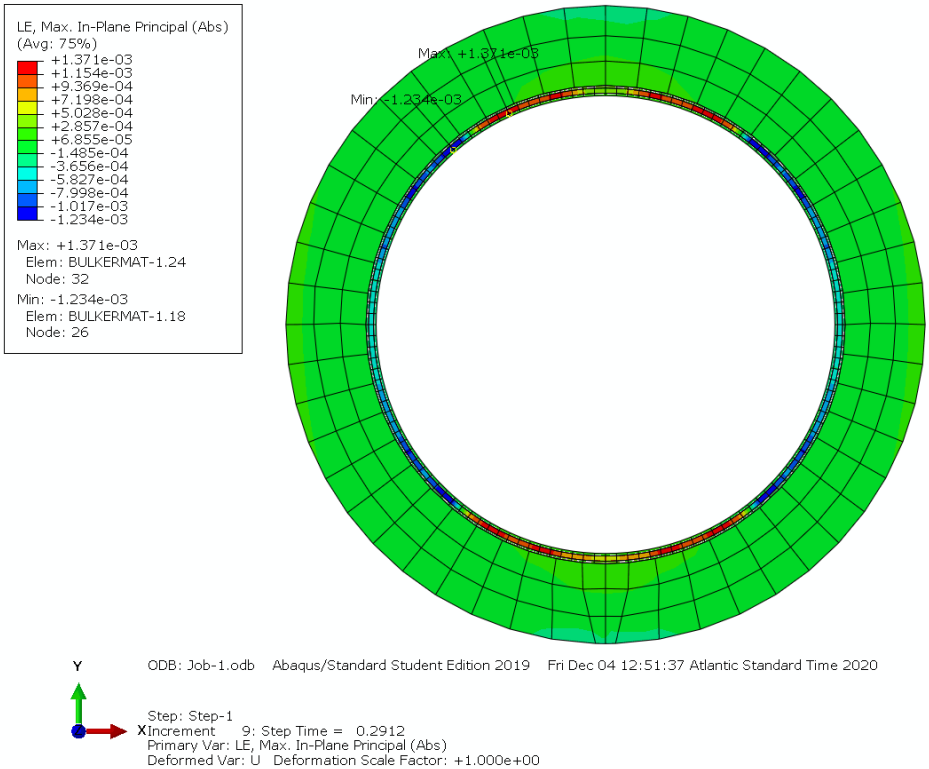

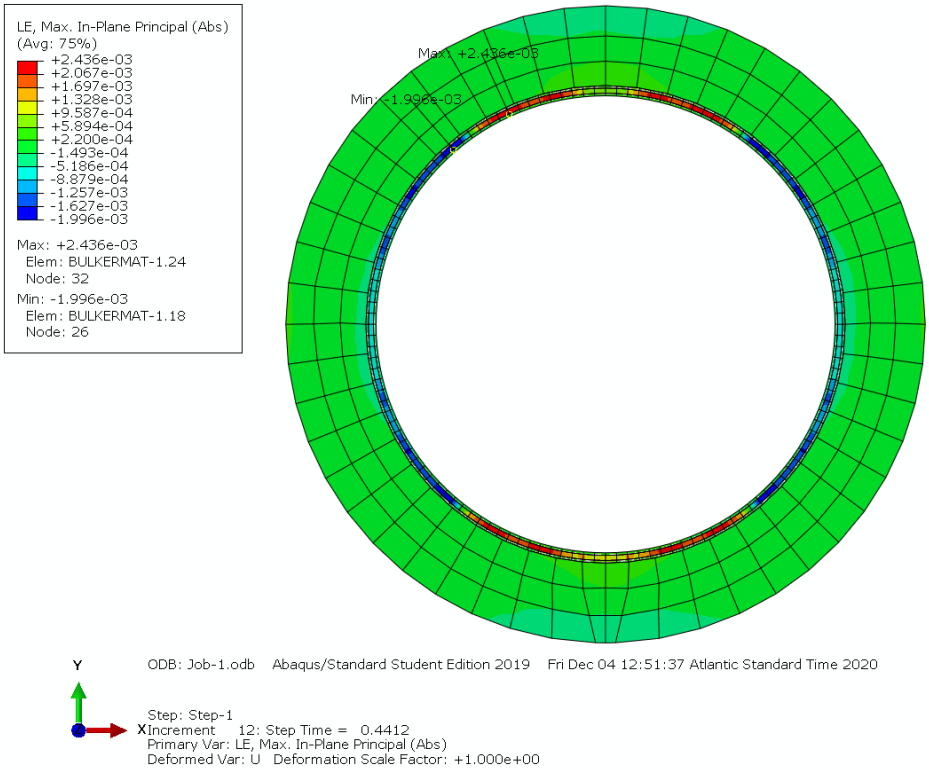
LE, Max. In-Plane Principal (Abs)
(Avg: 75%)
+2.436e-03
+2.067e-03
+1.697e-03
+1.328e-03
+9.587e-04
+5.894e-04
+2.200e-04
-1.493e-04
-5.186e-04
-8.879e-04
-1.257e-03
-1.627e-03
-1.996e-03
Max: +2.436e-03
Elem: BULKERMAT-1.24
Node: 32
Min: -1.996e-03
Elem: BULKERMAT-1.18
Node: 26
Max: +2.436e-03
Min: -1.996e-03
Y
X
ODB: Job-1.odb Abaqus/Standard Student Edition 2019 Fri Dec 04 12:51:37 Atlantic Standard Time 2020
Step: Step-1
Increment 12: Step Time = 0.4412
Primary Var: LE, Max. In-Plane Principal (Abs)
Deformed Var: U Deformation Scale Factor: +1.000e+00

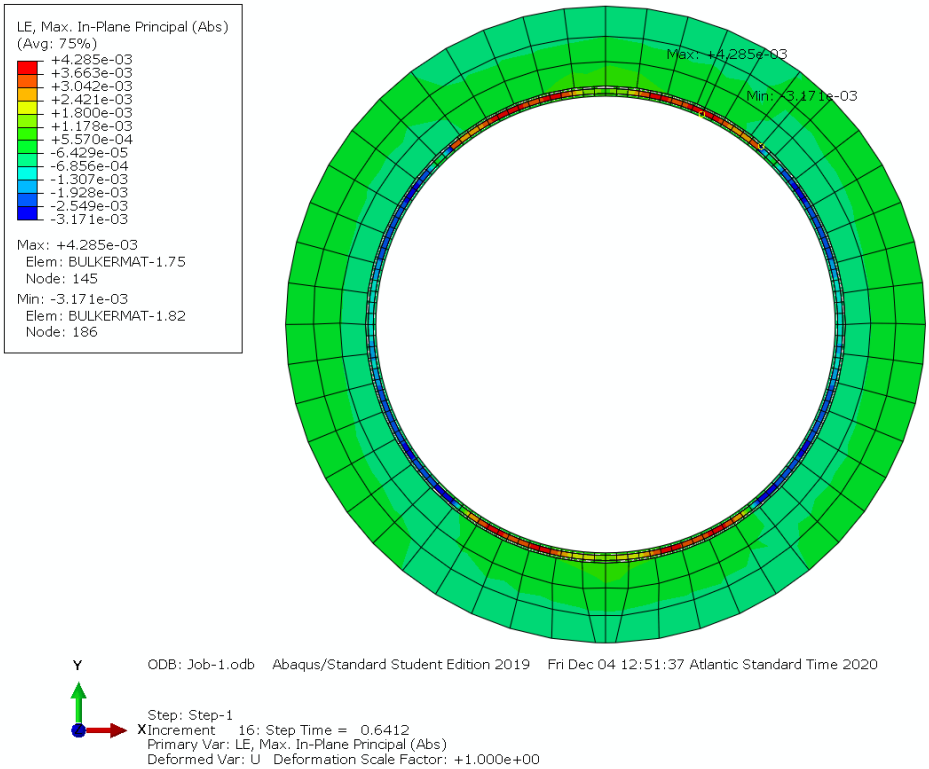
LE, Max. In-Plane Principal (Abs)
(Avg: 75%)
+4.285e-03
+3.663e-03
+3.042e-03
+2.421e-03
+1.800e-03
+1.178e-03
+5.570e-04
-6.429e-05
-6.856e-04
-1.307e-03
-1.928e-03
-2.549e-03
-3.171e-03
Max: +4.285e-03
Elem: BULKERMAT-1.75
Node: 145
Min: -3.171e-03
Elem: BULKERMAT-1.82
Node: 186
Max: +4.285e-03
Min: -3.171e-03
Y
X
ODB: Job-1.odb Abaqus/Standard Student Edition 2019 Fri Dec 04 12:51:37 Atlantic Standard Time 2020
Step: Step-1
Increment 16: Step Time = 0.6412
Primary Var: LE, Max. In-Plane Principal (Abs)
Deformed Var: U Deformation Scale Factor: +1.000e+00

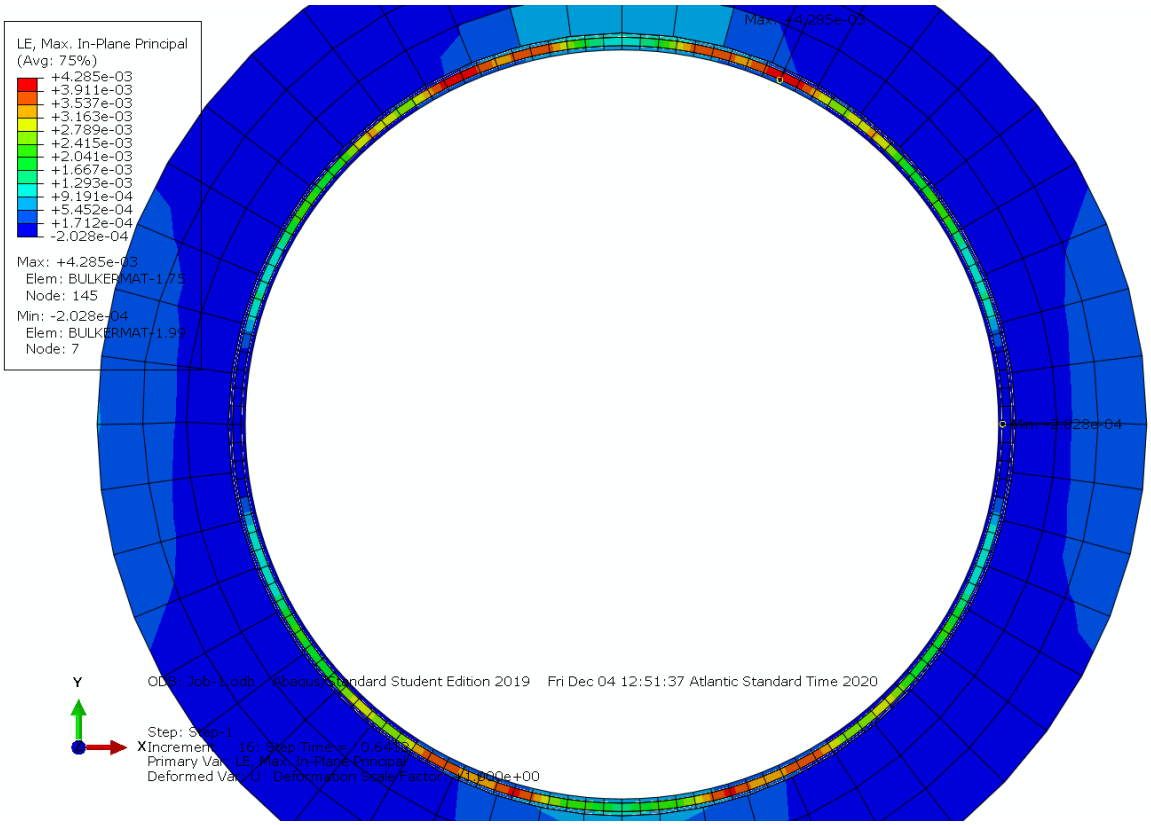
LE, Max. In-Plane Principal
(Avg: 75%)
+4.285e-03
+3.911e-03
+3.537e-03
+3.163e-03
+2.789e-03
+2.415e-03
+2.041e-03
+1.667e-03
+1.293e-03
+9.191e-04
+5.452e-04
+1.712e-04
-2.028e-04
Max: +4.285e-03
Elem: BULKERMAT-1.75
Node: 145
Min: -2.028e-04
Elem: BULKERMAT-1.99
Node: 7
Max: +4.285e-03
Min: -2.028e-04
Y
X
ODB: Job-1.odb Abaqus/Standard Student Edition 2019 Fri Dec 04 12:51:37 Atlantic Standard Time 2020
Step: Step-1
Increment 16: Step Time = 0.6480
Primary Var: LE, Max. In-Plane Principal
Deformed Var: U Deformation Scale Factor: +1.000e+00

CCBCC Strain Contour Plot for 28kN, 58kN, 88kN, 128kN

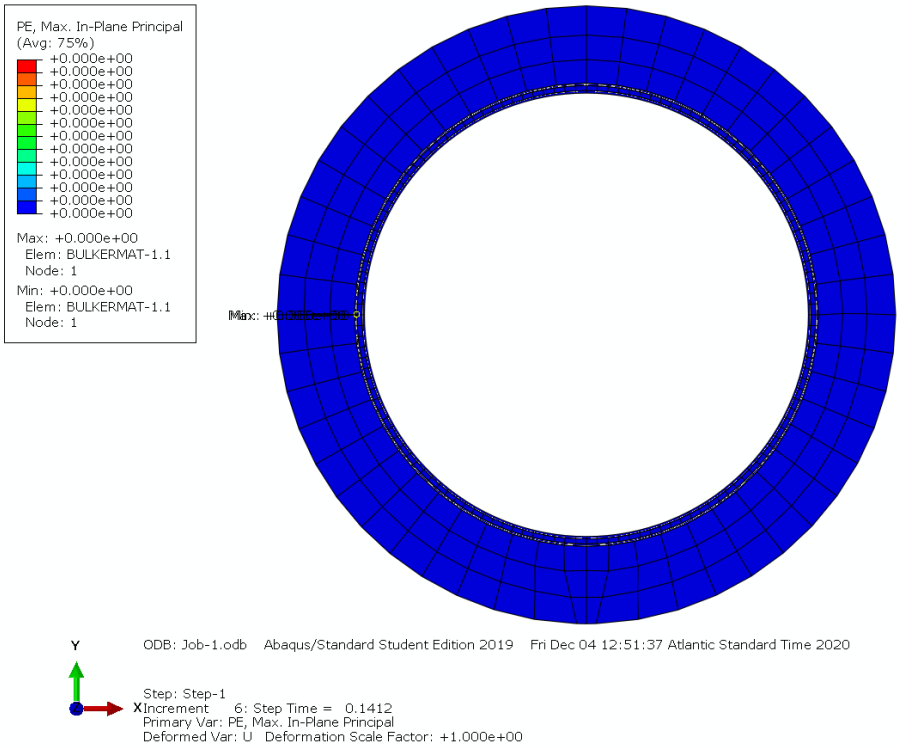

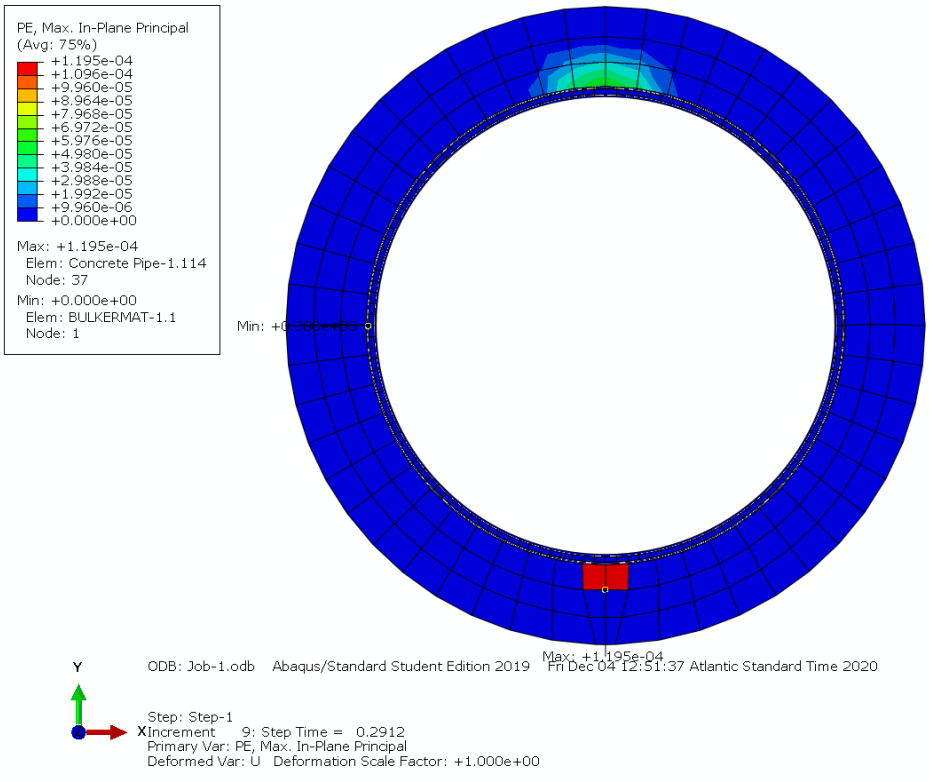

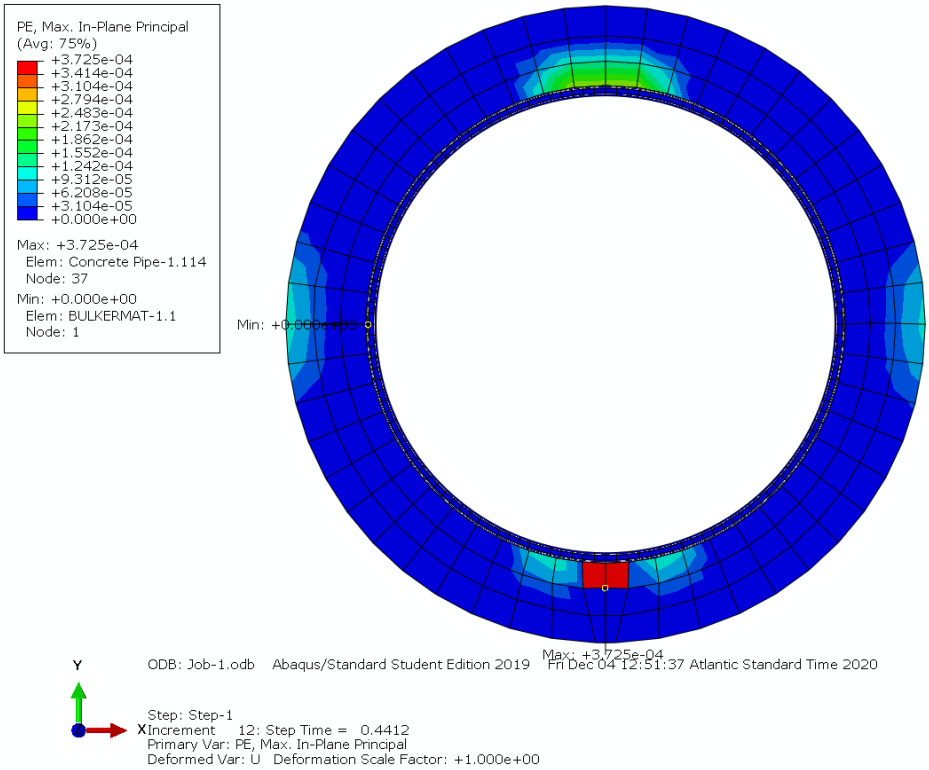
PE, Max. In-Plane Principal
(Avg: 75%)
+3.725e-04
+3.414e-04
+3.104e-04
+2.794e-04
+2.483e-04
+2.173e-04
+1.862e-04
+1.552e-04
+1.242e-04
+9.312e-05
+6.208e-05
+3.104e-05
+0.000e+00
Max: +3.725e-04
Elem: Concrete Pipe-1.114
Node: 37
Min: +0.000e+00
Elem: BULKERMAT-1.1
Node: 1
Min: +0.000e+00
Max: +3.725e-04
Y
X
ODB: Job-1.odb Abaqus/Standard Student Edition 2019 Fri Dec 04 12:51:37 Atlantic Standard Time 2020
Step: Step-1
Increment 12: Step Time = 0.4412
Primary Var: PE, Max. In-Plane Principal
Deformed Var: U Deformation Scale Factor: +1.000e+00

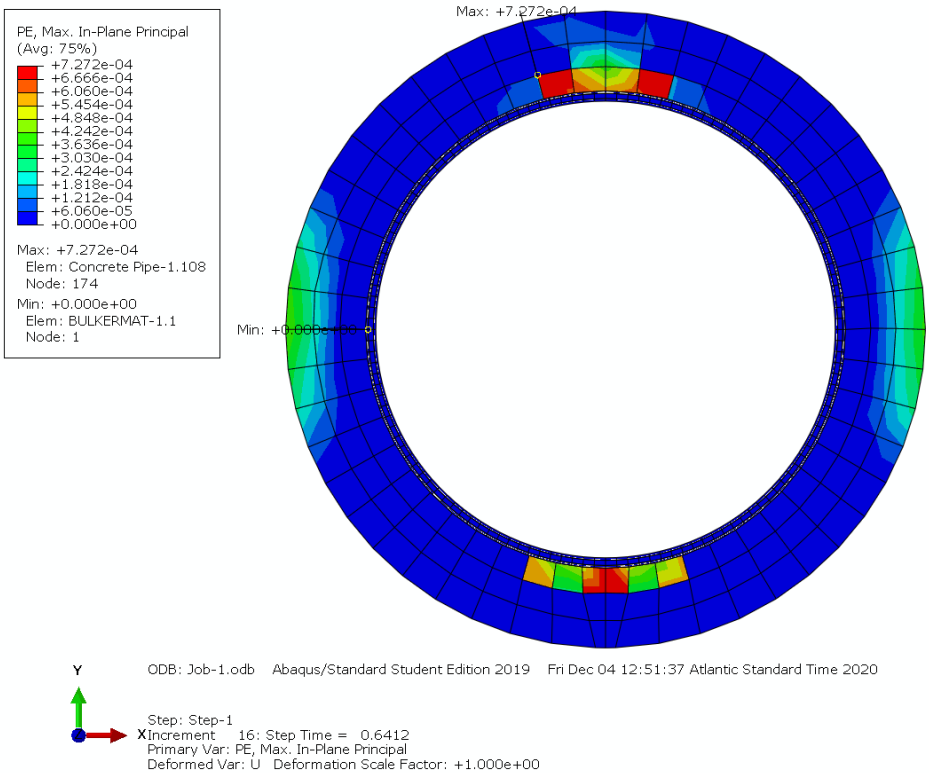
PE, Max. In-Plane Principal
(Avg: 75%)
+7.272e-04
+6.666e-04
+6.060e-04
+5.454e-04
+4.848e-04
+4.242e-04
+3.636e-04
+3.030e-04
+2.424e-04
+1.818e-04
+1.212e-04
+6.060e-05
+0.000e+00
Max: +7.272e-04
Elem: Concrete Pipe-1.108
Node: 174
Min: +0.000e+00
Elem: BULKERMAT-1.1
Node: 1
Max: +7.272e-04
Min: +0.000e+00
Y
X
ODB: Job-1.odb Abaqus/Standard Student Edition 2019 Fri Dec 04 12:51:37 Atlantic Standard Time 2020
Step: Step-1
Increment 16: Step Time = 0.6412
Primary Var: PE, Max. In-Plane Principal
Deformed Var: U Deformation Scale Factor: +1.000e+00

CCBCC Load vs. Strain Plots from ABAQUS

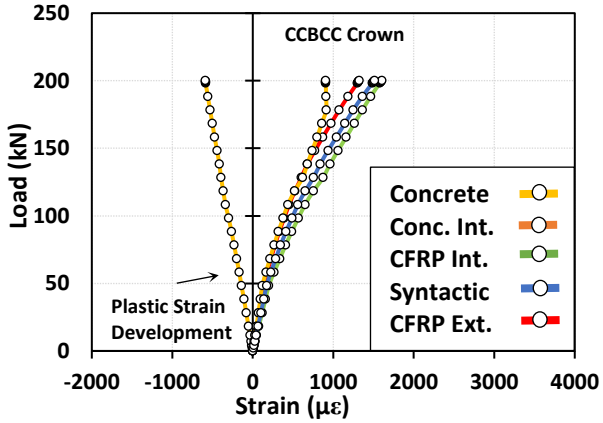

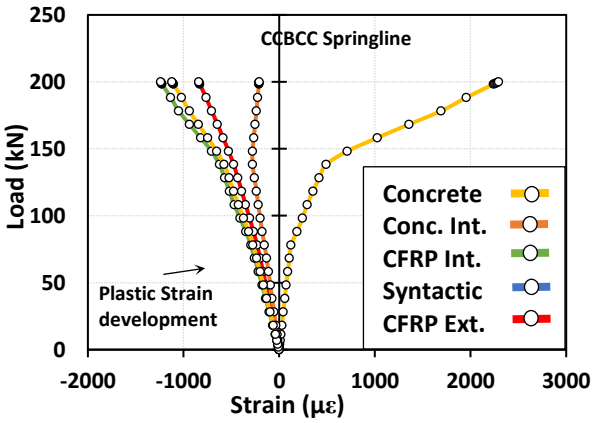

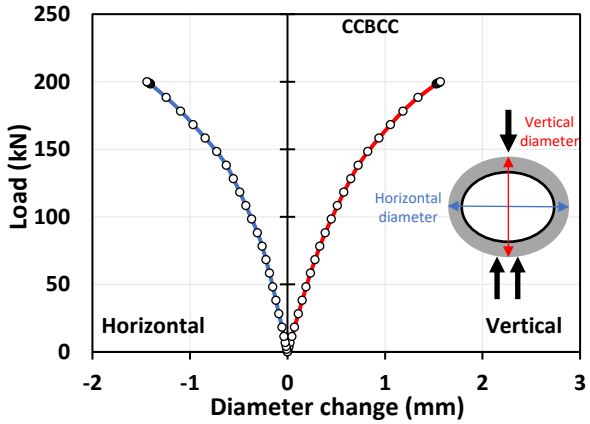

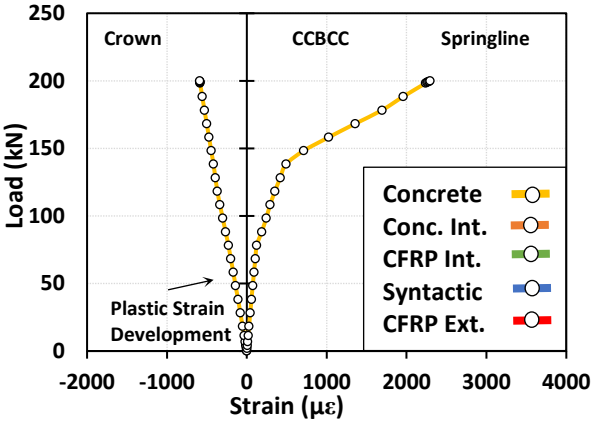
Crown
CCBCC
Springline
Plastic Strain Development
Concrete
Conc. Int.
CFRP Int.
Syntactic
CFRP Ext.
Load (kN)
0
50
100
150
200
250
-2000
-1000
0
1000
2000
3000
4000
Strain (με)

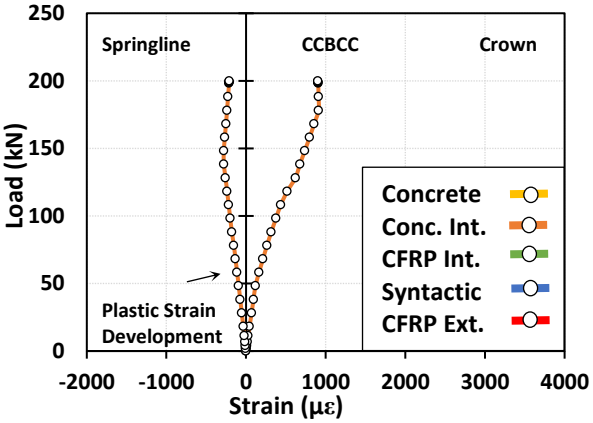
Springline
CCBCC
Crown
Plastic Strain Development
Concrete
Conc. Int.
CFRP Int.
Syntactic
CFRP Ext.
Load (kN)
0
50
100
150
200
250
-2000
-1000
0
1000
2000
3000
4000
Strain (με)

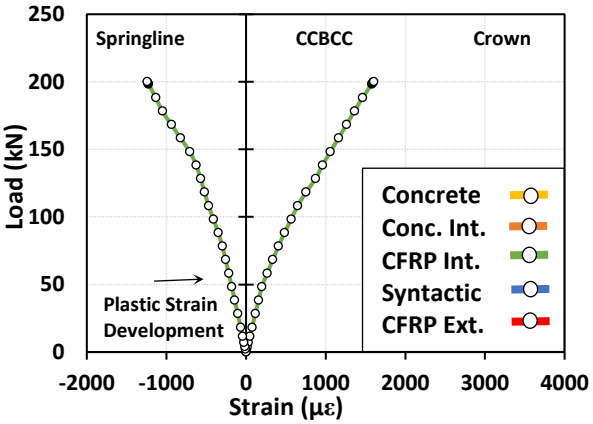
Springline
CCBCC
Crown
Plastic Strain Development
Concrete
Conc. Int.
CFRP Int.
Syntactic
CFRP Ext.
Load (kN)
0
50
100
150
200
250
-2000
-1000
0
1000
2000
3000
4000
Strain (με)

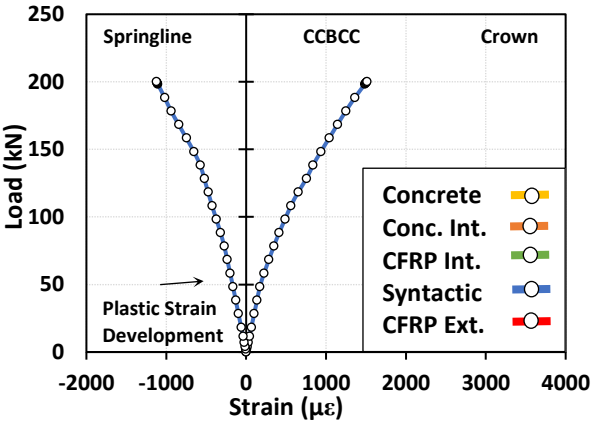
Springline
CCBCC
Crown
Plastic Strain Development
Concrete
Conc. Int.
CFRP Int.
Syntactic
CFRP Ext.
Load (kN)
0
50
100
150
200
250
-2000
-1000
0
1000
2000
3000
4000
Strain (με)

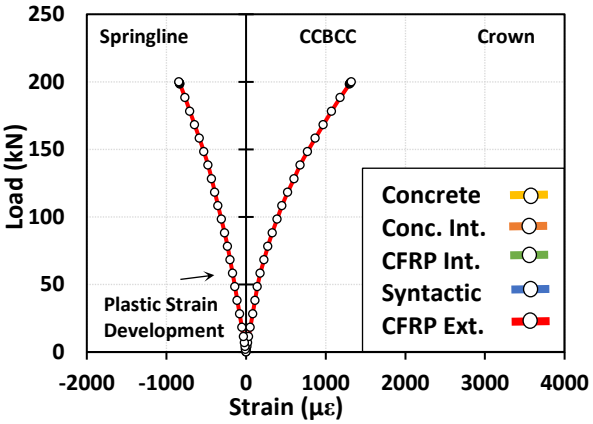
Springline
CCBCC
Crown
Plastic Strain Development
Concrete
Conc. Int.
CFRP Int.
Syntactic
CFRP Ext.
Load (kN)
0
50
100
150
200
250
-2000
-1000
0
1000
2000
3000
4000
Strain (με)

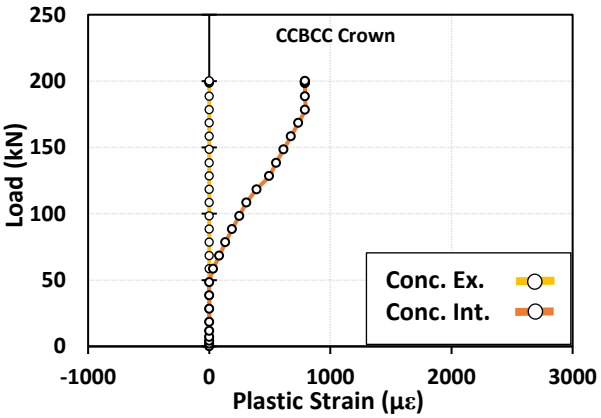
CCBCC Crown
Load (kN)
250
200
150
100
50
0
-1000
0
1000
2000
3000
Plastic Strain (με)
Conc. Ex.
Conc. Int.

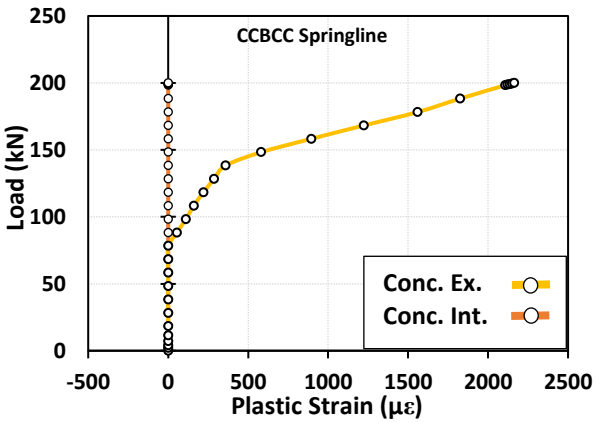
CCBCC Springline
Load (kN)
250
200
150
100
50
0
-500
0
500
1000
1500
2000
2500
Plastic Strain (με)
Conc. Ex.
Conc. Int.

GGBGG Stress Contour Plot for 28kN, 58kN, 78kN, 118kN

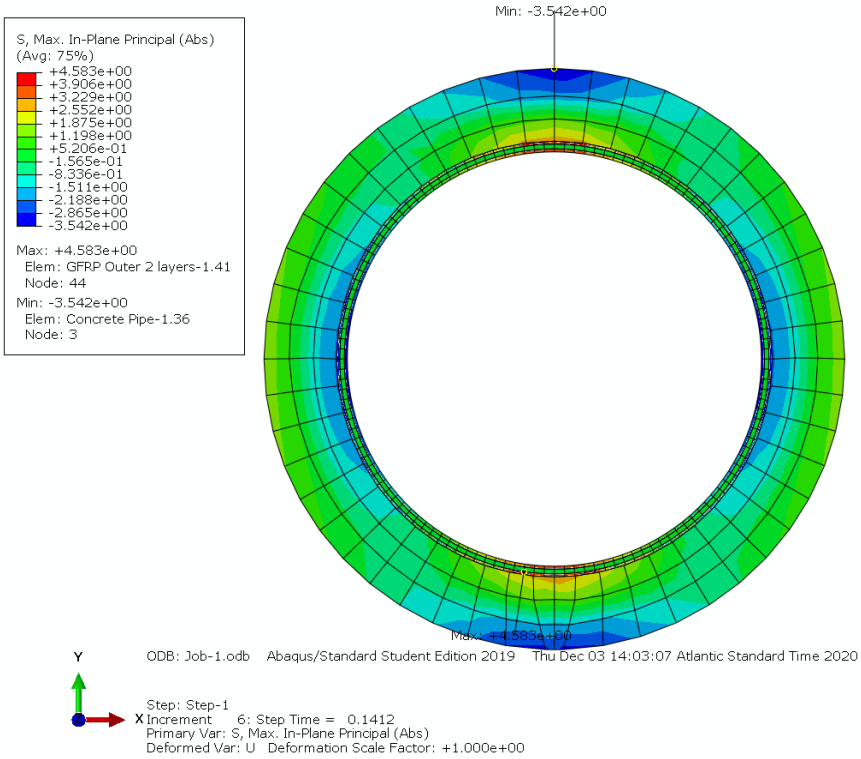

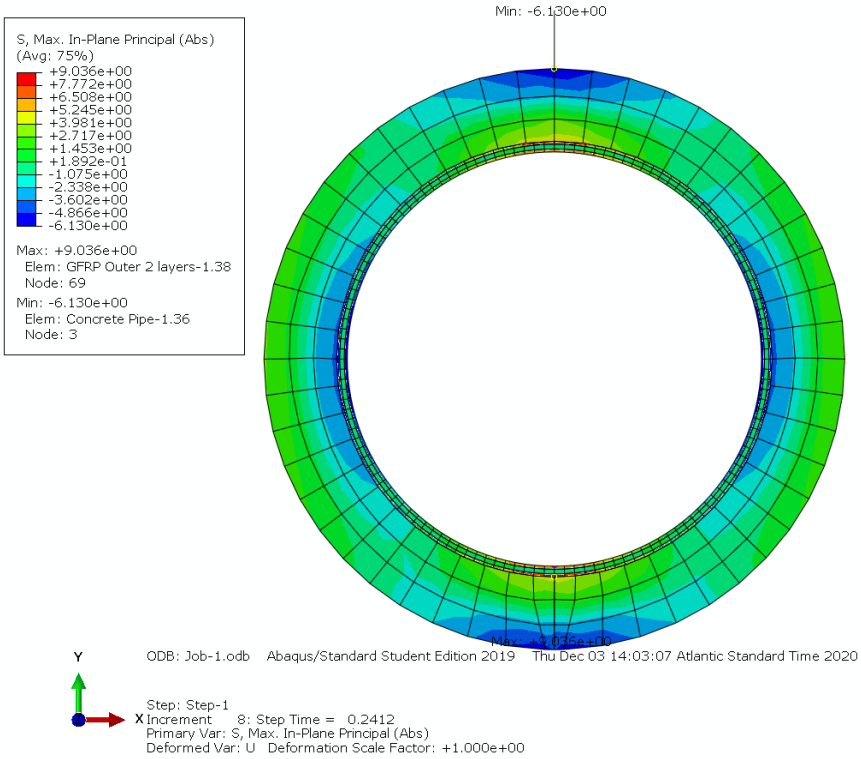

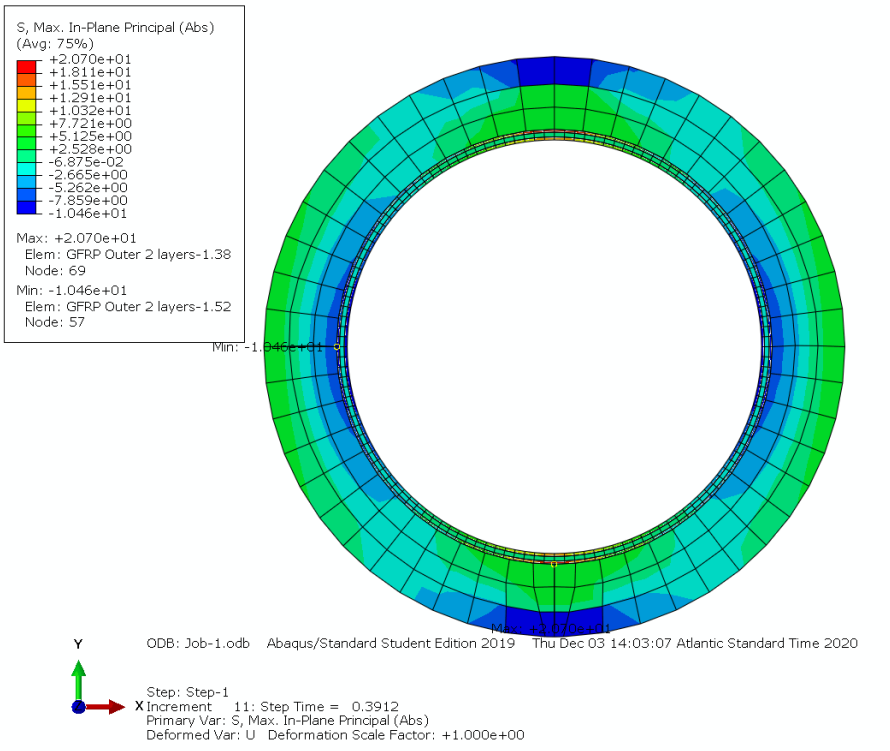
S, Max. In-Plane Principal (Abs)
(Avg: 75%)
+2.070e+01
+1.811e+01
+1.551e+01
+1.291e+01
+1.032e+01
+7.721e+00
+5.125e+00
+2.528e+00
-6.875e-02
-2.665e+00
-5.262e+00
-7.859e+00
-1.046e+01
Max: +2.070e+01
Elem: GFRP Outer 2 layers-1.38
Node: 69
Min: -1.046e+01
Elem: GFRP Outer 2 layers-1.52
Node: 57
Min: -1.046e+01
Max: +2.070e+01
Y
X
ODB: Job-1.odb Abaqus/Standard Student Edition 2019 Thu Dec 03 14:03:07 Atlantic Standard Time 2020
Step: Step-1
Increment 11: Step Time = 0.3912
Primary Var: S, Max. In-Plane Principal (Abs)
Deformed Var: U Deformation Scale Factor: +1.000e+00

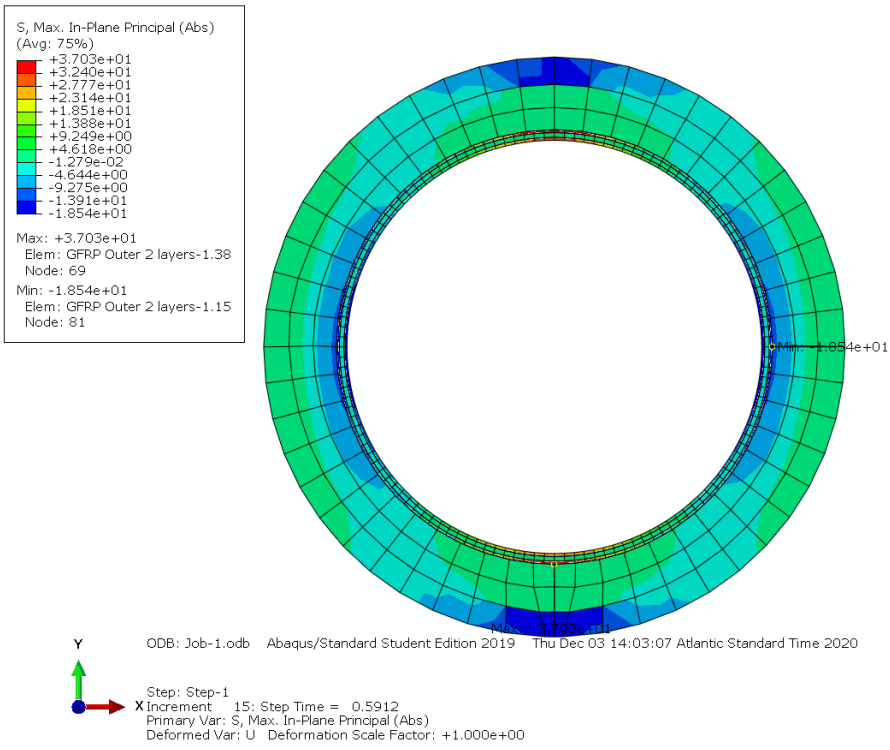
S, Max. In-Plane Principal (Abs)
(Avg: 75%)
+3.703e+01
+3.240e+01
+2.777e+01
+2.314e+01
+1.851e+01
+1.388e+01
+9.249e+00
+4.618e+00
-1.279e-02
-4.644e+00
-9.275e+00
-1.391e+01
-1.854e+01
Max: +3.703e+01
Elem: GFRP Outer 2 layers-1.38
Node: 69
Min: -1.854e+01
Elem: GFRP Outer 2 layers-1.15
Node: 81
Min: -1.854e+01
Max: +3.703e+01
Y
X
ODB: Job-1.odb Abaqus/Standard Student Edition 2019 Thu Dec 03 14:03:07 Atlantic Standard Time 2020
Step: Step-1
Increment 15: Step Time = 0.5912
Primary Var: S, Max. In-Plane Principal (Abs)
Deformed Var: U Deformation Scale Factor: +1.000e+00

GGBGG Strain Contour Plot for 28kN, 58kN, 78kN, 118kN

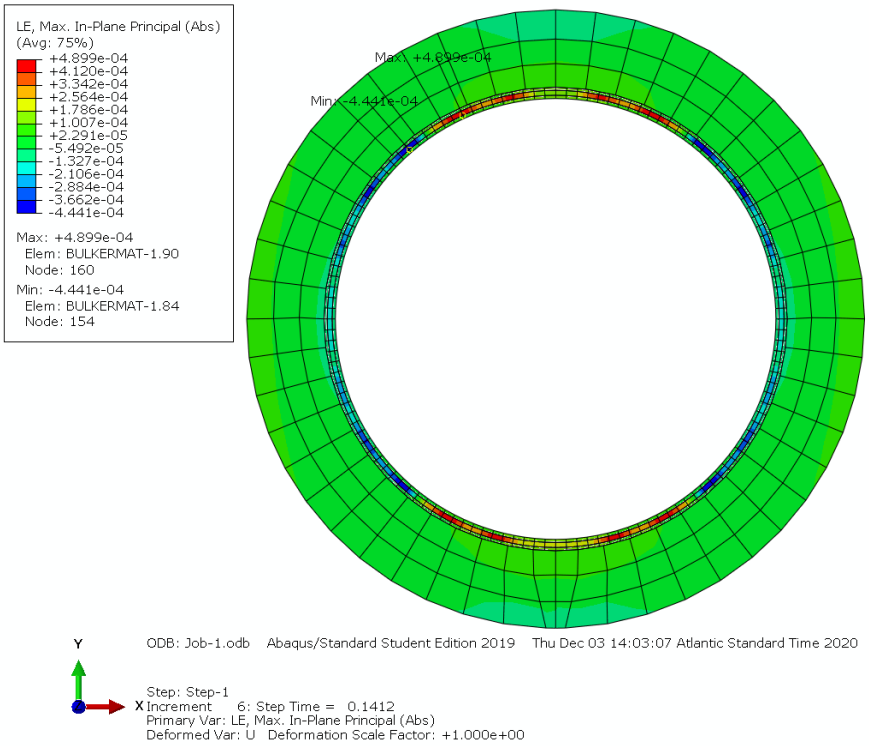

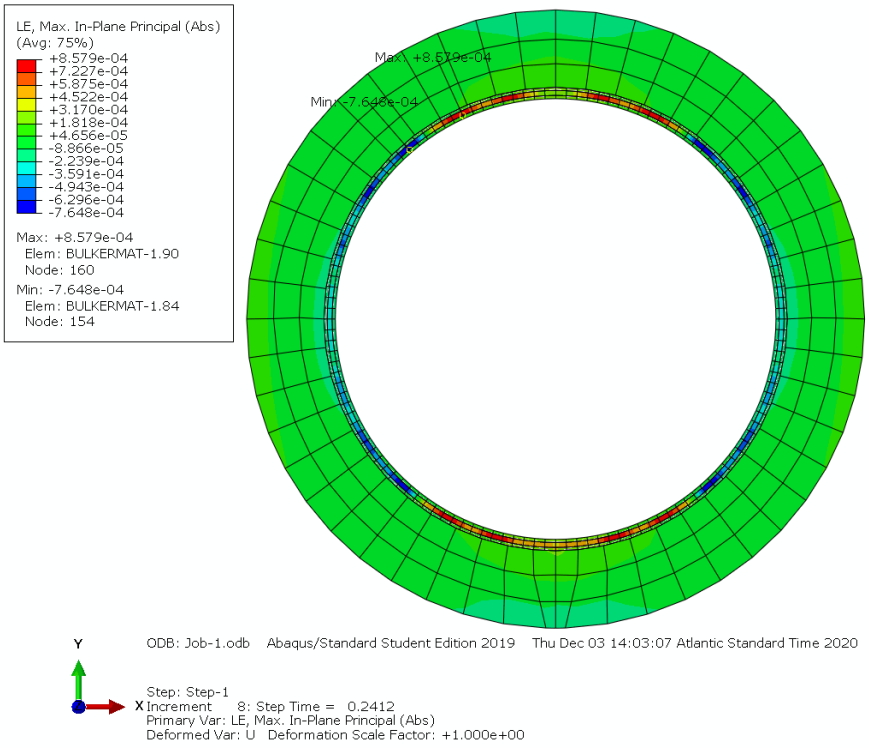

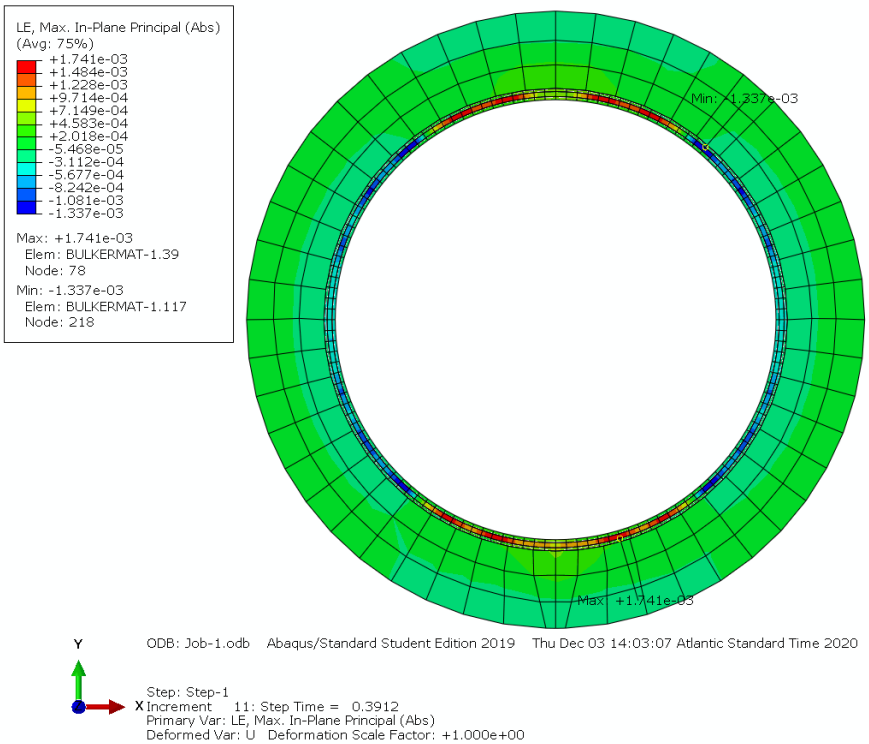
LE, Max. In-Plane Principal (Abs)
(Avg: 75%)
+1.741e-03
+1.484e-03
+1.228e-03
+9.714e-04
+7.149e-04
+4.583e-04
+2.018e-04
-5.468e-05
-3.112e-04
-5.677e-04
-8.242e-04
-1.081e-03
-1.337e-03
Max: +1.741e-03
Elem: BULKERMAT-1.39
Node: 78
Min: -1.337e-03
Elem: BULKERMAT-1.117
Node: 218
Min: -1.337e-03
Max: +1.741e-03
Y
X
ODB: Job-1.odb Abaqus/Standard Student Edition 2019 Thu Dec 03 14:03:07 Atlantic Standard Time 2020
Step: Step-1
Increment 11: Step Time = 0.3912
Primary Var: LE, Max. In-Plane Principal (Abs)
Deformed Var: U Deformation Scale Factor: +1.000e+00

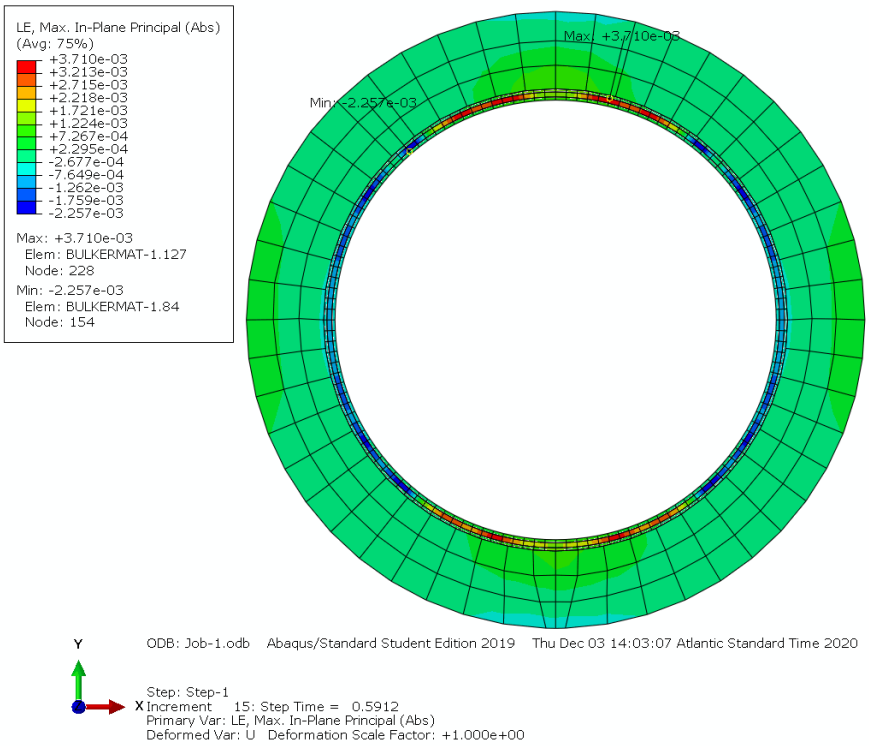
LE, Max. In-Plane Principal (Abs)
(Avg: 75%)
+3.710e-03
+3.213e-03
+2.715e-03
+2.218e-03
+1.721e-03
+1.224e-03
+7.267e-04
+2.295e-04
-2.677e-04
-7.649e-04
-1.262e-03
-1.759e-03
-2.257e-03
Max: +3.710e-03
Elem: BULKERMAT-1.127
Node: 228
Min: -2.257e-03
Elem: BULKERMAT-1.84
Node: 154
Max: +3.710e-03
Min: -2.257e-03
Y
X
ODB: Job-1.odb Abaqus/Standard Student Edition 2019 Thu Dec 03 14:03:07 Atlantic Standard Time 2020
Step: Step-1
Increment 15: Step Time = 0.5912
Primary Var: LE, Max. In-Plane Principal (Abs)
Deformed Var: U Deformation Scale Factor: +1.000e+00

GGBGG Plastic Strain Contour Plot for 28kN, 58kN, 78kN, 118kN

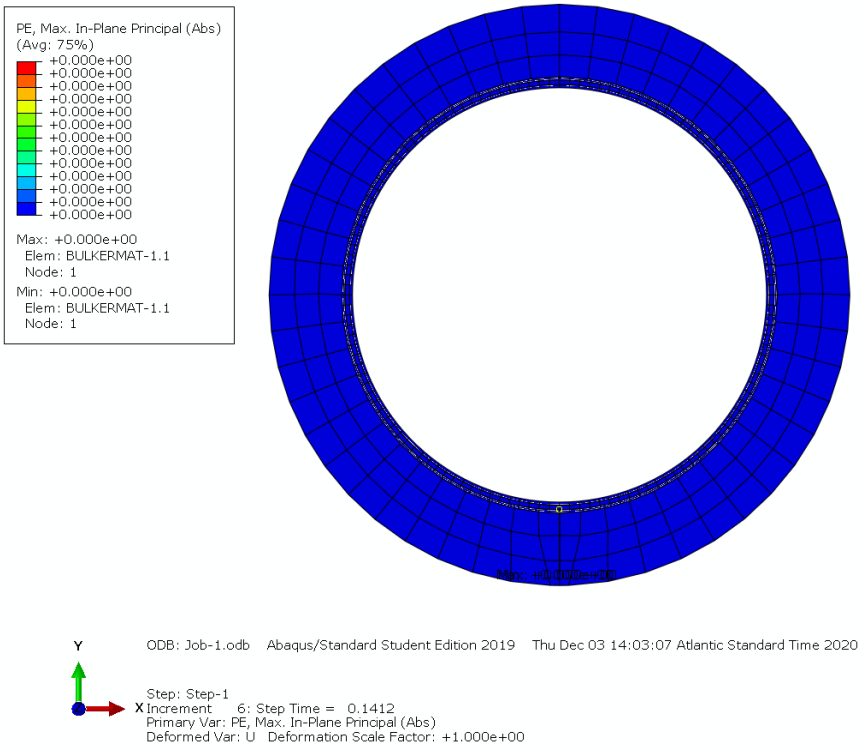

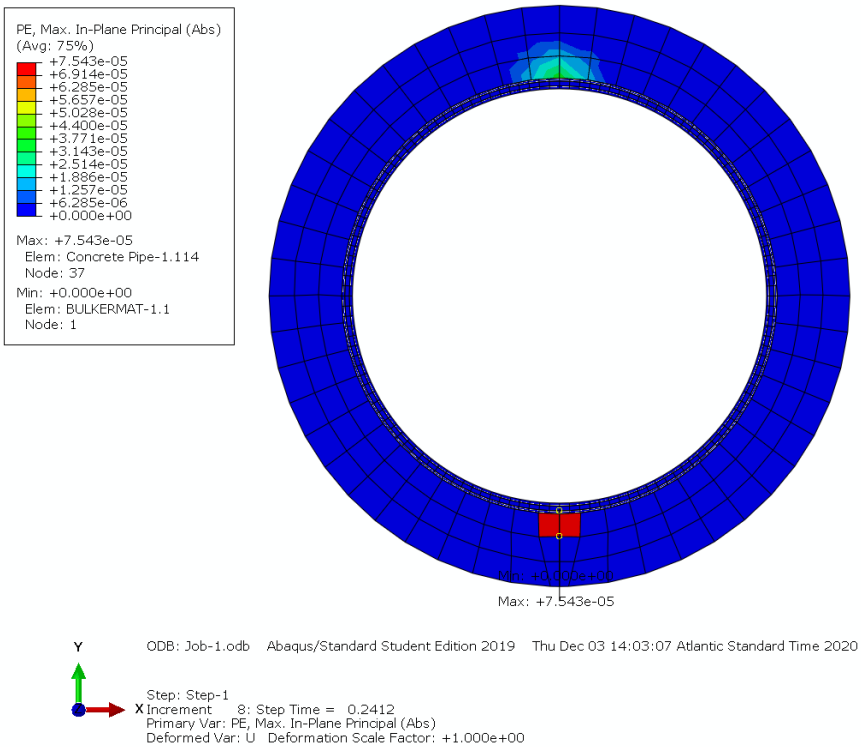

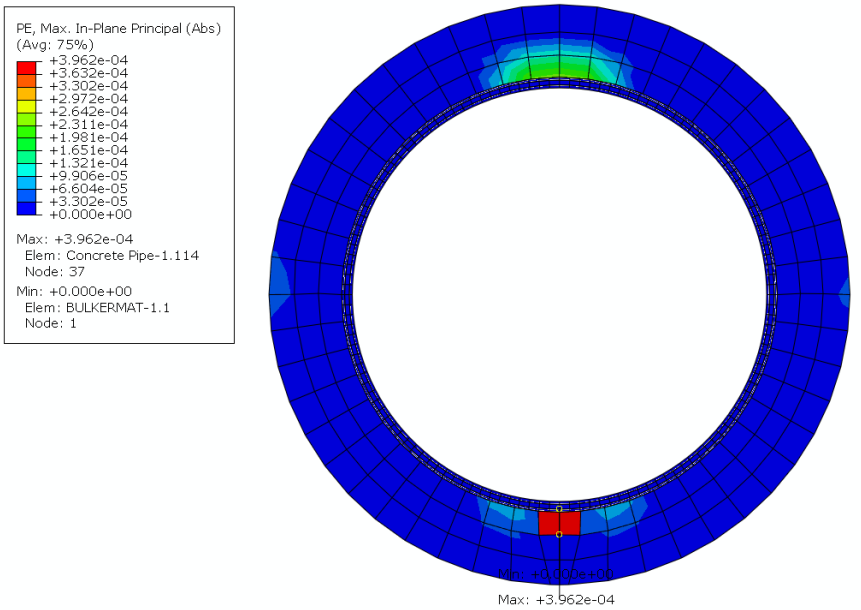
PE, Max. In-Plane Principal (Abs)
(Avg: 75%)
+3.962e-04
+3.632e-04
+3.302e-04
+2.972e-04
+2.642e-04
+2.311e-04
+1.981e-04
+1.651e-04
+1.321e-04
+9.906e-05
+6.604e-05
+3.302e-05
+0.000e+00
Max: +3.962e-04
Elem: Concrete Pipe-1.114
Node: 37
Min: +0.000e+00
Elem: BULKERMAT-1.1
Node: 1
Min: +0.000e+00
Max: +3.962e-04
Y
X
ODB: Job-1.odb Abaqus/Standard Student Edition 2019 Thu Dec 03 14:03:07 Atlantic Standard Time 2020
Step: Step-1
Increment 11: Step Time = 0.3912
Primary Var: PE, Max. In-Plane Principal (Abs)
Deformed Var: U Deformation Scale Factor: +1.000e+00

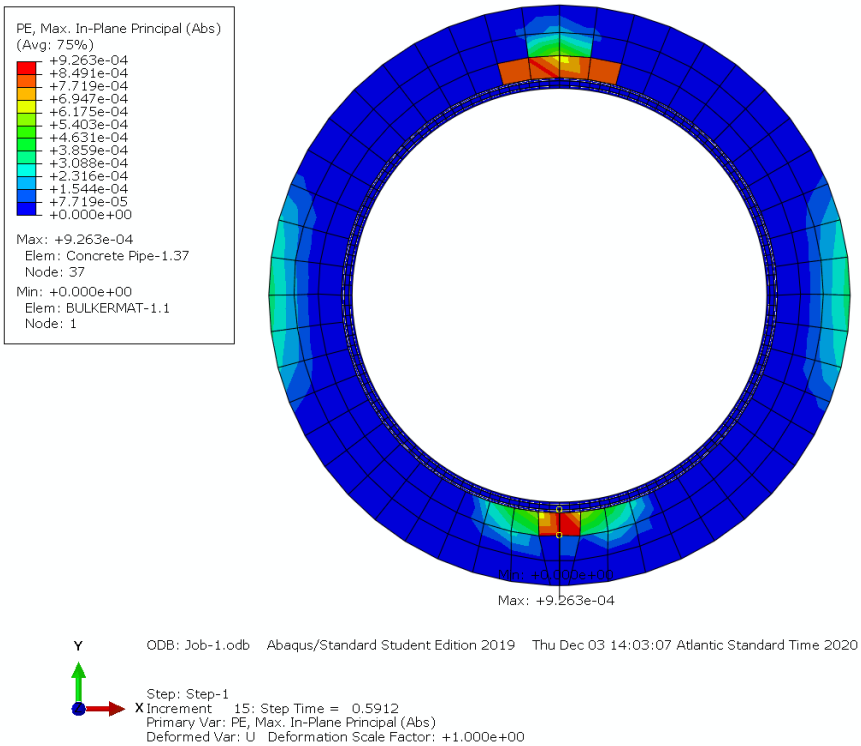
PE, Max. In-Plane Principal (Abs)
(Avg: 75%)
+9.263e-04
+8.491e-04
+7.719e-04
+6.947e-04
+6.175e-04
+5.403e-04
+4.631e-04
+3.859e-04
+3.088e-04
+2.316e-04
+1.544e-04
+7.719e-05
+0.000e+00
Max: +9.263e-04
Elem: Concrete Pipe-1.37
Node: 37
Min: +0.000e+00
Elem: BULKERMAT-1.1
Node: 1
Min: +0.000e+00
Max: +9.263e-04
Y
X
ODB: Job-1.odb Abaqus/Standard Student Edition 2019 Thu Dec 03 14:03:07 Atlantic Standard Time 2020
Step: Step-1
Increment 15: Step Time = 0.5912
Primary Var: PE, Max. In-Plane Principal (Abs)
Deformed Var: U Deformation Scale Factor: +1.000e+00

GGBGG Load vs. Strain Plots from ABAQUS

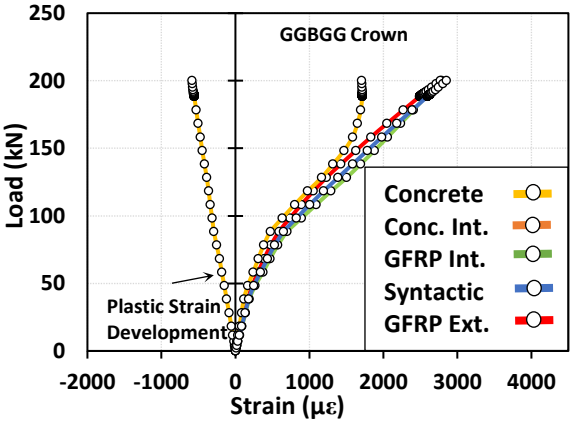

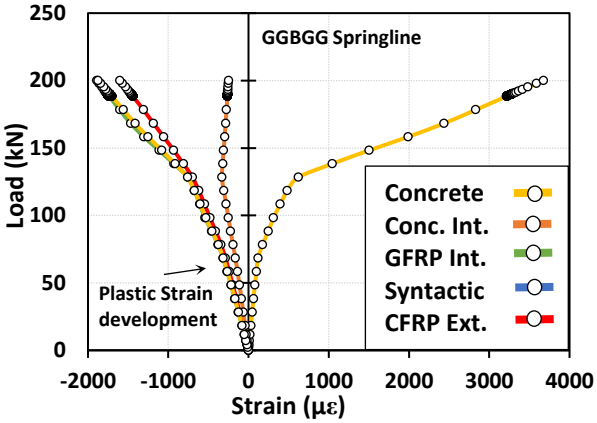

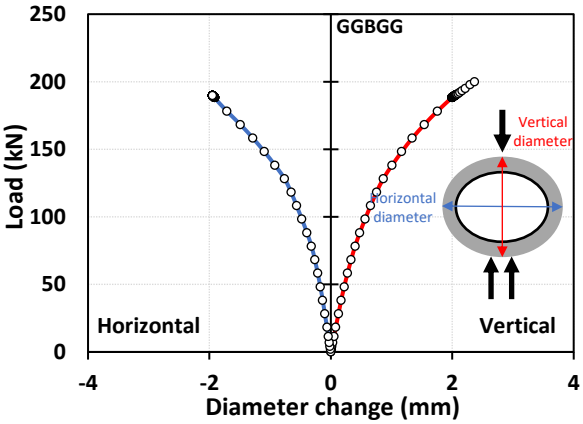

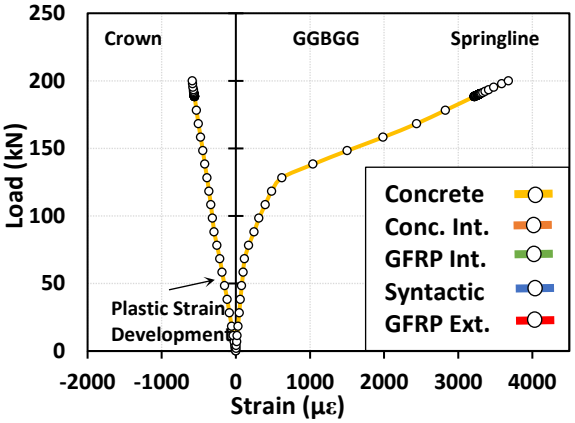
Crown
GGBGG
Springline
Load (kN)
Strain (με)
Plastic Strain Development
Concrete
Conc. Int.
GFRP Int.
Syntactic
GFRP Ext.

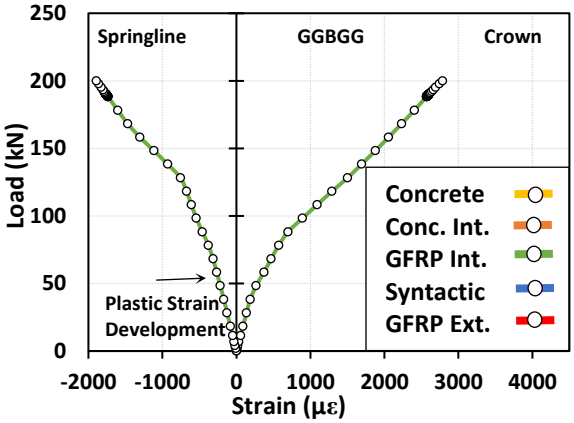
Springline
GGBGG
Crown
Load (kN)
Strain (με)
Plastic Strain Development
Concrete
Conc. Int.
GFRP Int.
Syntactic
GFRP Ext.

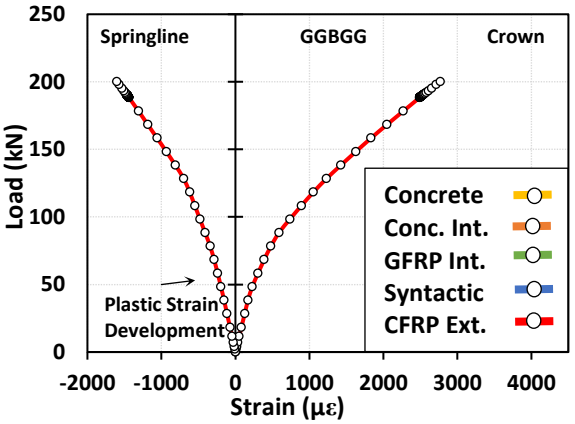
Springline
GGBGG
Crown
Load (kN)
Strain (με)
Plastic Strain Development
Concrete
Conc. Int.
GFRP Int.
Syntactic
CFRP Ext.

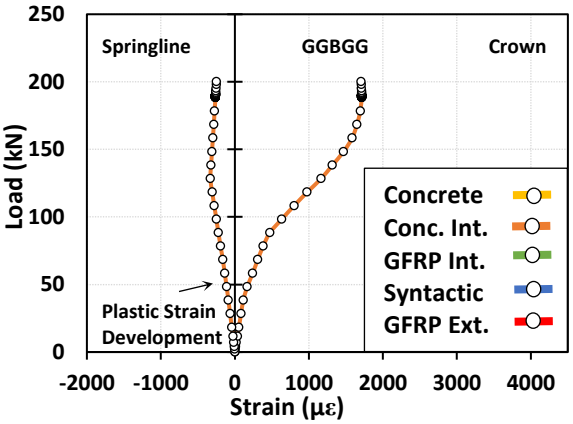
Springline
GGBGG
Crown
Load (kN)
Strain (με)
Plastic Strain Development
Concrete
Conc. Int.
GFRP Int.
Syntactic
GFRP Ext.

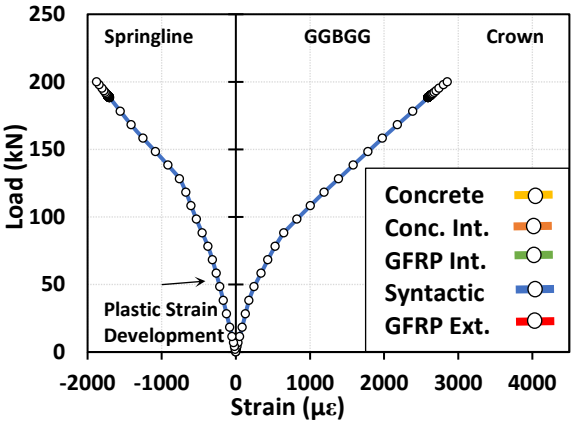
Springline
GGBGG
Crown
Load (kN)
Strain (με)
Plastic Strain Development
Concrete
Conc. Int.
GFRP Int.
Syntactic
GFRP Ext.

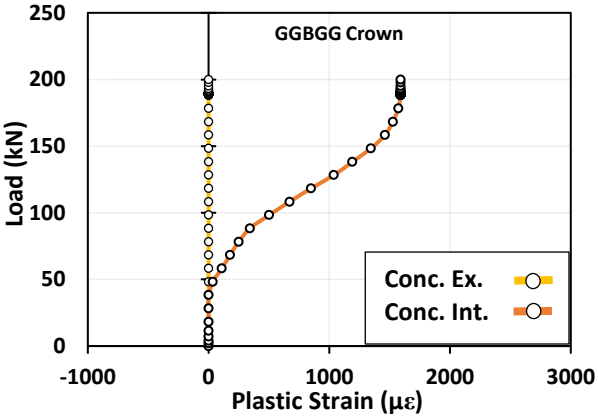
GGBGG Crown
Load (kN)
250
200
150
100
50
0
-1000
0
1000
2000
3000
Plastic Strain (με)
Conc. Ex.
Conc. Int.

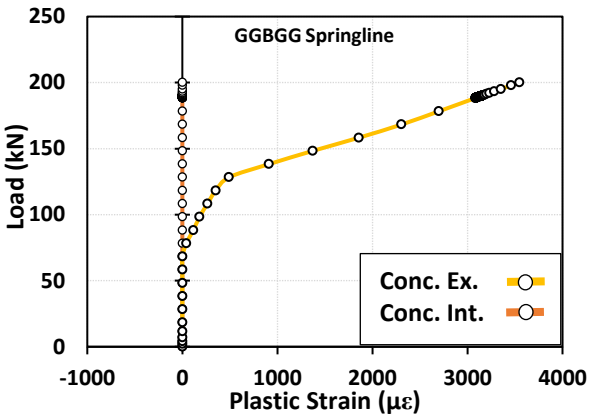
GGBGG Springline
Load (kN)
250
200
150
100
50
0
-1000
0
1000
2000
3000
4000
Plastic Strain (με)
Conc. Ex.
Conc. Int.

GGBCC Stress Contour Plot for 28kN, 48kN, 88kN, 148kN

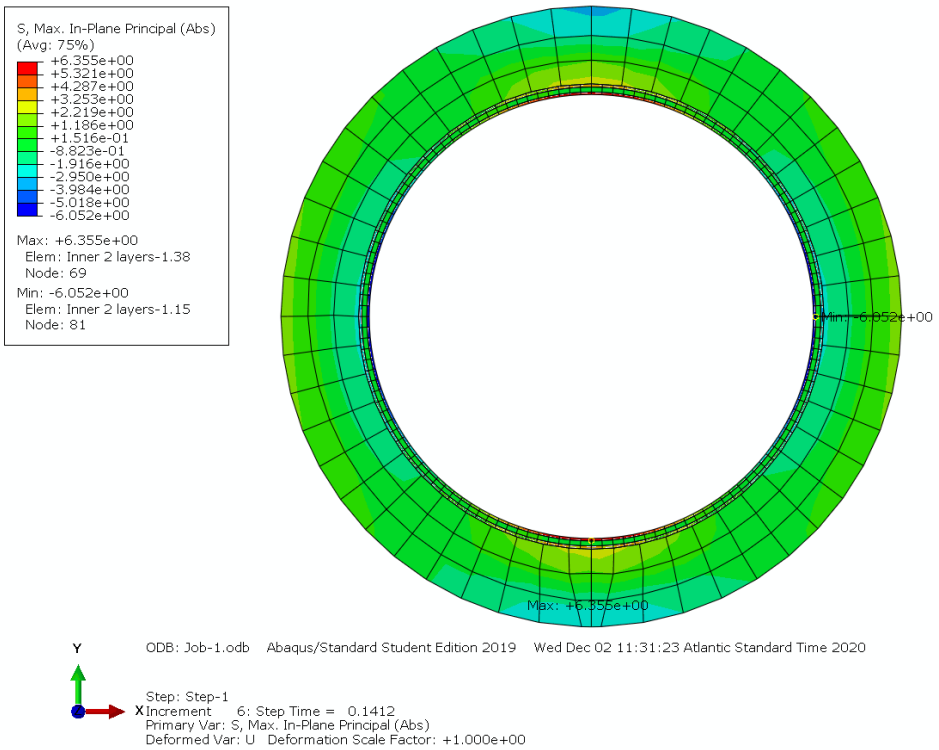

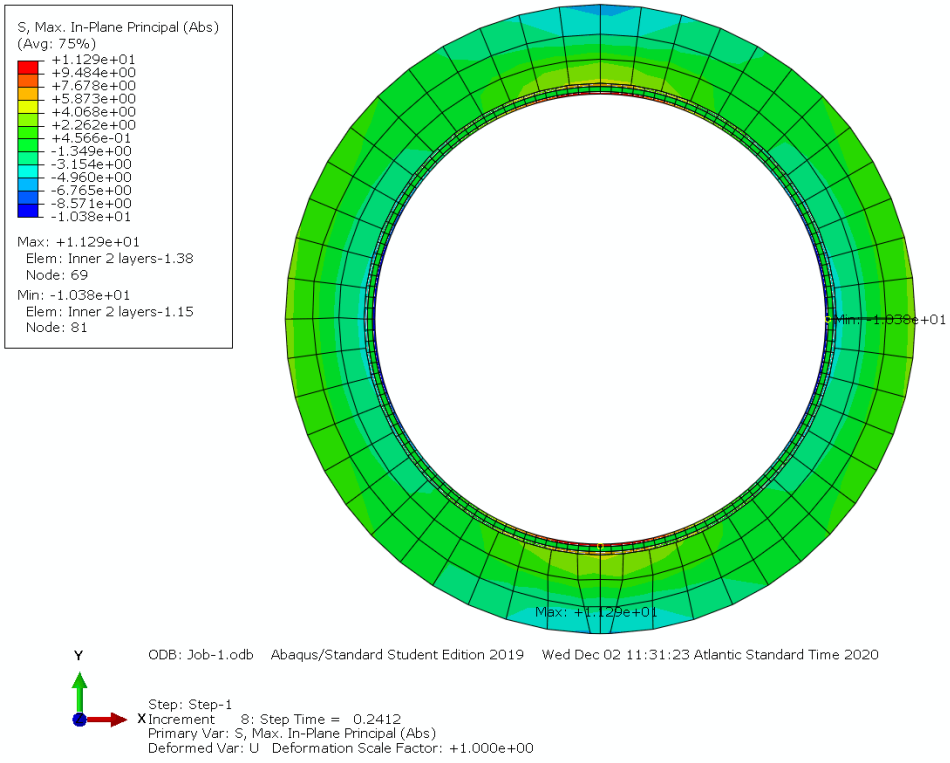

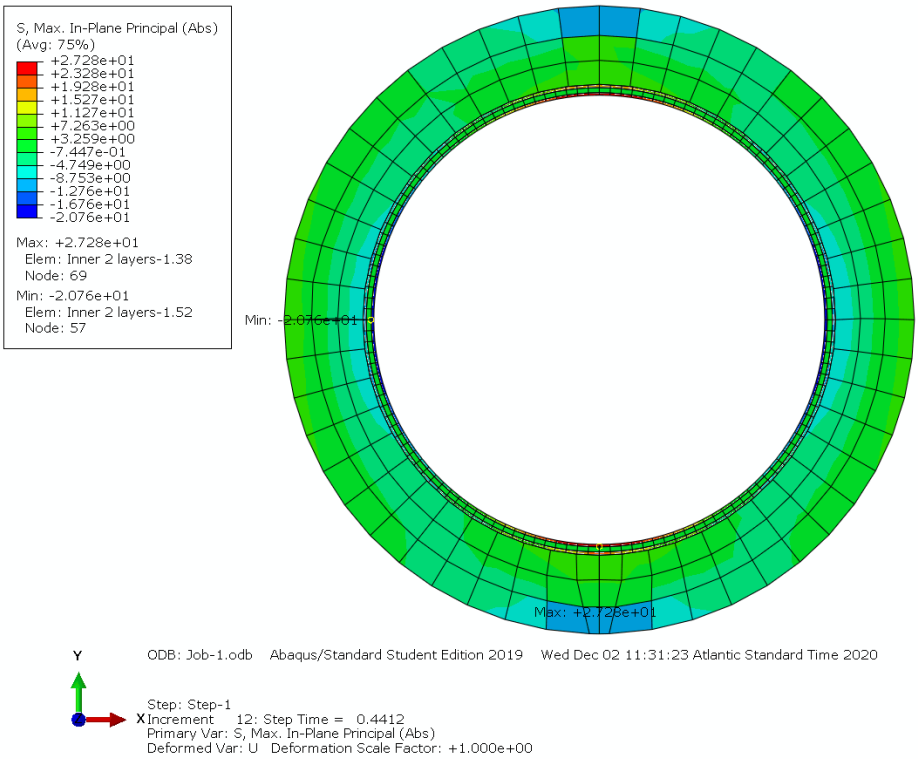
S, Max. In-Plane Principal (Abs)
(Avg: 75%)
+2.728e+01
+2.328e+01
+1.928e+01
+1.527e+01
+1.127e+01
+7.263e+00
+3.259e+00
-7.447e-01
-4.749e+00
-8.753e+00
-1.276e+01
-1.676e+01
-2.076e+01
Max: +2.728e+01
Elem: Inner 2 layers-1.38
Node: 69
Min: -2.076e+01
Elem: Inner 2 layers-1.52
Node: 57
Min: -2.076e+01
Max: +2.728e+01
Y
X
ODB: Job-1.odb Abaqus/Standard Student Edition 2019 Wed Dec 02 11:31:23 Atlantic Standard Time 2020
Step: Step-1
Increment 12: Step Time = 0.4412
Primary Var: S, Max. In-Plane Principal (Abs)
Deformed Var: U Deformation Scale Factor: +1.000e+00

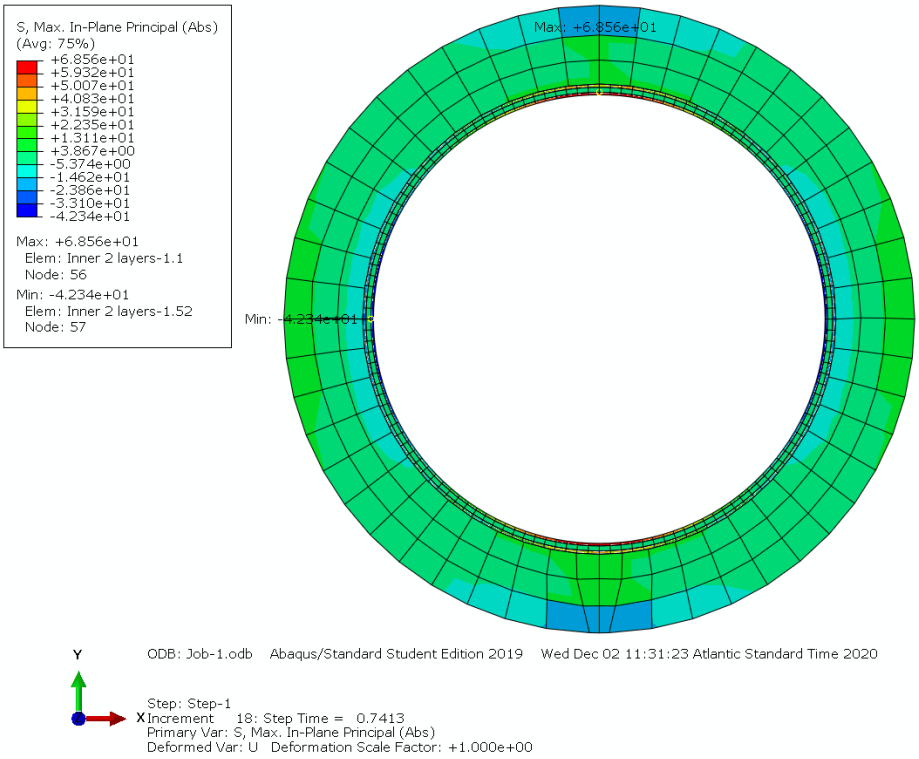
S, Max. In-Plane Principal (Abs)
(Avg: 75%)
+6.856e+01
+5.932e+01
+5.007e+01
+4.083e+01
+3.159e+01
+2.235e+01
+1.311e+01
+3.867e+00
-5.374e+00
-1.462e+01
-2.386e+01
-3.310e+01
-4.234e+01
Max: +6.856e+01
Elem: Inner 2 layers-1.1
Node: 56
Min: -4.234e+01
Elem: Inner 2 layers-1.52
Node: 57
Max: +6.856e+01
Min: -4.234e+01
Y
X
ODB: Job-1.odb Abaqus/Standard Student Edition 2019 Wed Dec 02 11:31:23 Atlantic Standard Time 2020
Step: Step-1
Increment 18: Step Time = 0.7413
Primary Var: S, Max. In-Plane Principal (Abs)
Deformed Var: U Deformation Scale Factor: +1.000e+00

GGBCC Strain Contour Plot for 28kN, 48kN, 88kN, 148kN

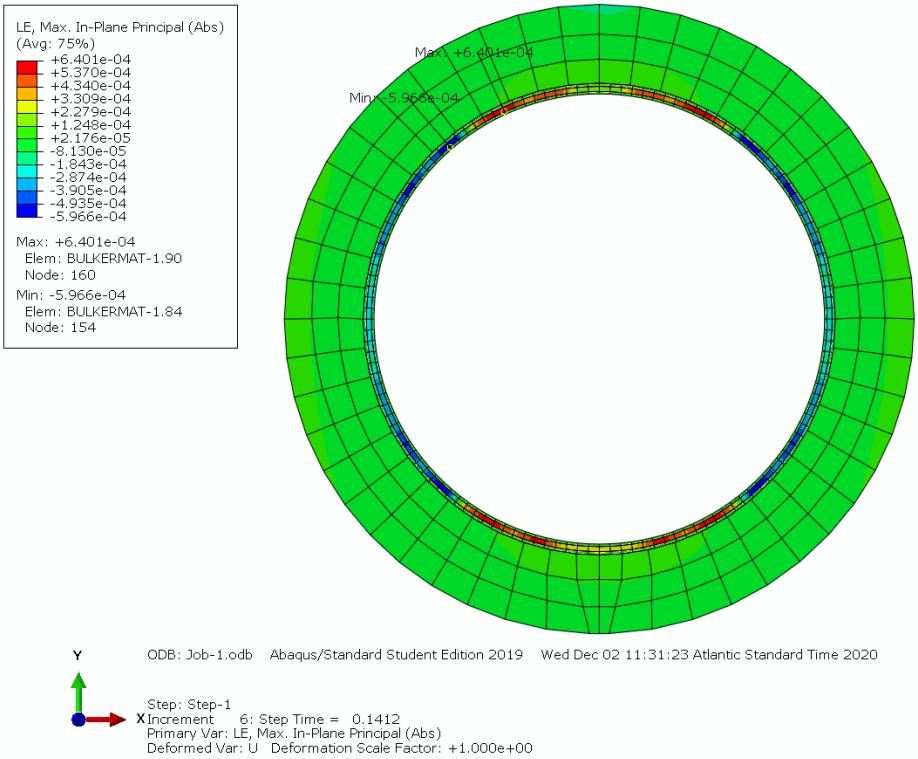

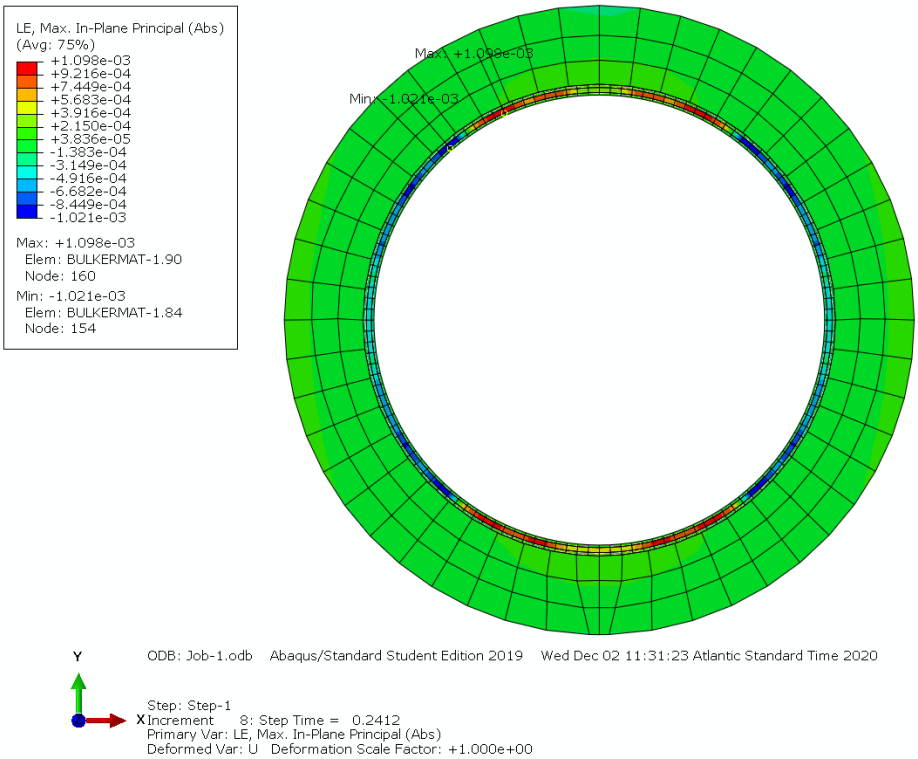

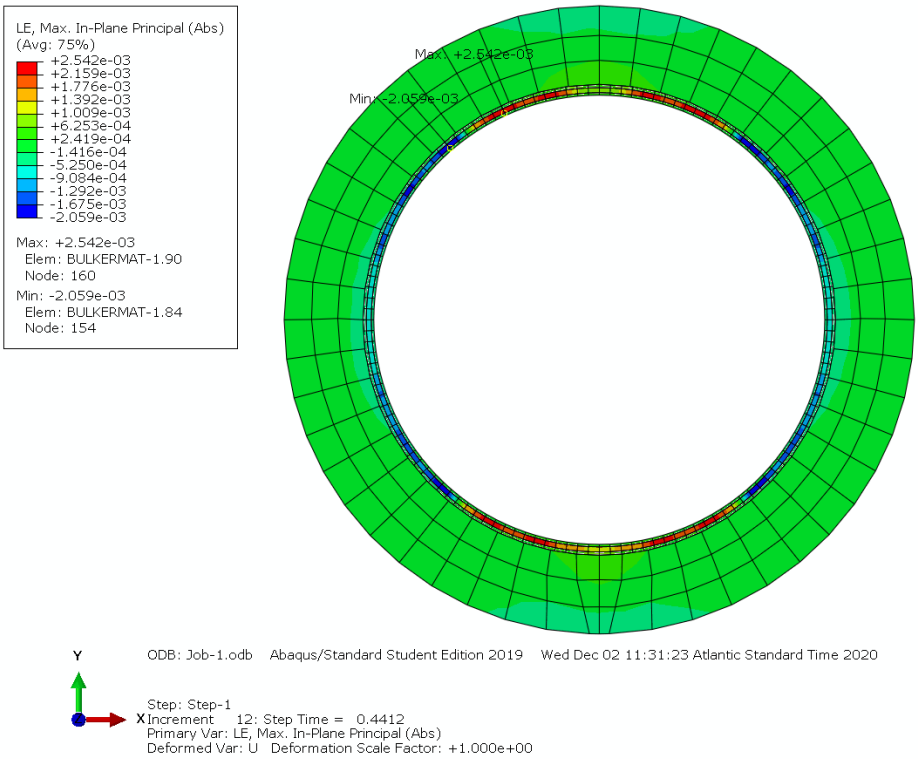
LE, Max. In-Plane Principal (Abs)
(Avg: 75%)
+2.542e-03
+2.159e-03
+1.776e-03
+1.392e-03
+1.009e-03
+6.253e-04
+2.419e-04
-1.416e-04
-5.250e-04
-9.084e-04
-1.292e-03
-1.675e-03
-2.059e-03
Max: +2.542e-03
Elem: BULKERMAT-1.90
Node: 160
Min: -2.059e-03
Elem: BULKERMAT-1.84
Node: 154
Max: +2.542e-03
Min: -2.059e-03
Y
X
ODB: Job-1.odb Abaqus/Standard Student Edition 2019 Wed Dec 02 11:31:23 Atlantic Standard Time 2020
Step: Step-1
Increment 12: Step Time = 0.4412
Primary Var: LE, Max. In-Plane Principal (Abs)
Deformed Var: U Deformation Scale Factor: +1.000e+00

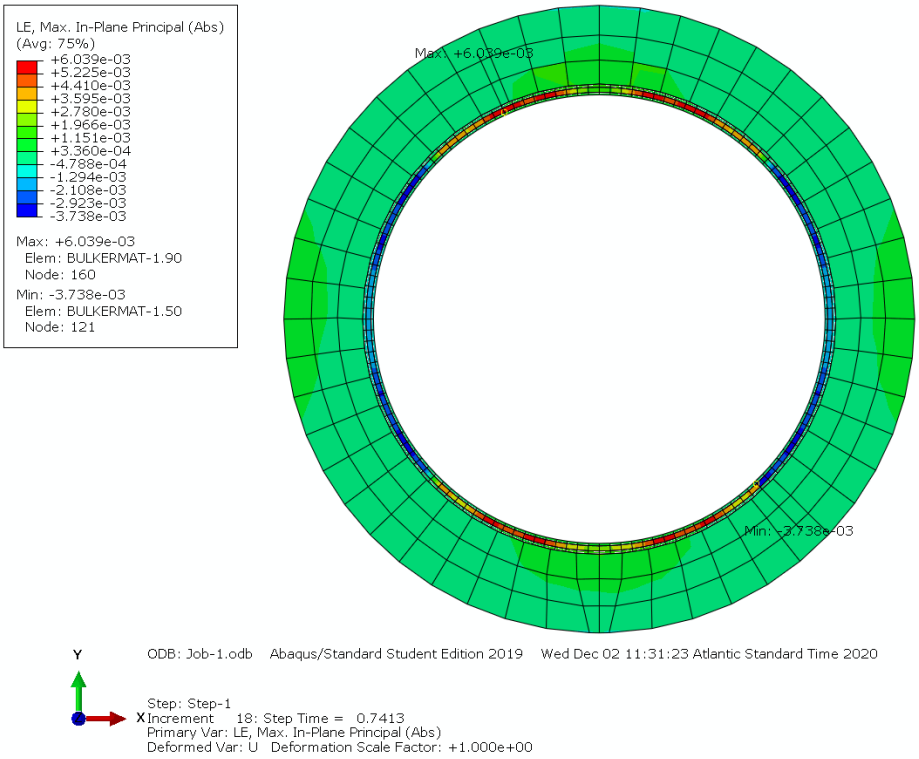
LE, Max. In-Plane Principal (Abs)
(Avg: 75%)
+6.039e-03
+5.225e-03
+4.410e-03
+3.595e-03
+2.780e-03
+1.966e-03
+1.151e-03
+3.360e-04
-4.788e-04
-1.294e-03
-2.108e-03
-2.923e-03
-3.738e-03
Max: +6.039e-03
Elem: BULKERMAT-1.90
Node: 160
Min: -3.738e-03
Elem: BULKERMAT-1.50
Node: 121
Max: +6.039e-03
Min: -3.738e-03
Y
X
ODB: Job-1.odb Abaqus/Standard Student Edition 2019 Wed Dec 02 11:31:23 Atlantic Standard Time 2020
Step: Step-1
Increment 18: Step Time = 0.7413
Primary Var: LE, Max. In-Plane Principal (Abs)
Deformed Var: U Deformation Scale Factor: +1.000e+00

GGBCC Plastic Strain Contour Plot for 28kN, 48kN, 88kN, 148kN

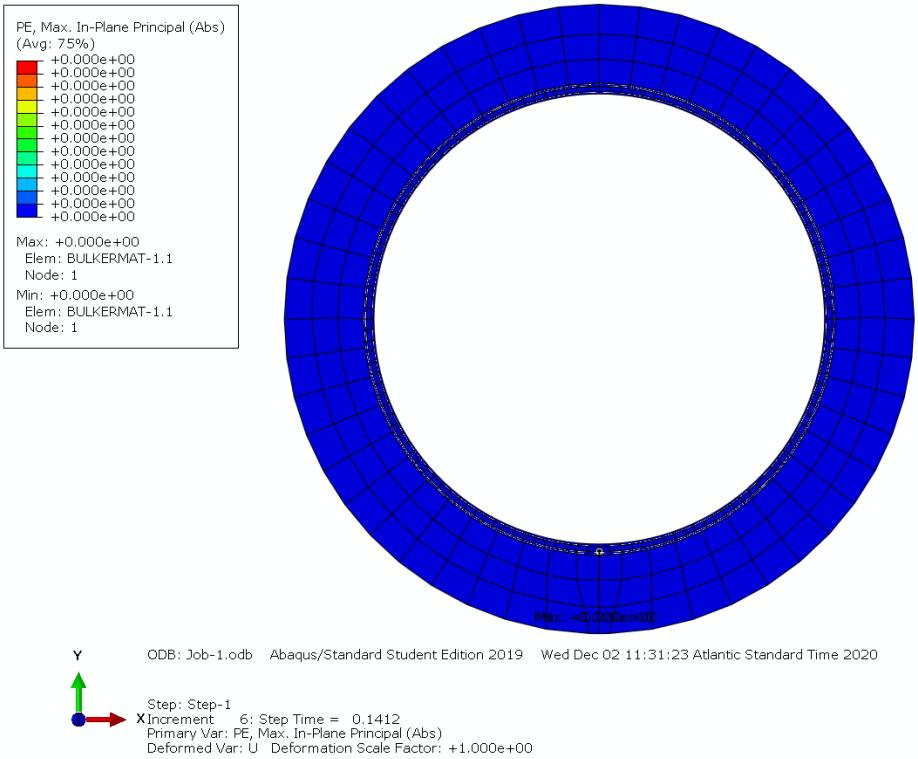

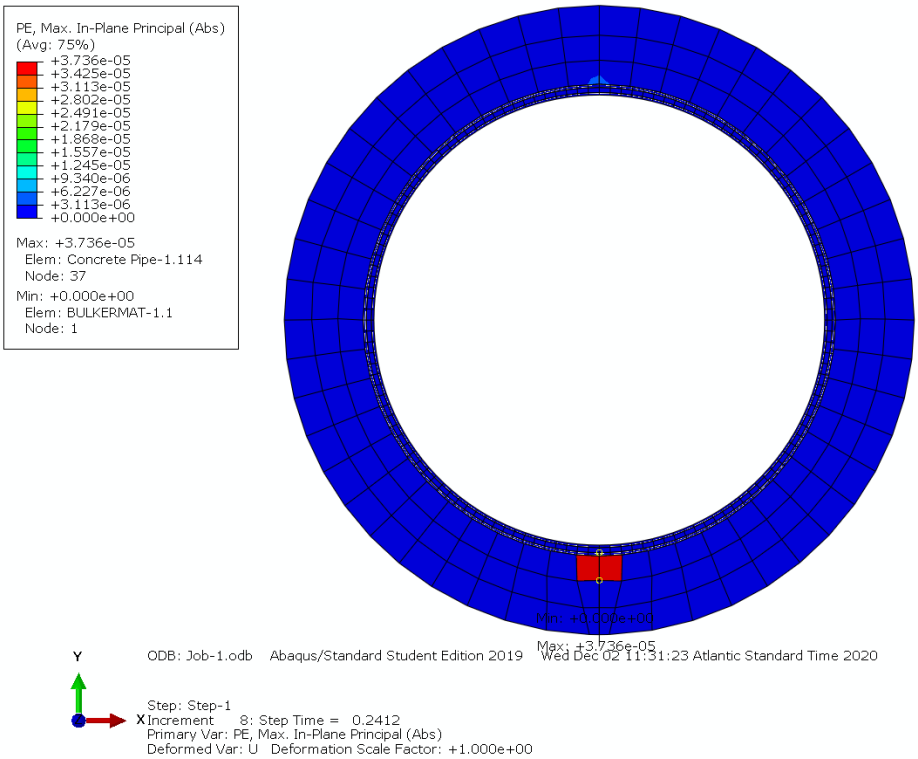

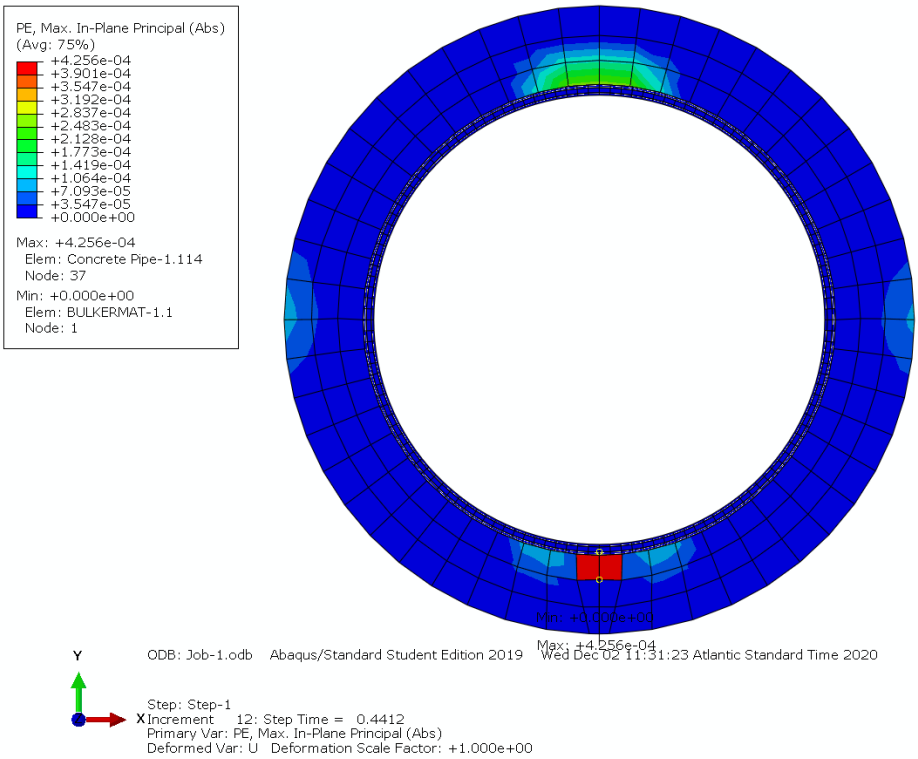
PE, Max. In-Plane Principal (Abs)
(Avg: 75%)
+4.256e-04
+3.901e-04
+3.547e-04
+3.192e-04
+2.837e-04
+2.483e-04
+2.128e-04
+1.773e-04
+1.419e-04
+1.064e-04
+7.093e-05
+3.547e-05
+0.000e+00
Max: +4.256e-04
Elem: Concrete Pipe-1.114
Node: 37
Min: +0.000e+00
Elem: BULKERMAT-1.1
Node: 1
Min: +0.000e+00
Max: +4.256e-04
Y
X
ODB: Job-1.odb Abaqus/Standard Student Edition 2019 Wed Dec 02 11:31:23 Atlantic Standard Time 2020
Step: Step-1
Increment 12: Step Time = 0.4412
Primary Var: PE, Max. In-Plane Principal (Abs)
Deformed Var: U Deformation Scale Factor: +1.000e+00

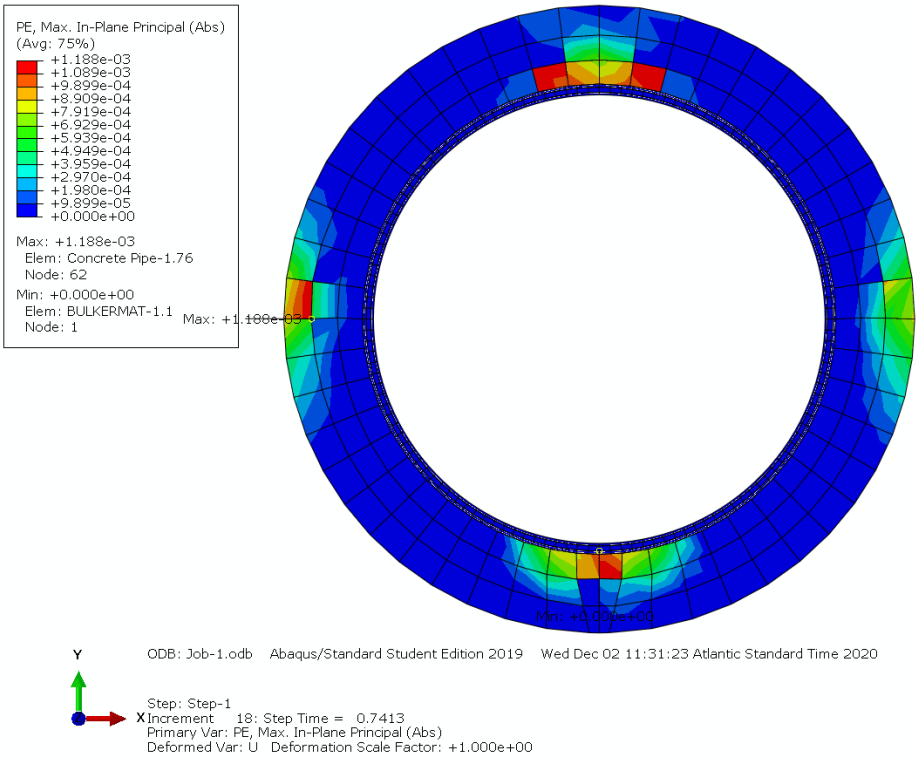
PE, Max. In-Plane Principal (Abs)
(Avg: 75%)
+1.188e-03
+1.089e-03
+9.899e-04
+8.909e-04
+7.919e-04
+6.929e-04
+5.939e-04
+4.949e-04
+3.959e-04
+2.970e-04
+1.980e-04
+9.899e-05
+0.000e+00
Max: +1.188e-03
Elem: Concrete Pipe-1.76
Node: 62
Min: +0.000e+00
Elem: BULKERMAT-1.1
Node: 1
Max: +1.188e-03
Min: +0.000e+00
Y
X
ODB: Job-1.odb Abaqus/Standard Student Edition 2019 Wed Dec 02 11:31:23 Atlantic Standard Time 2020
Step: Step-1
Increment 18: Step Time = 0.7413
Primary Var: PE, Max. In-Plane Principal (Abs)
Deformed Var: U Deformation Scale Factor: +1.000e+00

GGBCC Load vs. Strain Plots from ABAQUS

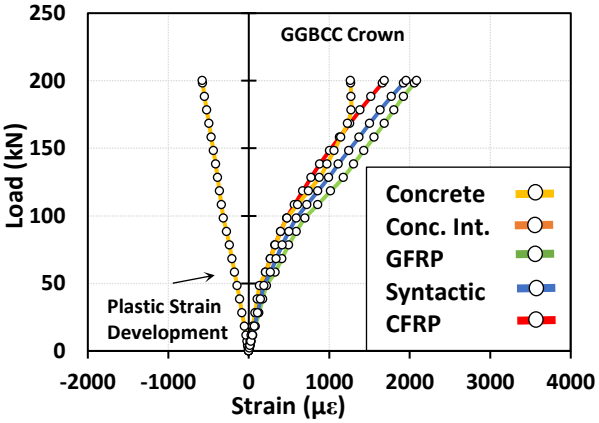

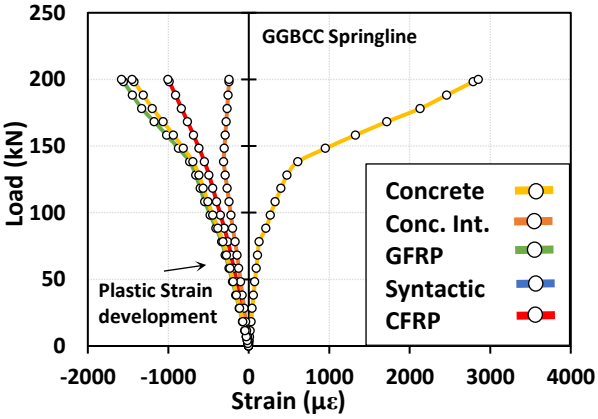

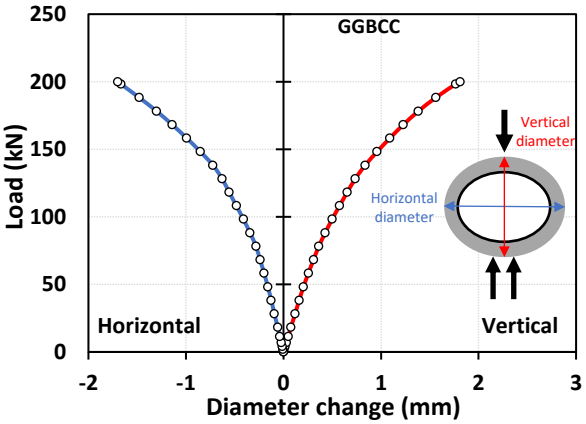

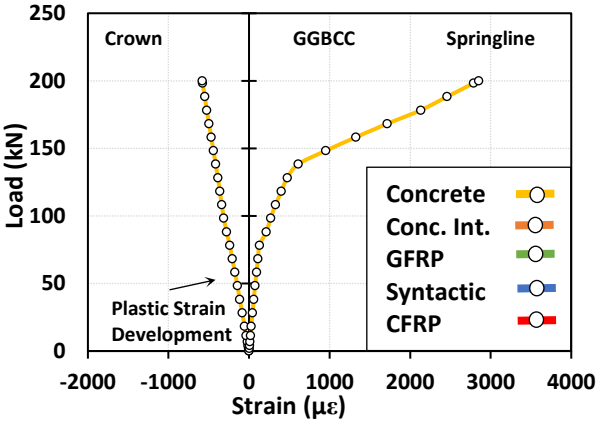
Crown
GGBCC
Springline
Load (kN)
Strain (με)
250
200
150
100
50
0
-2000
-1000
0
1000
2000
3000
4000
Concrete
Conc. Int.
GFRP
Syntactic
CFRP
Plastic Strain Development

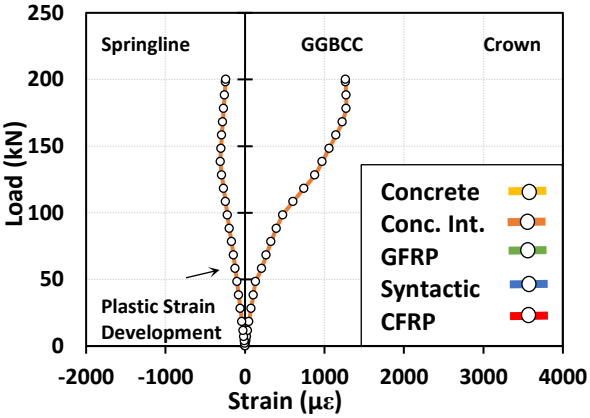
Springline
GGBCC
Crown
Load (kN)
Strain (με)
250
200
150
100
50
0
-2000
-1000
0
1000
2000
3000
4000
Concrete
Conc. Int.
GFRP
Syntactic
CFRP
Plastic Strain Development

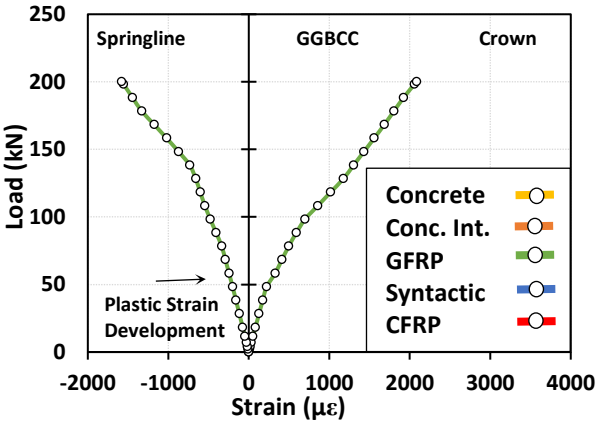
Springline
GGBCC
Crown
Load (kN)
Strain (με)
250
200
150
100
50
0
-2000
-1000
0
1000
2000
3000
4000
Concrete
Conc. Int.
GFRP
Syntactic
CFRP
Plastic Strain Development

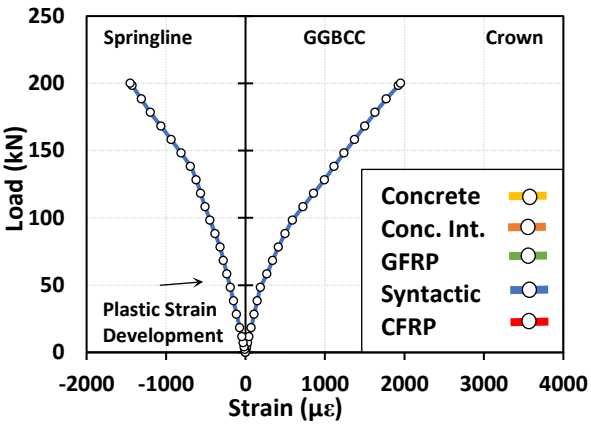
Springline
GGBCC
Crown
Load (kN)
Strain (με)
250
200
150
100
50
0
-2000
-1000
0
1000
2000
3000
4000
Concrete
Conc. Int.
GFRP
Syntactic
CFRP
Plastic Strain Development

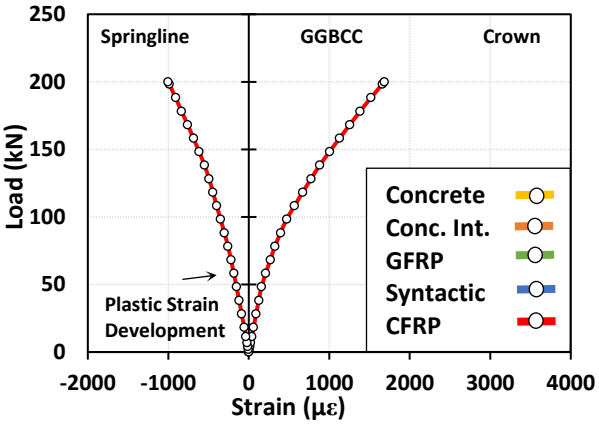
Springline
GGBCC
Crown
Load (kN)
Strain (με)
250
200
150
100
50
0
-2000
-1000
0
1000
2000
3000
4000
Concrete
Conc. Int.
GFRP
Syntactic
CFRP
Plastic Strain Development

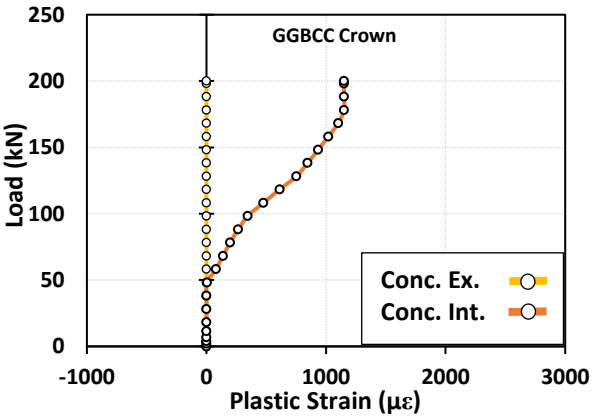
GGBCC Crown
Load (kN)
250
200
150
100
50
0
-1000
0
1000
2000
3000
Plastic Strain (με)
Conc. Ex.
Conc. Int.

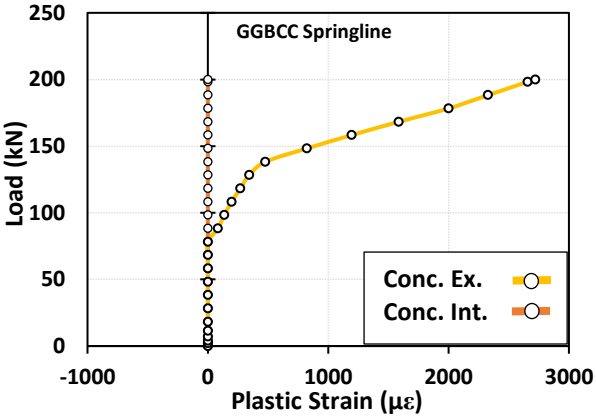
GGBCC Springline
Load (kN)
250
200
150
100
50
0
-1000
0
1000
2000
3000
Plastic Strain (με)
Conc. Ex.
Conc. Int.

Appendix III: Parametric Study Results from ABAQUS

2G2C:

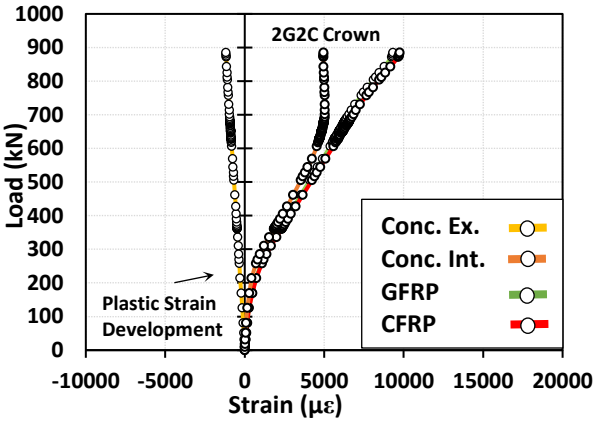

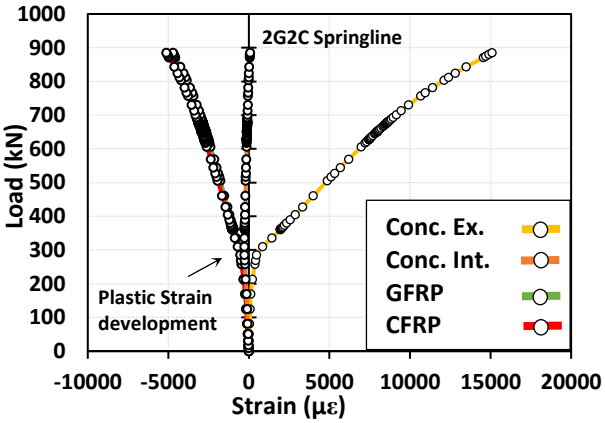

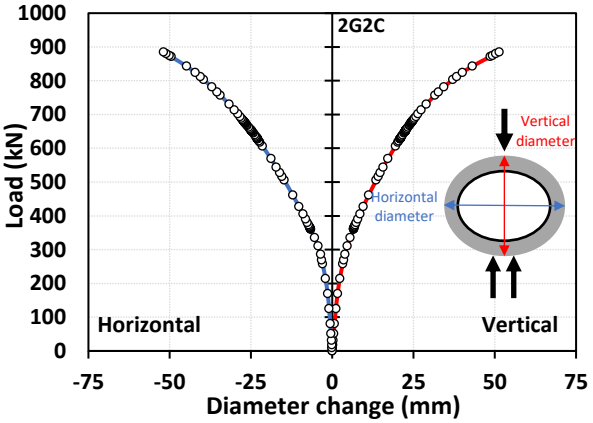

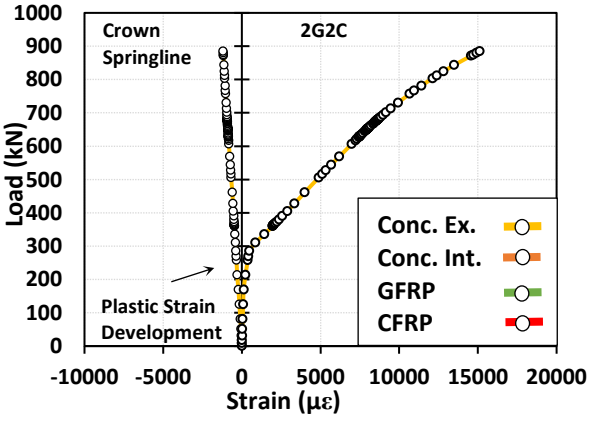

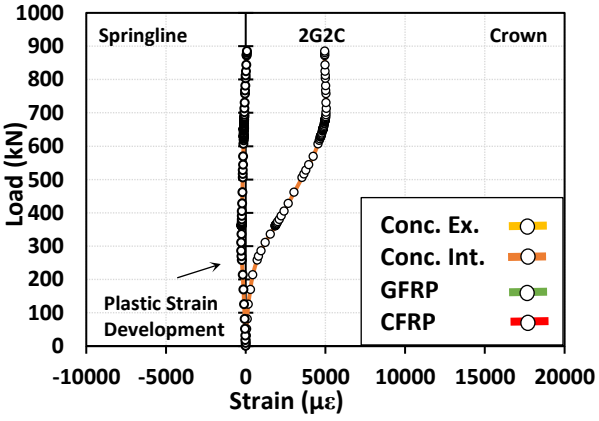

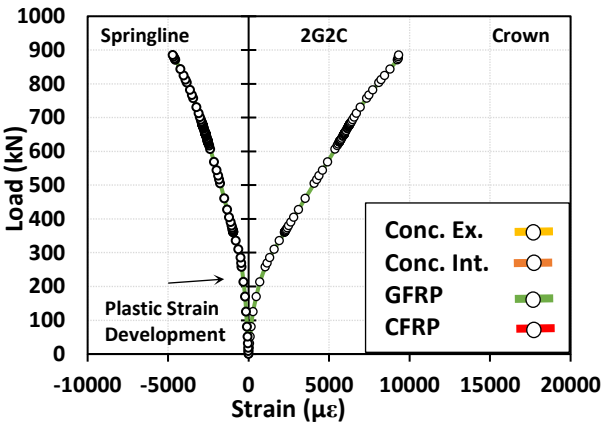

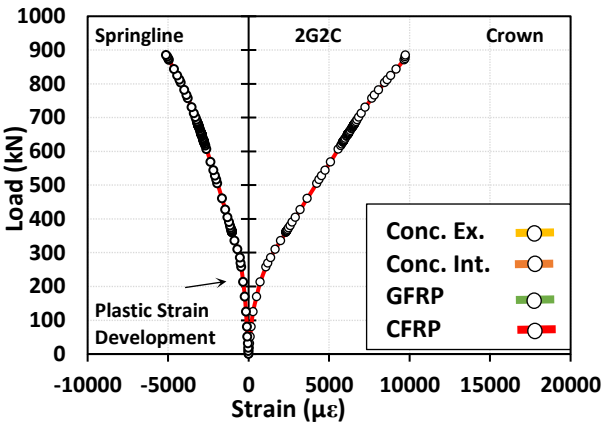

2G2C Plastic Strain:

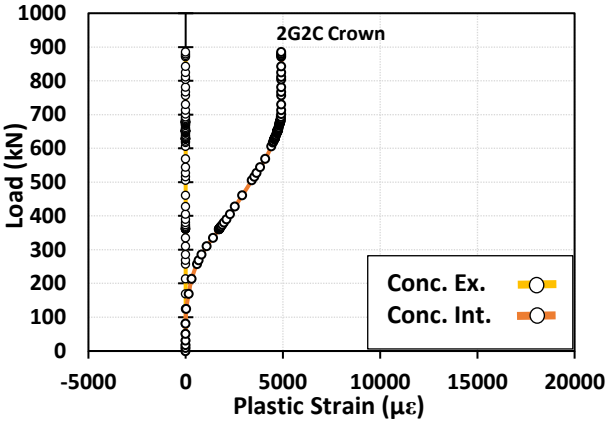

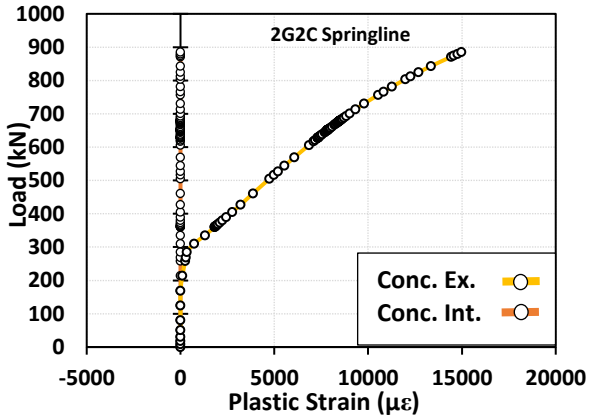

2G B 2C:

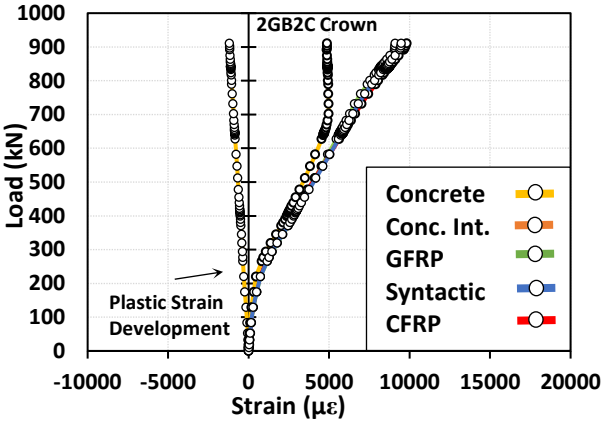
2GB2C Crown
Load (kN)
Strain (με)
Plastic Strain Development
Concrete
Conc. Int.
GFRP
Syntactic
CFRP

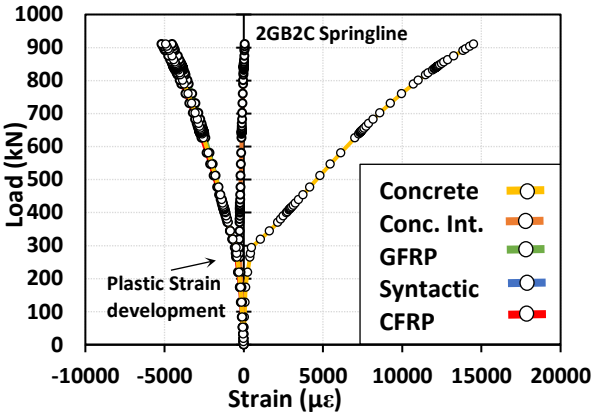
2GB2C Springline
Load (kN)
Strain (με)
Plastic Strain development
Concrete
Conc. Int.
GFRP
Syntactic
CFRP

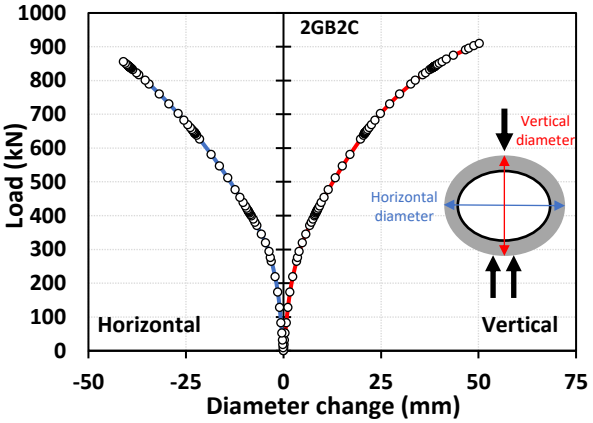
2GB2C
Load (kN)
Diameter change (mm)
Vertical diameter
Horizontal diameter
Horizontal
Vertical

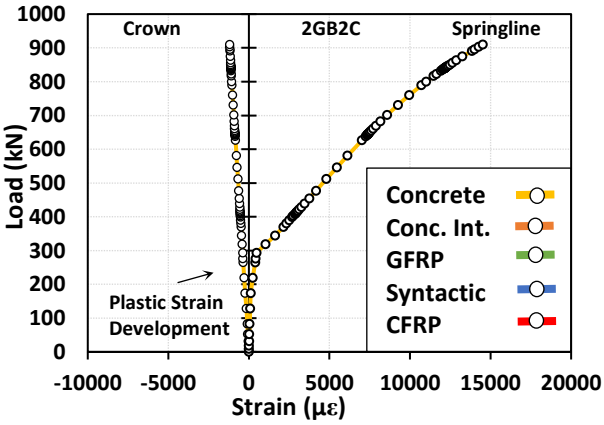
Crown
2GB2C
Springline
Load (kN)
Strain (με)
Plastic Strain Development
Concrete
Conc. Int.
GFRP
Syntactic
CFRP

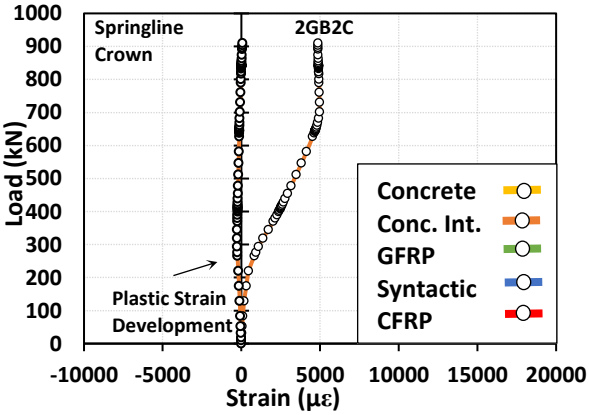
Springline
Crown
2GB2C
Load (kN)
Strain (με)
Plastic Strain Development
Concrete
Conc. Int.
GFRP
Syntactic
CFRP

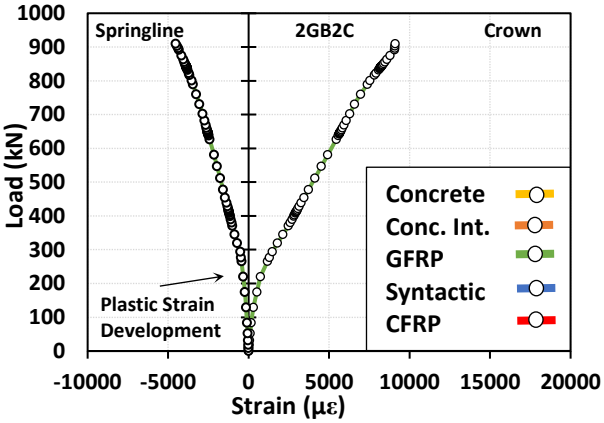

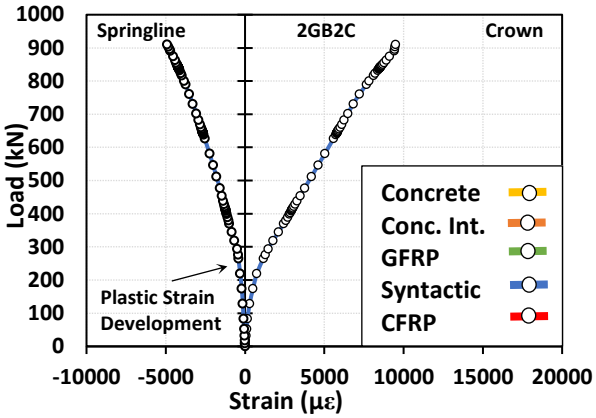

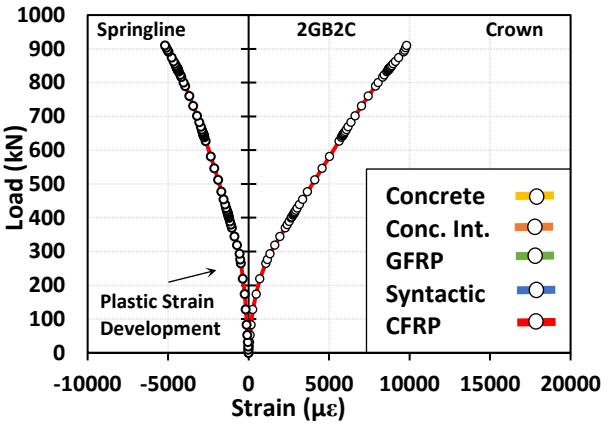

2G B 2C Plastic Strain:

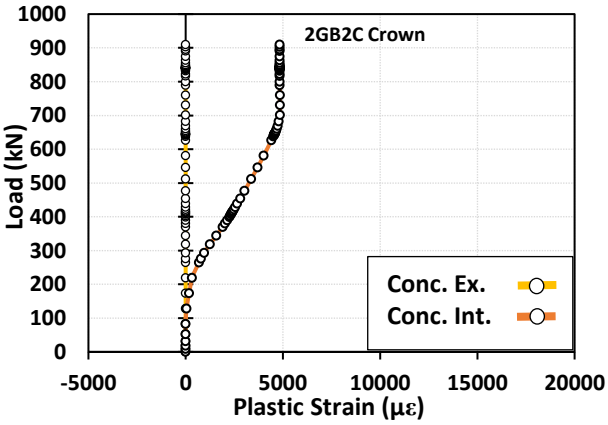

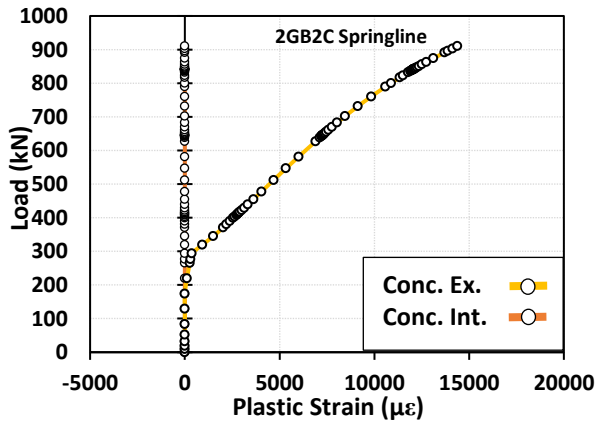

2G 2B 2C:

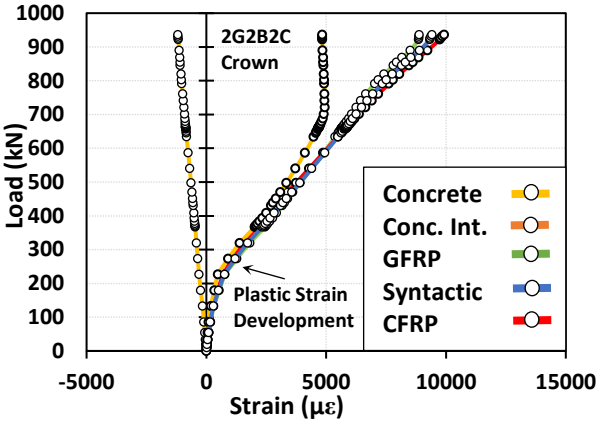
2G2B2C
Crown
Plastic Strain
Development
Concrete
Conc. Int.
GFRP
Syntactic
CFRP
Load (kN)
Strain (με)

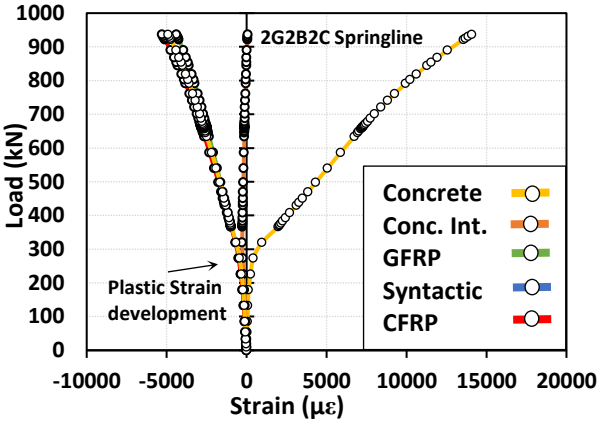
2G2B2C Springline
Plastic Strain
development
Concrete
Conc. Int.
GFRP
Syntactic
CFRP
Load (kN)
Strain (με)

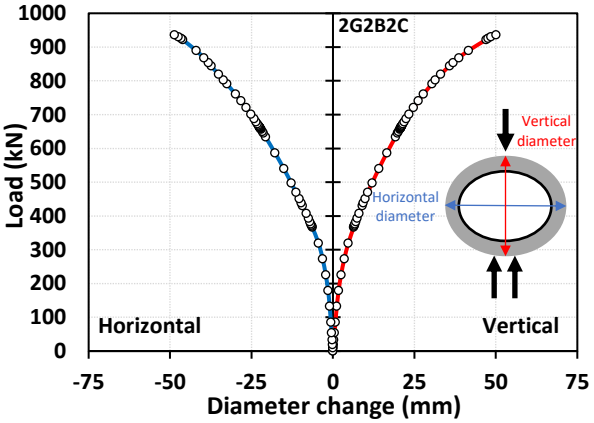
2G2B2C
Vertical
diameter
Horizontal
diameter
Horizontal
Vertical
Load (kN)
Diameter change (mm)

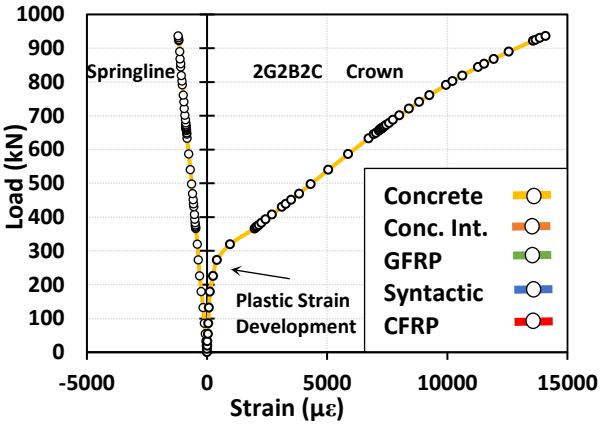
Springline
2G2B2C
Crown
Plastic Strain
Development
Concrete
Conc. Int.
GFRP
Syntactic
CFRP
Load (kN)
Strain (με)

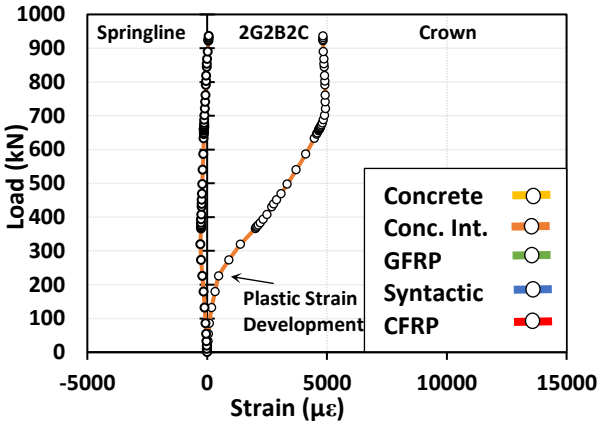
Springline
2G2B2C
Crown
Plastic Strain
Development
Concrete
Conc. Int.
GFRP
Syntactic
CFRP
Load (kN)
Strain (με)

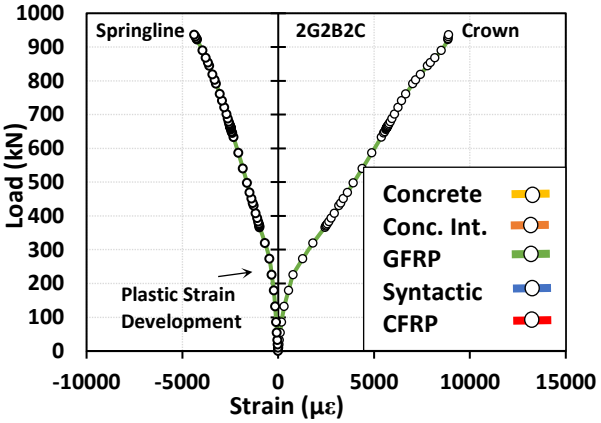

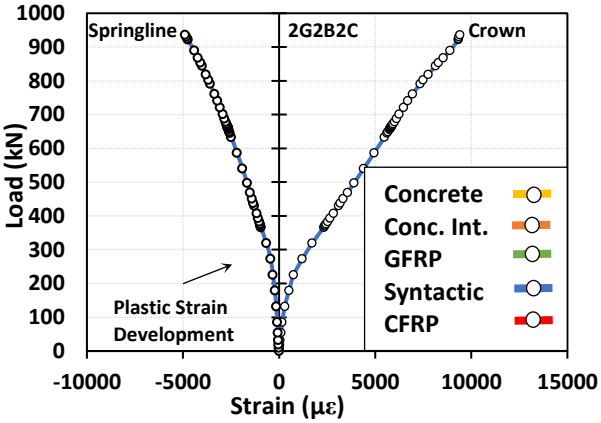

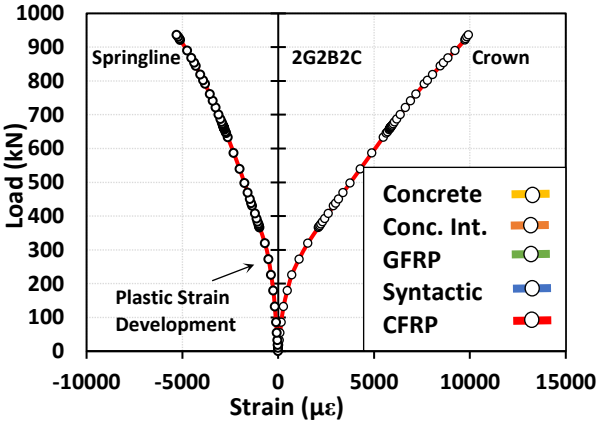

2G 2B 2C Plastic Strain:

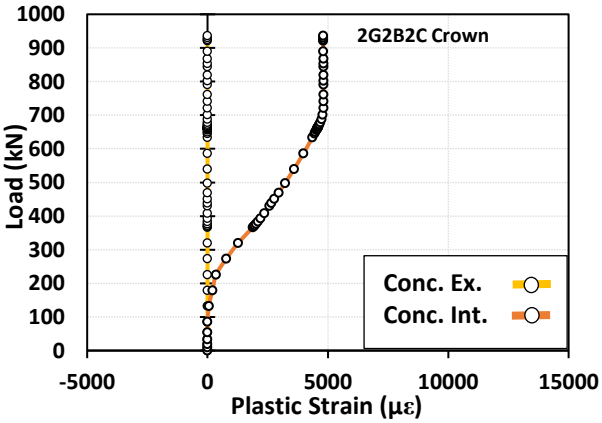

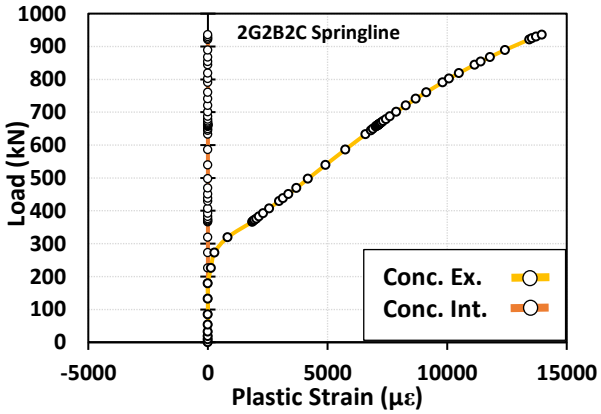

2G 3B 2C:

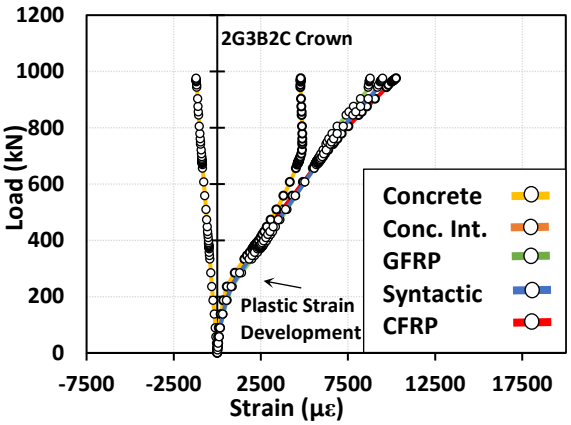
2G3B2C Crown
Load (kN)
Strain (με)
Plastic Strain Development
Concrete
Conc. Int.
GFRP
Syntactic
CFRP

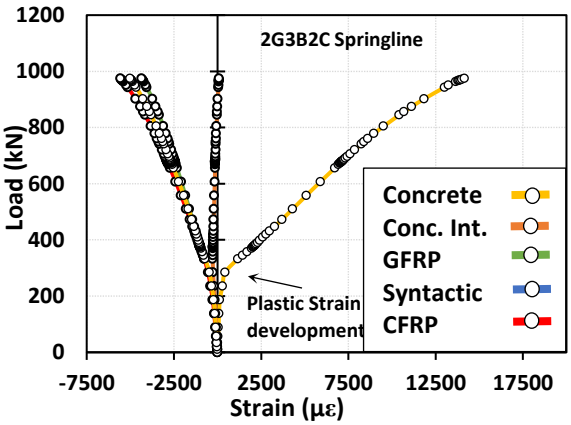
2G3B2C Springline
Load (kN)
Strain (με)
Plastic Strain development
Concrete
Conc. Int.
GFRP
Syntactic
CFRP

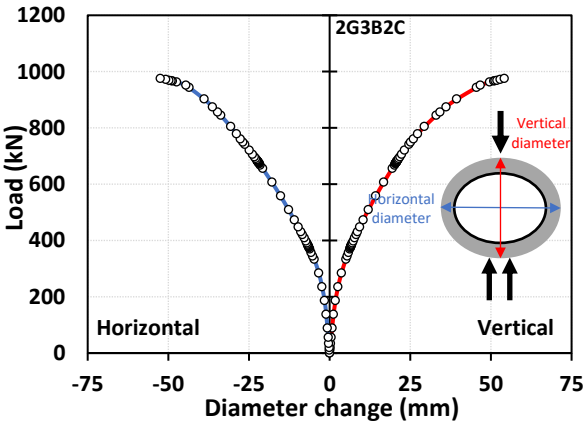
2G3B2C
Load (kN)
Diameter change (mm)
Vertical diameter
Horizontal diameter
Horizontal
Vertical

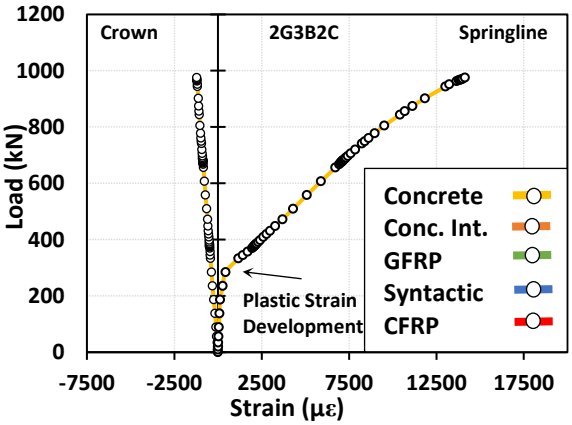
Crown
2G3B2C
Springline
Load (kN)
Strain (με)
Plastic Strain Development
Concrete
Conc. Int.
GFRP
Syntactic
CFRP

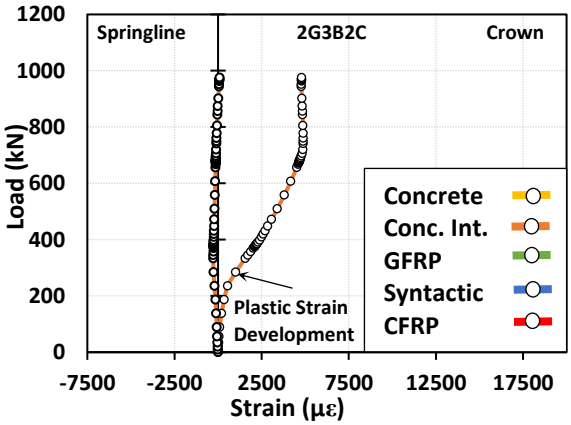
Springline
2G3B2C
Crown
Load (kN)
Strain (με)
Plastic Strain Development
Concrete
Conc. Int.
GFRP
Syntactic
CFRP

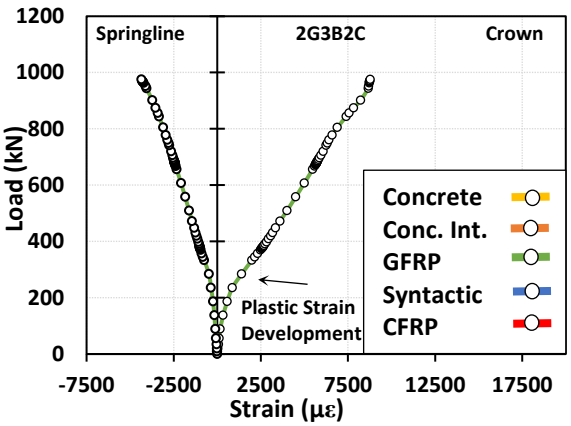

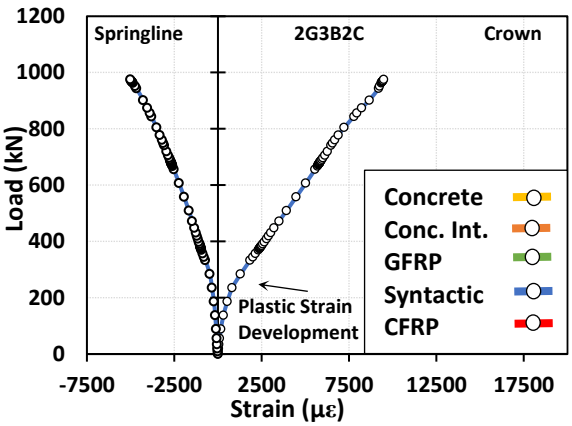

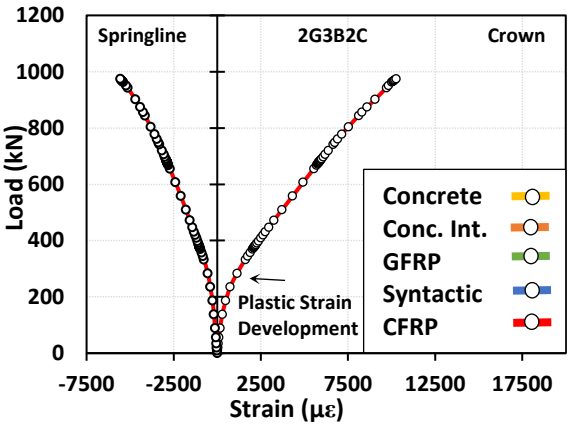

2G 3B 2C Plastic Strain:

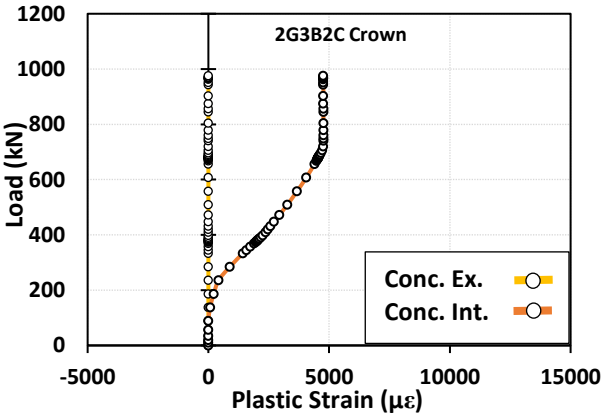

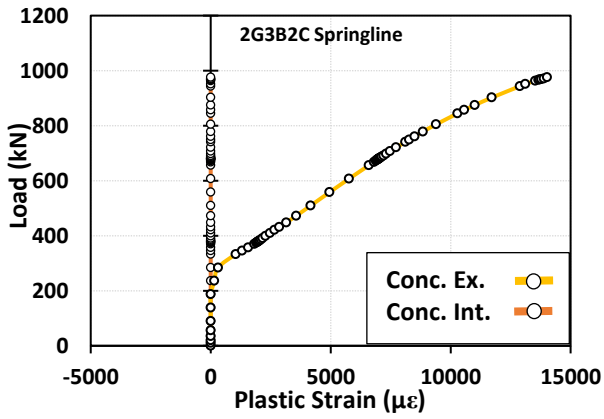

4G 4C:

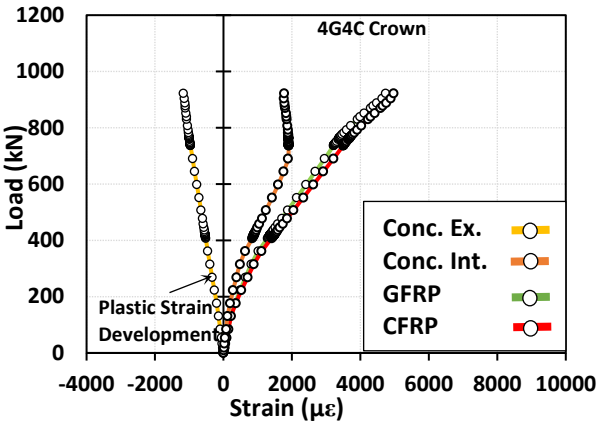
4G4C Crown
Load (kN)
Strain (με)
Plastic Strain Development
Conc. Ex.
Conc. Int.
GFRP
CFRP

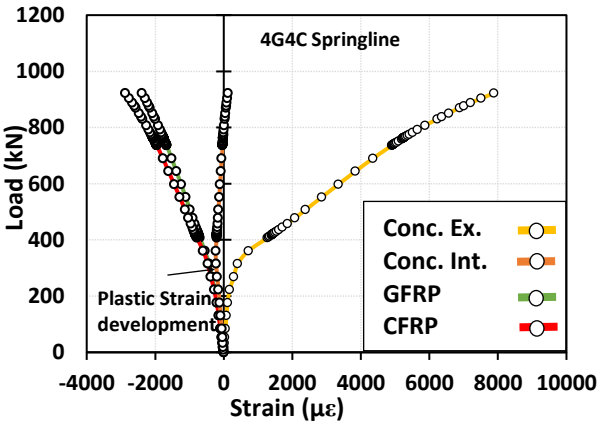
4G4C Springline
Load (kN)
Strain (με)
Plastic Strain development
Conc. Ex.
Conc. Int.
GFRP
CFRP

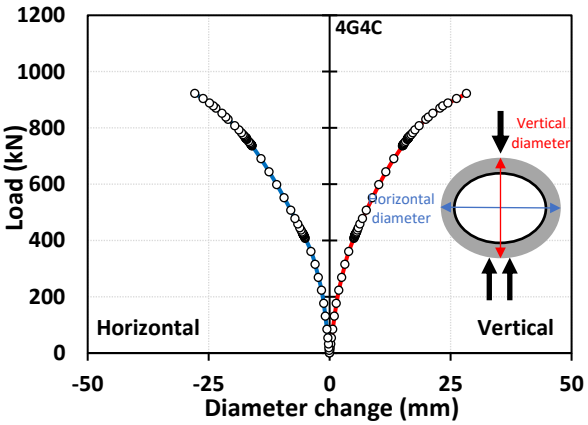
4G4C
Load (kN)
Diameter change (mm)
Vertical diameter
Horizontal diameter
Horizontal
Vertical

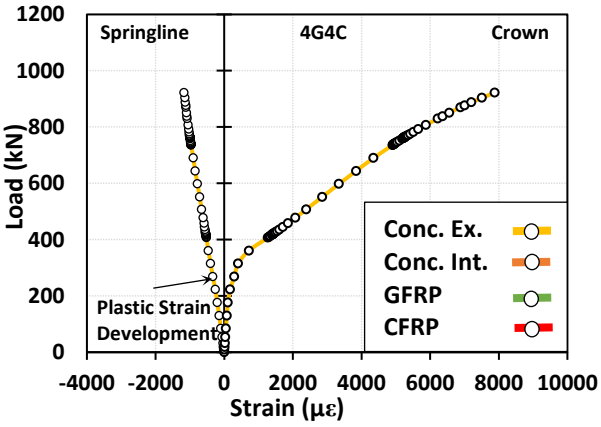
Springline
4G4C
Crown
Load (kN)
Strain (με)
Plastic Strain Development
Conc. Ex.
Conc. Int.
GFRP
CFRP

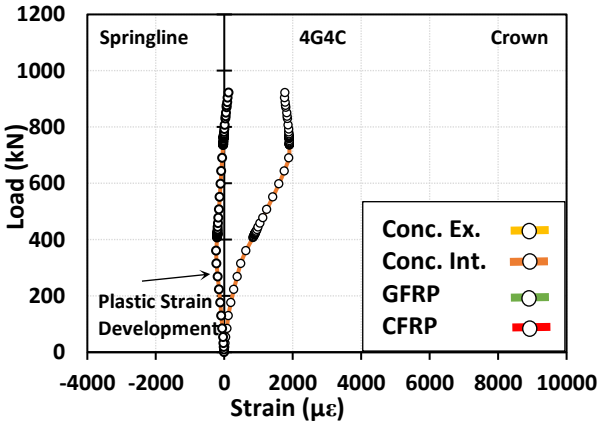
Springline
4G4C
Crown
Load (kN)
Strain (με)
Plastic Strain Development
Conc. Ex.
Conc. Int.
GFRP
CFRP

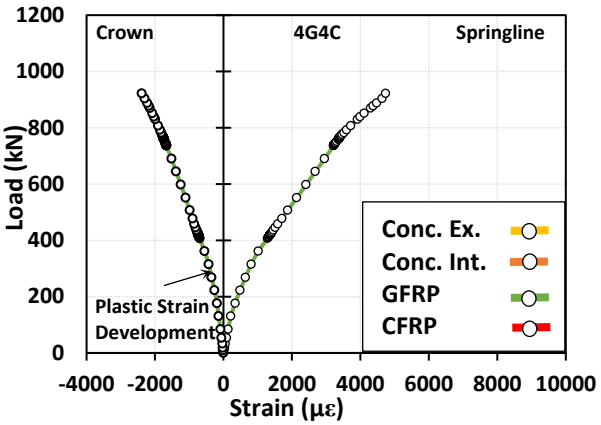

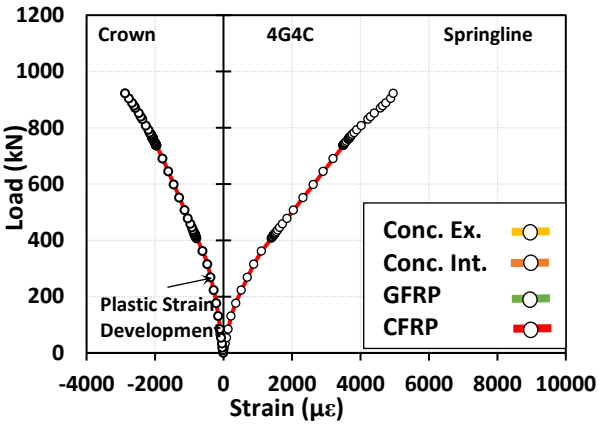

4G 4C Plastic Strain:

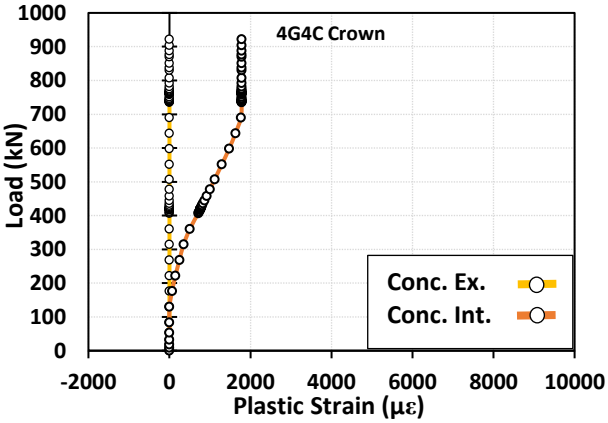

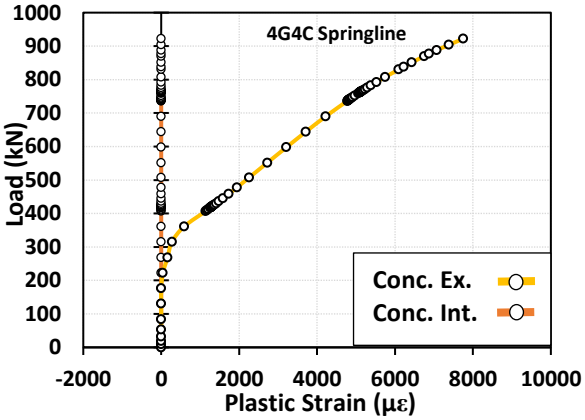

4G B 4C:

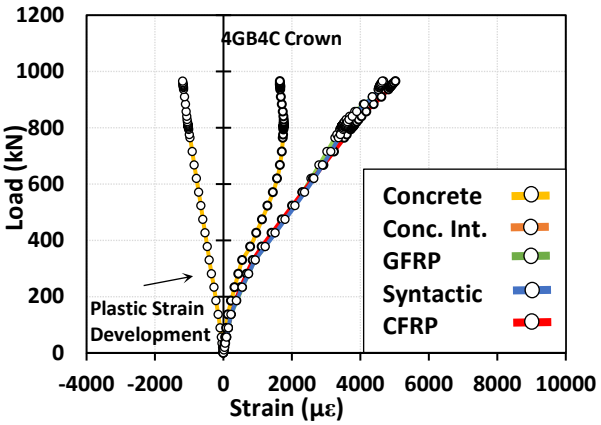
4GB4C Crown
Load (kN)
Strain (με)
Concrete
Conc. Int.
GFRP
Syntactic
CFRP
Plastic Strain
Development

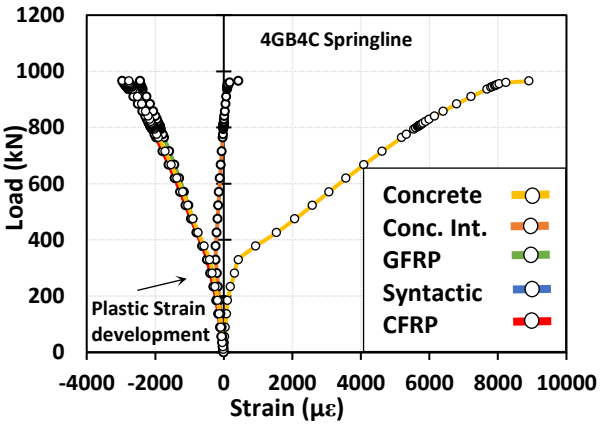
4GB4C Springline
Load (kN)
Strain (με)
Concrete
Conc. Int.
GFRP
Syntactic
CFRP
Plastic Strain
development

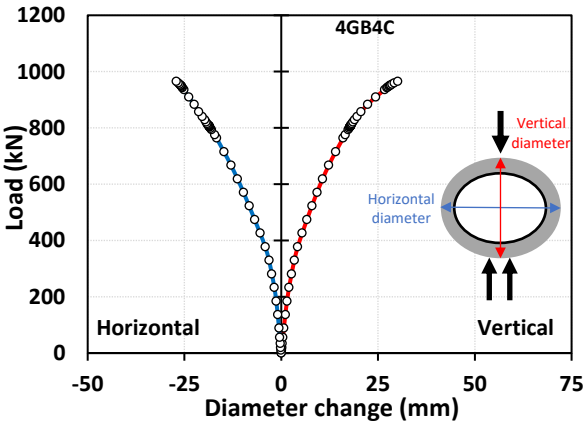
4GB4C
Load (kN)
Diameter change (mm)
Vertical
diameter
Horizontal
diameter
Horizontal
Vertical

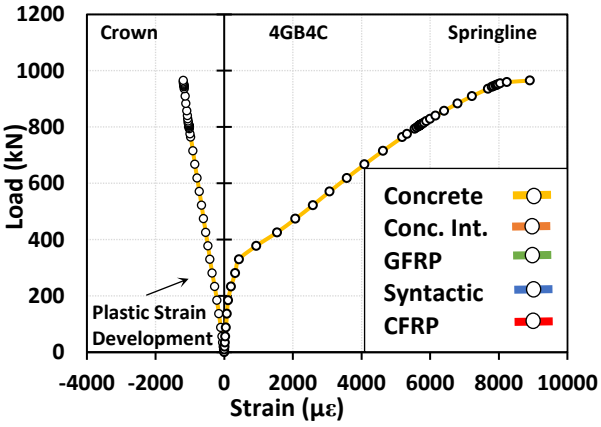
Crown
4GB4C
Springline
Load (kN)
Strain (με)
Concrete
Conc. Int.
GFRP
Syntactic
CFRP
Plastic Strain
Development

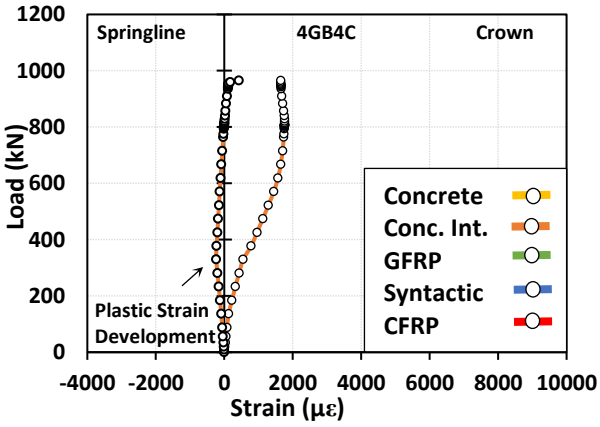
Springline
4GB4C
Crown
Load (kN)
Strain (με)
Concrete
Conc. Int.
GFRP
Syntactic
CFRP
Plastic Strain
Development

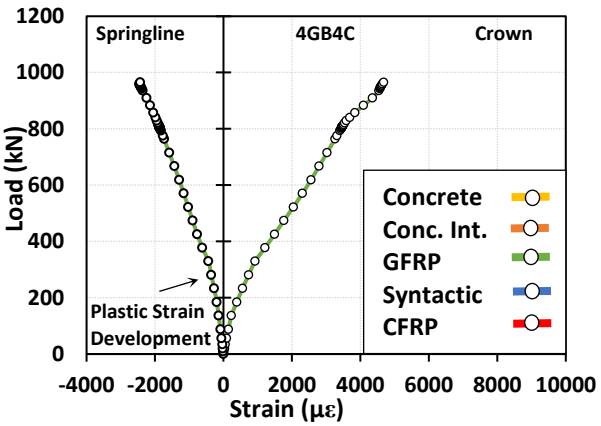

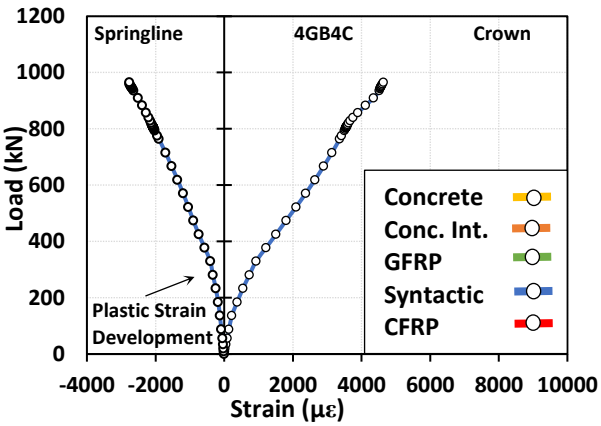

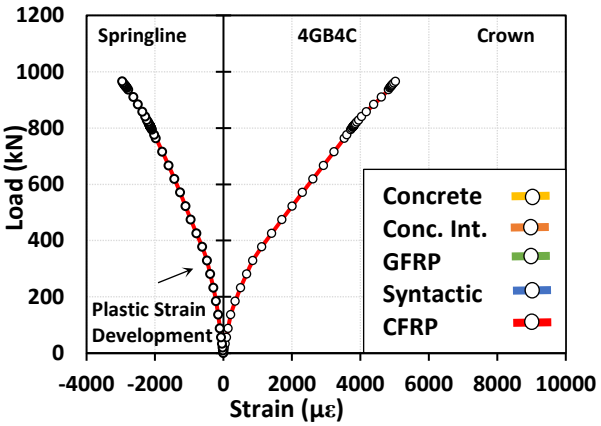

4G B 4C Plastic Strain:

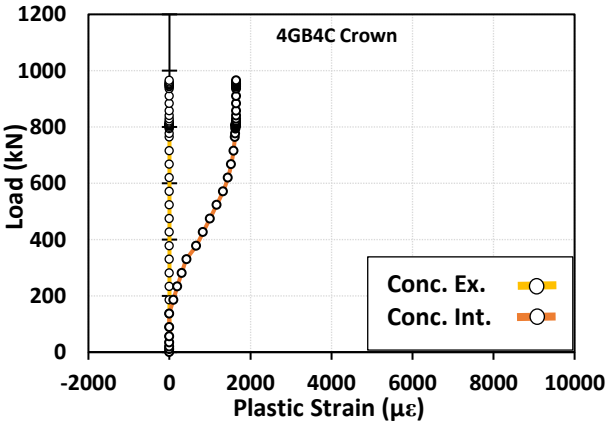

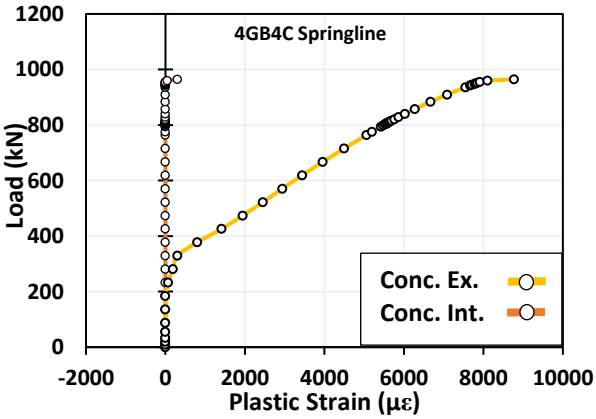

4G 2B 4C Plastic Strain:

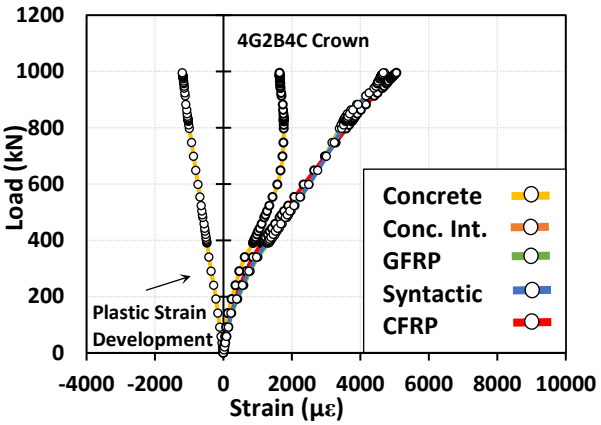

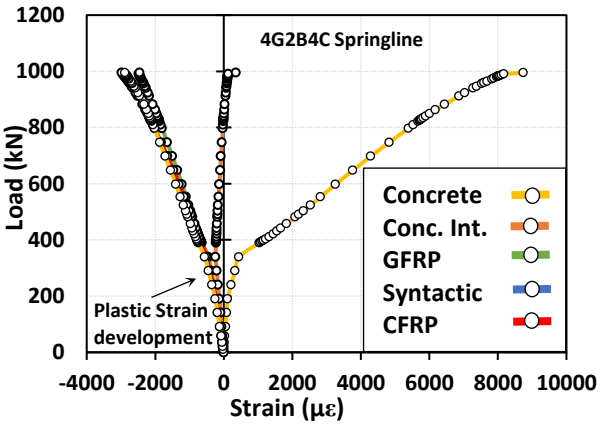

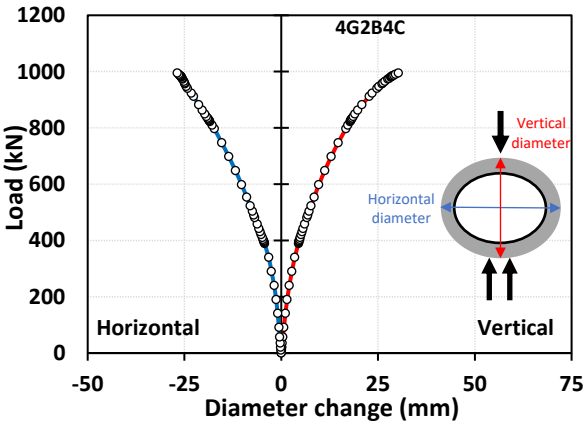

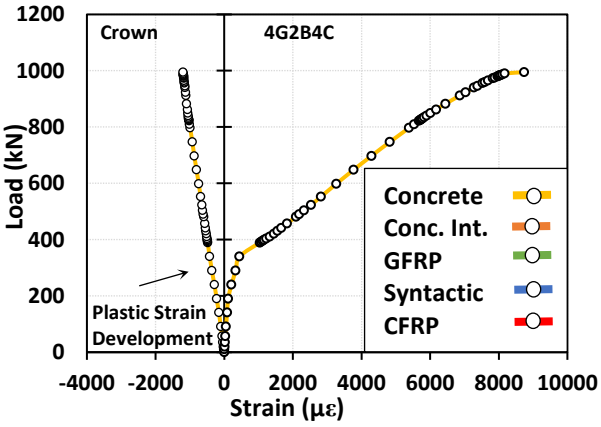

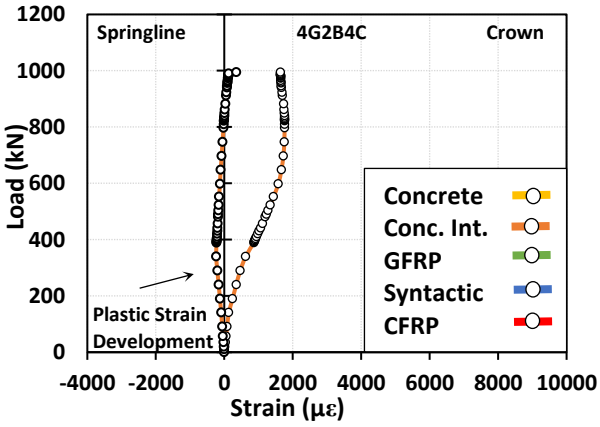

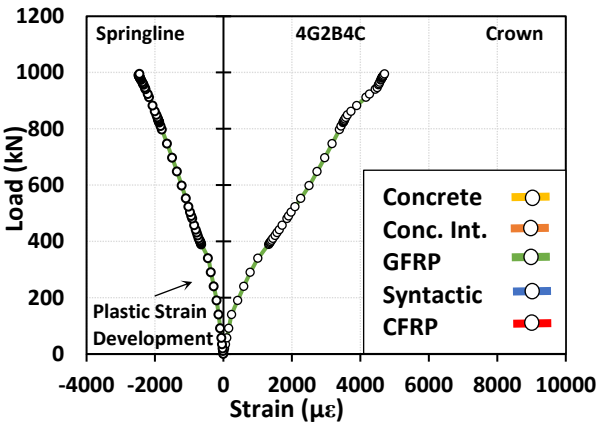

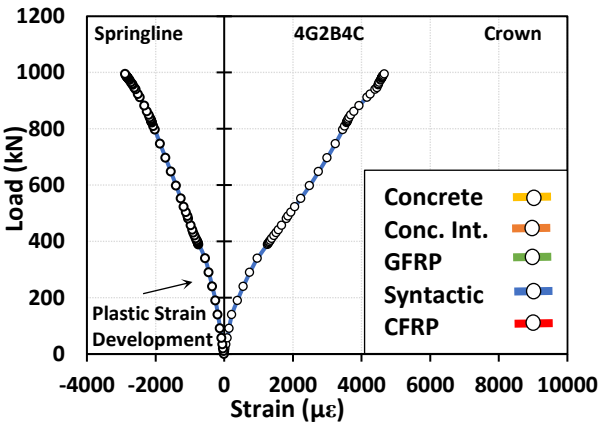

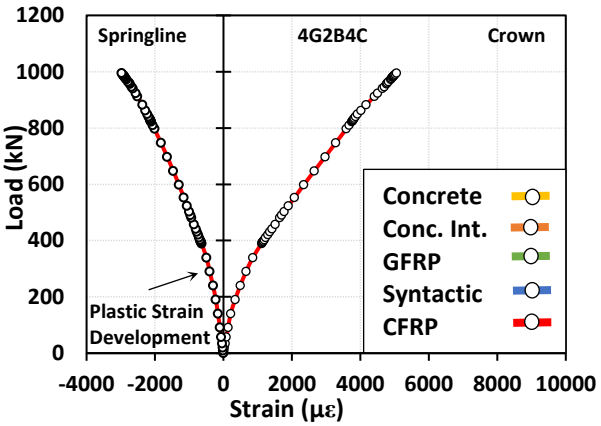

4G 2B 4C Plastic Strain:

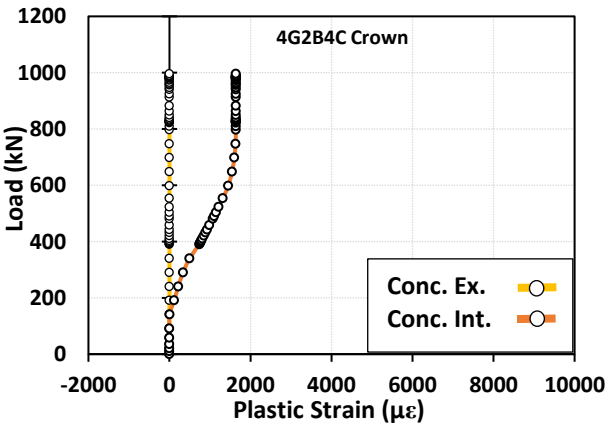

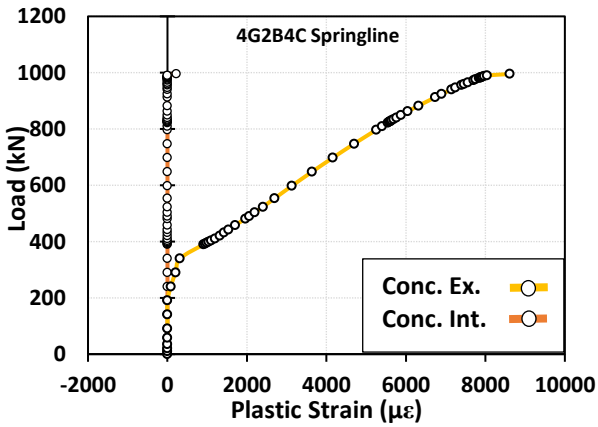

4G 3B 4C:

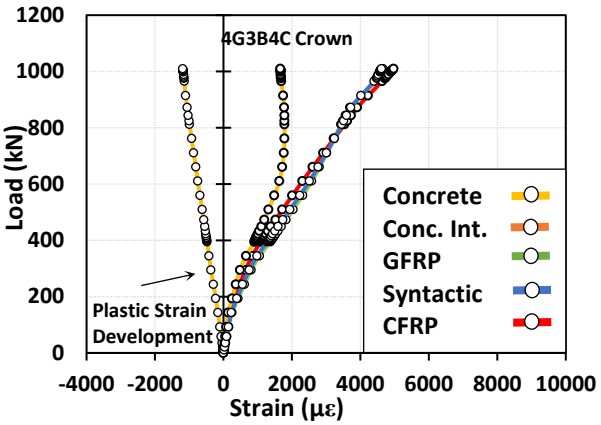
4G3B4C Crown
Load (kN)
Strain (με)
Plastic Strain Development
Concrete
Conc. Int.
GFRP
Syntactic
CFRP

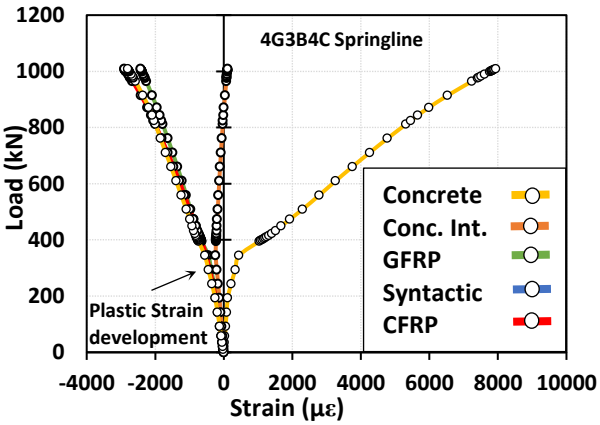
4G3B4C Springline
Load (kN)
Strain (με)
Plastic Strain development
Concrete
Conc. Int.
GFRP
Syntactic
CFRP

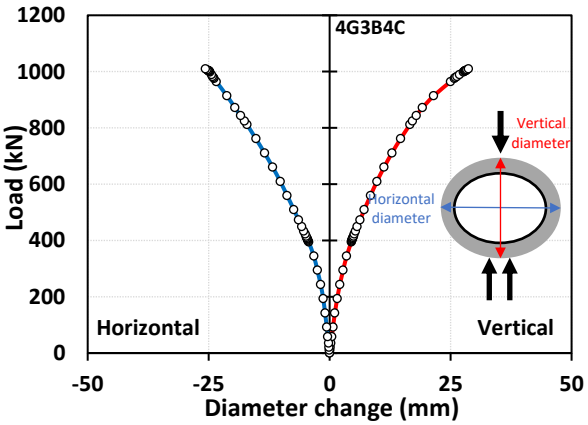
4G3B4C
Load (kN)
Diameter change (mm)
Vertical diameter
Horizontal diameter
Horizontal
Vertical

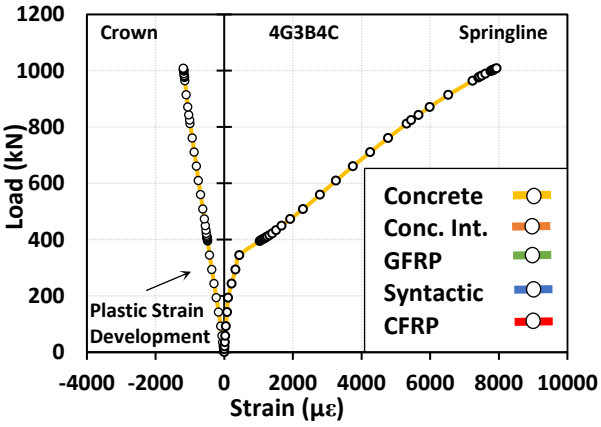
Crown
4G3B4C
Springline
Load (kN)
Strain (με)
Plastic Strain Development
Concrete
Conc. Int.
GFRP
Syntactic
CFRP

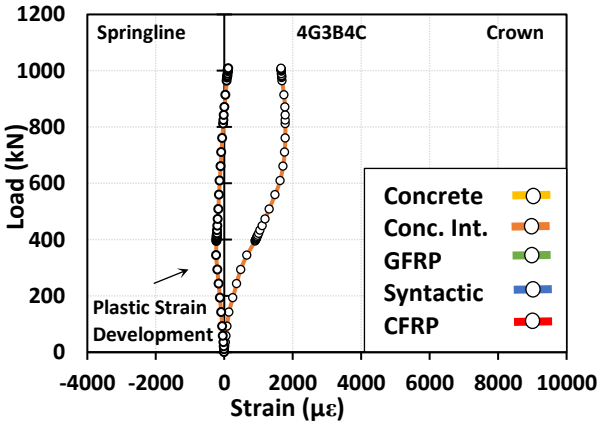
Springline
4G3B4C
Crown
Load (kN)
Strain (με)
Plastic Strain Development
Concrete
Conc. Int.
GFRP
Syntactic
CFRP

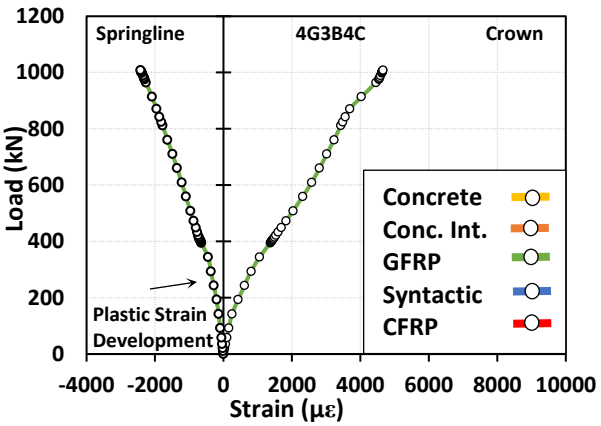

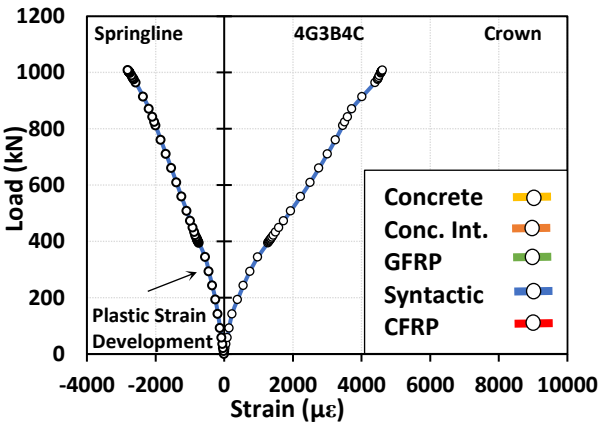

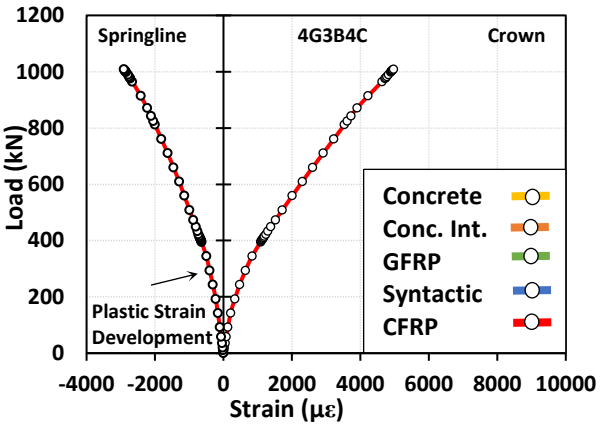

4G 3B 4C Plastic Strain:

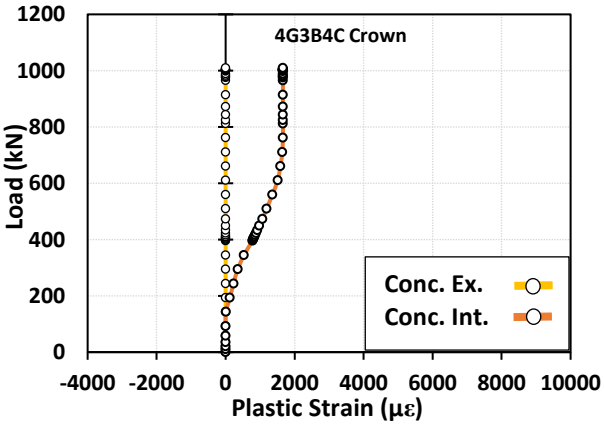

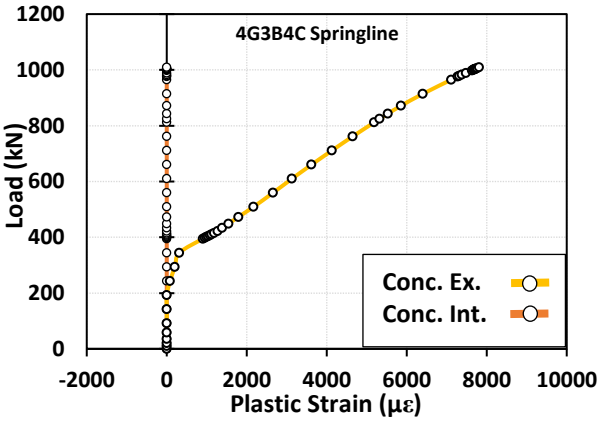

6G 6C:

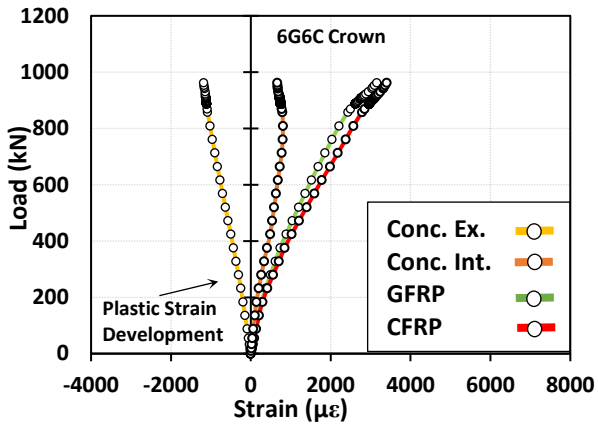
6G6C Crown
Load (kN)
Strain (με)
Plastic Strain Development
Conc. Ex.
Conc. Int.
GFRP
CFRP

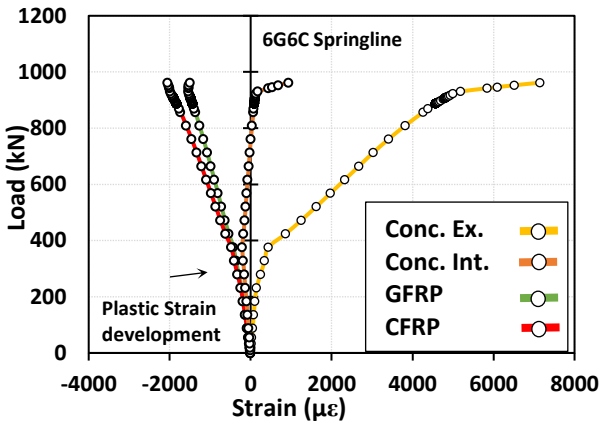
6G6C Springline
Load (kN)
Strain (με)
Plastic Strain development
Conc. Ex.
Conc. Int.
GFRP
CFRP

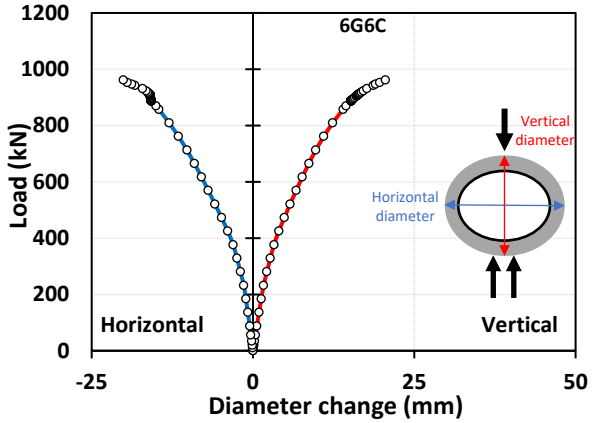
6G6C
Load (kN)
Diameter change (mm)
Vertical diameter
Horizontal diameter
Horizontal
Vertical

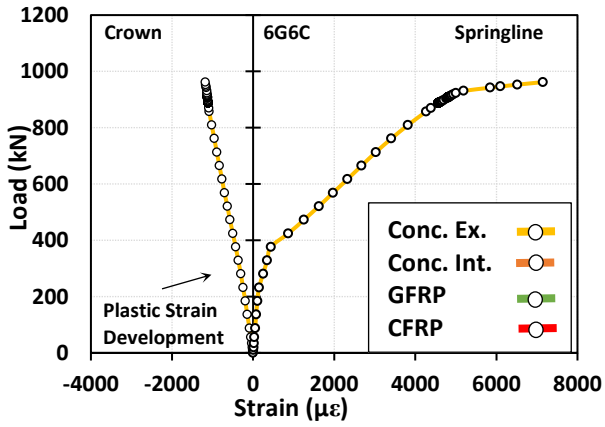
Crown
6G6C
Springline
Load (kN)
Strain (με)
Plastic Strain Development
Conc. Ex.
Conc. Int.
GFRP
CFRP

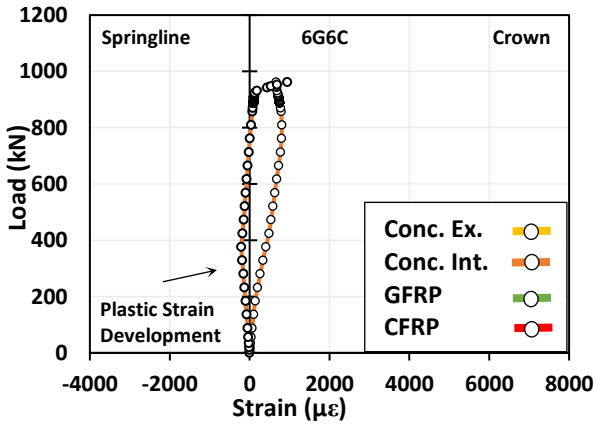
Springline
6G6C
Crown
Load (kN)
Strain (με)
Plastic Strain Development
Conc. Ex.
Conc. Int.
GFRP
CFRP

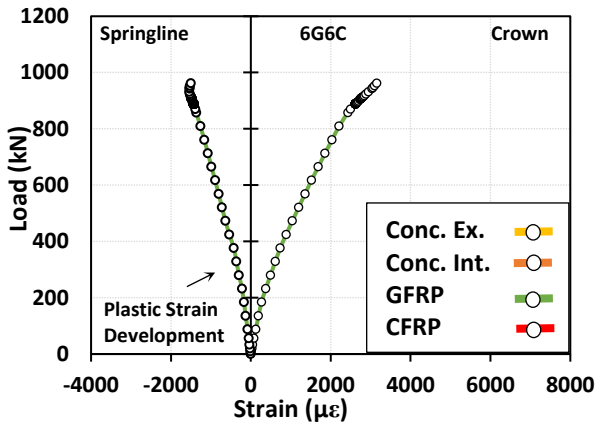

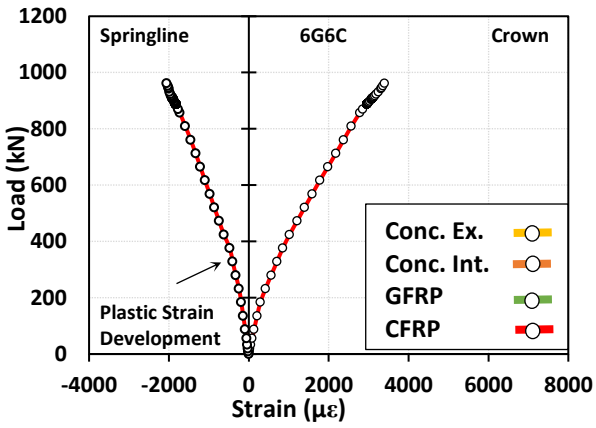

6G 6C Plastic Strain:

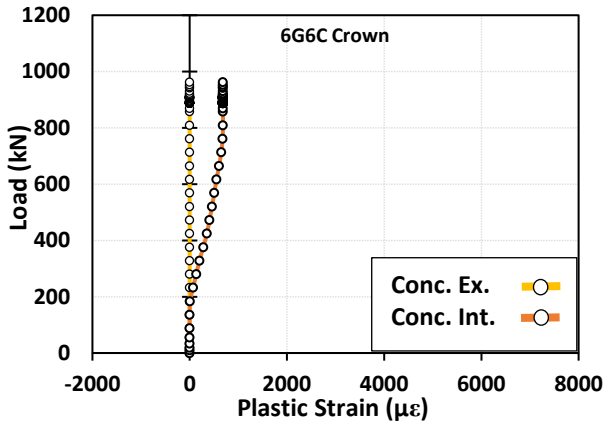

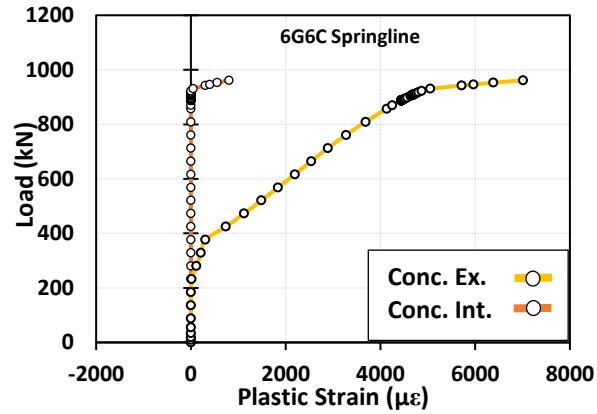

6G B 6C:

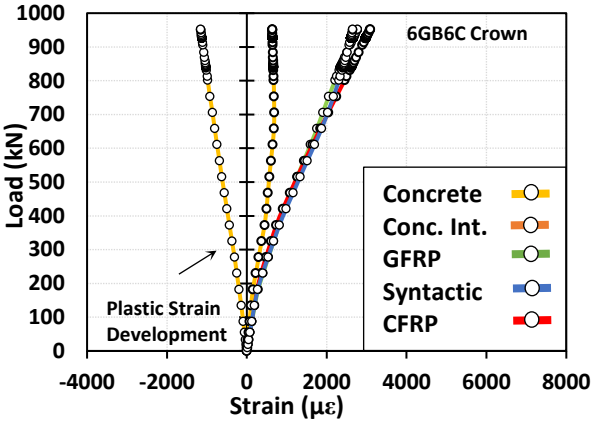
6GB6C Crown
Load (kN)
Strain (με)
Plastic Strain Development
Concrete
Conc. Int.
GFRP
Syntactic
CFRP

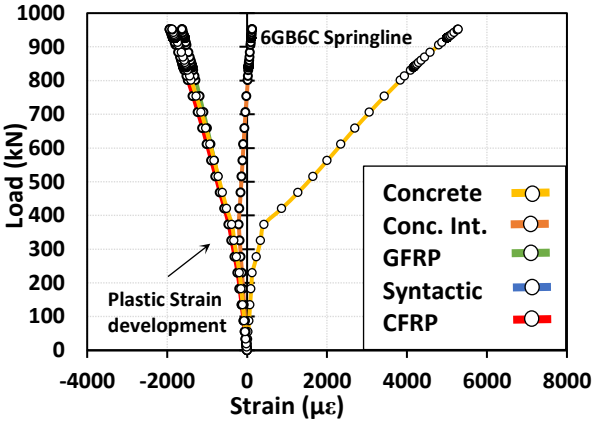
6GB6C Springline
Load (kN)
Strain (με)
Plastic Strain development
Concrete
Conc. Int.
GFRP
Syntactic
CFRP

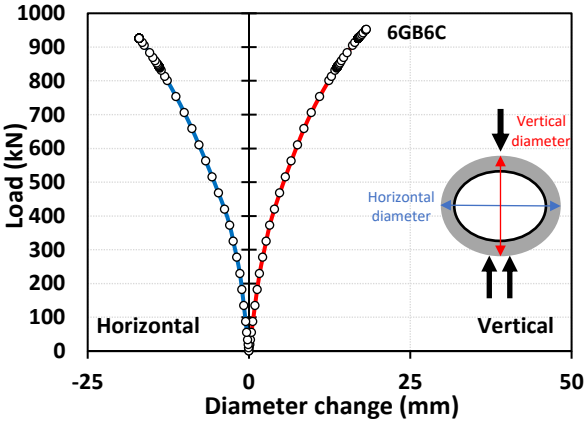
6GB6C
Load (kN)
Diameter change (mm)
Vertical diameter
Horizontal diameter
Horizontal
Vertical

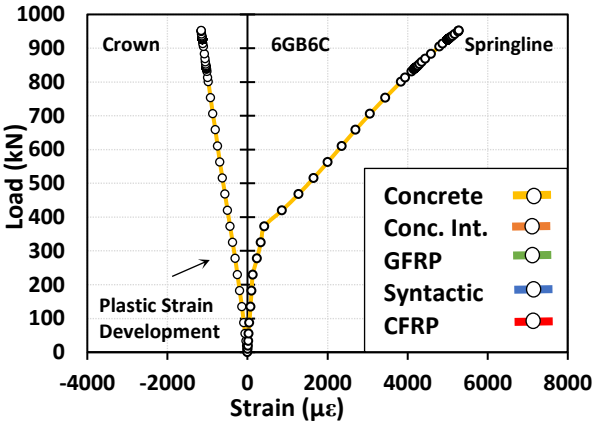
Crown
6GB6C
Springline
Load (kN)
Strain (με)
Plastic Strain Development
Concrete
Conc. Int.
GFRP
Syntactic
CFRP

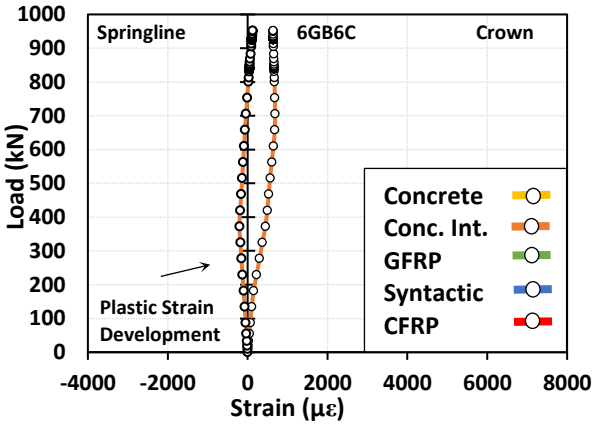
Springline
6GB6C
Crown
Load (kN)
Strain (με)
Plastic Strain Development
Concrete
Conc. Int.
GFRP
Syntactic
CFRP

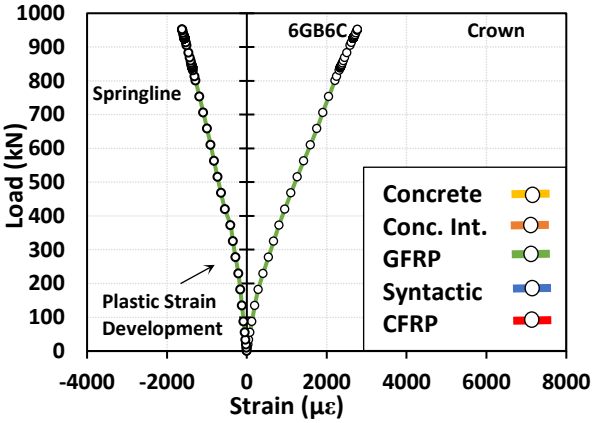

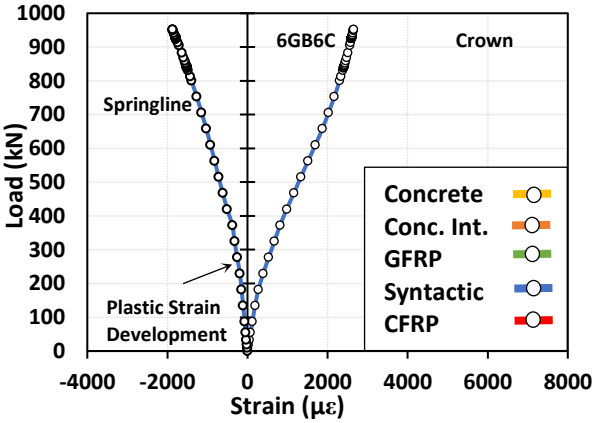

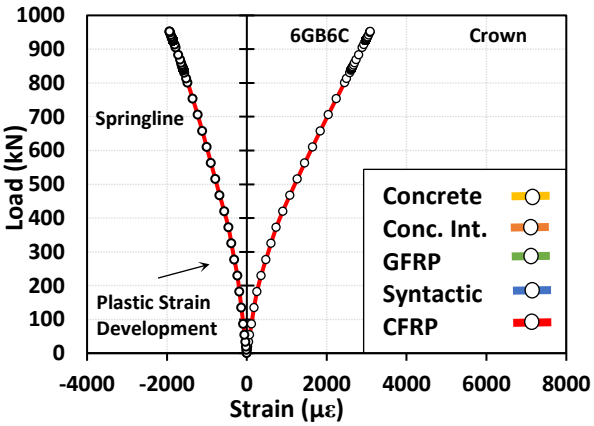

6G B 6C Plastic Strain:

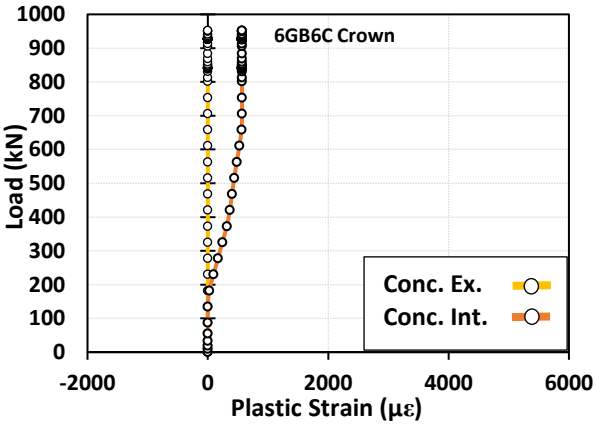

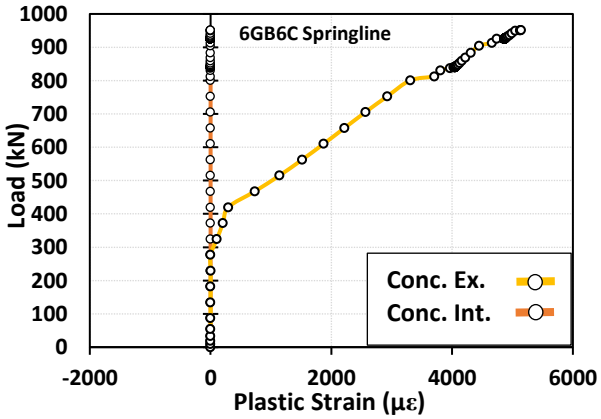

6G 2B 6C:

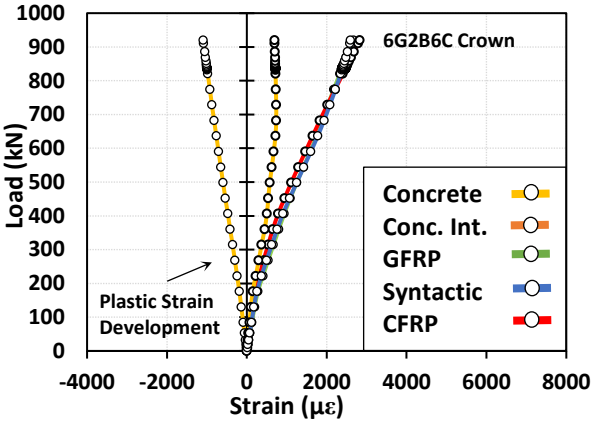
6G2B6C Crown
Load (kN)
Strain (με)
Plastic Strain Development
Concrete
Conc. Int.
GFRP
Syntactic
CFRP

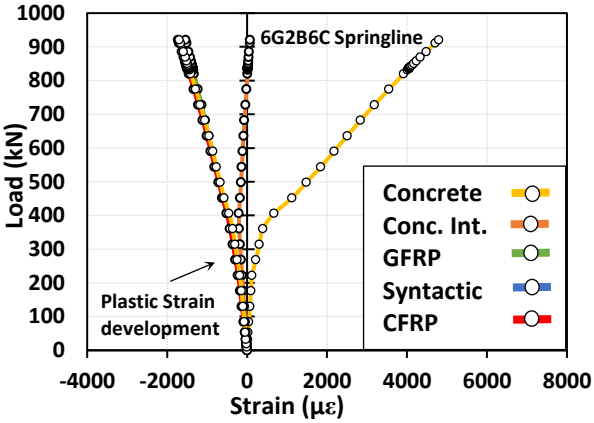
6G2B6C Springline
Load (kN)
Strain (με)
Plastic Strain development
Concrete
Conc. Int.
GFRP
Syntactic
CFRP

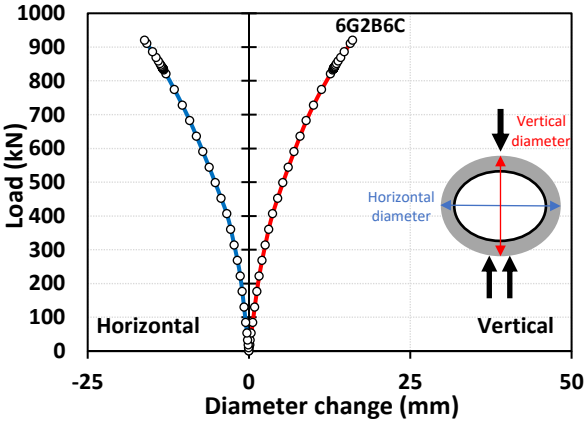
6G2B6C
Load (kN)
Diameter change (mm)
Vertical diameter
Horizontal diameter
Horizontal
Vertical

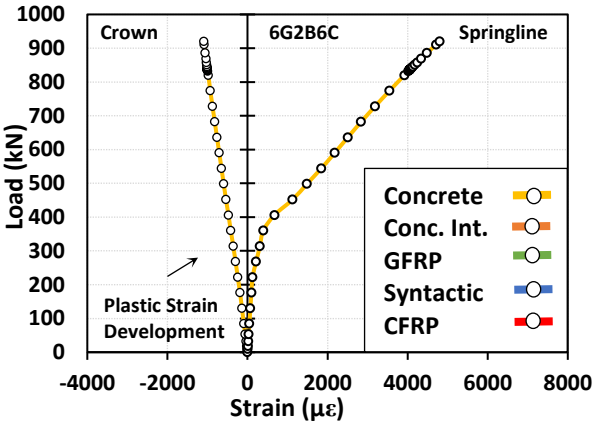
Crown
6G2B6C
Springline
Load (kN)
Strain (με)
Plastic Strain Development
Concrete
Conc. Int.
GFRP
Syntactic
CFRP

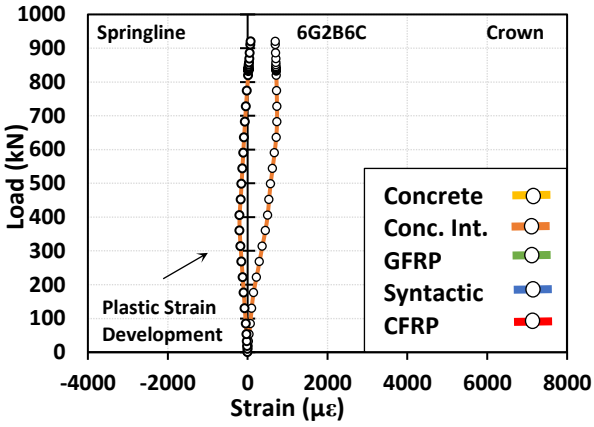
Springline
6G2B6C
Crown
Load (kN)
Strain (με)
Plastic Strain Development
Concrete
Conc. Int.
GFRP
Syntactic
CFRP

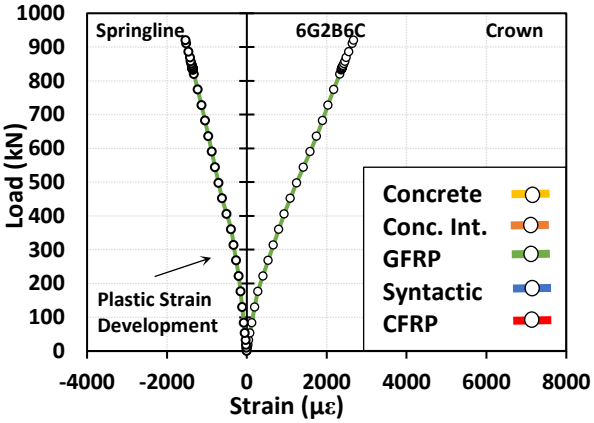

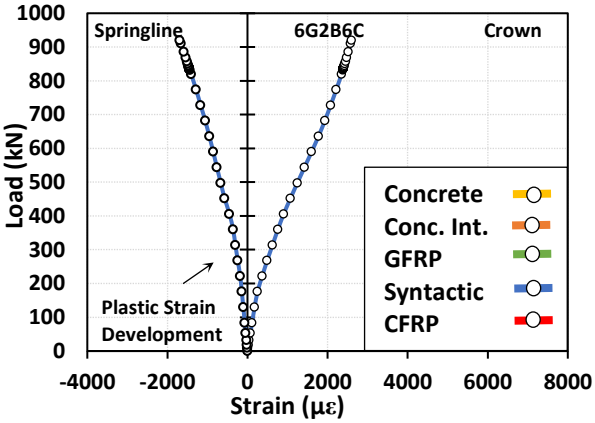

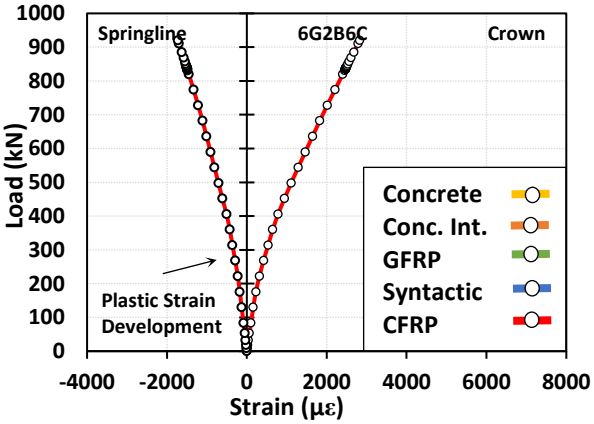

6G 2B 6C Plastic Strain:

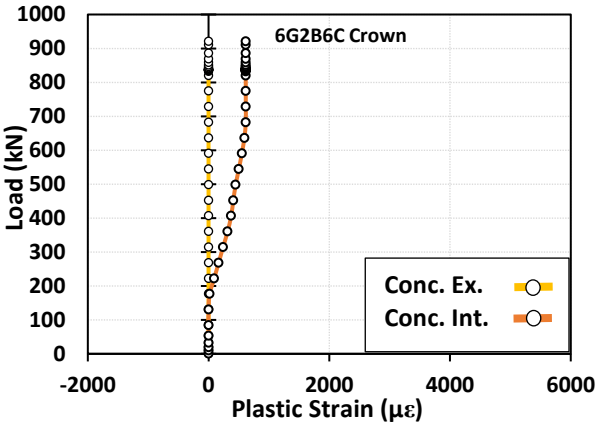

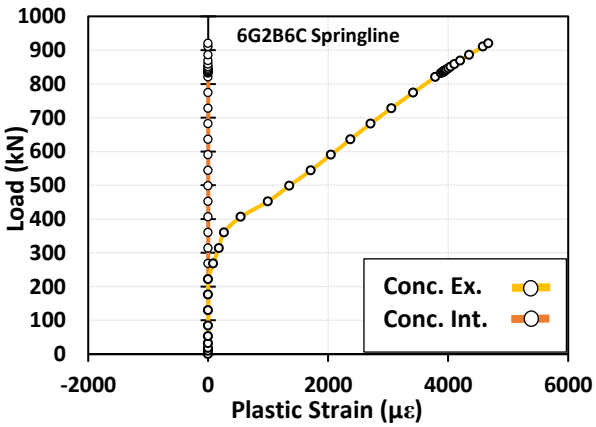

6G 3B 6C:

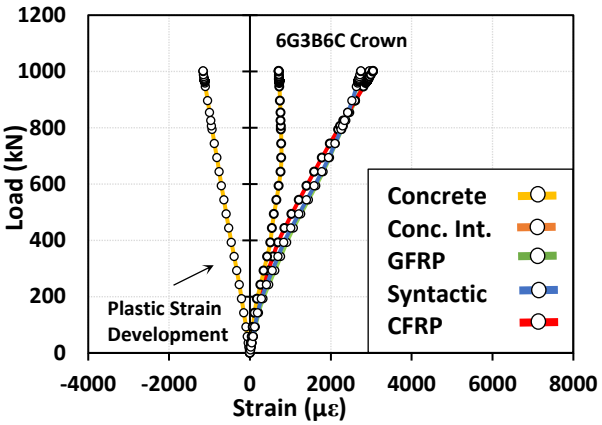
6G3B6C Crown
Load (kN)
Strain (με)
Plastic Strain Development
Concrete
Conc. Int.
GFRP
Syntactic
CFRP

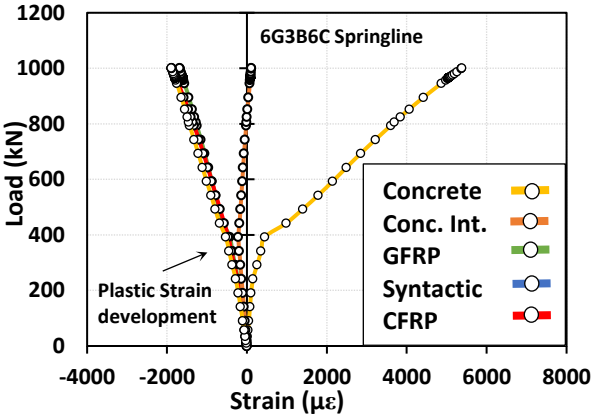
6G3B6C Springline
Load (kN)
Strain (με)
Plastic Strain development
Concrete
Conc. Int.
GFRP
Syntactic
CFRP

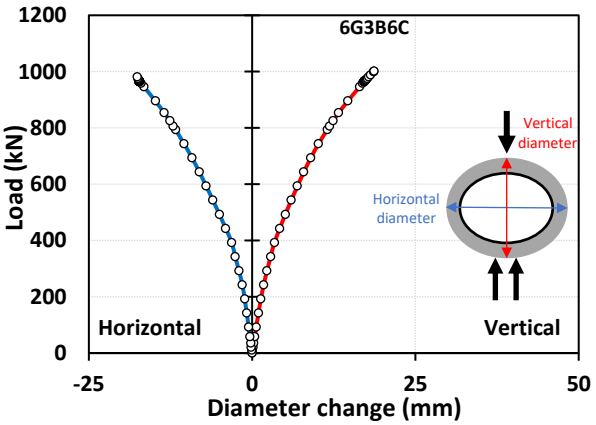
6G3B6C
Load (kN)
Diameter change (mm)
Vertical diameter
Horizontal diameter
Horizontal
Vertical

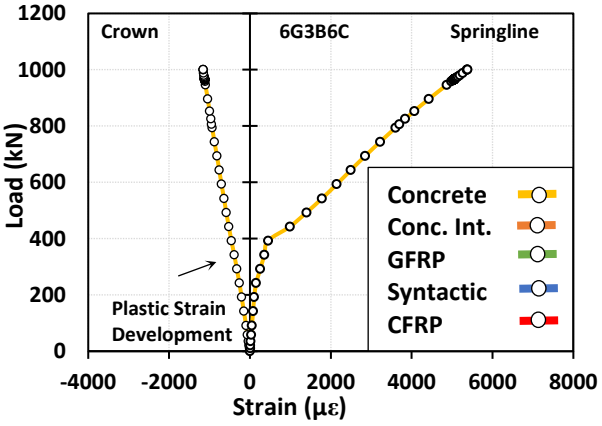
Crown
6G3B6C
Springline
Load (kN)
Strain (με)
Plastic Strain Development
Concrete
Conc. Int.
GFRP
Syntactic
CFRP

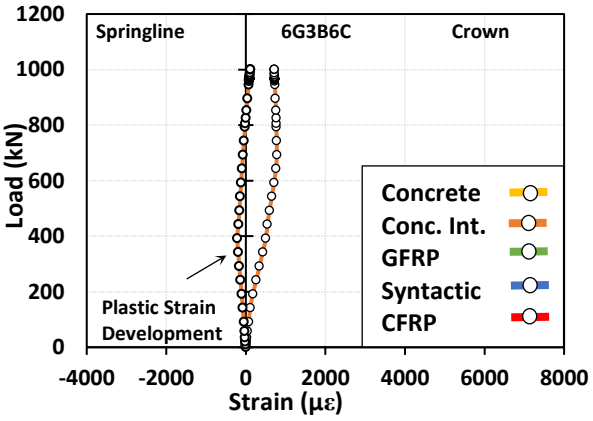
Springline
6G3B6C
Crown
Load (kN)
Strain (με)
Plastic Strain Development
Concrete
Conc. Int.
GFRP
Syntactic
CFRP

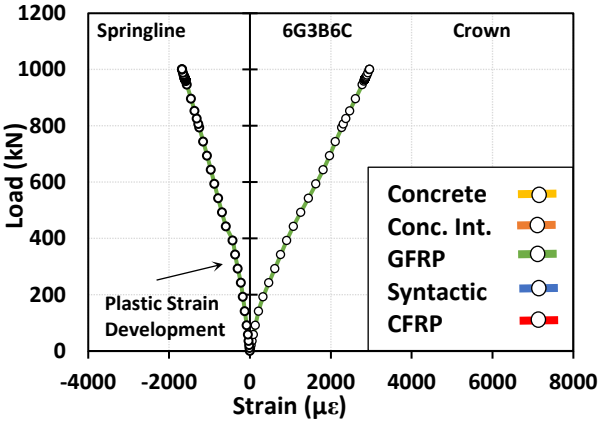

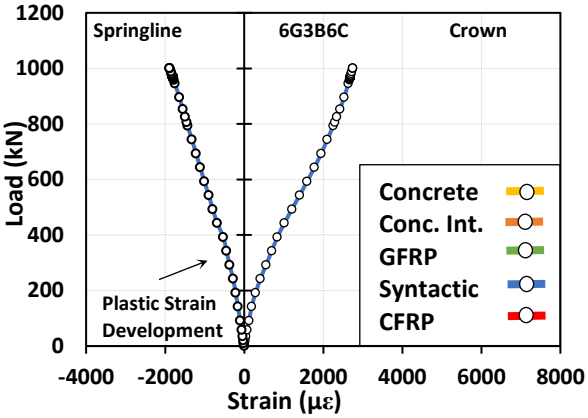

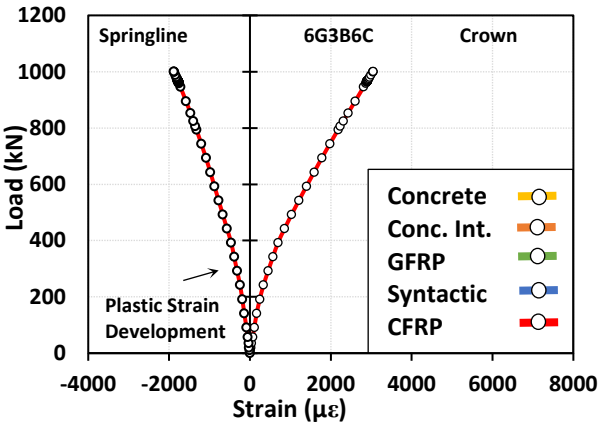

6G 3B 6C Plastic Strain:

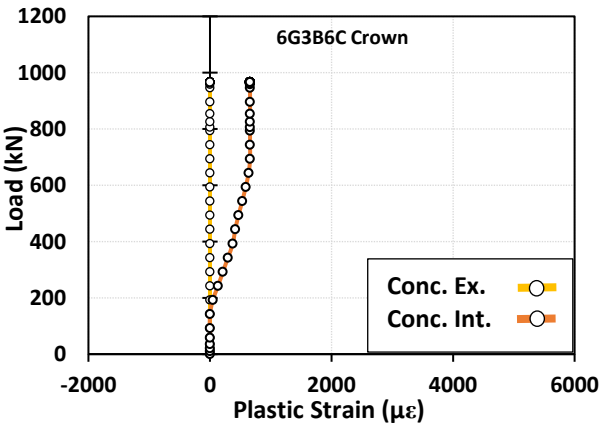

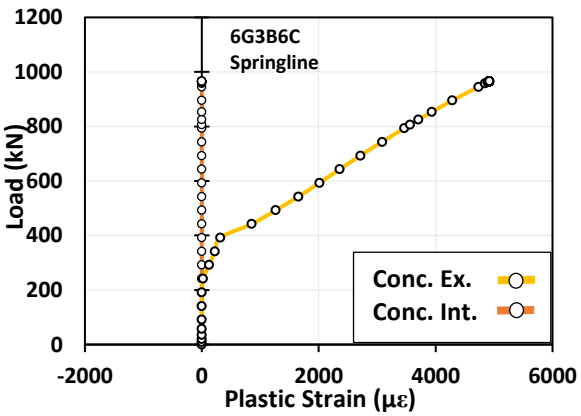

Appendix IV: Strain at multiple locations on CCCC-RCP 1

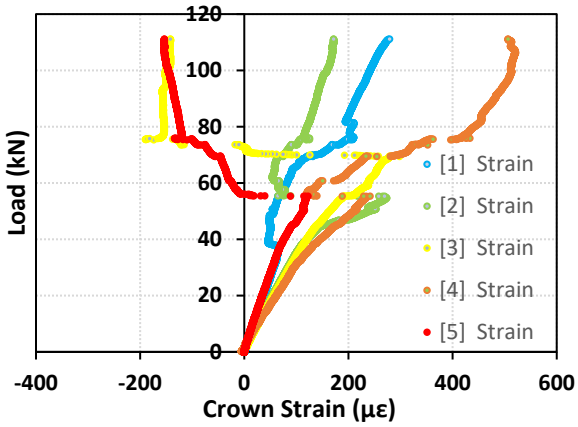

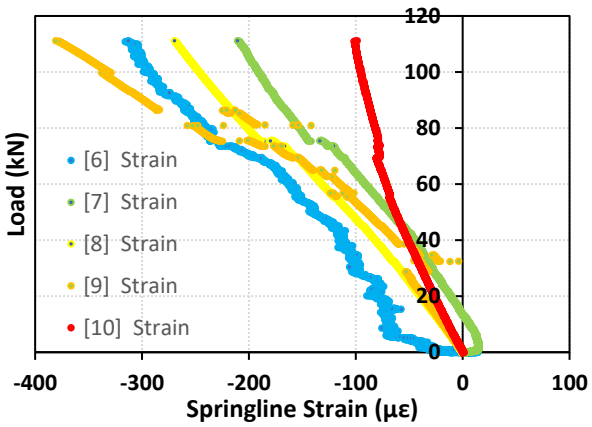

Strain Gauge (1-10) Layout on CCCC - RCP 1

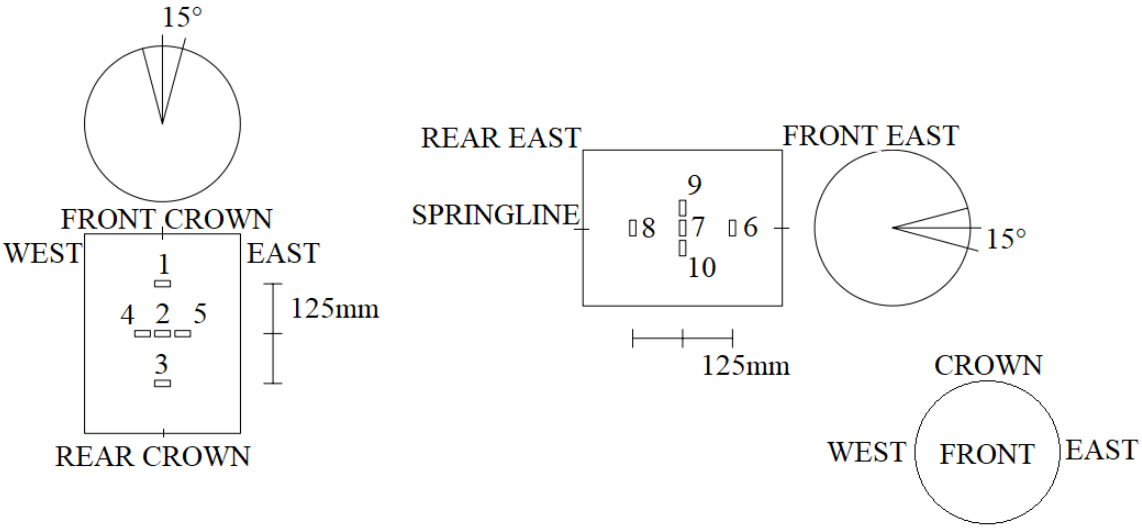

Appendix V: Complete D-Load vs. Vertical Displacement Plot

RCP 4 – GGBGG D-Load vs. Vertical displacement

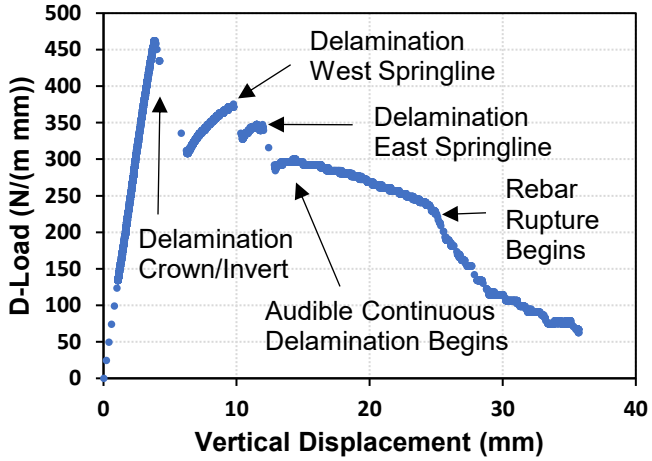

After delamination at peak load, the FRP liner continues to bear load until the concrete falls away as the rebar begins to rupture at the crown, invert and springline. After the load is released, the FRP liner often springs back to near circular shape. These measurements were not collected as they were not anticipated and not part of the study.